



INSTITUTO
SUPERIOR
TÉCNICO

UNIVERSIDADE TÉCNICA DE LISBOA
INSTITUTO SUPERIOR TÉCNICO

A MODAL-BASED CONTRIBUTION TO DAMAGE LOCATION IN LAMINATED COMPOSITE PLATES

Diogo Coelho de Carvalho Montalvão e Silva

(Mestre em Engenharia Mecânica)

Dissertação para obtenção do grau de Doutor em Engenharia Mecânica

Orientador: Doutor António Manuel Relógio Ribeiro

Júri

Presidente: Presidente do Conselho Científico do IST

Vogais: Doutor Manuel José Moreira de Freitas

Doutor Patrick Guillaume

Doutor José Fernando Dias Rodrigues

Doutor João Manuel Melo de Sousa

Doutor António Manuel Relógio Ribeiro

Doutor Mihail Fontul

Fevereiro de 2010



INSTITUTO
SUPERIOR
TÉCNICO

UNIVERSIDADE TÉCNICA DE LISBOA
INSTITUTO SUPERIOR TÉCNICO

A MODAL-BASED CONTRIBUTION TO DAMAGE LOCATION IN LAMINATED COMPOSITE PLATES

Diogo Coelho de Carvalho Montalvão e Silva

(Mestre em Engenharia Mecânica)

Dissertação para obtenção do grau de Doutor em Engenharia Mecânica

Orientador: Doutor António Manuel Relógio Ribeiro

Júri

Presidente: Presidente do Conselho Científico do IST

Vogais: Doutor Manuel José Moreira de Freitas
Doutor Patrick Guillaume
Doutor José Fernando Dias Rodrigues
Doutor João Manuel Melo de Sousa
Doutor António Manuel Relógio Ribeiro
Doutor Mihail Fontul

Fevereiro de 2010

Financially supported by Fundação para a Ciência e a Tecnologia and the European Social Fund under the III Community Support Framework.

Financiado pela Fundação para a Ciência e a Tecnologia e pelo Fundo Social Europeu no âmbito do III Quadro Comunitário de Apoio.

FCT Fundação para a Ciência e a Tecnologia

MINISTÉRIO DA CIÊNCIA, TECNOLOGIA E ENSINO SUPERIOR Portugal



União Europeia

Fundos Estruturais



Governo da República
Portuguesa



Programa Operacional Ciência e Inovação 2010

MINISTÉRIO DA CIÊNCIA, TECNOLOGIA E ENSINO SUPERIOR

Fui derrubado pelo vazio quando, por preconceito, considerei não manchar de tinta esta página; afinal, acabaria por ser nela que mencionaria os andarilhos que me fazem erguer a cada queda.

*aos meus Pais, Isabel e Júlio, por tudo
à minha irmã, Rita, pelo exemplo
à minha Quica, pelo futuro*

Título: Uma Contribuição para a Localização de Dano em Placas de Compósitos Laminados baseada em Análise Modal

Nome: Diogo Coelho de Carvalho Montalvão e Silva

Doutoramento em: Engenharia Mecânica

Orientador: Doutor António Manuel Relógio Ribeiro

Resumo

A necessidade de detectar dano em estruturas complexas levou ao desenvolvimento de técnicas que analisam parâmetros de vibração, dado que a resposta dinâmica de uma estrutura depende das suas características particulares. A maioria dos métodos tradicionais de detecção de dano com base no comportamento dinâmico assenta no pressuposto de que o dano conduz a uma redução local da rigidez.

Contudo, nenhuma abordagem se mostra eficaz para todas as situações de dano. Os materiais compósitos, que têm recebido uma crescente atenção por parte da indústria aeronáutica e não só, nomeadamente no que respeita a compósitos de matriz polimérica reforçados por fibras de carbono, são muito sensíveis a impactos de média e baixa energia. Tipicamente, ocorre Dano por Impacto Praticamente Invisível (*Barely Visible Impact Damage* - BVID), o que constitui uma falha que pode por em causa a integridade estrutural e é de difícil identificação. Identificar (detectar, localizar e quantificar) dano neste tipo de materiais ainda é um desafio, especialmente quando não se dispõe de uma grande quantidade de sensores ou de equipamento de custo elevado.

Neste trabalho é desenvolvida uma metodologia que faz uso de um número reduzido de sensores convencionais com o objectivo de localizar dano com um baixo custo, em compósitos laminados que estão sujeitos a impactos durante a sua utilização. Esta metodologia pode constituir um benefício considerável, em particular no caso da identificação de dano em componentes aeronáuticos, quando comparada com a maioria dos métodos usados actualmente.

Este trabalho também constitui um contributo para a comunidade científica uma vez que abordagens pouco comuns serão usadas para modelar o dano em materiais compósitos, nomeadamente no que respeita à utilização do amortecimento modal como parâmetro para a localização do dano.

Title: A Modal-based Contribution to Damage Location in Laminated Composite Plates

Name: Diogo Coelho de Carvalho Montalvão e Silva

PhD degree in: Mechanical Engineering

Supervisor: António Manuel Relógio Ribeiro, PhD.

Abstract

The need for damage detection on complex structures at an early stage, has led to the development of techniques that evaluate changes on vibration parameters, since the dynamic response of a structure is dependent on its particular characteristics. The generality of the vibration based damage detection techniques are based on the fact that damage will induce a local reduction on the component stiffness.

However, no single approach has proven appropriate for all situations. Composite materials, which are receiving an increasing attention in the aeronautical and other industries, namely Carbon Fibre Reinforced Polymers (CFRPs), are very sensitive to impacts of medium and low energy. Typically, Barely Visible Impact Damage (BVID) will occur, constituting an unsafe failure of difficult assessment. To assess (detect, locate and quantify) damage in this kind of material is still a challenge, especially if a huge amount of sensors or expensive equipments are not available.

In this work, a methodology that makes use of a reduced amount of conventional sensors is explored, with the aim of locating damage on laminated components that are subjected to impacts during service for a low cost. This represents a considerable benefit, namely for the assessment of damage in aeronautical components, when compared to most methods used today.

This work can also give a major contribution to the research community since uncommon approaches will be used to model damage in composite materials, namely the modal damping factor as feature for damage location.

Palavras-chave

Monitorização da Integridade Estrutural; Detecção de Dano; Delaminação; Amortecimento; Compósitos; Vibrações.

Keywords

Structural Health Monitoring (SHM); Damage Detection; Delamination; Damping; Composites; Vibrations.

Agradecimentos / Acknowledgments

I would like to express my thanks to everybody that, in one way or another, contributed to this work and helped me to develop it in its present stage.

First, I wish to express my innermost gratitude to my supervisor, Prof. António Manuel Relógio Ribeiro, PhD (IST), for his excellent guidance, for the enlightened discussions we had, for always being available, and for keeping me encouraged with his care and friendship.

I wish to dedicate my second acknowledgement to Prof. João Alexandre Botelho Duarte Silva, MSc (ESTS), former head of my division, for his learned advices in a wide range of topics, for his unending curiosity, interest shown and for the hours spent with me in the laboratory.

The institutions who contributed for the completion of this thesis are gratefully acknowledged:

- Instituto Superior Técnico (IST) for providing the main conditions for this research work, namely the Vibrations Laboratory of the Mechanical Engineering Department;
- Escola Superior de Tecnologia de Setúbal (ESTS), where I currently am a teaching assistant, for material and financial support and the use of many laboratory facilities;
- Fundação para a Ciência e a Tecnologia (FCT) and European Social Fund under the frame of III Community Support Framework, for financial support through grant reference number SFRH / BD / 27329 / 2006;
- Vrije Universiteit Brussel (VUB) for the use of equipment and laboratory facilities;
- Portuguese Aeronautic Industry (OGMA) for providing specimens' materials, either in the form of finished laminates or in the form of prepreg textiles, especially to Prof. Mário Almeida Santos, MEng and Prof. Carlos Alberto da Costa Domingos, MEng.

Special thanks are due to:

- Prof. Patrick Guillaume, PhD (VUB) and his PhD student and my former colleague Christof Maurits Gabriel Devriendt, MEng (VUB) for receiving me so kindly in Brussels several times, providing me all the comfort and technical conditions for my stay and study, as well as trusting me the use of top equipment;

- Prof. Mihail Fontul, PhD (IST) who provided pertinent recommendations and stimulating discussions, invaluable help during the experimental tests, and for all his support in general;
- Prof. Manuel José Moreira Freitas, PhD (IST) for all the help and advices, mainly in composite materials related subjects, and for the time spent helping me with the C-SCAN measurements;
- Prof. Ricardo António Lamberto Duarte Cláudio, PhD (ESTS) who was always available and wilful to help in many of the experimental tasks;
- Prof. João Manuel Candeias Travassos, PhD (ISEL) and his former student and laboratory technician Paulo Miguel Machado Caldeira, MEng (ISEL) for the expertise, hours of time spent and assistance during the manufacture of specimens;
- Prof. Rui José de Sousa Carvalho, PhD (IST) and Marco Alexandre de Oliveira Leite, MSc (ESTA) for the help in introducing damage into thin carbon fibre laminate specimens;
- Mr. Carlos da Conceição Faria (IST) for his technical support and companionship.

I would like to express my gratitude to my father, for understanding some of my frustrations, for his continuous encouragement, determined support and help over the years.

Finally, I wish to thank Francisca, for always displaying an enormous patience and for giving me strength by sharing all of my concerns with so much care.

Table of contents

Resumo.....	ix
Abstract.....	xi
Palavras-chave	xiii
Keywords.....	xiii
Agradecimentos / Acknowledgments.....	xv
Table of contents	xvii
List of abbreviations.....	xxi
List of symbols	xxv
List of figures	xxvii
List of tables	xxxiii
1. Introduction.....	1
1.1 Background	1
1.2 Objectives.....	5
1.3 Outline of the dissertation	6
1.3.1 General view	6
1.3.2 Second chapter: state-of-the-art	6
1.3.3 Third chapter: theoretical development	6
1.3.4 Fourth chapter: modelling and testing	8
1.3.5 Fifth chapter: validation of the index	8
1.3.6 Sixth chapter: conclusions	9
1.3.7 Annexes	9
2. State-of-the-art in SHM with special emphasis on composite materials.....	11
2.1 Introduction	11
2.1.1 Damage detection philosophy	14
2.1.2 The monitoring process	15
2.1.3 Composite materials: damage effects and modelling	17
2.2 Some damage detection techniques	19
2.2.1 Natural frequencies and FRFs	19
2.2.2 Mode shape changes	25
2.2.3 Mode shape and FRFs curvatures.....	27
2.2.4 ARMA family models	36
2.2.5 Dynamic flexibility	37
2.2.6 Modal strain energy.....	38
2.2.7 Transmissibility	40

2.2.8	Damping.....	42
2.2.9	Impedance based methods.....	44
2.2.10	Lamb waves	46
2.2.11	Neural networks	50
2.2.12	Time-frequency analysis	51
2.2.13	Hilbert transform	52
2.2.14	Principal component analysis and singular value decomposition	53
2.2.15	Instrumentation	57
2.2.16	Other methods.....	61
2.3	Prognosis.....	66
2.4	Final remarks.....	67
3.	Theoretical development.....	69
3.1	Foreword.....	69
3.2	Introduction to textile composites.....	70
3.3	Basics of the mechanics of composite materials	72
3.3.1	Engineering constants for orthotropic materials.....	72
3.3.2	Mechanics of materials approximation to stiffness.....	76
3.3.3	On estimating the properties of the laminate from the properties of the laminae	78
3.4	Fundamentals of vibration and modal analysis	81
3.4.1	Generalities.....	81
3.4.2	The Characteristic Response Function (CRF)	86
3.5	Damage in composite materials.....	89
3.5.1	Impact effects on composite materials	89
3.5.2	Damage effects on the response behaviour of composite materials	92
3.6	Proposal of a new damage index	93
3.6.1	Formulation of modal-based damage Indexes	93
3.6.2	On choosing the plane shape functions.....	97
4.	Modelling and testing	101
4.1	Specimens' build-up and material description	101
4.1.1	Material and layups	101
4.1.2	Manufacturing	103
4.1.3	Overall dimensions and density.....	106
4.2	Determination of mechanical properties	106
4.2.1	Young's modulus, shear modulus and Poisson's ratio.....	106
4.2.2	Hysteretic damping.....	111
4.3	Test setups for damage assessment.....	121
4.4	Finite element modelling.....	125
4.4.1	Relevance.....	125
4.4.2	Applying FE modelling to composite materials.....	126
4.4.3	Tests for FE model validation.....	129
4.4.4	Some considerations on FE modelling	131
4.4.5	Specimens' modelling	135

5. Numerical and experimental validation of the proposed index	141
5.1 Some notes on the procedural guidelines	141
5.1.1 Structural components	141
5.1.2 Extracting mode shapes and modal damping factors from the structure	142
5.1.3 Summary of the process	142
5.2 Numerical simulations	143
5.2.1 Damage characterization	143
5.2.2 Results	144
5.2.3 Final remarks	151
5.3 Experimental examples.....	151
5.3.1 Damaging the specimens.....	151
5.3.2 Results	156
6. Conclusions and future work	175
6.1 Conclusions	175
6.2 Future work	177
References.....	179
Annex A - About ANSYS®	199
Annex B – Summary of the equipment used during the dynamic tests.....	205
Annex C – On the improvement of experimental repeatability	207
Annex D – HARMONICA® Software.....	215
Annex E – BETAlab® Software	233
Annex F – MuDi® Software.....	251

List of abbreviations

2D	Two dimension
3D	Three dimension
ADSM	Absolute Difference of Strain Mode shapes
AE	Acoustic Emission
ARMAX	Auto-Regressive (AR) Moving Average (MA) with exogenous input (X)
ASCE	American Society of Civil Engineers
ASN	Aerospatiale Normalisation
BED	Boundary Effect Detection
BVID	Barely Visible Impact Damage
CAE	Computer Aided Engineering
CAMOSUC	Change of Mode Surface Curvature
CD	Curvature Differences
CDF	Curvature Damage Factor
CFRP	Carbon FRP
CLT	Classical Laminar Theory
CRF	Characteristic Response Function
COMAC	Coordinate MAC
DaDI	Damping Damage Indicator
DLAC	Damage Location Assurance Criterion
DLV	Damage Locating Vector
DRQ	Detection and Relative damage Quantification indicator
DSD	Dynamic learning rate Steepest Descent
DOF	Degree-of-Freedom
ECOMAC	Enhanced COMAC
EMA	Experimental Modal Analysis
EMD	Empirical Mode Decomposition
EMSDI	Element Modal Strain Damage Index
ESPI	Electronic Speckle Pattern Interferometry
ESTA	Escola Superior de Tecnologia de Abrantes
ESTS	Escola Superior de Tecnologia de Setúbal
EVS	Extreme Value Statistics
FCT	Fundação para a Ciência e a Tecnologia
FDAC	Frequency Domain Assurance Criterion
FDIE	Flexural Damage Index Equations
FE	Finite Element
FI	Flexibility Index
FFT	Fast Fourier Transform
FPDIM	False Positive Damage Indication Method
FreDI	Frequency Damage Indicator

FRF	Frequency Response Function
FRP	Fibre Reinforced Polymer
GAC	Global Amplitude Correlation
GLARE	Glass Laminated Aluminium Reinforced Epoxy
GLAST	Gamma-ray Large Area Space Telescope
GFRP	Glass FRP
GSC	Global Shape Correlation
HHT	Hilbert-Huang transform
HNDT	Holographic Non-Destructive Testing
IASC	International Association of Structural Control
ICF	Image Correlation Function
IMF	Intrinsic Mode Function
IRF	Impulse Response Function
ISEL	Instituto Superior de Engenharia de Lisboa
ISO	International Organization for Standardization
IST	Instituto Superior Técnico
ISVD	Iterative SVD
LAN	Local Area Network
LANL	Los Alamos National Laboratory
LASER	Light Amplification by Stimulated Emission of Radiation
LDV	LASER Doppler Vibrometer
MAC	Modal Assurance Criterion
MDLAC	Multiple DLAC
MEMS	Micro Electro-Mechanical Systems
MIMO	Multiple Input Multiple Output
MLE	Maximum Likelihood Estimator
MRPT	Minimum Rank Perturbation Theory
MSC	Mode Shape Curvature
MSCS	MSC Square
MSS	Mode Shape Slope
MSAC	Mode Shape Amplitude Comparison
MuDI	Multi-parameter Damage Indicator
NARMAX	Nonlinear ARMAX
NASA	National Aeronautics and Space Administration
NMD	Normalized Mode Difference
NWMS	Nonlinear Wave Modulation Spectroscopy
ODPR	Operational Deflection Pattern Recognition
ODS	Operational Deflection Shape
OGMA	Portuguese Aeronautic Industry
OMA	Operational Modal Analysis
PCA	Principal Component Analysis
PID	Proportional-Integral-Derivative
PMAC	Partial MAC

PSD	Power Spectral Density
PSF	Plane Shape Function
PVDF	Polyvinylidene fluoride
PZT	Piezoelectric Transducer / Piezoelectric lead-Zirconate-Titanate
RBF	Radial Basis Function
RD	Random Decrement
RMS	Root Mean Square
RMSD	RMS Deviation
RSVD	Robust SVD
RVAC	Response Vector Assurance Criterion
SD	Slope Differences
SDC	Specific Damping Capacity
sDNA	structural Diagnostics using Non-linear Analysis
SDOF	Single DOF
SEM	Spectral Element Method
SHM	Structural Health Monitoring
SIMO	Single Input Multiple Output
SIMONRAS	Single-Mode Nonlinear Resonance Acoustic Spectroscopy
SLM	Skeleton Linear Model
SQUID	Superconducting Quantum Interference Device
SVD	Singular Value Decomposition
TD	Translation Differences
TRP	Time Reversal Process
UFF	Universal File Format
VI	Virtual Instrument
VRD	Vector RD
VUB	Vrije Universiteit Brussel
WFEM	Wavelet FE Methods

List of symbols¹

A	Cross-sectional area
A_{ij}	Extensional stiffness matrix element (i, j)
\bar{A}	Modal constant
C_{ij}	Stiffness matrix element (i, j)
$[C]$	Viscous damping matrix
D	Damaged state of the system (when used as index)
$DaDI_{ij}$	Damping Damage Indicator (DaDI) at coordinates (i, j)
$[D]$	Hysteretic damping matrix
e	Exponential
E	Young's modulus
f, F	Force
$FreDI_{ij}$	Frequency Damage Indicator (FreDI) at coordinates (i, j)
G	Shear modulus
h	Laminate's thickness
H	Healthy (or reference, or baseline) state of the system (when used as index)
i	Imaginary unit, $i = \sqrt{-1}$
k	Stiffness
i, j, k	General indexes used to identify a coordinate, an element in a matrix, etc.
$[I]$	Identity matrix
\bar{K}^R	Stiffness residual
$[K]$	Dynamic stiffness matrix
$MuDI_{ij}$	Multi-parameter Damage Indicator (MuDI) at coordinates (i, j)
\bar{M}^R	Mass residual
$[M]$	Mass matrix element
n	Number of cycles
N	Number of DOFs; number of modes
${}_rPSF_{ij}$	Plane Shape Function (PSF) at coordinates (i, j) for mode r
Q_{ij}	Reduced stiffness matrix element (i, j)
r	Index generally used to define the mode number
\bar{R}	Complex residual
S_{ij}	Compliance matrix element (i, j)

¹ Due to the large amount of symbols that will not be used later in the text, those appearing in chapter 2 are not listed here. Furthermore, there are a few exceptions to the interpretation of the symbols as well as some indexes that have been removed from some symbols on this list, but the author believes they can be identified easily from the context. Anyhow, the entire notation is explained as it is introduced during the exposition, in order to clarify any questions that may arise.

t	Time
t_k	Thickness of a single layer
T_{ij}	Transformation matrix element (i, j)
U	Internal energy
U_0	Strain energy density
V	Volume
W_d	Damping weighting coefficient
W_{diss}	Energy dissipated per cycle of oscillation
W_f	Frequency weighting coefficient
δW	Incremental work per unit volume
x, X	Displacement in the x direction; or Cartesian coordinate; or response amplitude
\dot{x}	Velocity in the x direction
\ddot{x}	Acceleration in the x direction
\bar{X}	Phasor
y	Displacement in y direction; or Cartesian coordinate
z	Displacement in z direction; or Cartesian coordinate
α	Receptance
β	Characteristic Response Function (CRF)
δ	Logarithmic decrement
γ	Engineering shear strain
ε	Tensor shear strain
η	Hysteretic damping factor
θ	Fibres' orientation angle; or phase angle between the response and the force
κ	Scale factor for the weighting coefficients
λ^2	Complex eigenvalue
ν	Poisson's ratio
ξ	Viscous damping factor
σ	Stress; or standard deviation
τ	Shear stress
ψ	Mode shape element
ϕ	Mass-normalized mode shape element
$[\Phi]$	Mass-normalized mode shape matrix
ω	Angular frequency
ω_r	Natural angular frequency

List of figures

Figure 1.1: BMW Oracle Racing 90 trimaran (from http://bmworaccleracing.com).	2
Figure 1.2: Boeing 787 Dreamliner composite profile (Patterson (2009)).	2
Figure 2.1: Schematic concept of TRP based damage identification (in Sohn et al. (2005)).	63
Figure 3.1: Commonly used 2D weave patterns (Cox and Flanagan (1997)).	72
Figure 3.2: Stress on a cube element.	73
Figure 3.3: Layer's principal axis of a unidirectional reinforced lamina.	75
Figure 3.4: Rotation of the local coordinate system (123) around axis 3 towards the global coordinate system (xyz).	79
Figure 3.5: Dynamic models interrelation (hysteretic damping case).	84
Figure 3.6: Numerical simulation to show how low-frequency and high-frequency modes affect the receptance in the measured frequency range.	86
Figure 3.7: Orientation of delaminations (Abrate (1998)).	89
Figure 3.8: Delamination process in composite materials (Cantwell (2008)).	90
Figure 3.9: Pine tree and reverse pine tree damage patterns (Abrate (1998)).	90
Figure 3.10: Force vs. displacement curves for comparing an impact test with a quasi-static test during damage introduction in a composite material (Rilo et al. (2006)).	91
Figure 3.11: Damage extension seen in the direction of the fibres oriented to 0° at the centre plate cross section (Rilo et al. (2006)).	92
Figure 3.12: Failure modes of a laminate for a medium energy impact (Carvalho (2003)).	92
Figure 4.1: Lockheed Martin C-130 airplane.	102
Figure 4.2: ISEL's autoclave with the bagging schedule inside (left) and raw plates obtained after the polymerization process (right).	103
Figure 4.3: 1.2m width prepreg roll utilization for the production of 6 plates with 8 layers each.	103
Figure 4.4: Implantation of the raw plate into the autoclave and specimens' cutting scheme.	104
Figure 4.5: Polymerization cycle for production of specimens A1 to A6 and L1 to L3 (from OGMA's job plan no. 03/LAT/PRENSA - assembly no. F925.10902.200.00 A).	104
Figure 4.6: Glass tempered mould (left) and composite laminate mounted on the mould (right).	105
Figure 4.7: Bagging schedule for production of laminates A1 to A6 and L1-L3.	105
Figure 4.8: Example of the specimens used for the mechanical properties assessment in tensile testing.	107
Figure 4.9: Stress-strain charts in the elastic behaviour zone for specimens A2L and A2T in both the longitudinal and transversal directions.	108
Figure 4.10: Carbon fibre laminate specimen for the hysteretic damping assessment (obtained from specimen plate type 'A').	112

Figure 4.11: Hysteresis cycle (partial view).	114
Figure 4.12: Force-displacement quasi-static test: testing hardware.	115
Figure 4.13: Force-strain plot for a load magnitude of $\pm 3\text{kN}$ and a frequency of 0.1Hz	115
Figure 4.14: Force and strain for a load magnitude of $\pm 3\text{kN}$ and a frequency of 10 Hz . Left: force-strain plot; Right: superimposed force-time and strain-time plots.	116
Figure 4.15: Numerical extrapolations for the estimation of the hysteretic damping factor: Upper row: areas method; Lower row: phase method.....	117
Figure 4.16: Experimental free decay velocity (cantilevered CFRP laminate).....	119
Figure 4.17: Hysteretic damping along superimposed time blocks of 50 cycles.....	119
Figure 4.18: Hysteretic damping along superimposed time blocks of 50 cycles (larger clamping force).	120
Figure 4.19: Specimen beams type 'L' experimental setup.	122
Figure 4.20: Specimen plates' types 'A' and 'B' experimental setup.....	123
Figure 4.21: Specimen plate type 'A', with force excitation point and response measurement locations.	123
Figure 4.22: Specimen plate type 'B' force excitation points.....	124
Figure 4.23: 13×11 Scanning LDV mesh of measurement responses over specimen plate type 'B'.	130
Figure 4.24: Illustrating pictures of the experimental apparatus during missions 1 and 2.	131
Figure 4.25: Mission 3 experimental apparatus.	131
Figure 4.26: FE model of the specimen beam type 'L' with highlighted force transducer, push- rod and boundary conditions.	136
Figure 4.27: FE model of the specimen plate type 'A' with highlighted force transducer and damage locations.	136
Figure 4.28: FE model of the specimen plate type 'B' with highlighted force transducer locations.	137
Figure 5.1: Schematic representation of the algorithm sequential stack (steps illustrated with broken lines are only required to validate the FE model).....	143
Figure 5.2: First numerical results – 100x localized damping increase.....	145
Figure 5.3: Influence of the number of modes and modal order: numerical results for the lower order modes 1 to 8 (up to 400Hz).....	146
Figure 5.4: Influence of the number of modes and modal order: numerical results for the higher order modes 9 to 17 (from 400Hz up to 800Hz).....	146
Figure 5.5: Numerical results and weighting coefficients for a damping increase of 100x in region A1. These weighting coefficients are those used in the first result illustrated in figure 5.2.....	148
Figure 5.6: Numerical results and weighting coefficients for a damping increase of 10x in region A1.	148
Figure 5.7: Numerical results and weighting coefficients for a reduction in the Young's modulus of 10x in region A1.	148
Figure 5.8: Relative differences of the damping factor and frequency for three different damage simulations in the same location.....	149

Figure 5.9: Numerical results for the multi-damage scenarios.	150
Figure 5.10: IMATEK® impact test machine photos.....	151
Figure 5.11: Damage introduction into specimen plate B1H.	152
Figure 5.12: Experimental damage locations – specimen plates type A.....	153
Figure 5.13: Experimental damage locations – specimen plates type B.....	153
Figure 5.14: From left to right: ultrasonic imaging of specimen plates' cases A1DD, A2DD and A5DD.....	155
Figure 5.15: Frequency and damping between cases A0H, A0D and A0DD.....	156
Figure 5.16: Experimental location results for specimen beam type 'L'.....	158
Figure 5.17: Attempt to evaluate nonlinear effects caused by damage.....	159
Figure 5.18: Experimental location results for specimen plate type 'A'.....	161
Figure 5.19: Experimental location results for specimen plate type 'A' – lower order modes.	162
Figure 5.20: Experimental location results for specimen plate type 'A' – higher order modes.	163
Figure 5.21: Experimental location results (MuDI, FreDI and DaDI) and weighting coefficients for damage case A1D-A1DD in the whole measured frequency range (0 to 800 Hz, modes 1 to 18).	166
Figure 5.22: Experimental location results (MuDI, FreDI and DaDI) and weighting coefficients for damage case A2D-A2DD in the whole measured frequency range (0 to 800 Hz, modes 1 to 18).	166
Figure 5.23: Experimental location results (MuDI, FreDI and DaDI) and weighting coefficients for damage case A5H-A5DD in the whole measured frequency range (0 to 800 Hz, modes 1 to 18).	166
Figure 5.24: Experimental location results (MuDI, FreDI and DaDI) and weighting coefficients for damage case A2'H-A2'DD in the whole measured frequency range (0 to 800 Hz, modes 1 to 18).	167
Figure 5.25: Experimental location results (MuDI, FreDI and DaDI) and weighting coefficients for damage case A5'H-A5'DD in the whole measured frequency range (0 to 800 Hz, modes 1 to 18).	167
Figure 5.26: Specimen plate type 'A' experimental weighting coefficients – evolution with relative damage.	169
Figure 5.27: Frequency and damping relative differences for specimen plates A1, A2 and A5.	170
Figure 5.28: Experimental location results for specimen plate type 'B'.	172
Figure 5.29: Plot of the amplitude in dB of the sum of the 143 receptance FRFs obtained with the Scanning LDV for case B1H.	173
Figure A.1: SHELL63 geometry ("ANSYS® 11 Elements Reference Manual" (2007)).	199
Figure A.2: SHELL99 geometry ("ANSYS® 11 Elements Reference Manual" (2007)).	200
Figure C.1: Position of the accelerometers' connectors and cables.	208
Figure C.2: Comparison between FRFs obtained using different configurations of the accelerometers' cables.	209
Figure C.3: Drive-rod connection between exciter and force transducer.....	210

Figure C.4: Different types of push-rods and correspondent attachments to the shaker and to the structure (force transducer).	211
Figure C.5: Comparison between FRFs obtained using different push-rods.....	211
Figure C.6: Comparison between FRFs from different specimen plates.	212
Figure C.7: Amplitude of the averaged accelerance and accelerance standard deviation after 20 measurements on plate A4H.	213
Figure D.1: Example of a channel configuration on Measurement & Automation Explorer® ..	220
Figure D.2: Home Panel.	221
Figure D.3: Setup Panel.	222
Figure D.4: Measurement Panel.	227
Figure D.5: Results Panel. Plot of two FRFs' amplitudes.....	229
Figure D.6: Example of a results file generated by HARMONICA® (some cells were conveniently hidden for presentation purposes).	231
Figure E.1: Opening BETAlab® VI.	235
Figure E.2: Starting BETAlab® VI.	235
Figure E.3: Converting FRF data to receptance.	236
Figure E.4: BETAlab® screen after introducing the FRF input data.	237
Figure E.5: Zooming towards one single mode.	238
Figure E.6: Example of the influence of the "STEP" in the quality of the CRF. From top-left to right-bottom the value of the step is 1, 3, 5 and 7 respectively.....	239
Figure E.7: Frequency and Damping screens for the modal identification.	239
Figure E.8: Frequency and Damping screens for the modal identification: moving the band yellow horizontal lines.....	240
Figure E.9: Frequency and Damping screens for the modal identification: turning the "Negative values" red light off (into dark green).	241
Figure E.10: Lower part of BETAlab® screen after identifying the first mode.....	241
Figure E.11: Going towards the identification of the second mode.	242
Figure E.12: Going towards the identification of the second mode, after isolating the first mode from the experimental results.	242
Figure E.13: BETAlab® screen after finishing one identification round.	244
Figure E.14: Regenerated curve superimposed over the experimental curve before determining the residuals.	244
Figure E.15: Regenerated curve superimposed over the experimental curve after determining the residuals for curve number 1 (direct FRF).	244
Figure E.16: BETAlab® screen after finishing the whole identification process.	245
Figure E.17: HARMONICA®'s input file format example (some cells were conveniently hidden for presentation purposes).....	246
Figure E.18: PULSE™'s input file format example (some cells were conveniently hidden for presentation purposes).	247

Figure E.19: Mihail-Primoz's input file format example (some cells were conveniently hidden for presentation purposes).....	248
Figure E.20: BETAlab [®] results file structure (some cells were conveniently hidden for presentation purposes).	249
Figure E.21: BETAlab [®] auxiliary application screenshot for representing the mode shapes....	249
Figure F.1: Opening MuDI [®] VI.	252
Figure F.2: Starting MuDI [®] VI.	253
Figure F.3: Loading the file containing the geometrical Cartesian coordinates.	254
Figure F.4: Loading the file containing the FE model mode shapes (strains).	254
Figure F.5: Loading the file containing the BETAlab [®] 's project for the structural healthy state.	254
Figure F.6: Loading the file containing the BETAlab [®] 's project for the structural damaged state.	255
Figure F.7: MuDI [®] 's final screen for case B1H-B1D considering only modes 8 and 12 to 14....	255
Figure F.8: MuDI [®] 's upper part of the final screen for case B1H-B1D considering only modes 8 and 12 to 14 in which the cumulated error is less than 20%. Top right plot is FreDI's probability map alone and bottom right plot is DaDI's probability map. .	257
Figure F.9: Mode shape file format example (some cells were conveniently hidden for presentation purposes).	258
Figure F.10: Loading the files containing FE mode shapes individual modes (strains).	258
Figure F.11: Coordinates file format example (some cells were conveniently hidden for presentation purposes).	259

List of tables

Table 4.1: Specimens' types and designations adopted throughout the dissertation.	102
Table 4.2: Summary of the specimens' averaged values for the overall dimensions and density.	106
Table 4.3: Summary of the specimens' measured mechanical properties.	109
Table 4.4: Mechanical properties for generic carbon HR fibres and phenolique resin (Silva, A. J. P. F. (2001)).	110
Table 4.5: Specimens' type 'A' and 'B' material properties for a single (unidirectional-like) layer.	110
Table 4.6: Specimens' types 'A' and 'B' theoretical mechanical properties for the whole laminate.	111
Table 4.7: Hysteretic damping factor values obtained in the force-displacement tests.	117
Table 4.8: Hysteretic damping results summary.	121
Table 4.9: Comparison between experimental and numerical modes for specimen plate A1H (extract of the table comprising a total of 18 modes).	135
Table 4.10: Comparison between experimental and numerical modes for specimen plates B2H and B4H (selection from the table comprising a total of 22 modes).	138
Table 5.1: Snapshots of the final damage case in the loaded specimen plates (the images scales may not be exactly the same from case to case. All the photos were taken from around the same distance of 8 cm).	154
Table 5.2: Comparison between experimental and numerical modes for specimen plates A1H and A1D (first 8 modes in the 0 to 400Hz frequency range).	157
Table 5.3: Scoring table of the experimental results with specimen plate type 'A'.	165
Table 5.4: Specimen plate type 'A' experimental weighting coefficients.	168
Table B.1: Summary of the equipment used for the dynamic tests.	205

Chapter 1

Introduction

1.1 Background

The use of Fibre Reinforced Polymers (FRPs) as an alternative to conventional materials such as metallic alloys, is receiving an increasing attention, namely in the aeronautical, naval and automotive industries, because of their excellent mechanical properties in conjunction with their low weight and easy shaping.

In July 2009, the Swiss America's Cup Defender, Alinghi 5, set sail for the first time on lake Geneva. The 90 feet long catamaran will be used in a duel against the trimaran BMW Oracle Racing 90 in February 2010, in the 33rd edition of the America's Cup. Both these catamarans were totally built in carbon fibres. The goal is to have the lightest sailboat for travelling as fast as possible, yet being resistant to wind and sea adverse conditions.



Figure 1.1: BMW Oracle Racing 90 trimaran (from <http://bmworaccleracing.com>).

Composite materials are being used more commonly in aircraft construction to reduce weight. According to Patterson (2009) *“the Airbus A380 will be 25% by weight composites including 23% carbon fibre reinforced polymer and 3% GLARE fibreglass reinforced aluminium. Airbus has plans to expand the use of composites on future aircraft. (...) The Boeing 787 Dreamliner is pushing the envelope with a total composite of 50% by weight, including the integration of an all composite fuselage, wings and tail.”*

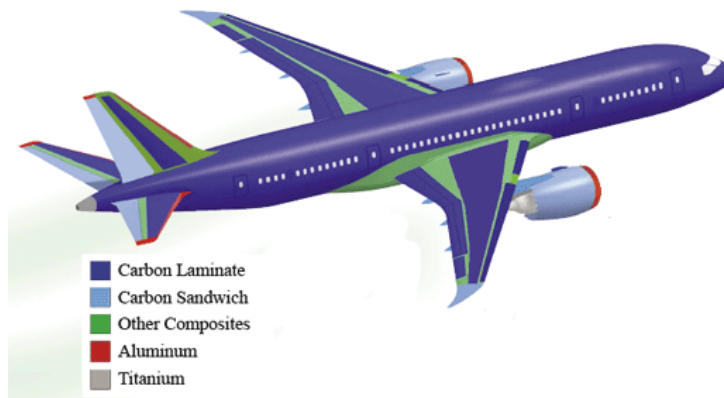


Figure 1.2: Boeing 787 Dreamliner composite profile (Patterson (2009)).

Nevertheless, composite materials are very different from metals with respect to their micromechanical interactions and their particular failure modes, which may be in the form of matrix cracking, fibre breakage, interlaminar delamination or voids (Sanders *et al.* (1992), Jacob *et al.* (1997), Matthews, F.L. (1999)).

Composite materials possess resistance and tenacity to density relationships many times greater than those of the most common metallic materials, such as steel, aluminium or

titanium. However, the extreme sensitivity of composite materials to impact loads constitutes a hindrance to its utilisation. In fact, in aeronautical structures, the components have to undergo (i) low energy impacts caused by dropped tools or mishandling during assembly and maintenance, (ii) medium energy impacts caused in-service by foreign objects such as stones or birds and (iii) high energy impacts caused by weaponry projectiles in military planes (Matthews, F.L. (1999), Silva, A. J. P. F. (2001) and Carvalho (2003)).

Typical failure modes in laminated composite materials caused by impacts may be found, for instance, in Carvalho (2003). In a high energy impact, penetration is total and the damaged area is generally small (order of magnitude of the projectile's cross-section). In a medium energy impact, it is usually possible to visually detect the damage location, which is characterized by a local indentation. In a low energy impact (but high enough to produce damage), only a very slight indentation will be seen on the impact surface. This level of damage is often referred to as Barely Visible Impact Damage (BVID). Generally, Carbon Fibre Reinforced Polymers (CFRPs) are very sensitive to medium and low energy impacts. Matrix cracks will appear and interact, leading to a delamination process. This matter has received some attention for damage analysis; for example, Morais *et al.* (2005) present a study on the influence of laminate thickness on the resistance to repeated low energy impacts on glass, carbon and aramid fabrics reinforced composites, for different levels of impact energy.

Interlaminar delamination highly reduces the part stiffness and buckling load, which, in turn, influences the structural stability. The influence on the resonant frequencies of the contact forces between delaminated layers, delamination extension and delamination location are studied by Zak *et al.* (1999).

Matthews, F.L. (1999) presents an overview which addresses the nature, consequences and detection of defects in FRPs. He distinguishes two groups in the nature of damage: the manufacturing defects and the handling, assembly and in-service damages. The consequences of damage and defects are also addressed, with respect to the composite performance when subjected to compression, tensile, flexural and shear loadings. Finally, some damage detection techniques applied to composite materials are summarized, embracing all the manufacturing and quality control processes.

Although composite materials are receiving a special attention from vibration-based damage detection techniques, other non-destructive techniques are also being developed, such as the HNDDT (Holographic Non-Destructive Testing), the ESPI (Electronic Speckle Pattern Interferometry) or the SQUID (Superconducting Quantum Interference Device) (Hiroshi *et al.* (2005), Ambu *et al.* (2006)).

Currently, a number of techniques exist for the identification and location of damage. Because all the techniques have their own advantages and disadvantages, there is not a general algorithm that allows the resolution of all kinds of problems in all kinds of structures. Every technique tends to have damage related sensitivities, i.e., a very sensitive technique may lead to the arising of false-positives², while a less sensitive technique may lead to false-negatives³, the latter case being more problematic.

Generally, damage can only be detected with a reasonable dimension. The quantification of damage and the remaining lifetime prediction are beyond any doubt the most difficult issues, the latter deserving a particular attention.

During the last years, a considerable investment in the development of instrumentation techniques has been observed, namely in the ones that recur to smart technologies for monitoring as well as in the use of high frequency waves, such as Lamb waves, for the detection of localized damage, i.e., with “small dimension”.

Most of the traditional methods are based on the fact that damage leads to appreciable reduction in the rigidity of a structural element. However, it must not be forgotten that a reduction in stiffness does not necessarily mean that there is a decrease in strength of the structural materials. This also represents one of the difficulties that Prognosis has to deal with in the future. Also, some authors argue that in some specific applications, combining static and dynamic experimental procedures is generally a good idea, since static and dynamic stiffness are different measurands. In structures made of composite materials there seems to be a tendency for the use of damping as a damage feature, once damping variations – associated to the dissipated energy – seems to be more sensitive to damage than the rigidity variations, mainly in what delamination is concerned (Keye *et al.* (2001), Kyriazoglou *et al.* (2004), Yam *et al.* (2004)). However, considering the more simple case of a crack in homogeneous materials, Testa (2005) observed there is a sharp transition in effects from closed to open crack conditions and that damping effects are greatly amplified at the transition state. Also the evaluation of nonlinearity seems to be a promising technique in damage detection in composite materials, since the delamination may cause nonlinear effects, again due to friction.

The use of statistic parameters has also deserved a considerable attention, given the experimental errors and incompleteness, as well as the environmental and operational conditions, which may disguise the damage effects. Nevertheless, the emergence of statistical

² In statistics, the failure to reject a false hypothesis is also called a *Type II error*.

³ In statistics, the rejection of a hypothesis that is true is also called a *Type I error*.

pattern recognition techniques, that allow the reduction of the number of used sensors, is not totally implemented so far.

1.2 Objectives

From the framework described above, this study will focus on some pending issues in the fields of damage detection and Structural Health Monitoring (SHM). However, no single approach has proven appropriate for all situations and, in many cases, the use of expensive equipment and a huge amount of sensors is required.

Also, recalling that composite materials are considerably used in the aeronautical industry, namely CFRPs, and that they are very sensitive to impacts of medium and low energy, BVID or damage not apparent on the surface may constitute an unsafe failure of difficult assessment.

The main purpose of the work presented in this thesis is to build a methodology that can be used by the industry to assess BVID on FRPs. To accomplish this, Frequency Response Functions (FRFs) will be measured to extract damage sensitivity features, such as frequency, modal damping and vibration modes.

In summary, this study aims at contributing for:

- understanding in which way the random variables inherent to experimental testing have an influence in the dynamic response measurements on laminated light structures;
- understanding in which way a real damage comprising multiple delaminations and fibre breakage, affects the laminate dynamic behaviour, namely with respect to:
 - the damping values;
 - frequency shifts;
 - nonlinear effects;
- the development of damage location techniques of existing damage in CFRPs' shell panels, by means of classical experimental procedures.

The importance of these goals, both for the industrial and academic communities, should be stressed out. First, assessing damage in this kind of components is still a challenge, especially if self-instrumented components, a huge amount of sensors or expensive equipments are unavailable. In this work, a methodology that makes use of a reduced amount of conventional sensors is explored, with the aim of giving a reliable prediction of damage location, for a low cost, on real components that are subjected to impacts during service. Secondly, this work can

give a major contribution to the research community since new approaches will be followed, including the experimentally measured hysteretic damping as indicator for damage assessment.

1.3 Outline of the dissertation

1.3.1 General view

Taking into account the main objectives mentioned above, the substructure of this thesis follows the development of the research performed in the vibration-based damage detection area. While it does not obey a chronological timeline of the events, its structure is meant to guide the reader into a certain line of thought. This work is structured in six chapters, including this one, and several annexes.

1.3.2 Second chapter: state-of-the-art

The second chapter consists of a thorough state-of-the-art review in SHM with special emphasis on composite materials. It should be noted, however, that this review is not intended to be a general, all-encompassing review; it was planned as the starting point for this study focusing on damage detection, location and assessment on a certain kind of structures. The major part of this review was earlier presented by the author, Montalvão *et al.* (2006a).

The bibliographic references are presented at the end of the main body, by alphabetic order, and its relatively large size is due to the extensive state-of-the-art presented in chapter two.

1.3.3 Third chapter: theoretical development

In the third chapter, what may be seen as an introduction to composite materials and modal analysis, including the aspects (and only those) that are relevant for the development of the proposed methodology, is presented. Some of the issues covered seem to be beyond the scope of the work itself, but their inclusion is appropriate for justifying some of the ideas approached as suggestions for future work. This chapter is divided into six sections.

The first section is a foreword note to the reader, to explain why some aspects received some attention while others, elsewhere considered more important, were deliberately left outside.

In the second section, some aspects concerning textile composites, namely weaves, are mentioned, starting from the definition of a textile to some of the particularities encountered when comparing to more conventional composite materials such as those built from layers of unidirectional fibres. The purpose is to justify some of the options made throughout the work, especially to what concerns modelling, as the experimental structures under test were all satin weaves.

In the third section, theoretical background in the domain of the mechanics of composite materials is summarized with the aim of introducing important equations that allow the determination of the elastic properties of the laminate from the properties of the layer. The relationships between the engineering constants are also established for both orthotropic and isotropic materials, which are typical approximations for most of the composite structures used in practice. Furthermore, the principles governing the damage location method proposed afterwards are partially based on some of the concepts addressed here.

Since this method is vibration-based, it is important to place the reader into the fundamentals of modal analysis, which is done in the fourth section of this chapter. Roughly speaking, the dynamic behaviour of a system can be described by means of three properties: the mass, the stiffness and the damping. Seeing that damage can be defined as a change in at least one of these properties, it is important to understand how this is related to composite structures and how these properties can be assessed from experimentally measured data.

In the fifth section, a brief description about the impact effects on composite materials is presented. It is important to know the morphology of damage in a composite laminate to understand why some assumptions are made and why this work can be relevant for the scientific community.

It is in the final section of this third chapter that an index for damage location in composite laminates is proposed. A first version of the index was already proposed by Montalvão *et al.* (2009). In real damage scenarios both delamination and fibre breakage can be expected, especially for thin laminates (Abrate (1998), Carvalho (2003)). In such a case, it seems to be reasonable to consider both frequency shifts and damping changes as features for locating damage. How significant is the contribution of either one of these features in the location index is determined by some sort of metric based on the standard deviation of the modal results. This section reflects this sequential process for a convenient understanding of the assumptions made throughout.

1.3.4 Fourth chapter: modelling and testing

Modelling of the specimens used to evaluate the proposed technique is explained in the fourth chapter. This chapter is divided into four major sections.

In the first section, the composite specimens are fully described. Composite materials, when in the form of laminates, can be seen as macroscopic structures that depend not only on the properties of an elementary block of material (the layer) but in the form it is manufactured as well. With the same elementary blocks it is possible to build laminates with completely different behaviours: from anisotropy to isotropy, everything seems possible. Thus, despite the fact the specimens used are simple structures (rectangular plates), it is important to have a deep knowledge of the material's constitution and arrangement, especially for modelling.

In the second section the mechanical properties of the specimens' constituting materials are determined, namely the Young's and shear's moduli, Poisson's ratios and damping factors. Several different approaches, from theoretical to experimental, are considered. As far as damping is concerned, the peculiarities of its measurement in composite materials was already addressed in an international conference by Montalvão *et al.* (2006b).

It is in the third section that the experimental apparatus used for the damage location is introduced. The reason for its inclusion at this point is that some of the test options will be required when building the Finite Element (FE) models: for instance, the numerical models used to simulate damage situations were built under similar conditions.

In the fourth and final section, FE modelling is addressed, where the assumptions and approximations made during modelling are clarified. Many of the issues that a FE modeller is concerned about, from the point of view of the user, are covered here: the choice of the software, element types, approximate value of the optimal number of elements, material behaviour, influence of added mass, etc. Validation and choices are accomplished by comparing the FE models with experimental results obtained using a Scanning LASER Doppler Vibrometer (Scanning LDV). This is necessary for computing a function, called Plane Shape Function (PSF), based on the mode shape of the entire structure which, in the studied cases, is composed by the specimen plus the force transducer. This PSF function was obtained with a commercial FE modelling software.

1.3.5 Fifth chapter: validation of the index

It is in chapter five that the numerical and experimental validation of the proposed index is accomplished. In other words, the results are presented and discussed. This chapter is divided

into three sections, starting with some notes on the procedural guidelines, which in fact is a summary with some of the steps to be performed during the entire application of the method.

In section two, numerical examples are introduced, tested and discussed. A total of eleven damage scenarios are considered. Damage was characterized by a local variation of either the damping factor or the Young's modulus. Multi-damage scenarios were also tested by increasing damping at two regions at the same time.

The third and last section of this chapter includes several experimental examples: a quasi-isotropic beam, a quasi-isotropic plate (five damage scenarios, plus four cases of increasing damage) and an orthotropic plate (three damage scenarios, plus two cases of changing force). A thorough discussion on the results is done in this chapter.

1.3.6 Sixth chapter: conclusions

The sixth chapter points out the conclusions, the level reached and the limitations of this work. It makes references to the original ideas developed in this work, highlighting the importance of this research and mentioning future work to be developed.

1.3.7 Annexes

The first annex, annex A, contains a brief description about the elements chosen, the analysis type and other options for FE modelling with ANSYS®.

In annex B, a table listing the equipment used during dynamic tests is presented.

The following annex, annex C, is concerned with the experimental apparatus, in the sense of minimizing systematic errors. Tests took place to identify some of the external variables in Experimental Modal Analysis (EMA) that affect the repeatability of the results. The effects of transducers' electric cables or changing push-rods showed to be of concern.

The next three annexes are user manuals/tutorials for the operation of custom software that were fully developed by the author: HARMONICA® (annex D), BETAlab® (annex E) and MuDI® (annex F). The first software is a stepped-sine spectrum analyzer which allows evaluating nonlinearities, and was presented at an international conference by Montalvão and Fontul (2006). The second software, BETAlab®, is a modal identification program for finding the dynamic properties of structures from the FRFs. The third software, MuDI®, is the program that allows implementing the damage location algorithm to its full extent. All this manuals are concluded with a section where developments that are foreseen to be useful in future versions are suggested.

Chapter 2

State-of-the-art in SHM with special emphasis on composite materials

2.1 Introduction

Vibration-based SHM and damage detection is a field of study of great interest to many people. Important advances in this field were described by Doebling *et al.* (1996), Doebling *et al.* (1998) and Sohn *et al.* (2003), which present very comprehensive surveys covering the period until early 2002. Many of the works cited in these surveys still represent the state of the art, motivating their inclusion in this work.

Other reviews may bring insight in more specific branches of damage detection and SHM. For example, a state-of-the-art overview on rotating machinery monitoring was given by Randall (2002). Carden and Fanning (2004) presented a review covering structural engineering related

aspects. Uhl and Mendrok (2004) discussed the applicability of modal model-based methods in structural diagnosis. Farrar *et al.* (2004) presented a brief, yet comprehensive overview of nonlinear system identification techniques used for damage-sensitive feature extraction from measured data. More recently, Su *et al.* (2006) provided a comprehensive review on the state of the art of Lamb wave-based damage identification approaches for composite structures, in which half of the review is focused on advances given between 2001 and 2004.

In the present chapter, mainly based on a review presented earlier by the author of this thesis (Montalvão *et al.* (2006a)), special attention will be given to methods in which composite materials and structures are used as case studies. Complementary reviews may bring further insight on vibration-based model-dependent damage detection in composite materials combined with modal analysis, such as the one from Zou *et al.* (2000). Nevertheless, given the huge range of methods described in the literature, many damage detection and SHM techniques will not be explored in detail in this review, even where they are touched on briefly. These include such examples as rotating machinery, online SHM and monitoring systems, updating, sensitivity-based methods (which are widespread in model updating), non-linear systems, wireless sensing, civil infrastructures, joints and couplings, conditioning, chaotic time series excitation. A positive decision was made, however, to include methods based on natural frequencies, FRFs, mode shapes, mode shape and FRF curvatures, Auto-Regressive Moving Average (ARMA) family models, dynamic flexibility, modal strain energy, transmissibility, damping, impedance, Lamb waves, time-frequency analysis, Hilbert transforms, Principal Component Analysis (PCA) and Singular Value Decomposition (SVD), neural networks, instrumentation and others.

A general definition of damage is given by Sohn *et al.* (2003) as “...changes introduced into a system that adversely affect its current or future performance. Implicit in this definition is the concept that damage is not meaningful without a comparison between two different states of the system, one of which is assumed to represent the initial, and often undamaged, state.” For example, one may have a structural crack (stiffness change), bridge pillar silting (boundary condition change), counterweight balancing loss (mass change) or looseness in a bolted joint (connectivity change) (Maia (2001)).

The need to be able to detect damage in complex structures has motivated the development of techniques based upon variations in the structure’s dynamic behaviour. For instance, the method used to monitor the condition of train wheels is much the same today as it was 100 years ago: a “modal specialist” walks along the train cars hitting the wheels with a hammer and listening to their response (Maia (2001)). In conditioning maintenance, vibration is without any doubt more straightforward as an indicator of the machine state than most other

indicators, such as temperature, pressure, flow or tribology features (Wowk (1991)). In another field of application, Vescovo and Fregolent (2005) use an acoustic, non-invasive experimental technique to assess the partial detachment of plaster portions in artistic frescoes. It is even argued by Bonfiglioli *et al.* (2005) that monitoring and assessing the health state of infrastructures is one of the largest industries in the world.

The main idea behind damage detection techniques based on structural dynamic changes is the fact that the modal parameters (natural frequencies, mode shapes and modal damping) are functions of the physical parameters (mass, stiffness and damping) and thus it is reasonable to assume that the existence of damage leads to changes in the modal properties of the structure.

According to Doebling *et al.* (1996), an ideal robust damage detection scheme should be able to identify damage at a very early stage, locate the damage within the sensor resolution being used, provide some estimate of the extent or severity of the damage and predict the remaining useful life of the structural component in which damage was identified. The method should also be well suited to automation, and should be independent of human judgment and ability.

Betti (2005) points out that no single approach is appropriate for all situations, making the following basic distinctions between approaches: linear vs. non-linear, output only vs. input/output, on-line vs. off-line, time domain vs. frequency domain, parametric vs. non-parametric and time varying vs. time-invariant.

Operational and environmental conditions, such as temperature, humidity, loads and boundary conditions, should also be addressed, since in many cases the changes they cause can “hide” those resulting from damage. For example, Farrar *et al.* (1994), having done several measurements on the I-40 bridge over the Rio Grande in Albuquerque in the state of New Mexico in the USA, observed that temperature plays a major role in the dynamic properties of the bridge. They introduced four different levels of damage by gradually cutting one of the bridge girders, corresponding to a loss of stiffness. However, instead of the expected result, they observed an increase in the fundamental frequency for the first two damage cases, and concluded that such results were mainly due to temperature changes and temperature gradients in the bridge. Many other researchers, such as Woon and Mitchell (1996a)(1996b), Andersen *et al.* (1997), Alampalli (2000), Peeters and De Roeck (2000), Kullaa (2002), De Roeck and Degrauwe (2005), Steenackers and Guillaume (2005) or Yan *et al.* (2005a)(2005b) address the effects of the environmental or operational conditions in SHM. Woon and Mitchell (1996a) studied the sensitivity of natural frequencies to the relative humidity, but concluded that this had little significance when compared to the effects of temperature. Cawley (1997) used an

analytical model of a cantilevered beam to compare the effect of crack formation to the effect of beam length in the natural frequencies, observing that thermal expansion (simulated by changes in the beam length) has more significant effects on the natural frequencies than cracks. Kullaa (2002) tried to eliminate the environmental influences in modal parameters, using an approach based on factor analysis, in which it is assumed that there exist a set of common factors with effects on the modal features that can be subtracted from the observations.

2.1.1 Damage detection philosophy

Rytter (1993) introduced a damage state classification system which has been widely accepted by the community dealing with damage detection and SHM. Following these lines, the damage state is described by answering the following questions (Sohn *et al.* (2003)):

1. Is there damage in the system? (existence)
2. Where is the damage in the structure? (location)
3. What kind of damage is present? (type)
4. How severe is the damage? (extension)
5. How much useful life remains? (prognosis)

Generally, identification of the damage type and extent require prior knowledge of the structural behaviour in the presence of each of the possible expected failure modes for future correlation with experimental data, which is normally achieved by resorting to analytical models. For example, in operational monitoring, the modal parameters of the damaged structure must be compared to the parameters of the structure in its undamaged state, in what is called *global diagnosis*. Once damage existence is detected, the use of a model of the structure in a damaged state may be used to determine the damage location, in what is called *local diagnosis* (Uhl and Mendrok (2004)).

Some difficulties may be encountered in the practical application of modal models, such as the knowledge of excitations and loads during machine operation, with several sources and with unknown distribution along the system. However, several output-only modal identification techniques can be found in the literature: for example Guillaume *et al.* (1999), Parloo *et al.* (2002a), Brincker and Andersen (2003), Rodrigues *et al.* (2004), Galvin and Dominguez (2005), and Devriendt *et al.* (2009)

Prognosis, which is traditionally related to fracture mechanics and fatigue, is starting to be brought up by the modal analysis community as a field of interest, as seen in Farrar *et al.* (2003) and Inman *et al.* (2005).

2.1.2 The monitoring process

The monitoring process involves the observation of a system over long periods of time, using samples of experimental data acquired periodically with adequate sensors. It also involves sensitivity feature extraction and statistical correlations to determine the actual “health” of the system. Farrar *et al.* (2001) and Sohn *et al.* (2003) acknowledge the problem of damage detection in the context of a statistical pattern recognition paradigm. Along these lines, this paradigm can be described as a four-step process:

1. Operational evaluation;
2. Data acquisition, fusion, and cleansing;
3. Feature extraction and information condensation;
4. Statistical model development for feature discrimination.

Sections 2.1.2.1 to 2.1.2.4 are mainly based on the very comprehensive survey of Sohn *et al.* (2003).

2.1.2.1 Operational evaluation

Operational evaluation answers questions related to the damage detection system implementation, such as economic issues, possible failure modes, operational and environmental conditions and data acquisition related limitations. For example, Aktan *et al.* (2000) present and discuss the prerequisite issues in creating a successful monitoring program.

Ruotolo and Surace (1997) were among the first to explicitly address the possibility of having multiple baseline configurations, proposing a technique to distinguish between changes caused by working conditions and resulting from damage, based on the SVD. Vanlanduit *et al.* (2005) also used a SVD based system to detect damage in structures subjected to different operational conditions, including different working excitation levels, geometrical uncertainties and surface treatments.

Kook and Sohn (2009) recently introduced a nonlinear PCA technique, where an auto-regressive and auto-regressive with exogenous inputs (AR-ARX) model is first constructed to

extract the damage-sensitive features from measured time signals. Then, nonlinear PCA is applied to characterize the hidden relationship between unmeasured environmental and operational parameters and extracted damage-sensitive features.

2.1.2.2 Data acquisition, fusion and cleansing

Data acquisition is concerned with the quantities to be measured, the type and quantity of sensors to be used, the locations where these sensors are to be placed, sensor resolution, bandwidth, and hardware. This part of the process is application specific and heavily dependent on economic factors. Another consideration is the periodicity for data acquisition. For instance, if the growth of a fatigue crack is to be monitored, then the data must be measured in an almost continuous way. On the other hand, if measurements are to be made under varying operational and environmental conditions, data normalization helps distinguish signal changes caused by operational and environmental conditions from those caused by damage. Sohn *et al.* (2001) observed that the natural frequency of a bridge over the Alamosa canyon in the state of New Mexico in the USA suffered 5% deviations over a 24 hour period due to temperature variations.

Sohn *et al.* (2003) acknowledged that, according to Klein (1999), data fusion first appeared as a result of defence organisations attempting to formalize procedures for integrating information from diverse sources, with the purpose of determining battlefield situations and preventing threats. Data fusion, as a discipline of SHM, is the ability to integrate data acquired from the various sensors in the measurement chain.

Data cleansing is the process of selecting significant data from the multitude of information, i.e., the determination of which data is necessary (or useful) in the feature selection process.

2.1.2.3 Feature extraction and information condensation

Within the paradigm defined by Farrar *et al.* (2001) and Sohn *et al.* (2003), the field of damage detection which has received the highest attention is feature extraction. Feature extraction is the process of identifying damage sensitive properties, which allow distinguishing between the damaged and undamaged structural states.

Information condensation becomes increasingly advantageous and necessary as the quantity of data increases, particularly if comparisons are to be made between sets of data obtained over the life cycle of a system. Condensation may be seen as a form of data fusion.

The evolution of the philosophy of damage detection and SHM over the last years can be best understood by comparing the surveys of Doebling *et al.* (1996) and Sohn *et al.* (2003). In the first one, the statistical pattern recognition paradigm, around which the second one was written, is not even mentioned; the concepts of operational evaluation, data acquisition, fusion and cleansing and statistical model development for features discrimination were matters whose relevance was not deemed to be noteworthy of exclusive and directed research, and were addressed only as parts of the feature extraction process.

2.1.2.4 Statistical model development for feature discrimination

This is the part of the SHM process that had received the least attention prior to the end of the last century. When data are available from both the undamaged and damaged structure, the statistical pattern-recognition algorithms fall into the general class referred to as *supervised learning*. *Unsupervised learning* refers to the class of algorithms that are applied to data not containing examples from the damaged structure (obtained, for instance, from models) (Sohn *et al.* (2003)).

An important issue in the development of statistical models is to establish the model features sensitivity to damage and to predict false damage identification. In this context, one may have either false-positives, in which damage is identified though it did not happen, or false-negatives, in which damage is not identified though it is present. Despite the fact that both these situations are undesirable, the second one can obviously lead to more severe consequences.

2.1.3 Composite materials: damage effects and modelling

Maheri and Adams (2003) used Classical Laminate Theory (CLT) in conjunction with a numerical Rayleigh-Ritz method for estimation of the modal damping of anisotropic laminates in free vibration, concluding that a good correlation between the theoretical and experimental results was achieved. Though not explicitly related to damage detection techniques, studies such as these can help researchers in the field of damage detection, since damping may represent a useful feature for damage evaluation in composite materials.

Kisa (2004) investigates the effects of multiple cracks on the dynamic properties of a cantilever Carbon Fibre Reinforced Polymer (CFRP) beam. The theoretical model integrates fracture mechanics and substructure coupling, where cracks are modelled as rotational springs. The

effects of the location and depth of the cracks, and the volume fraction and orientation of the fibres, on the natural frequencies and mode shapes of a beam with transverse cracks are explored. Kisa (2004) affirms that the approach followed can be used for the analysis of non-linear effects, such as the interface contact that occurs when the crack closes.

Shu and Della (2004) studied the free vibration of beams with multiple enveloping delaminations using an analytical model based on Bernoulli-Euler beam theory. The influence of the delamination size and its location on the first two natural frequencies and mode shapes is also discussed.

Ostachowicz and Zak (2004) presented some results on damped vibration of a laminated cantilever beam with a single closing delamination. The vibration of the beam is studied in the time domain using a dynamic contact algorithm developed by those authors, based on the Newmark method and incorporating a procedure based on the Newton-Raphson method for solving the equation of motion. They analyze the vibration in the frequency domain. The vibration responses of the beam due to various harmonic and impulse excitations are also considered, with different delamination locations and for different delamination lengths, as well as changes in the damping dissipation energy due to delamination.

Le Page *et al.* (2004) developed bi-dimensional (plane strain) FE models to analyze matrix cracking development in woven fabric laminates, as a function of the number of reinforcing layers. It was shown that stiffness is relatively insensitive to these geometric variations, although the strain energy release rate related to the crack formation is significantly influenced by its location. Notably, where the crack formation is associated with local bending, the energy release rate increases with deformation. The inclusion of geometric non-linearities showed to affect the results for models which exhibit higher bending deformation. Also, FE models of cross-ply laminates were used both to serve as a comparison and to evaluate whether the behaviour of woven fabric laminates can or cannot be described in terms of cross-ply laminates.

Tippetts and Hemez (2005) developed FE models to predict impact damage in composite plates. The failure modes addressed are ply splits (a special combination of matrix cracking and debonding with fibre breakage) and delamination. The plate structural model uses a finite element formulation with a cohesive zone model to simulate the possible fracture surfaces characteristic of impact damage. This model was validated with experimental tests.

Using a basis of linear fracture mechanics, the Castigliano theorem and CLT, Wang, K. *et al.* (2005) investigated the coupled bending and torsional vibration of a fibre-reinforced composite cantilever beam with an edge surface crack. Some important conclusions were

drawn: the natural frequency shifts, along with observations on the mode shape changes, may be used to detect both the crack location and its depth for on-line SHM. Also, the model and results presented may be useful for predicting flutter speed reduction in aircraft with composite wings due to fatigue cracking.

Mishnaevsky Jr. and Brøndsted (2008) present a review of mathematical methods for modelling deformation, damage and fracture in FRPs. The models were classified into five main groups (the first three belonging to the broader group of phenomenological approaches): shear lag-based; fibre bundle models and their generalisations; fracture mechanics and continuum damage mechanics based models; analytical models; and numerical continuum mechanical models. As conclusions, among many other challenges, they point out that when analyzing the strength, damage and fracture of FRPs, the points of interest lie in the area of the mesomechanics (rather than micromechanics): the interactions between many microstructural elements, and many microcracks/cracks play leading roles for the strength of the FRPs.

Hochard *et al.* (2001) and Thollon and Hochard (2009) developed ply-scale damage models (fibre-matrix debonding and cracks on the scale of the yarns) for predicting the mechanical behaviour of woven fabric composites based on continuum damage mechanics. The model describes the loss of stiffness and inelastic strain occurring in the warp, weft and shear directions and is obtained by replacing the woven ply by two stacked unidirectional plies, for which a classical model can be used.

2.2 Some damage detection techniques

2.2.1 Natural frequencies and FRFs

The development of modal analysis techniques for damage detection and SHM arose from the observation that changes in the structural properties have consequences on the natural frequencies. Nevertheless, the relatively low sensitivity of natural frequency to damage requires high levels of damage and measurements made with high accuracy in order to achieve reliable results. Moreover, the capacity to locate damage is somewhat limited, as natural frequencies are global parameters and modes can only be associated with local responses at high frequencies.

Methods based on natural frequency shifts often fall into one of two categories: the forward and the inverse problem. The forward problem consists in determining what the natural frequency changes due to a known damage case (which may include its location, extension and

type) will be. Typically, damage is modelled numerically and the natural frequencies are measured experimentally and compared to those related to each of the damage cases initially predicted. The inverse problem consists of determining damage parameters, such as crack length or location, from changes in the natural frequencies.

According to Doebling *et al.* (1996), Lifshitz and Rotem (1969) present what may be the first journal article to propose the use of vibration measurements for damage detection. They search for changes in the dynamic moduli, which can be related to shifts in the natural frequencies, to detect damage in elastomers.

Cawley and Adams (1979) give a formula for damage detection, location and quantification, based on the ratio between frequency shifts for modes i and j , $\Delta\omega_i/\Delta\omega_j$. Location is determined by minimizing the error between the measured frequency shifts of a pair of modes and those predicted by a local stiffness reduction model. In this formulation, neither multiple damage sites nor damping changes are considered, though the authors agreed that damping might suffer an increase with damage. The results are based on FE models of aluminium and CFRP plates.

Tracy and Pardoen (1989) presented the experimental results of a study into the effects of the length of a midplane delamination in the frequency shifts of the first four modes of orthotropic graphite-epoxy laminate beams. The analytical model divides the beam into a total of four sections: above, below and on the left and right sides of the delamination. For midplane centred delamination, it was observed that its presence degraded the even numbered vibration modes more rapidly than the odd numbered vibration modes. Unless the delamination was in a region of the mode shape where the shear forces were high, the natural frequency would not be significantly modified. Thus, in the presence of delamination in areas where the mode shape exhibits high curvatures (second derivative of deflection), only minor frequency shifts take place; natural frequency variations will be most obvious close to an area of higher shear force (related to the third derivative of deflection).

Stubbs and Osegueda (1990a)(1990b) developed damage detection methods based on modal changes of specific structural components such as beams, plates and shells. The method relates frequency shifts to changes in member stiffness using a sensitivity relationship. Stiffness reductions can be located solving an inverse problem, since damage is defined as a stiffness reduction of one of the elements forming the structure. They concluded that it is possible to locate multiple damage sites, at least in a beam. False positives occurred, however, although generally at a far smaller number of sites than those where damage was actually

present. Moreover, this method has difficulties when the number of modes is lower than the number of the damage parameters.

Sanders *et al.* (1992) use the frequency sensitivity method developed by Stubbs and Osegueda (1990a), combined with an internal-state-variable theory, to detect, locate and quantify damage in CFRP beams. This method includes parameters which indicate two types of damage: matrix micro-cracking (identified by changes in the extensional stiffness), and transverse cracks in the 90-degree plies (by changes in the bending stiffness). Despite the sensitivity equations used only being valid for viscous damping, they argued that the damping had little influence in the application of the methodology. Due to the fact that damage was distributed uniformly along the beam length, it was not possible to evaluate the ability of the method to locate damage.

Silva, J. M. M. and Gomes (1990) performed an extensive experimental dynamic analysis of free-free beams, with slots ranging in depths from 1/8 to 1/2 of the beam thickness, introduced in both dimensions (x and y) of the cross section and in different locations. Later, Silva, J. M. M. and Gomes (1991) compared the experimental and theoretical methods, based on the premise that the development of a crack, at a certain location, corresponds to a sudden reduction of the bending stiffness of the beam at the same location. The crack was modelled as a torsional spring representing the bending stiffness at the crack location.

Following on from this, Silva, J. M. M. and Gomes (1994) suggested a technique for damage detection in beams, based on the estimation of frequency shifts as a function of the crack length and position. An optimization algorithm, developed by Gomes and Silva (1992) and designated CRACAR[®], was used to search through combinations of crack lengths and locations. To overcome the differences between the experimental and analytical models, they suggested a simple correction quotient, based on the natural frequencies, which they showed to be a reliable tool.

Hearn and Testa (1991) developed a damage detection method which evaluates the ratio of frequency shifts for various vibration modes. Assuming that the mass does not change as a result of damage, and neglecting second-order terms in the formulation, they showed that the change in the i^{th} natural frequency that results from damage can be related to the matrix of change in element N stiffness $[\Delta k_N]$ and to the element deformation vector $\{\epsilon_N(\Phi)\}$ evaluated from the mode shape vectors:

$$\Delta\omega_i^2 = \frac{\{\epsilon_N(\Phi_i)\}^T [\Delta k_N] \{\epsilon_N(\Phi_i)\}}{\{\Phi_i\}^T [M] \{\Phi_i\}} \quad (2.1)$$

where $[M]$ is the mass matrix and $\{\Phi_i\}$ is the i^{th} mass-normalized mode shape vector. They noted this equation, which resembles Rayleigh's quotient, seems to support the idea that if an element must develop a high level of potential energy because of the deformations imposed by a vibration mode, then damage in that member will have a strong influence on the natural frequency of the mode shape. The converse is also true, and because the natural mode shapes are distinct, the contribution to potential energy made by any one member will be different for each mode. In the case where damage is limited to a stiffness component of the element and if the ratio between the frequency shifts for modes i and j is taken, it is possible to show that the effects of the damage will be reduced simply to a function of damage location, $\Delta\omega_i^2/\Delta\omega_j^2$, illustrating the characteristic influence of each member on the natural frequencies of the structure. The characteristic influence can be determined from pre-damaged modal properties. Damage is located by selecting the member for which the characteristic influence is closest to the ratio $\Delta\omega_i^2/\Delta\omega_j^2$.

Penny *et al.* (1993) applied a statistical method to identify the most likely damage location, using a generalized least squares theory. The method uses the ratio of natural frequencies from both the measured and analytical data. The damage case is indicated by the minimal error in this fit.

Messina *et al.* (1992) proposed the Damage Location Assurance Criterion (DLAC) in location j , which is a correlation similar to the Modal Assurance Criterion (MAC) of Allemang and Brown (1982), and is given by:

$$DLAC_j = \frac{|\{(\Delta\omega)_X\}^T \{(\Delta\omega)_A\}|^2}{(\{(\Delta\omega)_X\}^T \{(\Delta\omega)_X\})(\{(\Delta\omega)_A\}^T \{(\Delta\omega)_A\})} \quad (2.2)$$

where $\{(\Delta\omega)_X\}$ is the experimental frequency shift vector and $\{(\Delta\omega)_A\}$ is the analytical frequency shift vector obtained from an analytical model for a given damage location. A zero value indicates no correlation and a unity value indicates perfect correlation between the vectors involved in the DLAC relationship. Damage location and dimension is identified by maximizing this objective function.

Messina *et al.* (1996) showed that it is possible to locate damage more accurately if the frequency shifts are normalized relative to the undamaged structural frequencies, so that the contribution of each vibration mode can be weighed, since higher frequencies tend to suffer more pronounced shifts.

The Multiple DLAC (MDLAC), proposed by Messina *et al.* (1998), is an extension of the DLAC to detection of multiple damage sites. Using the same principles, the damage state is indicated by

search of a damage vector $\{\Delta D\}$ which maximizes the MDLAC. This formulation allows for relative quantification of the damage in each location, but not for absolute quantification. However, since the experimental frequency shift vector $\{(\Delta\omega)_X\}$ can be calculated, it is possible to estimate a scalar severity coefficient C , in such a way that $C \cdot \{\Delta D\}$ gives the actual damage prevailing. This scaling constant C can be estimated by either a first or second order approach, but these authors note that, although the second order approximation provides better results, for routine monitoring purposes where precise knowledge of the defect size is less important than its location, the first order approximation is likely to be an adequate choice due to its relative simplicity.

Boltezar *et al.* (1998) devised a method for locating transverse cracks in flexural vibrations of free-free beams by following an inverse problem. The method is based on the assumption that the crack stiffness does not depend on the frequency of vibration (i.e., the values of the crack stiffness, which is modelled as a linear torsional spring, must be the same at the crack position for all of the measured natural frequencies). As a result, by plotting the relative stiffness along the length of the beam for at least two distinct natural frequencies, the crack location can be identified by the intersection of these curves. These authors mentioned that this idea had already been proposed by Adams *et al.* (1978) for axial vibrations, and was extended in their article to include flexural vibrations in one-dimensional beams, allowing better results to be obtained. Since this model is based on the Bernoulli-Euler beam theory, the authors pay special attention to the problem of accurately knowing the values of the material properties, in particular the Young's modulus, which can be overcome by calculating its "effective" value as suggested by Adams *et al.* (1978).

Sampaio *et al.* (2003) and Sampaio and Maia (2004) propose the Detection and Relative damage Quantification indicator (DRQ), based on the use of the Frequency Domain Assurance Criterion (FDAC), as an effective damage indicator, capable of distinguishing a positive occurrence from a false alarm. The column vector j of the receptance matrix $\{\alpha_j(\omega)\}$ is the Operational Deflection Shape (ODS) which describes the shape (in space) exhibited by the structure at each excitation frequency, ω , given by the responses normalized by the applied forces. When a structure is damaged, its stiffness and damping change and, in consequence, so does the receptance matrix $[\alpha(\omega)]$. Thus, it is reasonable to assume that the smaller the degree of correlation between the column vectors (ODSs) of $[\alpha(\omega)]$ and $[\alpha^D(\omega)]$, where the superscript D stands for damaged, the larger is the damage. To measure the degree of correlation between the ODSs, Pascual *et al.* (1997) proposed the FDAC. A simplified form is referred to as the Response Vector Assurance Criterion (RVAC) (Heylen *et al.* (1998)), with only

one applied force (so that the receptance matrix becomes a single vector) and pairs of ODSs at the same frequency ω :

$$RVAC(\omega) = \frac{|\sum_{i=1}^N \alpha_i^D(\omega) \alpha_i^*(\omega)|^2}{\sum_{i=1}^N [\alpha_i^D(\omega) \alpha_i^{D*}(\omega)] \sum_{i=1}^N [\alpha_i^D(\omega) \alpha_i^*(\omega)]} \quad (2.3)$$

where N is the total number of coordinates or measurement points and $*$ stands for complex conjugate. From this definition, Sampaio *et al.* (2003) and Sampaio and Maia (2004) formulate the DRQ, which is nothing more than an arithmetic average of the RVACs along the frequency. They also proposed a normalization algorithm for the DRQ, based on various damage cases, which is referred to as *normalization of the maximum occurrences*, DRQi. Finally, and because some of the best known damage location methods, such as the damage index and Mode Shape Curvature (MSC) (Sampaio *et al.* (1999) e Maia *et al.* (2003)), use the second spatial derivative of the ODSs to locate damage, the DRQ" can instead be calculated based on these derivatives and using, for the ODSs, a central difference approximation. It was found that the DRQ indicator is able to detect damage, distinguish a true damage state from a false one and distinguish adequately between damage cases of different severity. It was also found that the versions of the DRQ indicator using the second spatial derivatives of the ODSs did not perform much better than the versions using only the ODSs.

Zang *et al.* (2003a) presented two criteria to correlate measured FRFs from multiple sensors and proposed using them as indicators for structural damage detection. The first criterion is the Global Shape Correlation (GSC) function, which is sensitive to mode shape differences but not to relative scales; and the second criterion, based on actual response amplitudes, is the Global Amplitude Correlation (GAC). Each of the correlation criteria is a function of frequency and uniquely maps a set of complex responses to a real scalar between zero and unity. These authors argue that a simultaneous use of both correlation criteria should be able to quantify the closeness of two sets of vibration data. The averaged integrations of the GSC and GAC functions along the frequency points over the measurement range are also proposed, referred to as *averaged integration* GSC and *averaged integration* GAC, as damage indicators for SHM. An experimental test on a bookshelf structure was conducted, but it was concluded that further studies would be needed to develop approaches that could accurately assess structural states and damage. An intelligent decision making method based on the Radial Basis Function (RBF) neural network is suggested by Zang *et al.* (2003b).

2.2.2 Mode shape changes

According to Doebling *et al.* (1996), West (1984) presents what is possibly the first systematic use of mode shape information for the location of structural damage without the use of a prior FE model. West (1984) uses the MAC to determine the level of correlation between modes from the test of an undamaged Space Shuttle Orbiter body flap and the modes from the test of the flap after it was exposed to acoustic loading.

Kim, J. H. *et al.* (1992) investigated the use of the MAC and some of its forms for locating structural damage. The MAC, which is probably the most common way of establishing a correlation between experimental and analytical models, is defined by Allemang and Brown (1982) as:

$$MAC(\{\Phi_X\}_i, \{\Phi_A\}_j) = \frac{|\{\Phi_X\}_i^T \{\Phi_A^*\}_j|^2}{(\{\Phi_X\}_i^T \{\Phi_X^*\}_i)(\{\Phi_A\}_j^T \{\Phi_A^*\}_j)} \quad (2.4)$$

where the X and A subscripts refer to, respectively, experimental and analytical vibration modes. This correlation results in a single scalar number with a value ranging from zero to unity. A unity value means that the mode shapes are identical, whereas a zero value indicates orthogonality between the vectors, i.e., the mode shapes are “totally different”. Although the MAC can provide a good indication of the disparity between two sets of data, it does not show explicitly where in the structure is the source of discrepancy. The Coordinate MAC (COMAC) was developed from the original MAC. It is the reverse of the MAC in that it measures the correlation at each Degree-of-Freedom (DOF) averaged over the set of correlated mode pairs. The COMAC identifies the co-ordinates at which two sets of mode shapes do not agree, and is defined as (Lieven and Ewins (1988)):

$$COMAC_i = \frac{(\sum_{j=1}^N |(\phi_A)_{ij}(\phi_X^*)_{ij}|)^2}{\sum_{j=1}^N |(\phi_A)_{ij}|^2 \sum_{j=1}^N |(\phi_X)_{ij}|^2} \quad (2.5)$$

where N is the number of correlated mode shapes. Although the COMAC can be useful as a tool to locate a discrepancy, it does not have a physical basis. It is advisable to use this method in cases where the structure is tested and modelled in a free-free configuration, because grounding of the structure will amplify the effect of anti-nodes away from the region of constraint and dominate the error prediction (Maia and Silva (1997)). On the other hand, although the COMAC is a useful algorithm to detect errors in spatial models, it does not provide a unique solution to localize the source of error in the structure. Another form of the MAC is the Partial MAC (PMAC), which correlates parts of modal vectors and allows easy

comparison of the selected parts. Kim, J. H. *et al.* (1992) propose the combined use of the COMAC and the PMAC concepts, referred to as the *total* MAC, so that the structural area where damage occurred can be isolated.

Parloo *et al.* (2002b)(2004) compared input-output and output-only damage identification setups for an aluminium beam structure suffering from fatigue induced crack formation. As shown in the literature, there are several methods available for the calculation of sensitivity (derivatives) of eigenvalues and eigenvectors. Expressions for the sensitivity of mode shapes to local changes on mass and stiffness can be found, for instance, in Vanhonacker (1980), Maia and Silva (1997) or Parloo *et al.* (2003). These expressions are exact if all mode shapes of the test structure are taken into account, though a good approximation can be obtained in practice, where only a limited number of modes are available. In practice, the stochastic errors due to the presence of measurement noise reveal that calculating mass sensitivities can be numerically more stable than the calculation of the sensitivity to stiffness. If the reference condition of a structure is altered by either a local change in mass or in stiffness, first-order approximations with respect to the damage parameter can be written. However, it is noted that these approximations are only valid for relatively small damage; this poses no problem, since early damage is meant to be detected. In the case where frequency sensitivities to a change in a structural parameter are considered, Parloo *et al.* (2004) use an iterative weighted pseudo-inverse algorithm technique which allows to better locate damage (Guillaume *et al.* (2002)).

In order to reduce the calculated sensitivity errors, the estimated modal parameters from output-only data should be as accurate as possible. For this purpose, Guillaume *et al.* (1998) and Guillaume *et al.* (1999) propose the use of a Maximum Likelihood Estimator (MLE), which is an unbiased estimator taking into account the noise information in the data. Instead of using FRFs, the MLE uses spectral density functions.

Vecchio *et al.* (2002) present an experimental validation of a modal model based approach to structural damage detection, where output-only vibration data is used. However, operational working conditions are not necessarily stationary, and if small deviations are observed in the modal parameters, it is very difficult to decide whether damage is present or not. The approach requires continuous monitoring of the system. The damage detection algorithms reduce time data to covariance data and perform a statistical χ^2 -test that assesses whether the recent data fit the reference model. In a previous work, Vecchio and Van der Auweraer (2001) identified the modal parameters based on the stochastic subspace method, but, in order to improve pole extraction (making it faster and easier) and with the aim of achieving more automation in the damage detection process, Vecchio *et al.* (2002) introduced a new

approach based on the MLE. This approach is applied to a reticular structure that was built for several dynamic tests in the context of the EC Brite-Euram SAM project.

Park, N. G. and Park (2003) introduced a damage detection and location technique based on incomplete experimental models, since it is not possible in practice either to measure the responses in all DOFs or to have a reference FE model that can represent the real structure in a precise manner, unless simple structures are being studied. However, this method has the disadvantage of requiring heavy experimentation, because one needs to measure all the FRFs of the reference structure for each considered DOF. Furthermore, this technique is not effective over the whole frequency range, and solutions are presented for the frequency range choices by error analysis.

Lazarov and Trendafilova (2004) investigated the influence of damage on the dynamic characteristics of linear elastic plates. This study was based on the plate theory of Kirchhoff, and tests were carried out on a square plate. Damage is introduced as thickness changes and as saw cuts perpendicular to the boundary contour of the plate, and its influence on the mode shapes and the modal frequencies of the structure are then derived and analyzed. They first concluded, from both the numerical and experimental models, that the natural frequencies of thin plates are not influenced noticeably by damage, but that the mode shapes undergo considerable changes as a result of the presence of damage. Despite the fact that these conclusions may not seem remarkable, they confirm some hypotheses that were discussed during this work. These authors also propose a mode shape based damage location index.

Kim, B. S. *et al.* (2005) used several damage detection criteria, including COMAC, ECOMAC (Enhanced COMAC, which is based on the average difference between the analytical and experimental modal vector components, and first introduced by Hunt (1992)), ADSM (Absolute Difference of Strain Mode shapes, which is based on the absolute difference of strain mode shapes, proposed by Qin and Zhang (1998)) and a new method based on the absolute difference of the absolute value strain mode shapes, with a focus on finding differences of these damage detection criteria caused by different geometry and boundary conditions of gusset plates with cracks. Considering crack location, these authors concluded that the new method generally performed better than the other methods for the studied example, though it is hard to find its physical meaning.

2.2.3 Mode shape and FRFs curvatures

Mode shape and FRFs curvatures are widely used as an alternative to damage identification from mode shape changes.

Salawu and Williams (1994) evaluated the performance of some procedures for locating damage using MSC and mode shape changes. The first method estimates the mode shape curvatures using a central difference approximation as proposed by Pandey *et al.* (1991):

$${}_r\vartheta_j'' = \frac{{}_r\phi_{(j+1)} - 2{}_r\phi_j + {}_r\phi_{(j-1)}}{h^2} \quad (2.6)$$

Here, h is the distance between the measurement coordinates and ${}_r\phi_j$ are the modal displacements for mode shape r at the measurement coordinate j . Since a local reduction in stiffness results in a local increase in the curvature ϑ'' , it is reasonable to suppose that these can be used to detect, locate and quantify damage. The second method studied by Salawu and Williams (1994) is based on the mode shape relative differences proposed by Fox (1992), in which a graphical comparison of displacement mode shapes is used to indicate damage position. Those authors also use the MAC and COMAC to correlate mode shapes, but although these criteria proved to be sensitive to damage, they did not provide a clear location of the damage position in a cantilevered beam. The performance of both the MSC and mode shape relative differences methods was not as good as desired, since it is necessary to decide which are the most adequate mode shapes to use. Only the MSC method was able to give an indication of simulated multiple damage locations.

In a paper where the applicability of the MSC changes to damage detection in a prestressed concrete bridge is investigated, Wahab and De Roeck (1999) introduce the Curvature Damage Factor (CDF), where the difference in the MSC for all modes can be summarized in one number for each measurement point. This technique was then applied to a real structure: the Z24 bridge which lies between the villages of Koppigen and Utzenstorf and crosses the highway A1 between Bern and Zurich in Switzerland. The CDF is based on the MSC central difference approximation (equation 2.6), and is given by:

$$CDF = \frac{1}{N} \sum_{r=1}^N |{}_r\vartheta'' - {}_r\vartheta''^D| \quad (2.7)$$

where N stands for the total number of modes to be considered, ${}_r\vartheta''$ is the curvature of the r^{th} mode shape of the intact structure and ${}_r\vartheta''^D$ is the curvature of the r^{th} mode shape of the damaged structure. These authors note that a relatively dense measurement grid is required in order to get a good estimation of the curvatures of higher modes. When more than one fault exists, it is not possible to detect the various damage locations from a single vibration mode, i.e., all modes should be carefully examined in order to locate all the existing flaws.

Ho and Ewins (2000) attempted to evaluate whether the presumption that damage is located at the point where the mode shape change is the greatest is valid using both simulated and experimental data, since the differentiation process enhances the experimental variations inherent to mode shapes. They addressed five methods based on mode shapes and their derivatives: Flexibility Index (FI), Mode Shape Curvature (MSC), Mode Shape Curvature Square (MSCS), Mode Shape Slope (MSS) and Mode Shape Amplitude Comparison (MSAC). If more than one mode is defined, it follows that:

$$FI_i = \sum_{r=1}^N |(\phi_i^D)^2 - (\phi_i')^2| \quad (2.8)$$

$$MSC_i = \sum_{r=1}^N |\phi_i^{D''} - \phi_i''| \quad (2.9)$$

$$MSCS_i = \sum_{r=1}^N |(\phi_i^{D''})^2 - (\phi_i'')^2| \quad (2.10)$$

$$MSS_i = \sum_{r=1}^N |(\phi_i^{D'})^2 - (\phi_i')^2| \quad (2.11)$$

$$MSAC_i = \sum_{r=1}^N |\phi_i^D - \phi_i| \quad (2.12)$$

The last two methods, corresponding to expressions (2.11) and (2.12), are presented by Ho and Ewins (2000). The first (2.11) corresponds to an attempt to introduce the mode shape deflection as a feature sensitive to damage but relatively insensitive to experimental variation. The second equation (2.12) has the advantage of not requiring the mode shape differentiation. In calculating the derivatives of mode shapes, instead of using finite difference approximation, polynomial functions are used: a local polynomial is fitted through every set of four consecutive measurement points and the resulting polynomial is differentiated. These authors conclude that the experimental results show that higher derivatives are more promising for damage identification, but that false damage indications may be observed at mode shape nodal points or where the quality of the measurements is relatively poor. It was also observed that this may also occur at the boundaries.

Battipede *et al.* (2001) extend the gapped-smoothing technique to bi-dimensional models or plate-like structures, showing that the method is able to locate single and multiple damage sites of medium and great extent. This technique, which had already been applied to one-

dimensional models by Ratcliffe and Bagaria (1998) and Ratcliffe (2000), takes advantage of the presence of an irregularity in the curvature shape in order to detect damage. The displacement shape is converted into curvatures by applying a second order finite differentiation procedure, like the one proposed by Pandey *et al.* (1991) (equation (2.6)) but distinguishing the curvatures in the x and y directions, i.e., writing them in terms of $r\vartheta''_{xx}(x_i, y_j)$ and $r\vartheta''_{yy}(x_i, y_j)$. In the absence of damage and other irregularities, the curvature has a smooth shape and can thus be represented as a polynomial function. If the smooth function and the measured curvature are different when evaluated at the same location, (x_i, y_j) , this can be an indicator of damage at that location. Furthermore, the fact that one is dealing with a bi-dimensional model allows the cross curvature, $r\vartheta''_{xy}(x_i, y_j)$, to be taken into account so that a damage index can be formulated as:

$$\begin{aligned}
 DI_{ij} = & a_{xx} \left(r\vartheta_{xx}^{X''}(x_i, y_j) - r\vartheta''_{xx}(x_i, y_j) \right)^2 \\
 & + a_{yy} \left(r\vartheta_{yy}^{X''}(x_i, y_j) - r\vartheta''_{yy}(x_i, y_j) \right)^2 \\
 & + a_{xy} \left(r\vartheta_{xy}^{X''}(x_i, y_j) - r\vartheta''_{xy}(x_i, y_j) \right)^2
 \end{aligned} \tag{2.13}$$

where the superscript X stands for experimental (or measured). The a_{ij} coefficients can be set to 0 or 1, to either consider or neglect the corresponding curvature. However, Battipede *et al.* (2001) considered $a_{xy} = 0$ since it is difficult to estimate $r\vartheta''_{xy}(x_i, y_j)$ from experimental data. For an undamaged structure, the difference between measured and fitted data is mainly due to measurement noise, so that in an experimental case the damage index DI_{ij} is irregular without any sharp peak. If the structure is faulty, however, some clear peaks will appear, corresponding to the sensors located around the damaged region of the model under consideration. The major advantages of this technique, when applied to a plane rectangular homogeneous plate, are: the possibility of locating multiple damage sites without knowledge of a reference model of the structure; and only a single test is needed to determine the current state of the structure, without knowledge of its history. In practice, however, measured data tend to be polluted by noise, detrimentally affecting the effectiveness of the technique.

Yoon *et al.* (2005) proposed the generalization of the one-dimensional gapped smoothing technique to bi-dimensional models. As before, it is shown that it is possible to locate damage using only data from the damaged structure, i.e., without resorting to a reference model. Provided that it is known that the structure, in its undamaged state, is homogeneous with respect to stiffness, the procedure will detect the non-homogeneous areas that are caused by

damage. Variability indices are generated for each test point on the structure, after which statistical treatment and outlier detection enables discrimination of areas with significant variation in stiffness. It was shown that this method allows for the determination of the size and location of relatively small localized stiffness reductions in homogeneous plate-like structures. Analytical models or reference experimental models of the structure in the undamaged state are not needed. The results generated using the broadband ODS data showed superior performances to those produced using the mode shapes. However, in the case of large areas or uniform damage (when compared to the spacing and number of measurement points), the algorithm identifies only the edges of the damage, which can make the interpretation of results more difficult. It was concluded that further research is required in order to establish a quantitative relationship between the local stiffness reductions and the irregularity indices.

Maia *et al.* (2003) presented a series of numerical simulations as well as an experimental example using a simple beam in order to compare various damage detection methods based on mode shape changes. They also proposed a generalization of these methods to the whole frequency ranges of measurement, i.e., methods based on mode shapes become based on ODSs. This way, modal identification, which can be a time consuming process and can filter relevant information, may be avoided. The studied methods fall into two major groups: mode shape damage detection methods and FRF-based damage detection methods. In the first group, they included all the methods overviewed by Ho and Ewins (2000), except the FI method. They also included the damage index method developed by Stubbs *et al.* (1995), which is based on the modal strain energy decrease between two structural DOFs for linear-elastic Bernoulli-Euler beams, and given by.

$$B_{ij} = \frac{\left(\int_a^b [\phi_j^{D'''}(x)]^2 dx + \int_0^L [\phi_j^{D'''}(x)]^2 dx \right) \int_0^L [\phi_j''(x)]^2 dx}{\left(\int_a^b [\phi_j''(x)]^2 dx + \int_0^L [\phi_j''(x)]^2 dx \right) \int_0^L [\phi_j^{D'''}(x)]^2 dx} \quad (2.14)$$

where a and b are the limits of a segment i of the beam where damage is being evaluated and L is the total length of the beam. For the purpose of the article presented by Maia *et al.* (2003), the discrete formulation of equation (2.14) was used. For more than one mode, the damage index can be defined as:

$$DI_i = \sum_j B_{ij} \quad (2.15)$$

Cornwell *et al.* (1997) generalized the damage index method to plate-like structures characterized by a two dimensional curvature. One of the advantages of this strain energy based method is that it does not require a well correlated FE model and/or mass normalized mode shapes. The mode shape detection methods group is based on the assumption that damage is located between the DOFs where the change of a mode shape function is greatest. The second group distinguished by Maia *et al.* (2003), the FRF-based damage detection methods, includes the FRF-based MS, the FRF-based MSS, the FRF-based MSC (also presented by Sampaio *et al.* (1999)), the FRF-based MSCS and the FRF-based damage index; these methods are equivalent to the mode shape detection methods, but using FRFs instead of mode shapes. In Maia *et al.* (1997) it is noted that when calculating the damage indexes for the FRF-based methods, as progress is made along the frequency range, compiling information, the results eventually begin to degenerate instead of improving. To overcome this, the location where the difference of damage and undamaged case is a maximum is looked up for each frequency and an occurrence is counted at that location. The occurrences are summed up along the frequency range for each location, and the location where the greatest number of occurrences was counted is proposed as the damage site. Maia *et al.* (2003) found that the methods based on the curvatures performed better, although false damage indications remain a problem requiring close attention. Maia *et al.* (2003) suggested that some improvements could be made in the interpolation process, in defining a noise level under which the results are not considered, in the method to calculate the maximum occurrences, in applying statistics to the results, and, finally, in the set-up and skill of the experimentalist.

Sampaio *et al.* (1999) compared the FRF curvature method, which encompasses the first three levels of the damage identification process (existence, location and extent), with two of the most cited methods in literature: the MSC method and the damage index method. The FRF curvature method is based only on the measured data without need for any modal identification, and is an extension of the method of Pandey *et al.* (1991) to include all frequencies in the measurement range and not just the modal frequencies, i.e., it uses FRF data rather than just mode shape data. In fact, the method uses something like an ODS defined, for each frequency, by the frequency response at different locations along the structure. The absolute difference between the FRF curvatures of the damaged and undamaged structure at location i , along the chosen frequency range ω , is calculated, for an applied force at point j , by:

$$\Delta\alpha''_{ij} = \sum_{\omega} |\alpha''_{ij}(\omega) - \alpha''_{ij}(\omega)| \quad (2.16)$$

Finally, the results from several force location cases can be summed up. This technique was tested using experimental data gathered from the I-40 bridge over the Rio Grande in Albuquerque, New Mexico, USA, following previous work done by Jauregui and Farrar (1986a)(1986b) of the Los Alamos National Laboratory (LANL) in the USA. From work on the FRF curvature method, Sampaio *et al.* (1999) point out the following: point out the following: (i) the method works better for a range before the first anti-resonance or resonance frequency (whichever comes first), since for wider frequency ranges (including several modes) the difference between the curvatures of the damaged and undamaged models becomes less significant when compared with the amplitude difference arising from the resonances' frequency shift, because of the loss of stiffness; (ii) the position of the exciting force seemed not to be an important influence, according to the numerical model; (iii) the method is considerably insensitive to noise; (iv) it can be used to detect, locate and quantify damage, though this last aspect deserves further developments; (v) the method has the great advantage of being simple and not requiring prior modal identification. With respect to the comparison established between the three methods, Sampaio *et al.* (1999) argue that the FRF curvature method had the best overall performance, although the MSC method produces better results for higher order modes.

Pirner and Urushadze (2004) compared the CAMOSUC (Change of Mode Surface Curvature) with earlier methods for detection of the magnitude and location of damage; specifically MAC, COMAC, and the error-matrix. The CAMOSUC is defined as the difference of the mode shape curvatures between the undamaged and damaged states. Thus, each term in the CDF equation (2.7) is the CAMOSUC itself. These authors present detailed applications of some of these methods to real cases, such as a square Plexiglas plate, a Plexiglas model of a railroad bridge section, a three-span prestressed concrete bridge, floor slabs of a department store and a hyperbolic cooling tower.

Hamey *et al.* (2004) approached the experimental aspects of methods which make use of mode shape curvatures, comparing four methods: the absolute difference of curvature mode shape method, the CDF method, the damage index method and the FRF curvature method. However, instead of obtaining approximations to the second derivatives of the displacements, as usual, they proposed the use of direct measurements of the curvatures of the mode shapes obtained from piezoelectric materials. They used piezoceramic patches for sweep-sine continuous excitation and a hammer for impulse excitation. Sixteen polymeric PVDF (polyvinylidene fluoride) sensors were distributed along the length of one face of the beam. They tested several cases of damage: a transverse crack, three scenarios of controlled non-symmetric delamination and impact damage, and observed that, in general, the impulse

excitation produced slightly better results than the continuous excitation. With respect to the identification methods, they observed that the damage index method performed better than the others both on damage detection and location. According to these authors, the FRF curvature method turned out to be the one which produced the worst results. Also, they observed that when the sensors are placed on the opposite side of the beam to the delamination, it was possible to obtain better results for the cases where the delamination had greater dimensions, although sensor position seemed not to affect the results for the other damage cases.

Kim, B. H. *et al.* (2005) attempted to extend the MSC and damage index methods by resolving some deficiencies of these methods. They solved a set of linear algebraic equations referred to as Flexural Damage Index Equations (FDIE), which avoid the singularity problem near the inflexion points and the mode selection problem of the MSC and damage index methods. The FDIE shows that there is a strong relationship between the damage and the curvature of flexibility. This method is also able to detect, locate and determine the size of structural damage in a plate-like structure using the measured modal parameters. However, a very small interval between sensors is required if an accurate estimate of the severity of damage is wanted.

Zhu and Xu (2005) presented a sensitivity-based method for location and assessment of damage in mono-coupled periodic structures, in which slopes and curvatures of mode shapes are used to localize damage, and natural frequencies are then used to quantify its extent. The equations of sensitivity coefficients of mode shapes, slopes and curvatures of a mono-coupled periodic system are first derived in terms of receptances of a periodic element. The numerical and experimental examples show that curvatures of modal shapes are the most sensitive to damage, but slopes of mode shapes seem to provide a better indication of the damage location. Also, the larger changes in the natural frequencies imply higher sensitivity of these modes to damage, which is useful for choosing a few of the lower frequency modes to localize damage. The method allows for detection and location of multiple damage sites, with different simultaneous extents, using a few of the slopes and curvatures of the lower order mode shapes, though the accuracy with which the damage size can be quantified depends on the number of frequencies used.

Santos *et al.* (2006) presented and discussed three methods for the damage location of impact damage in laminated composite plates. The authors refer to these methods as Translation Differences (TD), Slope Differences (SD) and Curvature Differences (CD) methods, that correspond closely to the formulations of the above mentioned MSAC, MSS and MSCS respectively. Tests were conducted using free-free suspended rectangular quasi-isotropic CFRP

specimens with dimensions 277x199x1.8mm. Double pulse TV holography with acoustic excitation was used for the acquisition of the mode shapes. For computation of the rotations and curvatures, the mode shapes' translations were processed using a differentiation/smoothing technique. The MAC and a MAC-based Normalized Mode Difference (NMD) were used as tools for choosing amongst the modes most sensitive to damage to be used in the indexes. It was observed that the best results were obtained with the CD method for the single damage case study; in this case, the location was correct, even for light damage difficult to detect with an X-ray or a C-SCAN.

Guan and Karbhari (2008) proposed the Element Modal Strain Damage Index (EMSDI), which attempts to address some of the weaknesses of the modal curvatures based methods. The use of numerical differentiation procedures is identified as the main cause for the poor performance of the modal curvature method under sparse and noisy measurements. The proposed damage index can be calculated directly from the measured modal displacements, since estimates of derivatives are obtained through the use of spline interpolation and numerical optimization. It is demonstrated through the use of numerical simulation examples that the proposed method is able to correctly locate a damage region using only noisy sparse measurement even in cases when the modal curvature method fails. Experimental tests were carried out using cantilevered aluminium beams with transverse saw cuts.

Seeing both the benefits and the difficulties associated to the use of FRF shapes as proposed by Maia *et al.* (1997), Liu, X. *et al.* (2009) recently introduced a scheme of using FRF shapes for structural damage location. They point out that, so far, no solid foundation has been given in the literature about the use of FRF shapes for damage location. In addition, they observe that this method only works for a low-frequency range. To improve the performance of the method, they include some modifications like using the imaginary parts of FRF shapes and normalising FRF shapes before comparison. Using the gapped smoothing technique proposed by Ratcliffe (2000), for a structure with a smooth shape (e.g., a straight beam or a bridge), the unavailability of measurement data from a healthy or baseline system is surpassed: local damage on the structure, if sufficiently large, will cause an abnormality of the FRF shapes at the damage location. As expected because of the nature of such method, the major drawback found is that the damage-induced small abnormalities in the FRF shapes must be included in the measured data to successfully locate damage, which in turn requires measuring a lot of points over the structure.

2.2.4 ARMA family models

Brincker *et al.* (1995a) used a statistical analysis based on shifts in the natural frequencies to detect damage in two concrete beams with different reinforcement ratios. The modal parameters (natural frequencies and modal damping factors) are estimated from the response time series (accelerations) using the so called Auto-Regressive Moving Average (ARMA), identical to the one used by Brincker *et al.* (1995b) in an offshore platform. Referring to Davies and Hammond (1984), Pandit and Metha (1985) and Safak (1991), Brincker *et al.* (1995a) mention that the ARMA models have been developed mainly for application in economics and electrical engineering, but since they are considered to be a more effective way of estimating modal parameter than Fast Fourier Transform (FFT) based techniques, their use on structural systems has been increasing during recent years. A more complete version is the ARMA with exogenous input (ARMAX). The $[n, m]$ order ARMAX model that describes the time response $y(t)$ as a linear combination of the last n responses as well as the last m unknown inputs and p known inputs is given by:

$$y(t) = \sum_{i=1}^n c(i)y(t-1) + \sum_{i=1}^p b(i)x(t-1) - \sum_{i=1}^m d(i)e(t-1) + e(t) \quad (2.17)$$

where $c(i)$ is the auto-regressive parameter describing the response $y(t)$ as a linear regression of the last n values and $d(i)$ and $b(i)$ are the moving average parameters which describe the response $y(t)$ as a linear regression of the last values of, respectively, an unknown input time series, $e(t)$, which may be assumed as white noise, and a known time series, $x(t)$. The $c(i)$ (AR), $d(i)$ (MA) and $b(i)$ (X) parameters are determined by minimizing the variance of the noise time series $e(t)$, i.e., based on the measured response and on the predicted response given by (2.17). When the AR parameters are estimated, the roots of the characteristic polynomial equation that contains these parameters can be related to the natural frequencies and modal damping factors. Hence, the ARMAX can be utilized to examine these parameters' variations with time. Brincker *et al.* (1995a) also defined a statistical significance indicator which takes account of the changes in the natural frequencies, so that they can give a quantifiable estimate of the structural changes. It was shown that the significance indicators are sensitive to structural damage, but they are not able to provide an accurate estimate of damage location. Finally, it was observed that, for the studied beams, the

differences between the ARMA and ARMAX were quite small. Thus, it was concluded that knowing the input signal is not essential for the detection of damage in the studied beams.

Wei *et al.* (2005) used Nonlinear ARMA with exogenous input (NARMAX) models to assess internal delamination in multi-layer composite plates. These authors state that the relationship between input and output is nonlinear for multilayer composite panels. According to them, the NARMAX model was proposed by Leontaritis and Billings (1985a)(1985b) NARMAX models describe the nonlinear systems in terms of difference equations relating the current output to combinations of inputs and past outputs. The structure of the proposed model is used to estimate model parameters for damaged vibration systems, and internal delamination is detected by comparing the model parameters of the intact and damaged systems. The results show that, for the case studied, NARMAX models allow investigation of the behaviour of composite models as well as assessment of damage (especially delamination) in composites.

Lu and Gao (2005) proposed an approach formulated as a predictive Auto-Regressive model with exogenous input (ARX), based on the linear dynamic system theory. After some simplifications, the model is expressed in such a way that only response signals are involved, with a response at one location chosen as the input of the model. The residual error of the established model, when applied to actual measured signals, reflects the structural change, and the standard deviation of the residual error is found to be a damage sensitive feature. It was observed that the proposed ARX model can behave undesirably when the location of the chosen input response is near the location of the damage. For this reason, they recommend that in a diagnosis situation two separate runs of the procedure are carried out using two different input locations. It was also noted that the standard deviation of the residual error of the ARX model, although sensitive to the presence of damage, does not give a precise indication of the degree of damage, and further research is therefore required.

In an earlier work, Sohn and Farrar (2001) had presented a two iteration AR-ARX model in order to predict the time series and subsequently use the standard deviation ratio of the residual errors as the damage sensitivity feature. The residual error is the difference between the actual measurements and the predicted responses from the combination of the AR and ARX models.

2.2.5 Dynamic flexibility

Another class of damage detection methods is based on the use of the dynamic flexibility matrix to estimate changes in the static behaviour of the structure. The dynamic flexibility matrix is a transfer function, defined as the inverse of the static stiffness matrix. Thus, each

column of the flexibility matrix represents the displacement pattern of the structure associated with a unit force applied at the associated DOF. Damage is then identified by comparison of the flexibility matrices of the structure in the undamaged (which may be obtained using a FE model) and damaged states. Due to the inverse relation to the square of the modal frequencies, the dynamic flexibility matrix is very sensitive to changes in the lower order modes, whereas the stiffness matrix is more sensitive to higher order modes. Based on this, Doebling *et al.* (1996) distinguished five different approaches: comparison of flexibility changes, unity check method, stiffness error matrix method, effects of residual flexibility and changes in measured stiffness matrix.

Park, Y. S. *et al.* (1988) suggested the use of the weighted error-matrix method, comparing it to the error-matrix method (Sidhu and Ewins (1984) and He and Ewins (1985)). The stiffness error matrix can provide valuable information on the position of the damaged area, being defined as:

$$[E] = [K_D] - [K_H] \quad (2.18)$$

where $[K_D]$ and $[K_H]$ are the stiffness matrices of the evaluated members in the damaged and undamaged states, respectively. Although $[K_H]$ can be estimated from a FE model, it is possible to determine $[E]$ using only experimental data. When the stiffness error matrix $[E]$ is plotted, the highest peak will indicate the most probable damage location. Due to measurement noise, this method is only reliable when the measured natural frequency shifts and modal vector changes exceed the magnitude of the measurement errors. This lead Park, Y. S. *et al.* (1988) to propose the weighted error-matrix method, which magnifies the amount of stiffness error only at certain nodal points related to the damaged element. Although it was shown that the weighted error-matrix method is more sensitive to damage, since it was possible to accurately detect the damaged structural member at lower levels of damage, its complexity does not make it an attractive method. In order to reduce the time required for computation and experiments, an iterative method, in which the number of elements used is refined at each step, was proposed.

2.2.6 Modal strain energy

Choi and Stubbs (2004) developed a method to locate and determine the size of damage in a structure measuring time domain responses in a set of measurement points. The mean strain energy for a specified time interval is obtained for each element of the structure, and used in

turn to build a damage index that represents the ratio of the stiffness parameters of the pre-damaged and post-damaged structures. Possible locations of damage in a structure can be identified by utilizing a classification algorithm and a statistical decision technique of hypothesis testing, in which the damage indexes are normalized, assuming that the damage index is a random variable and the collection of the damage indices are distributed normally. Once the possible locations of damage are isolated, corresponding damage severities can be obtained (i.e., the fractional loss in stiffness). These authors present, as major conclusions, the fact that the time domain response may be used directly to localize and determine the size of damage in a structure, and that it is possible to reduce false-negatives by lowering the significance level for damage location, at the expense of increasing the number of false-positives. Thus, the balance between them represents a measure of the sensitivity of the method as well as of the quality of the results and the effectiveness of the algorithm for damage location.

Patil and Maiti (2005) provided an experimental verification of an energetic method for prediction of the location and size of multiple cracks based on the measurement of natural frequencies for slender cantilevered beams with two or three normal edge cracks. In the theoretical model the beam was divided into a number of segments and each segment was considered to be associated with a damage index. The cracks are represented as torsional springs. The damage index behaves as an indicator of the amount of strain energy stored in the crack (or torsional spring). The method is based on the concept that the strain energy U of a beam containing a crack is reduced because the beam can deform more easily to the same extent than an uncracked beam. This reduction is equal to the amount of energy stored in the fictitious torsional spring (or crack), which, for the case where m cracks are present is:

$$U = U_r - \sum_{i=1}^m \frac{M_i^2}{2K_i} \quad (2.19)$$

where U_r is the stored energy in the corresponding uncracked beam for vibration mode r and M_i and K_i are the bending moment at the crack location $x = l_i$ and stiffness associated to the crack, respectively. Based on these principles, and after performing several simplifications and some mathematical manipulation, an expression for the location of a crack in a segment of the beam is suggested. It is concluded that, on the whole, the accuracy of the method is good for the prediction of the crack location, but lower for the prediction of the crack size. Accuracy decreases as the number of cracks increases. One of the major drawbacks of this method is revealed when it is observed that it is necessary to measure a number of frequencies equal to

twice the number of cracks in order to predict the location and size of all cracks, which number it may not, in practice, be possible to determine in advance.

Hu and Wang (2009) explored the use of a modal strain energy method for the detection of surface cracks on woven fabric composite laminates. The specimen used was a 10 layer plain weave carbon fibre orthotropic laminate rectangular plate with dimensions 310x220x2.2mm. A surface crack, that may include matrix cracks and fibre fracture but does not significantly affect the global stiffness of the woven laminate, is introduced with a knife (16mm long by 1 mm depth). EMA is conducted on the woven laminate to obtain the modal displacements before and after damage. The modal displacements are used to compute the modal strain energies and a damage index is defined by employing the fractional modal strain energy of the woven laminate before and after damage, and then used to identify the location of the surface crack. These authors claim that only a few measured mode shapes are required and that the method has a relatively low cost and can be used for real-time detection in woven laminates. The damage indices properly identified the surface crack location, but the authors agree that limitations and applicability to different types and different levels of damage in woven fabric composites are still to be validated in future work. Only one experimental case is presented to illustrate the efficiency of the technique.

2.2.7 Transmissibility

Sampaio *et al.* (2000) showed that a minor stiffness change can result in a significant change of transmissibility relating responses at points around damage. Considering a general structure with i measuring coordinates and j excitation coordinates, it is possible to compute the transmissibility matrix for both the reference (undamaged) and damaged states. The transmissibility matrices are square, with $m \times m$ elements and a zero diagonal. With this arrangement, it is possible to write:

$$\{x\} = [T]\{x\} \quad (2.20)$$

This is a special case of the transmissibility matrix, which relates the set of m responses with itself. The sum of all the transmissibility matrices in the frequency range of interest produces a unique matrix for each case, $[ST^D]$ for the damaged and $[ST^H]$ for the undamaged case. The difference $[\Delta ST] = [ST^D] - [ST^H]$ between them will show the location of damage, since its values should display a significant increase near the damaged region. To further clarify the

location, the different values in each line i of the $[\Delta ST]$ matrix are summed and the second derivative $\Delta ST''$ is calculated by a central difference approximation. Matrices $[ST^D]$ and $[ST^H]$ can be represented in a contour plot, where the rows are the x axis and the columns are the y axis. Any noticeable change of these plots may indicate the presence of damage, which will be located between the coordinates of $\Delta ST''$ that show major differences. Sampaio *et al.* (2000) demonstrated another way of applying the transmissibility concept to damage detection, referred as the *pseudo-transmissibility matrix* method, which uses FRFs instead of responses. Despite the fact that this version performed better, these authors note that the former (using the transmissibility matrix) is more consistent because the pattern change is correlated among the various plots. These authors also developed the frequency of maximum differences algorithm, to improve the accuracy of the transmissibility method and others, such as the FRF curvature method, that use raw data directly from the FRFs. The transmissibility matrix, pseudo-transmissibility matrix and FRF curvature methods were applied to a 10-DOF numerical model. It was concluded that using the frequency of maximum differences algorithm greatly improves the methods which use FRFs in damage detection and location. However, the version which uses the transmissibility matrix for several simultaneous forces did not work in the examples tried.

Mares *et al.* (1999) applied genetic algorithms to damage assessment where the objective function is based on the measured transmissibilities. The method was tested on a numerical model of a four story steel frame structure. The model was developed with the intention of having a high in-plane rigidity (of the floors) with respect to the out-of-plane rigidity (of the columns). Four damage scenarios were considered, using combinations of Young modulus reductions and removal of columns and braces. These authors observe that not all the transmissibilities are sensitive to damage in the same way. Therefore, they performed a two-step procedure to select the “best” transmissibility functions before running the genetic search, in order to enhance the optimization process and hence the damage assessment procedure. The procedure used enabled transmissibility functions to be ranked in terms of their sensitivity to damage. The transmissibilities found to be the most sensitive to damage were used in the formulation of the cost function. The optimization process follows two iterations to obtain the global minimum of cost function. First, a genetic search is applied to the cost function, and then a classical gradient-based algorithm is run to refine the solution, so that global minima are correctly distinguished from local minima. Mares *et al.* (1999) observed that, according to the numerical simulations they performed, the use of transmissibility functions provide estimates of the state of damage that are sufficiently accurate. However, for

the steel frame structure model used, damage in braces was easier to identify than damage in columns.

Johnson, T. J. *et al.* (2004) presented work on smart sensor arrays with the goal of implementing local vibration-based diagnostic algorithms inside a *smart black box* to demonstrate the feasibility of distributed health monitoring for damage detection, location and quantification. It was shown that the transmissibility is a good indicator feature of structural damage in spite of environmental fluctuations and boundary condition non-linearities. For this reason, the transmissibility-based damage identification technique is referred to as the structural Diagnostics using Non-linear Analysis (sDNA) approach. They demonstrated that this approach reduces the number of false diagnoses due to non-linearities. Experiments were carried out on two large distributed structures; a building and a rotorcraft fuselage.

Maia *et al.* (2007) acknowledged that the use of ODSs, such as in the DRQ earlier presented by Sampaio and Maia (2004), implies that the loads applied to the structure with and without damage are either known or, at least, the same. When a structure is subjected to ambient excitation, those conditions can hardly be assured. The loads may vary quite significantly and the ODS changes may be due to the difference of loads instead of the presence of damage. To avoid this handicap, Maia *et al.* (2007) explore instead the use of Transmissibility functions in the DRQ, since the response Transmissibility is load invariant. Multiple Input Multiple Output (MIMO) tests were carried out on a free-free steel beam with two shakers attached to each of the beam's tips. However, even using the transmissibility, the amount of the DRQ deviation happened to be load dependent. The authors point the non-linear behaviour as a plausible cause, although further study is still needed.

2.2.8 Damping

Based on the observation that modal damping is a parameter with higher sensitivity to internal delamination of CFRPs than the natural frequencies, Keye *et al.* (2001) developed a method which is capable of relating modal damping deviations caused by structural damage to the damage location on the structure. They call attention to two important aspects of the experiments. First, when only a single sensor (or a small number) is available, the experimental data provides no spatial information on the dynamic response, i.e., on the mode shapes, and the process of localizing structural damage has to cope with eigenfrequencies and modal damping values, which can be extracted from the measured FRFs. In such a case, a FE model

should be used to locate the damage. Second, since in practice the damage location is unknown, a range of damage locations must be simulated in the numerical model and the modal data must be computed for each damage case. After testing the method on a plate-like CFRP structure, they proposed some improvements: (i) to enhance the correlation between numerical and experimental data, updating techniques should be used; (ii) implementation of a systematic mode selection strategy and the weighting of individual modes based on their sensitivity to damage location; (iii) optimization of actuator/sensor placement and evaluation of their influence on the damage identification capability; (iv) evaluation of other aspects, such as temperature effects and influence of the excitation method.

Kyriazoglou *et al.* (2004) explore the use of the Specific Damping Capacity (SDC) for damage detection and location in composite laminates. One important observation is that the resonant frequency allows detection of cracks in glass fibre-reinforced laminates, while for carbon fibre-reinforced laminates no detectable changes in the resonant frequencies could be found. However, large changes were found in the SDC. The method consists of measurements and analysis of the SDC of composite beams vibrated in free-free flexure in their first mode. The SDC is defined as:

$$SDC = \frac{\Delta U}{U} \quad (2.21)$$

where ΔU is the energy dissipated in one cycle and U is the total energy stored in that cycle. The energy stored by the beam in bending, U , is calculated from the mode shape maximum deflection at the centre of the beam. The energy dissipated in one cycle is equated to the energy input. Tests were carried out both in air and in vacuum, and it was found that air damping significantly affected the measurements, particularly when the beam possessed off-axis reinforcement.

Yam *et al.* (2004) proposed to develop a practical method for the location and prediction of damage in CFRP plates by means of a combination of the measured modal damping and the computed strain energy distribution. First, a FE model is established to estimate the modal parameters, such as natural frequencies, mode shapes and modal strain energy. Based on the numerical model and on the fact that delaminations in different regions produce characteristic increases in the modal damping, they were able to experimentally locate damage. These authors note that the numerical simulations provide a good explanation for damping increase due to delamination, i.e., the energy dissipation is mostly induced by interfacial slip across the delamination and the tendency for penetration between the upper and lower surfaces in the delamination region.

Various authors have tried to study the damping mechanisms in composite materials. For example, Nayfeh (2004) developed a model for vibration parallel to the plane of lamination of a symmetric five-layer elasto-viscoelastic sandwich beam, since it is known that a sandwich beam consisting of alternating elastic and viscoelastic layers can be designed to exhibit large damping on flexural vibration in the direction normal to the plane of lamination. Berthelot and Sefrani (2004) experimentally analyzed damping of unidirectional glass fibre and Kevlar composites, comparing them to the models of Adams-Bacon, Ni-Adams and complex stiffness. The purpose was to develop an analysis of the effect of the fibre-reinforcement orientation in the case of unidirectional layers, since it is known that, at the constituent level, the energy dissipation in fibre-reinforced composites is induced by different mechanisms such as the viscoelastic nature of the matrix and fibre materials, damping at the fibre-matrix interface, damping due to damage, etc.

Curadelli *et al.* (2008) presented a method to monitor the structural integrity on civil infrastructures by means of the instantaneous damping coefficient identification. Laboratory tests as well as numerical simulations showed that in many commonly used structural systems damage causes important changes in damping. Thus, parameters that characterize structural damping can be used as damage-sensitive system properties. According to Feldman (1997), the instantaneous (viscous) damping coefficient may be calculated as:

$$h_0(t) = -\frac{\dot{A}(t)}{A(t)} - \frac{\dot{\omega}(t)}{2\omega(t)} \quad (2.22)$$

where $A(t)$ and $\omega(t)$ are the instantaneous amplitude and the instantaneous damped angular frequency of the vibratory system with their time derivatives. The instantaneous amplitude $A(t)$ can be extracted from the free vibration time signals employing a continuous wavelet transform.

2.2.9 Impedance based methods

Park, G. *et al.* (2003) present an overview of piezoelectric impedance-based health monitoring where the hardware and software issues are summarized, including a discussion of future research areas and the path forward.

Park, G. *et al.* (1999) introduced an impedance-based method which uses a Piezoelectric Transducer (PZT) as both actuator and sensor. It can be shown that the electrical impedance of the PZT is directly related to the structure's mechanical impedance (Liang *et al.* (1994)). Thus, a

relationship can be found to allow determination of the structural properties; specifically, the mass, stiffness and damping. Any change in the mechanical impedance, which could be caused by the presence of damage, will show up in the electrical impedance of the PZT. The damage state is identified when a defined metric, given by the sum of the squared differences of the impedance between the current and reference states, increases above a predefined threshold. These authors point out that this technique possesses the twin advantages of not requiring numerical models and the fact that its high-frequency excitation nature makes it very sensitive to local structural modifications.

Grisso *et al.* (2004) used an impedance-based SHM system to detect the onset of transverse matrix cracking in cross-ply graphite/epoxy composite. Ceramic PZT patches are attached to the composite samples (in this case, beams) to simultaneously excite the structure with high-frequency excitations (two frequency ranges, from 10 to 20 kHz and from 40 to 60 kHz) and monitor any changes in structural mechanical impedance. In order to detect damage severity, these authors use the Root Mean Square Deviation (RMSD), using the squared differences of the impedance between the undamaged and actual states. These authors conclude that acoustic emissions testing showed a good correlation only for thicker specimens, while the impedance-based method gave better correlation for thinner specimens.

Moura Jr. and Steffen Jr. (2004) tried to identify the best frequency bands for impedance-based structural damage identification in flexible structures. Damage was simulated in a cantilevered aluminium beam by adding a mass to the free end of the beam. By observing the results, these authors agreed that, at least for the conditions used, the best low frequency value is 15 kHz, while the best bandwidth value is the intermediate one (4 kHz).

Peairs *et al.* (2005) developed a modelling technique for impedance-based SHM, combining the Spectral Element Method (SEM) with electric circuit analysis. These authors argue that SEM has several advantages over other conventional FE techniques, for example because SEM more accurately models higher frequency vibrations because the mass is modelled “exactly” and incorporates higher order models more easily. Sensor multiplexing for transfer impedance and high frequency modelling were also investigated. However, modelling at higher frequencies is more complex because of the presence of the PZT resonances.

Simmers Jr. *et al.* (2005) applied an impedance-based method to detect and quantify the onset and growth of pre-crack surface corrosion. Three metrics were used: one similar to the one used by Park, G. *et al.* (1999), the RMSD and a crosscorrelation. The experimental results on an aluminium beam indicate that the impedance-based method is effective for corrosion detection and tracking, and that there is a relationship between the metrics and corrosion location, surface coverage and pit depth.

Park, G. *et al.* (2005) proposed the use of statistical pattern recognition methods to address damage classification and data mining issues associated with large numbers of impedance signals for health monitoring applications. In order to diagnose damage with statistical confidence, the impedance based monitoring is cast in the context of an outlier detection framework. The statistical process control developed consists of a two-stage prediction model that is a combination of AR and ARX models, the AR-ARX. The damage-sensitive feature is then computed by differentiating the measured impedance and the output of the ARX model. Because of the non-Gaussian nature of the extracted features, Extreme Value Statistics (EVS) is employed to develop a robust damage classifier. The proposed technique was tested in a numerical example using a 5-DOF system and an experimental investigation on a multi-story building model, and it was found that the algorithm could assess the condition of a structure in a more quantifiable manner than the traditional impedance approaches. Some issues that need close attention were identified: (i) the robustness of the proposed algorithm against environmental condition changes should be improved; (ii) different damage sensitive features could be used, such as relative and/or absolute changes in exogenous or auto-regressive ARX coefficients; (iii) a prior curve fitting on the impedance data should be performed before constructing the ARX model in order to minimize the effect of leakage in the frequency response measurements; (iv) the differentiating process involved in feature extraction often led to amplifications of existing noise in data; (v) the selection of proper EVS distribution for each data set and the evaluation of associated distribution parameters are still strongly based on an initial guess and on a trial-and-error method.

2.2.10 Lamb waves

One approach that has received much attention in the last few years is the use of Lamb waves. Lamb waves are a type of elastic perturbation that can propagate across large areas of a free-free solid plate with low dispersion of energy, even in materials with a high attenuation ratio. This type of wave was first described in theory by Lamb (1917), although he never tried to produce them. Alleyne and Cawley (1992) were among the first to discuss interaction of Lamb waves with defects for non-destructive testing. Saravanos *et al.* (1994) presented a procedure for delamination detection in composite materials using Lamb Waves and embedded piezoelectric sensors.

Kessler *et al.* (2002) maintain that techniques using Lamb waves have proven to provide more information about damage type, severity and location than previously tested methods using FRFs, since Lamb waves are more sensitive to local structural defects. Piezoceramic patches

were used to excite the first anti-symmetric Lamb wave (A_0 mode). The PZT actuators were chosen because of their high force output at relatively low voltages and also due to their good response qualities at low frequencies. Kessler *et al.* (2002) explored the optimization of Lamb wave methods for damage detection in composite materials, covering the problems of choosing the appropriate actuating frequency, pulse shape and sensor geometry for Lamb wave application. The results were compared by performing a wavelet decomposition using the Morlet wavelet, and plotting the magnitude of the coefficients at the driving frequency. Although Lamb waves display great capabilities in damage detection and location, these authors point out, as the major disadvantage of this method, that it has to be active; i.e., it requires a voltage supply and function generating signal. Another awkward requirement is the high data acquisition rate needed to gain useful signal resolution. Finally, the Lamb wave method should most likely be placed into a SHM system in conjunction with another passive detection method, such as an FRF method, in order to conserve power and data storage space and because the Lamb wave data can be more difficult to interpret.

Su *et al.* (2002) state that noteworthy efforts have been made since the 1980s in the field of wave propagation based identification methods. Nevertheless, it is known that the propagation characteristics of Lamb waves are relatively complicated because of the dispersion phenomenon. These authors studied the interaction between the fundamental Lamb wave modes and delamination in carbon fibre-reinforced laminates. Models (FE and experimental) of a plate with a delamination were tested, using PZT wafers as sensors/actuators. The calculated and measured dynamic responses were processed using wavelet transform-based analysis in the time-frequency domain for the purpose of damage evaluation, which proved to be very effective in diminishing the influence of broadband noises and structural vibration patterns and also showed that the response in the time-frequency space is noticeably sensitive to the delamination location.

Lee and Staszewski (2002) discussed acoustic-ultrasonic wave propagation modelling techniques, focusing on two dimensional wave interactions with defects in metallic structures.

Ricci *et al.* (2004) presented a methodology for automatic damage identification and location in composite structural components. The damage is inflicted in the form of an impact, and identification is based on the calculation of a set of damage correlation indices obtained from the frequency analysis of the signals, obtained from PZT sensors, from the reference and damaged state of the structure. The main idea behind this approach is that elastic waves, propagating from the site where they are generated to the location where the signals are sensed, carry information about the portion of the structure through which they travelled.

Elastic waves can be very sensitive to small local defects. An indicator of any change in the propagation characteristics of the wave can be given by:

$$DI_i = \left| 1 - \frac{\{H_i^D\}^T \{H_i^D\}}{\{H_i\}^T \{H_i\}} \right| \quad (2.23)$$

where DI_i is the damage index evaluated at the sensor location i and $\{H_i\}$ is the frequency response vector at location i . These authors argued that this damage index approach can be used for detection and, under certain conditions, characterization of degradation in aircraft, aerospace and civil structures and that the analysis of the waveform signals would provide information on the location and nature of small defects.

Sohn *et al.* (2004a) proceeded with the work developed by Sohn *et al.* (2004b) and proposed a multi-scale structural health monitoring approach for detecting defects in composite structures by combining Lamb wave propagation, impedance-based methods and time reversal acoustics using a common active sensing system for local non-destructive evaluation. These authors mention that the ultrasonic research community has studied Lamb waves for the non-destructive evaluation of plates since the 1960s. They also define Lamb waves as mechanical waves corresponding to vibration modes of plates with a thickness of the same order of magnitude as the wavelength. In the study presented, the wave attenuation feature, identified using a wavelet based damage index, is used to locate the region of damage (Sohn *et al.* (2004b)). Damage was introduced by firing a small projectile at different locations on a graphite fibre/epoxy matrix square plate with varying velocities. It was found that the three methods studied can be complementary because they can use the same sensors/actuators, which in this case were commercially available thin films with embedded PZT sensors. For instance, while it was observed that the Lamb wave propagation method is effective for thin plates, the impedance method is more suitable for detecting damage near structural joints or connections.

Toyama and Okabe (2004) studied the effects of tensile strain and transverse cracks in the propagation velocity of Lamb waves in cross-ply FRP laminates, since the waves' propagation velocity is sensitive to changes in the in-plane stiffness of the laminates. It is noted that some composite materials, such as CFRP, exhibit non-linear stress-strain responses, which makes Lamb wave velocity based damage detection methods more complex under external loading. The Lamb wave propagation velocity was measured in Glass Fibre Reinforced Polymer (GFRP) and CFRP laminates during tensile tests and the elastic behaviour was studied. These authors make two interesting observations: First, that it seems that measuring the first symmetric

Lamb wave (S_0 mode) velocity is a more accurate means of evaluating the elasticity of laminates than the tensile test. Secondly, they noted that the wave velocity depends on both damage and the laminate elasticity. Finally, they state that the laminate stiffness as a function of strain must be known when under external loadings for damage detection purposes.

Sundararaman *et al.* (2005) use sparse phased sensor/actuator arrays for online damage detection and location on heterogeneous and homogeneous plates and discuss the theory of narrowband and broadband beamforming of propagating plate waves in damaged elastic media. According to these authors, a beamformer is a spatial-temporal filter that can be used to “look” in the direction of transmitted signal while eliminating interference that cannot be removed through temporal filtering or carrier demodulation alone. Beamformers consist of sensor arrays that are used to extract directional damage signatures. The principle on which this method is based is equivalent to an acoustic impedance discontinuity in the solid medium, so that damage, in the form of debonding, delamination, fibre breakage, matrix cracking, or voids, can be detected, localized and quantified. Experimental evaluation of this procedure was carried out on glass/epoxy woven composite, steel and aluminium plates.

Kim, Y. H. *et al.* (2007) acknowledged that the processing of simultaneous symmetric and antisymmetric Lamb wave modes, generated by the use of piezoceramic transducers of the surface mounted type, brings difficulties in the signal processing for extracting damage information. In order to overcome these difficulties, the modes were separated by using two sensors bonded on the opposite surfaces of the specimen at the same point. By combining the use of spectral analysis, they claim to present a real time damage assessment technique that extracts damage information from complicated PZT signals that could not be interpreted in the time domain. Experiments were carried out in an aluminium plate and in a composite beam laminate with Teflon-induced delamination.

Harri *et al.* (2008) proposed an interesting on-line method to control the critical length of existing surface cracks on wing-like structures during in-service fatigue loading. The method is based on the variation in transmission of a multisine ultrasonic Lamb wave: when a crack occurs, the variability of the received signal begins to grow due to the opening and the closing of the crack. Thus, the load must contain both tension and compression components and be large enough for the crack to open and close. The sensors can be placed at a certain distance in front of the critical length crack in order to monitor the health of the structure at that location. The major drawback of the method, as pointed out by the authors, is that the location where the crack is must be previously known for the correct placement of the transmitting and receiving transducers.

2.2.11 Neural networks

The use of neural networks in damage detection procedures and SHM was motivated by the possibility of the existence of different types of damage at several different locations within the same structure, making damage detection a complicated process.

Hanagud and Luo (1997) used three layer feed-forward neural networks to identify two different types of damage in GFRPs: delamination and stiffness reduction (due to transverse cracks or impact damage). It was assumed that only one of these defects existed, and analytical models were built to predict the dynamic behaviour of the structure considering various scenarios of damage. The main neural-network identifies the type of existing damage using a non-linear dynamic response criterion, which directs the problem to one of two sub-networks. Both these sub-networks use FRFs as inputs. Using the same beam as “case study”, Luo and Hanagud (1997) proposed the Dynamic learning rate Steepest Descent (DSD) for training neural networks, with the aim of increasing the learning convergence speed relative to the simple steepest descent method.

Krawczuk *et al.* (2000) presented the results of the application of a genetic algorithm and a neural network to the detection and location of delamination in a numerical model of a multi-layered GFRP beam. Two different procedures were followed to identify the damage location and size: the first is based on FE model updating and error location, while the second considers a set of possible damage scenarios (including damage type, location and size). These authors used an objective function, based on changes in the first four natural frequencies and on the DLAC proposed by Messina *et al.* (1992). The genetic algorithm converges after a reasonable number of generations, although these authors considered that this procedure deserved future development by including more processes that are observed in nature, for example elitism. The neural network’s performance in detecting the delaminated layer location across the thickness was poor, possibly because the authors considered a relatively small population of delaminated cases for training.

Hatem *et al.* (2004) also applied genetic algorithms and neural networks to damage detection in CFRP composites. Four types of damage were considered in the model of a cantilevered beam: circular holes (with different diameters and locations), delaminations (with different areas and locations), linear surface cracks (with different lengths, orientations and locations), and linear through cracks (with different lengths, orientations and locations). Damage type is identified by the generalized regression network. A special sub-network is used for each damage type, in an ensemble of five: a generalized regression network, a linear network, two back-propagation networks (with and without regularization) and a radial basis network. These

authors state that the generalized regression networks successfully classified damage type, with a success rate ranging from 85% to 98%. After damage is classified, an appropriate neural network or genetic algorithm is run to detect the remaining damage parameters, namely location, size and, in the case of a crack, orientation. Damage size was predicted with good accuracy, but the results on damage position and orientation were not particularly accurate.

Zheng, S. *et al.* (2004) combined computational mechanics and neural networks, in this case the back-propagation method, for prediction of delamination in CFRP beams. The neural network was trained with FE models, which were designed assuming various delamination sizes and locations. As inputs, it used the first five natural frequencies. According to these researchers, the neural network correctly predicted delamination size and location within a small error margin.

2.2.12 Time-frequency analysis

Zabel (2004)(2005a)(2005b) applied a wavelet-based damage indicator to damage detection on reinforced concrete structures, using several case-studies, including the Z24-bridge in Switzerland already mentioned in this work. The indicator is based on the analysis of signal energy components in discrete time-scale domain. Normally, the wavelet coefficients of the Impulse Response Function (IRF) make different contributions to the considered system response. Thus, if the excitation force is known, it is easy to normalize the response relative to the excitation force. Another normalization possibility is to relate each response to the response in a reference location, thus leading to the transmissibility function. According to this author, it is possible (and adequate) to consider the transmissibility functions and their wavelet decompositions in a context of SHM when the ambient excitation is unknown. However the analysis so far is based on the assumption of similar excitations for all the observations, which means that further research is needed to evaluate how this restriction can be surpassed without the need for a known excitation.

Savov and Wenzel (2005) used a wavelet approach in order to locate damage in civil structures, based on the system's acceleration time history responses. A FE model of a three story shear-resisting frame excited by white noise ground acceleration and a prestressed reinforced concrete test beam under impact loading conditions were used as test structures. The first level fast wavelet decomposition of the measurements for both the undamaged and damaged structures was applied using the Haar mother wavelet, and the approximation and detail coefficients were obtained. Reconstruction of the actual system response was accomplished by a cross combination of the approximation coefficients of the undamaged

structure with the detail coefficients of the actual measurement. The sensitive feature is defined as the standard deviation of the error between this reconstructed signal and the actual measured signal. This method is based on the premise that the detail coefficients carry information about the local structural integrity in the time history response at the damaged sites. The advantage of this method is that the excitation mechanism is not needed to be known, since the method is entirely based on the measured responses. However, damage location is compromised by the sensor mesh refinement. Extension of this approach to quantification of damage, to prediction of remaining structural life and to evaluation of more complex structures, varying operational and environmental conditions and non-linear damage phenomena are issues to which these authors will give further attention.

Li, B. *et al.* (2005) present a methodology for determining crack location and size in a beam, taking advantage of Wavelet Finite Element Methods (WFEM). The idea of the WFEM is to discretize a body into wavelet finite elements which are interconnected at nodal points on the element boundaries. Some of the advantages of WFEM over traditional FE methods for modal analysis of crack problems are pointed out. The natural frequencies of the beam with various crack locations and sizes are obtained, through the use of a WFEM, and used as features in the damage detection process. The accuracy of the method was tested on the experimental data of a beam studied by Silva, J. M. M. and Gomes (1990). Finally, these authors suggest that this procedure could be easily extended to complex structures with multiple cracks.

2.2.13 Hilbert transform

Testa (2005) argues that the Hilbert-Huang transform (HHT) is very useful for non-stationary, non-zero mean and non-linear real signals. The HHT makes an Empirical Mode Decomposition (EMD) of the time signal into narrow band components with zero mean, in which each component is called an Intrinsic Mode Function (IMF). Unlike their equivalents in the FFT, these components do not have a specific analytical representation, but each component can be associated with a physical meaning, i.e., the components are related to the mode shapes and existence of damage.

Lin, S. *et al.* (2005) use the HHT technique on the phase I IASC-ASCE benchmark problem for SHM. This benchmark was developed to simplify the side-by-side comparison of various analysis techniques for damage identification in structures on a common basis. The scale-model structure is a 3.6 m high four-story steel frame with 2.5×2.5 m cross sectional area. Johnson, E. A. *et al.* (2004) present two analytical models of the structure, both finite element based: one is a 12-DOF shear-building model, the other a 120-DOF model. Based on the noisy

acceleration data (due to ambient excitation), Lin, S. *et al.* (2005) confirm that HHT is capable of identifying the natural frequencies, damping ratios, mode-shapes, stiffness matrix and damping matrix of a structure with a reasonable accuracy. Damage was identified by comparing the stiffness of each floor before and after introducing damage. Simulation results show that the HHT technique can detect, locate and quantify damage with good accuracy. Finally, these authors acknowledge that, despite the fact that normal modes are assumed to exist in the current benchmark model, the technique can also be used on linear structures with complex eigenproperties, as demonstrated by Yang *et al.* (2003).

Zhang *et al.* (2005) presented the implementation of a method for nonlinear, non-stationary data processing, namely HHT in traditional vibration-based approaches to characterize structural damage. Also, the HHT is compared to the Fourier transfer function technique in detecting local damage with a computer model and experiments in two pile foundations of the Trinity River Relief bridge in Texas, USA. The HHT analysis showed a more significant frequency downshift than Fourier-based approaches for measurements made near the damage location. These authors observed one point which, although only applicable to very specific structures such as bridges, remains of interest: by selecting two or more similar structural members (e.g., two of four columns with the same size, cross section, and construction in a bridge), the need for data from a reference state may be avoided if only one of these members experienced damage.

Shi and Law (2005a)(2005b) presented a HHT-based technique for parameter (stiffness and damping) identification in damage detection for, respectively, linear time-varying discrete dynamic systems and nonlinear systems. Both procedures are tested using analytical models in free vibration. Shi and Law (2005a) identify the non-linear system using a so-called Skeleton Linear Model (SLM), which has similar dynamic behaviour to the corresponding nonlinear system.

2.2.14 Principal component analysis and singular value decomposition

Santos *et al.* (1999)(2000) presented a technique for the identification of damage in laminated composite structures using, as case study, a numerical simulation of a rectangular plate. The algorithm was formulated by considering the sensitivities of the orthogonality conditions of the mode shapes, which allow for the calculation of a damage parameter in each finite element. This damage parameter is directly related to the stiffness reduction in the damaged finite element. They argue that the proposed method allows for detection and location of multiple damage sites. These authors formulate a set of $M = m(m + 1)/2$ linear independent

equations with N unknowns, where m is the number of vibration modes and N is the number of elements, based on the orthogonality condition sensitivities of the damaged structure. In the cases where $M \geq N$, the solution can be efficiently found by a Gauss-Jordan elimination method, whereas if the system is underdetermined, i.e., $M < N$, it is possible to find the $N - M$ family of solutions using the SVD (Golub and Van Loan (1983)). These authors argue that the proposed technique allows for an efficient quantification of damage over either small or larger areas and that this methodology is a promising tool for the research community working on experimental damage identification.

More recently, Santos *et al.* (2004)(2005) presented a damage identification technique based on FRFs sensitivities. Considering that a single-input unit force is applied to the i^{th} DOF of both the undamaged and damaged structure, they show that:

$$[H(\omega)][\Delta Z(\omega)]\{H_i^D(\omega)\} = \{H_i^H(\omega)\} - \{H_i^D(\omega)\} \quad (2.24)$$

where $[\Delta Z(\omega)] = [Z^D(\omega)] - [Z^H(\omega)]$ is the difference between the dynamic stiffness matrices of the damaged and undamaged structures and $\{H_i(\omega)\}$ is the i^{th} column of the mobility matrix. After some mathematical manipulation, including a first-order Taylor expansion, the above equation can be rewritten in a compact form, where the solution is found using a least-squares method. In that formulation, it is implicit that all DOFs of the damaged structure are known, which is not feasible in practice because rotational DOFs are very difficult to obtain experimentally, as can be seen, for example, in Montalvão *et al.* (2004a)(2004b). Consequently, the unknown DOFs of the damaged structure should be determined using an expansion of the measured DOFs. For example, Santos *et al.* (2003a)(2003b) propose the use of either static or dynamic expansions for this purpose. Santos *et al.* (2004)(2005) observed that the mobility matrices should be computed using at least three times the number of natural frequencies and mode shapes contained in the frequency range of interest. On the other hand, they observed that the best identification results are obtained at lower frequency ranges. Also, for damage of small extent, the errors are the main influence in the identification quality, whereas for large damage incompleteness becomes the most important factor. These authors also used a procedure for the weighting and elimination of equations, based on Ren and Beards (1995), once the solution depends not only on the quality of the FRF measurements but also on the frequencies and co-ordinates in which the vibration amplitude is largest. Finally, it is argued that this technique presents better results than those obtained when using a technique based on modal data sensitivities.

Bernal (2002b) used the Damage Locating Vector (DLV) approach to locate damage, using as case study the 4-story steel frame building of the phase II IASC-ASCE benchmark problem. The proposed damage characterization strategy is grounded in a cascade methodology that contains the following modules: (i) compression of the measured data and identification (stochastic state-space realization); (ii) extraction of flexibility proportional matrices; (iii) location of damage using the DLV approach and (iv) quantification of damage. The DLV is a theoretically based technique for mapping changes in flexibility to the spatial distribution of damage. According to Bernal (2000)(2002a), the DLVs are a set of vectors that have the property of inducing stress fields whose magnitude is zero in the damaged elements. Consider a system that can be treated as linear in both the undamaged and damaged states, with flexibility matrices $[F^H]$ and $[F^D]$ (respectively) at m sensor locations, and assume there are a number of load vectors, defined in the sensor coordinates, which produce identical deformations at the sensor locations in both the undamaged and damaged states. If the linearly independent vectors that satisfy this requirement are collected in a matrix $[L]$, and according to the compatibility of displacements, one may write:

$$([F^H] - [F^D])[L] = [DF][L] \quad (2.25)$$

where $[DF]$ is computed from an SVD of the change in the flexibility matrix of the system. This equation can be satisfied either if $[DF]$ is zero or rank deficient, and $[L]$ is a basis for the null space of $[DF]$. Bernal (2002a) shows that the first possibility implies that either there is no damage (though in practice no one ever computes $[DF]$ equal to zero) or that damage is confined to a region of the structure where the stresses are zero for any loading sensor coordinates. On other words, the null space of the change in flexibility contains vectors that lead to identical displacements at the sensors locations in both the undamaged and damaged states. More developments of this issue for practice purposes are shown in Bernal (2000)(2002a), such as selecting thresholds for the definition of the null space and the “zero stress region”, since in fact the stress level will never be exactly zero in any element. As a result, two drawbacks of this method can be pointed out: it is not sensitive to damage which does not introduce changes in the flexibility at the measurement points, and identification may be poor if the damage region is too large when compared to the number of sensors. However, it is worth mentioning that the authors claim that (i) it has the ability to detect both single and multiple damage scenarios, (ii) it can operate with an arbitrary number of sensors without reference to DOF expansion or reduction strategies and (iii) the DLV vectors are computed strictly from the measured data without reference to a mathematical model of the system.

Also, this method is equally applicable to static measurements. Finally, since in Bernal (2002b) the inputs could not be measured, he used flexibility proportional matrices obtained following the procedure introduced by Bernal and Gunes (2002). This latter is an extension of the DLV damage location technique to the output-only case.

Yan *et al.* (2005a) proposed a damage detection method for SHM under varying operational and environmental conditions based on PCA, also known as Karhunen-Loève transform or proper orthogonal decomposition. One advantage of the use of PCA is that it is not necessary to measure the environmental parameters because they are taken into account as embedded variables. This method relies on the principle that the measured feature changes due to environmental causes are different from those arising from structural damage. Novelty analysis on the residual errors provides a statistical indication of damage. The environmental conditions are assumed to have a linear effect on the vibration features. The application of this method to numerical and experimental data of a wooden bridge shows that different levels of damage can be correctly assessed independently from the environmental effects. This method was extended to the non-linear case by Yan *et al.* (2005b), in which a two step procedure is conceived, consisting of clustering the data space into several regions and then applying the PCA in each local region. The local PCA-based damage detection method is applied, using vibration data measured in-situ over a one-year period, in the SHM of the Z24-bridge mentioned previously. During the monitoring period measurements of the environmental parameters (temperature, wind, humidity, etc.) were recorded, and it was observed that the asphalt layer on the bridge surface plays a different role during warm and cold periods, thus causing non-linearity. For example, in an earlier work, Peeters and De Roeck (2000) established ARX models for the first four modes, in order to obtain a good correlation between temperatures at selected locations and the natural frequencies of each mode, with the aim of analyzing different damage scenarios. A comparison was made by Yan *et al.* (2004) between the work of Peeters and De Roeck (2000) and that by Yan *et al.* (2005b), leading to the argument that by using the PCA-based damage detection method the problem is simplified, as only vibration features are needed to determine whether the structure is damaged.

Vanlanduit *et al.* (2005) introduced the Robust SVD (RSVD) for damage detection from measurements taken under different operational conditions, i.e., different excitation levels, geometrical uncertainties and surface treatments. This method is based on the SVD of a matrix $[H] = [H_1, \dots, H_N]$, where H_1, \dots, H_N are observation features taken from N experimental conditions. These features can be FRFs, response spectra or estimated modal parameters. The RSVD computes the SVD of the intact structure from a set of observations of both intact and damaged structural states, possibly obtained under different conditions. The RSVD

performance is then compared to the classical least-squares SVD and to the Iterative SVD (ISVD). The experimental results show that the classical least-squares SVD is not able to correctly classify damage because it gives an incorrect decomposition when both damaged and undamaged measurements are used to compute the subspace. This occurs because it is assumed that it is not known which observations are the healthy ones. If a set of observations belonging to the undamaged case is previously known, the authors agree that the SVD performance will be comparable to that of the RSVD. It was also shown that the ISVD slightly improved the classification results, though it was not capable of identifying the smallest damage case considered. Finally, these researchers claim that the RSVD provided the most reliable results.

2.2.15 Instrumentation

Lin, M. (1999) developed a printed circuit film layer of piezoceramic materials which can be embedded into composite structures during the production process. This film can support temperatures above the curing temperature for most composites, and Lin, M. (1999) argues that it has little or no effect on the mechanical properties of composite structures.

Sundaresan *et al.* (2001) discuss the use of a Scanning LDV and piezoceramic materials for distributed sensing, with the purpose of evaluating the application of widely distributed sensors for wide area health monitoring of composite materials. The Scanning LDV is used for field tests as a rapid non-contact detector for larger hidden damage, and the highly distributed embedded smart sensors are investigated for in situ real-time monitoring of composite structures. Two methods of damage detection using the laser vibrometer were presented. The first, called Boundary Effect Detection (BED), performs post processing of the ODSs, and, according to the authors, is somewhat akin to the wavelet method, thus allowing for small damage detection in the low frequency range. The second method, called Operational Deflection Pattern Recognition (ODPR), is able to identify faults by evaluating irregularities in the vibration response patterns, avoiding the need for reference pre-damage data.

Fritzen *et al.* (2002) designed an intelligent self-diagnosis system to detect the existence of delaminations in plate-like CFRP structures. The plate is instrumented with an array of four piezoceramic sensors and is excited with a random signal by means of a piezoceramic actuator. Different delamination severities were introduced by impacts at different velocities. As a damage indicator, they used the subspace-based fault detection algorithm, based on the work presented by Basseville *et al.* (2000). To determine the eigenfrequencies, damping and mode shape changes, the stochastic subspace identification method was used, following the

approach proposed by Peeters and De Roeck (1999). They also performed a statistical χ^2 -test to assess whether the recent data fit the baseline data.

Deraemaeker and Preumont (2004a)(2004b) presented an approach to vibration based damage detection based on the use of a large number of sensors to which a programmable linear combiner is attached, using a simply supported beam as a test case. The linear combiner is programmed to work as a modal filter, i.e., the converted time-domain to frequency output content of the modal filter is used as the damage detection feature. First, these authors show that if local damage exists, then peaks will appear in the FRF of the modal filter. If temperature changes are registered instead, the modal filter is shifted but its shape remains unchanged. Thus, the proposed approach allows the user to distinguish between local damage and global changes (due to the surrounding environment, for example). For the case where the excitation forces are unknown, it is suggested that the square root of the Power Spectral Densities (PSDs) be used instead of the FRFs, because the square root of the PSD has, in principle, the magnitude of the transfer function if the excitation force is white noise. It was demonstrated that this method allows the detection of low levels of damage, as well as being able to distinguish damage from temperature effects.

Lynch *et al.* (2004) developed an active wireless sensing unit to command a PZT sensor surface mounted on an aluminium plate. Low energy Lamb waves are introduced in the plate and the unit collects the signals measured by a second PZT sensor placed elsewhere on the plate surface. The potential of this unit to locally perform system identification analysis is illustrated by calculating ARX models.

Sundaresan *et al.* (2004) studied a structural health monitoring system that employs an embedded Acoustic Emission (AE) sensor, developed by Sundaresan *et al.* (2001). One of the advantages of this continuous sensor is that it avoids separate cabling and individual support electronics. They monitored fatigue crack growth in a GFRP laminate specimen with two circular notches. They stated that the performance of the continuous sensor was superior to the traditional single node sensors, and also used wavelet maps to classify the AE signals.

Nichols *et al.* (2005) reported recent advances in the fields of sensing and signal processing, with the aim of damage detection. A nine fibre Bragg grating strain sensor network was used to measure the vibrational responses of a thin steel plate subjected to successive growing saw-cut damage levels. The relationship between a reference (or undamaged) state and the actual (or damaged) state can be mathematically established when the structure is interrogated with a deterministic chaotic signal. This method relies on the principle that this function loses differentiability when damage exists. Thus, the use of the local Holder exponent is proposed as

a means of quantifying the differentiability of this function relating the undamaged to the damaged state responses. An algorithm to determine these quantities from time series data is also described.

Park, J. M. *et al.* (2005) evaluated the performance of different sensors for damage detection in glass fibre/epoxy composites through acoustic emission measurements. The sensors analyzed were: PZT, PVDF and P(VDF-TrFE) (poly(vinylidene fluoride-trifluoroethylene)). The PVDF sensors were tested both surface mounted and embedded on the composite structure, whereas the PZT unit was only surface mounted. It was observed that the embedded sensors are more sensitive to damage.

Motivated by the recent research advances, technological changes and commercial activities in sensors and acquisition systems for monitoring, Bonfiglioli *et al.* (2005) studied the measurement errors of electric strain gauges on FRP. They extended a theoretical deterministic approach developed in previous works to a probabilistic approach, with the aim of performing a sensitivity analysis of the variables that may result in errors on strain measurements. The experimental tests on several specimens made of different composite materials allowed some conclusions to be drawn with respect to the thickness of the resin, the strain gauges length, deviation angle and the sensors bonding glue. It was observed that the strain gauges length is the most important factor and that short strain gauges are to be avoided when the surface of the FRP material is very rough. One interesting conclusion stated by these authors is that the proposed model allows evaluation of the Young's modulus of the adhesive, which is very difficult to determine experimentally.

Qing *et al.* (2005) developed a hybrid piezoelectric/fibre optic diagnostic system for quick non-destructive evaluation and long term health monitoring of aerospace vehicles and structures. Piezoelectrics are used as actuators and fibre gratings as sensors. One of the major advantages mentioned is the excellent actuator/sensor decoupling, since the transducers use different mechanisms for signal transmission (one is electrical and the other optical). Another advantage is that these transducers can be used for a range of measurements; the fibre-optic sensors can be used for temperature sensing, while the piezoelectric system can be used for hydrogen sensing, and both can be used for acoustic emission measurements.

Wu *et al.* (2005) studied the correlation between the mechanical and electrical properties of concrete beams strengthened with hybrid CFRP sheets. These have the simultaneous aims of reinforcement and providing built-in self-structural health monitoring through the electrical conductivity and piezoresistivity of the carbon fibres. The hybrid CFRPs have self-diagnosis capabilities due to the relationship between strain/load and electrical resistance. These authors observed that different damage stages, failure processes and ultimate failure modes

of the hybrid CFRP reinforced concrete structures can be identified through the electrical resistance changes.

Castellini *et al.* (2005) produced software for data acquisition, control of a Scanning LDV and automatic measurement for the purpose of detecting delamination in composite plates, using as case study a delaminated composite panel made from 10 layers of aluminium sheets and Glass Laminated Aluminium Reinforced Epoxy (GLARE) for Airbus Deutschland aeronautical applications. These authors point out that the Scanning LDV has several advantages: it does not interfere with the structure, it has a high spatial resolution and sensitivity, it is adequate for high frequency analysis and it is suitable for use in operational conditions. The software uses a multivariate projection method, PCA, to extract and display the systematic variation in a data matrix. Also, statistical processing aids are used to pre-process the measured data, reducing the amount of information. Consequently, multivariate analysis methods, such as PCA, offer the possibility of eliminating systematic effects like noise. These researchers are continuing to search for optimal settings for the measurements, so that the number of measurement points is reduced. Research is also continuing in the field of composite materials excitation, because it is important that the excitation energy is constant and high for the entire frequency band.

In a survey of current smart sensor technologies for monitoring, Spencer Jr. *et al.* (2004) show that many efforts have been made to use remotely operated wireless systems, especially for damage detection in civil structures. Since traditional impedance-based methods require the use of bulky and expensive analyzers, Grisso *et al.* (2005) present the initial steps in the development of an automatic wireless system for impedance-based damage detection, which they claim is cheaper, more eco-efficient and has smaller dimensions. The final purpose is to develop a sensor that can be permanently attached to the structure and provide meaningful data concerning structural integrity. Other features include utilizing energy from the ambient environment, exciting the host structure with a high-frequency excitation, analyzing the results and wirelessly providing the status of the structure to an end user. The hardware development of a prototype version of this sensor is described in detail. This sensor was built and developed within the scope of the MEMS (Micro Electro-Mechanical Systems) augmented structural sensor (MASSpatch) joint-venture.

Angelidis and Irving (2007) manufactured 2mm thick quasi-isotropic CFRPs with in-built arrays of electrodes which were used to introduce an electric DC current and to measure the resultant potential distribution on the top and bottom surfaces of the laminate. Contrary to the technologies that involve the use of embedded or surface mounted optic fibres or PZTs, in the electrical potential technique the electrical conductivity of carbon fibre as a damage

sensing element is exploited. The electrical potential technique detects the presence of damage by measuring changes in the potential field on the surface of a current carrying composite laminate. The presence of cracks and delaminations causes modification of the current path along and between the carbon fibres. Changes in the potential field can be measured and characterized in terms of size and location and thus related to damage.

2.2.16 Other methods

Afolabi (1987) observed that anti-resonance shifts could be used to detect and locate damage, and showed the dependence of anti-resonance frequencies on the measurement points. Consequently, he observed that as the point of measurement gets closer to the location of the defect, fewer anti-resonances are shifted from their original values, until one reaches the location of the defect, when all the anti-resonances are as they were in the undamaged state. Although this is an interesting observation for the beam model and for the simulation used, it should not be forgotten that the stiffness relates to at least two co-ordinates, which means that the interpretation of the results obtained in real structures may be more complicated. Also, he only formulated relationships for direct FRF measurements, since this method may not work for transfer functions. The transfer FRF relationships, which are very simple to derive following the same lines as Afolabi (1987), can be found, for instance, in Montalvão (2003). More recently Wahl *et al.* (1999) presented a work in which they discuss the significance of antiresonances in experimental structural analysis for lightly damped linear systems. d'Ambrogio and Fregolent (2000) observed that the distribution of antiresonances may be significantly altered by small changes in the structural model. They use an updating technique that includes antiresonances in the definition of the output residual, showing that the use of antiresonances extracted from point FRFs allows for robust model updating procedures, mainly because antiresonances can be identified from experimental FRFs with much less error than mode shapes. Bamnios *et al.* (2002) monitored the change of the first antiresonance as a function of the measuring location along the beam and proposed a prediction procedure for transverse open crack location in beams under bending vibrations. Dilella and Morassi (2004) used antiresonances to avoid the non-uniqueness of the damage location problem, which may occur in symmetrical beams with a single open crack when only frequency data is employed.

Zimmerman *et al.* (1995a) discuss the implementation of the Minimum Rank Perturbation Theory (MRPT) based techniques to identify both the location and extent of damage, using data from the NASA 8-bay dynamic scale model truss test-bed. The evaluation of damage location was included in this study, as well as the selection of the number of vibration modes

to measure, eigenvector and damage vector filtering to minimize the effects of measurement noise, filtering of dynamic residual decomposition among various property matrices (mass, damping and/or stiffness) when multiple property matrices are being updated and rank-estimation algorithms. Zimmerman *et al.* (1995b) extended the MRPT theory to determine matrix perturbations directly from FRF data, discussing the benefits of this formulation. They concluded that the MRPT algorithm implementation using FRFs simplifies the analysis by avoiding the need to perform modal parameter identification. Another interesting conclusion is that, contrary to what would be intuitively expected, the regions away from resonances and anti-resonances are those containing the richest data. More recently, Zimmerman (2005) investigated the effect of measurement noise on damage detection performance and sensitivity of the MRPT and resulting stiffness perturbation matrices. It was concluded (by performing a Monte-Carlo simulation) that the use of linear sensitivity theory for estimation of the variance and standard deviation of each element in the damage vector and stiffness perturbation matrix is accurate. These standard deviations were used to establish a threshold for damage existence and, after that, for damage location and extent assessment.

Worden *et al.* (2000) presented a study of a statistical method for damage detection using outlier analysis. These authors claim that the method not only allows for novelty detection (deviation from normal condition), but also suggests the optimal reduction of the dimension of the data set without compromising the diagnosis. A discordant outlier in a data set is an observation that appears inconsistent with the rest of the data. The discordance test is based on the Mahalanobis squared distance for multivariate data sets, where the threshold value to classify whether an observation is an outlier or not is determined using a Monte Carlo method. The method was tested in four different situations: transmissibility data in a simulated 3 DOF system, gearbox experimental data, composite plate Lamb wave experimental data, and ball-bearing experimental data. In conclusion, they point out that for the 3-DOF numerical model the method was unable to detect any of the 1% stiffness reduction cases as outliers, though for higher reduction cases the method correctly identified the outliers. However, it should be noted that some simplifications were made. Firstly, it was considered that only a single outlier is present, which considerably simplifies the problem. Also, when choosing the Mahalanobis squared distance, it is implicit that the normal condition set has Gaussian statistics. In the case of, for example, multi-modal distribution, these authors suggest other techniques such as the Kernel density estimation.

Gutschmidt and Cornwell (2001) presented a False Positive Damage Indication Method (FPDIM) and applied it to experimental data for a plate that was progressively damaged. The purpose was to establish statistical bounds in order to distinguish damage from the natural

variability associated with any measurement. The statistical bounds are defined using several sets of data from the baseline structure. The FPDIM was applied to two damage identification techniques that do not require a prior numerical model: the flexibility and the strain-energy methods. Using both of these methods, standard deviations σ_{DI} of the damage indices DI_i in each element i for the undamaged structure were determined. A prediction interval is then calculated, within which it is expected that the next data point will fall. Any point outside that interval represents a certain probability of failure. Eight damage cases were considered, and tests were carried out under the same experimental and environmental conditions. It was observed that application of the FPDIM to results from the strain-energy method eliminated false-positives. When it was applied to the flexibility method, however, false-positives still occurred; i.e., the flexibility method successfully determined damage, but was unsuccessful in locating it.

Within the statistical pattern recognition paradigm established by Sohn *et al.* (2003), damage is in most cases identified by comparison between signals corresponding to two different structural states, one of them often corresponding to the undamaged state. Still, the operational and environmental variability, if not considered, may cause the unpredictable occurrence of either false-negatives or false-positives. In order to address this issue in the context of continuous online monitoring, Sohn *et al.* (2005) proposed a technique which does not rely on any past baseline signals for assessment of damage in composite panels. The test setup consists of a square CFRP plate with surface mounted PZT patches, to which delamination is introduced by impact damage with varying velocities. A Time Reversal Process (TRP) of modern acoustics is adapted to Lamb wave guided propagation. According to the TRP, an input signal can be reconstructed at an excitation point A if an output signal recorded at point B is reemitted to the original source point A after being reversed in a time domain. This process is referred to as the *time reversibility of waves*, and can be better understood with the aid of figure 2.1.

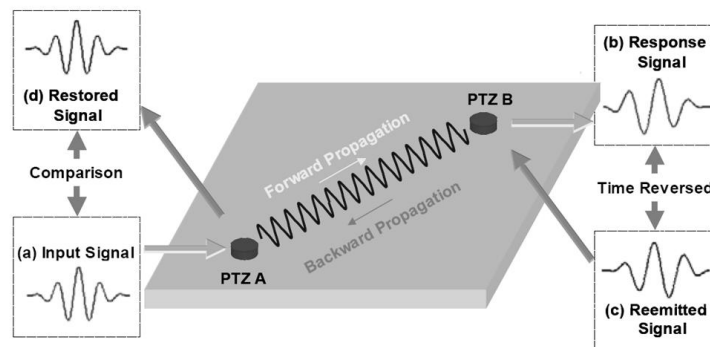


Figure 2.1: Schematic concept of TRP based damage identification (in Sohn *et al.* (2005)).

Damage detection is based on the fact that if a non-linear defect exists in the wave propagation path, time reversibility will no longer hold. A damage index based on the comparison between the original input waveform and the reconstructed signal is used to classify damage. A zero value means that time reversibility of Lamb waves is preserved and thus no non-linear defects are present. Once the damage index value exceeds a threshold value, the state of the system is defined as damaged in a conventional sense. These authors employ the use of a consecutive outlier analysis (Barnett and Lewis (1994)) to establish the threshold value without requiring past reference data and to address the issue of multiple outliers. By using this approach, these authors successfully located and quantified damage in the test plate without relying on prior baseline signals. Further investigations on the TRP applied to Lamb waves were very recently presented by Park, H. W. *et al.* (2009). These authors addressed the fact that while the TRP has been widely used in modern acoustics, its use in Lamb waves has been limited due to the amplitude and velocity dispersion characteristics of Lamb waves: when the TRP is applied to Lamb waves in a homogeneous regular waveguide, the refocusing capability is limited due to permanent residual sidebands.

According to Ibrahim *et al.* (1997) and to Li, H. C. H. *et al.* (2004) the introduction of the Random Decrement (RD) technique is attributed to Cole (1968)(1973). Ibrahim *et al.* (1997) proposed the Vector RD (VRD) technique. Later, Asmussen *et al.* (1999) showed that the VRD can be considered as a generalization of the RD. Rodrigues *et al.* (2004) explored the idea of estimating the spectral densities as the Fourier transform of the RD functions for the application of frequency domain output-only modal identification methods. Li, H. C. H. *et al.* (2004) investigated the potential of the RD technique for damage detection in composite beams by introducing different levels of delamination at the midplane of the beam at various locations. The initial formulation consists of obtaining the free-response signature of the beam by processing its random response based on the global average. This can be achieved by summing up many records of random responses in previously defined periods of time with appropriate criteria. This summation will result in a random decrement signature which minimizes the random component of the response. Each record can be seen as representing a linear system response composed of the overlapping of a step response, an impulse response, a random response and random noise. The step and impulse responses occur due to the initial displacement and initial velocity, respectively. When the various records are summed up, the random components, including noise, and impulse responses, average to zero, thus leaving only the step response of the system. It is shown that the RD signature is affected by both the delamination dimension and the sensor location. This may mean that damage detection can only be carried out successfully if a large database of RD signatures is created from predicted

defects or by the use of pattern recognition algorithms, such as neural networks. Li, H. C. H. *et al.* (2004) also note that the generation of such a database requires accurate modelling with appropriate treatment of structural damping, which they say plays an important role in the vibration of composite materials.

Coppotelli *et al.* (2004) compared two different experimental techniques for damage identification in composite plates. One approach is based on measurements of the dynamic displacement of the plate surface, which are evaluated through the speckle fringe patterns resulting from ESPI, a high resolution holographic technique explored by Caponero *et al.* (2000) exploiting both interference and diffraction in optics. The other approach is based on EMA techniques for the extraction of eigenproperties following the complex exponent based method (Ewins (1984), Maia and Silva (1997)). The damage identification procedure used for the first procedure is based on the Image Correlation Function (ICF), which is the square root of the FDAC in the special case where the vectors involved are real and positive, whereas for the second case, they use the MAC. One of the two test-structures used to evaluate the techniques was a sandwich plate structure made from two carbon fibre skins and an aluminium honeycomb core. This plate belongs to the Gamma-ray Large Area Space Telescope (GLAST), an international space mission intended to collect gamma-ray data from the universe. The GLAST was launched in the 11th June 2008 from the Cape Canaveral air force station in Florida, USA.

Peil *et al.* (2004) acknowledge that, in order to predict the remaining lifetime of a structure, the existing accumulated damage must be first assessed. To accomplish this task on civil engineering structures such as bridges, they use either a theoretical model of past actions, or an experimental method using acoustic emissions to assess damage. In the latter case, they take into account the entire transient signal, based on the assumption that different material damage processes lead to different transient signal forms, and the signals are assigned to certain damage state classes.

Lenzen (2005) presents a procedure for damage detection and location using the deterministic and stochastic subspace method for black box identification, which was tested on a steel frame and two bridges. If it is not practical to set up physical equations for a system, black box modelling can be used to describe the input-output relations of the system, in accordance with the theory of systems and the principle of cause and effect, in which systems are generally formulated as transfer functions. The black box models of both the intact and damaged systems, which have to be identified first, are compared and used to detect and localize system variations. This comparison is made by determining the so-called *dynamic influence coefficients*, which are then used for the evaluation of the COMAC instead of normal modes.

The theoretical backgrounds of black box modelling and subspace identification are described, as well as some of their limitations. Also, it is stated that the advantage of subspace identification is the physical weighting of the vibration modes with respect to the excitations.

Taylor and Zimmerman (2005) presented a non-model based method for detecting and locating structural damage (by evaluating linear stiffness changes) using load dependent Ritz vectors (Wilson *et al.* (1982)). They state that Ritz vectors are more sensitive to localized structural damage than mode shape vectors, which is an advantage when one cannot deal with a FE model of the structure (which can often occur in large civil structures) and because of the incompleteness problem. Also changes in mode shapes or shifts in the natural frequencies are often poor damage locators without the application of some model updating technique. Experiments were carried out on a steel bay welded frame structure and showed that Ritz vectors performed better than mode shape vectors in detecting low severity localized damage without the use of a FE model.

Thien *et al.* (2005) presented some guidelines for the development of a low-cost active-sensing based diagnostic system for pipeline structures. Integration of impedance-based and Lamb wave propagation methods in a common SHM is investigated. The impedance-based methods are used to detect and locate damage at the pipeline connection joints, while Lamb wave propagation methods are used to identify cracks and corrosion along the surface and through the thickness of the piping. Both techniques make use of the electromechanical coupling effects of piezoelectric-based active sensors, which in this case are small and non-intrusive macro-fibre composite patches. The procedure requires measurements in a reference state prior to damage. Minor defects can be detected through operation at high frequencies.

Polimeno and Meo (2009) studied nonlinear based approaches by monitoring the elastic material behaviour of damaged plates. Two methods were investigated: a Single-Mode Nonlinear Resonance Acoustic Spectroscopy (SIMONRAS) and a Nonlinear Wave Modulation Spectroscopy (NWMS). The methods were tested on different CFRP plates with BVID. The overall results showed a capability for providing an indication of the damage severity, but no results were presented concerning its location.

2.3 Prognosis

Prognosis – or the prediction of a system's lifetime, which corresponds to the last level of the classification of damage detection methods introduced by Rytter (1993) – is a matter that is traditionally approached in terms of fracture mechanics and fatigue. However, considering the

benefits that such technology may bring to the security, economics and resource management fields, the scientific community that deals with vibration analysis is now beginning to take some interest in this area.

Farrar *et al.* (2003) published a report whose purposes were to define the technology involved in prognosis. This work approaches (among other topics) the following: (i) a summary of the technologies and tools necessary to solve the problem of predicting a system's lifetime; (ii) a summary of the state of the art in damage prognosis; (iii) a generic approach to the problem, considering, however, that until that time all the prognosis solutions were directed at specific cases; (iv) the limitations inherent in such technologies; (v) a brief description of several applications in damage prognosis.

More recently, Inman *et al.* (2005) presented the first book to address this technology in a comprehensive way. The book is divided into four main parts including a total of twenty chapters: (i) damage models; (ii) monitoring algorithms; (iii) hardware and instrumentation; (iv) applications.

2.4 Final remarks

A survey of some of the representative advances in damage detection and SHM in the last years, with special emphasis on composite materials - given the growing interest in the use of this kind of materials in several engineering applications - was hereby made.

It must be noted that the more than two hundred works referred to in this chapter only represent a very small fraction of the published works available on the topic. Other works are not mentioned for several different reasons, most often because they use approaches that were not considered as relevant for the present work, such as those in which the excitation is applied using mathematical models of chaotic time series (Chang *et al.* (2004), Fasel and Todd (2005) or Olson *et al.* (2005)), techniques dealing with model updating (Yu *et al.* (2005) and De Roeck *et al.* (2005)) or other diverse methods and applications (Cioara and Alampalli (2004), Liu, M. and Chelidze (2005), Moura Jr. (2005), Nejad *et al.* (2005) or Law and Lu (2005)).

Chapter 3

Theoretical development

3.1 Foreword

This chapter is not intended to probe deeply into the theories that serve as the sustaining background for this work, namely science of composite materials and vibration and modal analysis. It starts from some of the basic concepts and leads the reader towards the introduction of an original approach in damage detection in composite materials. Many aspects that, albeit being related, do not play a very important role in the development of the proposed methodology, were deliberately left aside. It will be apparent that some of those developments are interrupted and that explanations are left unfinished. Yet, this incompleteness was intentional, as entering into further details and deeper into the subject would not bring any considerable benefit. Furthermore, most of the covered subjects do not constitute novelty and may be found in many wide spread textbooks.

The chapter's organization was chosen in such a way that an interrelation between both science of composite materials and modal analysis could be established. First, the basics of the mechanics of composite materials are introduced, followed by the fundamentals of vibration and modal analysis. Next, a section about damage in composite materials is introduced where a bridge between the preceding sections is established. Finally, a new damage index is proposed, based on the understanding of the described concepts.

More concerned readers may also be interested in reading, for instance, Cox and Flanagan (1997), Abrate (1998), Jones, R. M. (1999) and Moura *et al.* (2005) for a thorough and more extensive explanation of some of the covered issues, such as textiles, the micromechanics, constitutive laws or failure mechanisms of composite materials. For an overview about vibration and modal analysis, the books from Ewins (1984) or Maia and Silva (1997) are suggested.

3.2 Introduction to textile composites

Long fibre composites are used nowadays in structural applications of great responsibility due to their high resistance and other mechanical properties. In general, they appear in the form of laminates, i.e., they are built by superimposing plies (or layers) in which the fibres are oriented along well defined directions. Therefore, each layer acts as an elementary part which mechanical behaviour is fundamental to characterize. The mechanical properties of the fibre and matrix will determine the internal distribution of stresses and the mechanical properties of each layer.

Textile composites are favoured for their superior damage tolerance (Cox and Flanagan (1997)). A textile composite has internal structure on several scales. At the molecular scale, both the polymer matrix and the fibres exhibit structural details that profoundly affect strength and stiffness. Matrix properties are determined by chain morphology and crosslinking, among other things. Carbon fibres, which are often the preferred choice in aerospace materials, owe their axial stiffness and strength to the arrangement of carbon atoms in oriented graphitic sheets. Fibres are bundled into yarns or tows which, within the finished composite, behave as highly anisotropic solid entities, with far greater stiffness and strength along its axis than in transverse directions. Finally, the textile forms part of an engineering structure, perhaps the stiffened skin of a wing or fuselage. To manufacture the textile composite is to build that structure. The first processing step is the formation of yarns from fibres. In the second step, the yarns are woven into plain woven cloth. The cloths are

then laid up in the shape of the skin and stiffener and stitched together to create an integral preform. Finally, the composite part is consolidated by the infiltration of resin and curing in a mould.

A textile is said *periodic* when its geometry is conveniently described in terms of unit cells, following the example of crystallography. The unit cell is defined by the requirement that the entire textile can be constructed from spatially translated copies of it, without the use of rotations or reflections.

Weaves may be classified by the pattern of interlacing (figure 3.1). The simplest pattern is the plain weave. Of particular interest are the satin weaves. The satin weave pattern is defined by the number of yarn widths between exchanges. For example, the five harness satin weave has a 4-over, 1-under pattern. In addition, the exchanges are arranged so as not to connect; or in the case of the crow's foot pattern, so as not to lie on continuous diagonals. Individual layers of satin weave fabric are asymmetric. One side of the fabric is predominantly warp yarns; the other fill. The selection of a weave involves manufacturing considerations as well as final mechanical properties. The type of weave affects dimensional stability and the conformability (or drape) of the fabric over complex surfaces. Satin weaves, for example, exhibit good conformability. Unfortunately, good conformability and good resistance to shear are mutually exclusive. Thus, while woven fabrics are frequently the material of choice for complex geometries, the designer must be aware that specified material directions may be impossible to maintain: initially orthogonal yarns may not remain orthogonal in the fabricated product. Most 2D weaves involve two orthogonal directions of yarn, implying weak in-plane shear resistance within a single ply.

Regardless of the above, when modelling their macroscopic properties, all 2D textile composites can be considered to function as laminates (being called, in this case, *quasi-laminar*), with relatively minor allowance for their textile nature, even though the routes to their manufacture are very different from conventional tape⁴ layup. When large in-plane stiffness and strength are demanded, the majority of fibres must lay in-plane; relatively few can be dedicated to through-thickness reinforcement without unacceptable loss of in-plane properties. Compared to tape laminates, quasi-laminar textile composites with equal volume fractions of in-plane fibres will usually have slightly smaller in-plane stiffness because of tow waviness. In a 2D textile, such as a plain weave, waviness is topologically inevitable: tows must

⁴ A tape is a prepreg consisting of resin impregnated unidirectional fibres. It is usually available in rolls, as its length is many times greater than its width.

be wavy to pass under and over one another. The waviness can be reduced by selecting a satin weave rather than a plain weave, or using tows with flat cross-sections; but not eliminated.

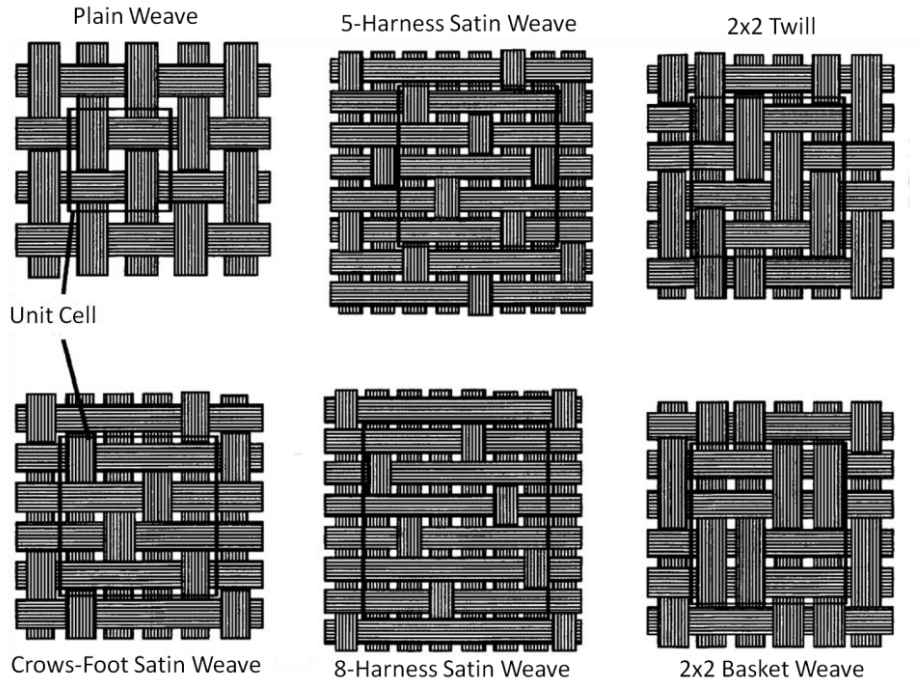


Figure 3.1: Commonly used 2D weave patterns (Cox and Flanagan (1997)).

3.3 Basics of the mechanics of composite materials

3.3.1 Engineering constants for orthotropic materials

Considering a material is linear elastic, the generalized Hooke's law relating stresses to strains can be written in short notation as:

$$\sigma_i = C_{ij}\varepsilon_j \quad i, j = 1, \dots, 6 \quad (3.1)$$

where σ_i are the stress components (shown on a three-dimensional elementary cube in figure 3.2, in which τ_{23} , τ_{13} and τ_{12} correspond, respectively, to σ_4 , σ_5 and σ_6), C_{ij} is the stiffness matrix and ε_j are the strain components⁵.

⁵ Note that the strain components ε_4 , ε_5 and ε_6 correspond, respectively, to the engineering shear strains γ_{23} , γ_{13} and γ_{12} and not to the tensor shear strains ε_{23} , ε_{13} and ε_{12} . The engineering shear strains are related to the tensor shear strains by $\gamma_{ij} = 2\varepsilon_{ij}$.

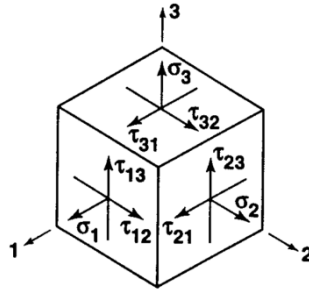


Figure 3.2: Stress on a cube element.

In a similar manner, the compliance matrix S_{ij} can be defined by the inverse of the stress-strain relations, namely the strain-stress relations:

$$\varepsilon_i = S_{ij} \sigma_j \quad i, j = 1, \dots, 6 \quad (3.2)$$

with:

$$S_{ij} = C_{ij}^{-1} \quad (3.3)$$

Both the stiffness C_{ij} and the compliance S_{ij} matrixes can be proven symmetric ($C_{ij} = C_{ji}$ and $S_{ij} = S_{ji}$). By definition, the elastic potential or strain energy density function has incremental work per unit volume of:

$$\delta W = \sigma_i \delta \varepsilon_i \quad (3.4)$$

If Hooke's generalized law (3.1) is now used, then, for linear elastic materials, it may be written that:

$$\frac{\partial W}{\partial \varepsilon_i} = C_{ij} \varepsilon_j \quad (3.5)$$

whereupon:

$$\frac{\partial^2 W}{\partial \varepsilon_i \partial \varepsilon_j} = C_{ij} = C_{ji} = \frac{\partial^2 W}{\partial \varepsilon_j \partial \varepsilon_i} \quad (3.6)$$

Since the order of differentiation is immaterial, the symmetry of the stiffness matrix is proven. Furthermore, attending to relation (3.3), the symmetry of the compliance matrix is also proven. Hence the number of independent elastic constants is reduced to 21 (instead of 36). In the case that there are no null terms in neither of the matrixes, the relations in equations (3.1) and (3.2) are referred to as characterizing *anisotropic* materials, because there are no planes of symmetry for the material properties (an alternative name is *triclinic* material). This is the most general case in the world of linear elasticity.

If there are two orthogonal planes of material symmetry for a material, symmetry will exist relative to a third mutually orthogonal plane. The stress-strain relations in coordinates aligned with principal material directions are:

$$\begin{Bmatrix} \sigma_1 \\ \sigma_2 \\ \sigma_3 \\ \tau_{23} \\ \tau_{13} \\ \tau_{12} \end{Bmatrix} = \begin{bmatrix} C_{11} & C_{12} & C_{13} & 0 & 0 & 0 \\ C_{12} & C_{22} & C_{23} & 0 & 0 & 0 \\ C_{13} & C_{23} & C_{33} & 0 & 0 & 0 \\ 0 & 0 & 0 & C_{44} & 0 & 0 \\ 0 & 0 & 0 & 0 & C_{55} & 0 \\ 0 & 0 & 0 & 0 & 0 & C_{66} \end{bmatrix} \begin{Bmatrix} \varepsilon_1 \\ \varepsilon_2 \\ \varepsilon_3 \\ \gamma_{23} \\ \gamma_{13} \\ \gamma_{12} \end{Bmatrix} \quad (3.7)$$

and are said to define an *orthotropic* material. Note that there is no interaction between normal stresses and shearing strains. Similarly, there is no interaction between shearing stresses and normal strains as well as none between shearing stresses and shearing strains in different planes. Finally, there are now only 9 constants in the stiffness matrix instead of 21. The strain-stress relations will have a similar aspect.

Engineering constants (sometimes known as *technical constants*) are generalized Young's moduli, Poisson's ratios, shear moduli and some other behavioural constants. According to Jones, R. M. (1999) these constants are measured in simple tests such as uniaxial tension or pure shear tests. Most simple material characterization tests are performed with a known load or stress. The resulting displacement or strain is then measured. The engineering constants are generally the slope of a stress-strain curve (e.g., $E = \sigma/\varepsilon$) or the slope of a strain-strain curve (e.g., $\nu = -\varepsilon_2/\varepsilon_1$ for $\sigma_1 \neq 0$ and all other stresses are zero). In fact, the components of the compliance matrix S_{ij} are determined more directly than those of the stiffness matrix C_{ij} . For an orthotropic material, the compliance matrix components in terms of engineering constants are:

$$[S_{ij}] = \begin{bmatrix} \frac{1}{E_1} & -\frac{\nu_{21}}{E_2} & -\frac{\nu_{31}}{E_3} & 0 & 0 & 0 \\ -\frac{\nu_{12}}{E_1} & \frac{1}{E_2} & -\frac{\nu_{32}}{E_3} & 0 & 0 & 0 \\ -\frac{\nu_{13}}{E_1} & -\frac{\nu_{23}}{E_2} & \frac{1}{E_3} & 0 & 0 & 0 \\ 0 & 0 & 0 & \frac{1}{G_{23}} & 0 & 0 \\ 0 & 0 & 0 & 0 & \frac{1}{G_{13}} & 0 \\ 0 & 0 & 0 & 0 & 0 & \frac{1}{G_{12}} \end{bmatrix} \quad (3.8)$$

and, because S_{ij} is symmetric:

$$\frac{\nu_{ij}}{E_i} = \frac{\nu_{ji}}{E_j} \quad (3.9)$$

To define the material's principal directions, the composite layer is first considered orthotropic. The intersection lines between each couple of planes allow defining the principal axes of orthotropy 1 , 2 and 3 (figure 3.3), in such a way the axis 1 is oriented in the longitudinal direction (along the fibres), the axis 2 is oriented in the transverse direction (across the fibres) and the axis 3 is in the out-of-plane direction. These are the material principal directions, meaning that normal stresses induce only linear strains and that shear stresses induce only shear strains.

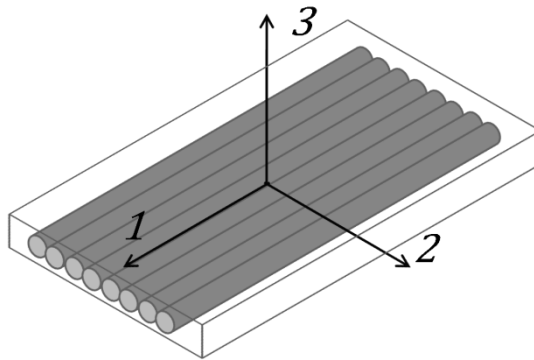


Figure 3.3: Layer's principal axis of a unidirectional reinforced lamina.

The composite layer of unidirectional fibres is transversely isotropic: if at every point of a material there is one plane in which the mechanical properties are equal in all directions, then the material is called *transversely isotropic* and such plane is called *plane of isotropy*. If, for

example, the 2-3 plane is the plane of isotropy, as occurs in layers of composite materials with unidirectional fibres, then:

$$E_3 = E_2; \quad \nu_{13} = \nu_{12}; \quad G_{13} = G_{12}; \quad G_{23} = \frac{E_2}{2(1 + \nu_{23})} \quad (3.10)$$

Thus, the independent elastic constants necessary to characterize the stress-strain behaviour of transversely isotropic materials are reduced to five: E_1 , E_2 , ν_{12} , G_{12} and ν_{23} or G_{23} .

If an infinite number of planes of material property symmetry exists, then the foregoing relations simplify to the *isotropic* material relations, as occurs with most of the common metallic alloys used in engineering applications, with E and ν or G as the only two independent constants:

$$E_i = E; \quad \nu_{ij} = \nu; \quad G_{ij} = G; \quad G = \frac{E}{2(1 + \nu)}; \quad i, j = 1, 2, 3 \quad (3.11)$$

3.3.2 Mechanics of materials approximation to stiffness

As a first approach to determine the elasticity constants of the layer, the assumption that the strains in the fibre direction of a unidirectional fibre reinforced composite material are the same in the fibres as in the matrix is made, otherwise a fracture between the fibres and the matrix would be implied (Jones, R. M. (1999)). Because the strains in both the matrix and fibre are the same, it may be assumed that the sections normal to the 1 axis, which were plane before being stressed, remain plane after stressing. Thus, it is possible to state that the strain ε_1 applies for both the fibres and the matrix. Then, if both constituent materials behave elastically, the stresses σ in the fibre direction are:

$$\sigma_f = E_f \varepsilon_1 \quad \sigma_m = E_m \varepsilon_1 \quad (3.12)$$

where the subscripts f and m stand for fibre and matrix respectively. The average stress σ_1 acts on the cross-sectional area A of the representative volume element, σ_f acts on the cross-sectional area of the fibres A_f and σ_m acts on the cross-sectional area of the matrix A_m . Thus, the resultant force on a representative volume element of composite material is:

$$F = \sigma_1 A = \sigma_f A_f + \sigma_m A_m \quad (3.13)$$

Combining equations (3.12) and (3.13), and recognition from macromechanics that:

$$\sigma_1 = E_1 \varepsilon_1 \quad (3.14)$$

and defining the volume fractions of fibres and matrix as:

$$V_f = \frac{A_f}{A} \quad V_m = \frac{A_m}{A} \quad (3.15)$$

it is possible to write:

$$E_1 = E_f V_f + E_m V_m \quad (3.16)$$

which is known as the *rule of mixtures* for the apparent Young's modulus of the composite material in the direction of the fibres E_1 . Using analogous reasoning, it is possible to write the apparent Young's modulus of the composite material in the direction transverse to the fibres E_2 as:

$$\frac{1}{E_2} = \frac{V_f}{E_f} + \frac{V_m}{E_m} \quad (3.17)$$

The so-called *major* Poisson's ratio ν_{12} is obtained by an approach similar to the analysis for E_1 :

$$\nu_{12} = \nu_f V_f + \nu_m V_m \quad (3.18)$$

Finally, the in-plane shear modulus of a lamina, G_{12} , is determined in the mechanics of materials approach by assuming that the shearing stresses in the fibre and in the matrix are the same (which is not true, since the shear deformations cannot be the same). Jones, R. M. (1999) shows that:

$$\frac{1}{G_{12}} = \frac{V_f}{G_f} + \frac{V_m}{G_m} \quad (3.19)$$

which is the same type of expression as was obtained for the transverse Young's modulus E_2 .

3.3.3 On estimating the properties of the laminate from the properties of the laminae

A laminate is made of two or more layers of laminae bonded together to act as an integral structural element. The various plies are oriented with (local) principal material directions at different angles to the global laminate axes to produce a structural element capable of resisting loads in several directions. The stiffness and strength of such a composite material structural configuration are obtained from the properties of the constituent laminae. The reason why laminae are combined to create a laminate is to achieve the largest possible bending stiffness for the materials used.

Using CLT it is possible to consistently proceed directly from the basic element, the lamina, to the end result, the structural laminate. First, it must be noticed that the laminates are generally used in the form of relatively thin plates. Thus, the approximation that the layers are in a state of plane stress is legitimate, i.e., the stresses are negligible with respect to the smaller dimension as they are not able to develop within the material and are small compared to the in-plane stresses ($\sigma_{zz} = 0$). Therefore, the face of the element is not acted by loads and the structural element can be analyzed as two-dimensional. In such a case, the stress-strain relations in principal material coordinates for a lamina k of an orthotropic material are:

$$\begin{Bmatrix} \sigma_1 \\ \sigma_2 \\ \tau_{12} \end{Bmatrix}^{(k)} = \begin{bmatrix} Q_{11} & Q_{12} & 0 \\ Q_{21} & Q_{22} & 0 \\ 0 & 0 & Q_{66} \end{bmatrix}^{(k)} \begin{Bmatrix} \varepsilon_1 \\ \varepsilon_2 \\ \gamma_{12} \end{Bmatrix}^{(k)} \quad (3.20)$$

where $[Q_{ij}]$ is the so-called *reduced stiffness matrix* for a state of plane stress⁶ in which:

⁶ This matrix can be obtained from the stress-strain relations (3.7) by imposing $\sigma_3 = 0$ to obtain an expression for ε_3 and get the relation: $[Q_{ij}] = [C_{ij}] - \frac{C_{i3}C_{j3}}{C_{33}}$, $i, j = 1, 2, 6$.

$$\begin{aligned} Q_{11} &= \frac{E_1}{1 - \nu_{12}^2 E_2/E_1}; & Q_{12} &= \frac{\nu_{12} E_2}{1 - \nu_{12}^2 E_2/E_1} \\ Q_{22} &= \frac{E_2}{1 - \nu_{12}^2 E_2/E_1} & Q_{66} &= G_{12} \end{aligned} \quad (3.21)$$

or, using the inverse relationship:

$$\begin{Bmatrix} \varepsilon_1 \\ \varepsilon_2 \\ \gamma_{12} \end{Bmatrix}^{(k)} = \begin{bmatrix} S_{11} & S_{12} & 0 \\ S_{21} & S_{22} & 0 \\ 0 & 0 & S_{66} \end{bmatrix}^{(k)} \begin{Bmatrix} \sigma_1 \\ \sigma_2 \\ \tau_{12} \end{Bmatrix}^{(k)} \quad (3.22)$$

where $[S_{ij}]$ is the compliance matrix in state of plane stress in which:

$$\begin{aligned} S_{11} &= \frac{1}{E_1}; & S_{12} &= -\frac{\nu_{12}}{E_1} \\ S_{22} &= \frac{1}{E_2} & S_{66} &= \frac{1}{G_{12}} \end{aligned} \quad (3.23)$$

Now, considering the global coordinate system (xyz) is obtained from the rotation of an angle θ around the axis 3 of the local coordinate system (123) as illustrated in figure 3.4, the following coordinate transformation matrixes may be written:

$$[T_{ij\sigma}]^{(k)} = \begin{bmatrix} \cos^2(\theta) & \sin^2(\theta) & 2\cos(\theta)\sin(\theta) \\ \sin^2(\theta) & \cos^2(\theta) & -2\cos(\theta)\sin(\theta) \\ -\cos(\theta)\sin(\theta) & \cos(\theta)\sin(\theta) & \cos^2(\theta) - \sin^2(\theta) \end{bmatrix}^{(k)} \quad (3.24)$$

$$[T_{ij\varepsilon}]^{(k)} = \begin{bmatrix} \cos^2(\theta) & \sin^2(\theta) & \cos(\theta)\sin(\theta) \\ \sin^2(\theta) & \cos^2(\theta) & -\cos(\theta)\sin(\theta) \\ -2\cos(\theta)\sin(\theta) & 2\cos(\theta)\sin(\theta) & \cos^2(\theta) - \sin^2(\theta) \end{bmatrix}^{(k)} \quad (3.25)$$

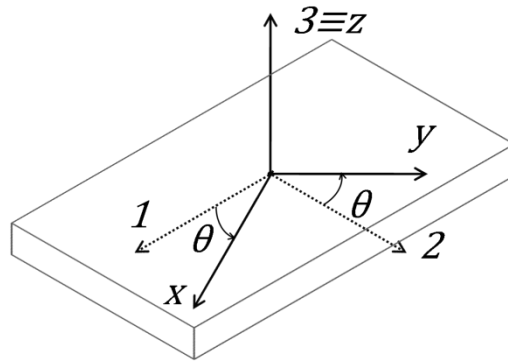


Figure 3.4: Rotation of the local coordinate system (123) around axis 3 towards the global coordinate system (xyz) .

Using these transformation matrixes it is possible to re-write both the stiffness and the compliance matrixes in the global coordinate system (xyz) for each layer k as:

$$[Q_{ij}']^{(k)} = [T_{ij\sigma}]^{(k)} \cdot [Q_{ij}]^{(k)} \cdot [T_{ij\sigma}]^{(k)T} \quad (3.26)$$

$$[S_{ij}']^{(k)} = [T_{ij\epsilon}]^{(k)} \cdot [S_{ij}]^{(k)} \cdot [T_{ij\epsilon}]^{(k)T} \quad (3.27)$$

and (Moura *et al.* (2005)):

$$[S_{ij}'] = \begin{bmatrix} \frac{1}{E_x} & -\frac{\nu_{xy}}{E_x} & -\frac{\eta_{xy}}{E_x} \\ -\frac{\nu_{xy}}{E_x} & \frac{1}{E_y} & -\frac{\mu_{xy}}{E_y} \\ -\frac{\eta_{xy}}{E_x} & -\frac{\mu_{xy}}{E_y} & \frac{1}{G_{xy}} \end{bmatrix} \quad (3.28)$$

in which the η_{xy} and μ_{xy} are traction-shear coupling terms which, according to Jones, R. M. (1999), were called *coefficients of mutual influence* by Lekhnitskii (1963).

From the CLT (Kirchhoff hypothesis), which establishes relations between the strains and curvatures and the forces and moments acting on a plate, it is possible to obtain (after a rather complex procedure) the matrix of extensional stiffness (Jones, R. M. (1999)):

$$A_{ij} = \sum_{k=1}^n Q_{ij}'^{(k)} \cdot t_k \quad (3.29)$$

in which n is the total number of layers in the laminate and t_k is each layer's thickness. Finally, it is possible to determine the elasticity constants of the laminate in the global Cartesian coordinate system (xyz) using the relationship:

$$h \cdot [A_{ij}]^{-1} = [S_{ij}'] \quad (3.30)$$

in which h is the thickness of the laminate.

3.4 Fundamentals of vibration and modal analysis

3.4.1 Generalities

A mention to forward and inverse problems was previously done in section 2.2.1 when talking about natural frequencies and FRFs damage detection based methods. Utterly, forward and inverse problems are forms of the logic methods of reasoning of deduction and induction respectively. Deductive reasoning works its way from the more general (theory) to the more particular, being also commonly known as a *top-down* approach. On the contrary, induction reasoning is the inverse of deduction, working from particular observations towards a generalization or theory, being informally referred to as a *bottom-up* approach.

Inverse problems in engineering can be compared in some way as inductive reasoning: an experimental description of the behaviour of the structure (data) is analyzed in order to extract more specific details (model parameters) governing the whole model.

According to Maia and Silva (1997), in dynamics, the properties of a N DOF system can be described by means of either one of three models - spatial, modal or response model – that can be related between each other by either forward or inverse approaches.

In the first case, the dynamic characteristics are contained in a spatial distribution of the mass, stiffness and damping properties described in terms of matrixes of mass $[M]$, stiffness $[K]$ and damping $[D]$ (in the case of the hysteretically damped model) or $[C]$ (in the case of the viscously damped model). Considering each DOF is described by a coordinate $x_i(t)$ with an associated applied force $f_i(t)$ in which $i = 1, 2, \dots, N$ DOFs, then this model can be described using Newton's 2nd law of motion by:

$$[M]\{\ddot{x}(t)\} + ([K] + i[D])\{x(t)\} = \{f(t)\} \quad (3.31)$$

in the case of the hysteretically damped model, or by:

$$[M]\{\ddot{x}(t)\} + [C]\{\dot{x}(t)\} + [K]\{x(t)\} = \{f(t)\} \quad (3.32)$$

in the case of the viscously damped model. The viscously damped model described by (3.32), in the general case where damping is non-proportional⁷, is not so easy to deal with (Maia and Silva (1997)). Furthermore, the constant hysteretic damping model is often used to describe the dynamic behaviour of structures undergoing various loading conditions, such as the dissipation mechanism of CFRPs (Montalvão *et al.* (2006b)). Hence, from this point forward and without loss of generality, the formulations will be based on hysteretic proportional damping. So, assuming that a solution exists that is of the form:

$$\{x(t)\} = \{\bar{X}\}e^{i\lambda t} \quad (3.33)$$

where $\{\bar{X}\}$ is a $N \times 1$ vector of time-independent complex response amplitudes⁸, and substituting into the homogeneous form of (3.31), the spatial model described by these matrixes can be written as a generalized eigenvalue problem:

$$[K] - \lambda^2[M] + i[D]\{\bar{X}\} = \{0\} \quad (3.34)$$

which, when solved, leads to the modal model described by matrixes $[\lambda_r^2]$ and $[\Phi]$. The first matrix contains N complex eigenvalues with information on the natural frequencies of the system and the second is a mass normalized matrix containing N eigenvectors with information on the mode shapes. The quantity λ_r^2 is often referred to as a *complex eigenvalue* and can be written as:

$$\lambda_r^2 = \omega_r^2(1 + i\eta_r) \quad (3.35)$$

where ω_r and η_r are the natural frequency and damping loss factor, respectively, for mode r .

It is possible to show that the spatial model can be related with the modal model by the so called *orthogonality conditions*:

⁷ Proportional damping – whether it is viscous or hysteretic – may be defined as a dissipative situation where the damping matrix is directly proportional to the stiffness matrix, to the mass matrix or to a linear combination of both: $a[K] + b[M]$ where a and b are constants. This type of damping is often referred to as Rayleigh damping.

⁸ The response amplitude is a complex quantity also called *phasor* because it includes the phase angle θ between the response and the force: $\bar{X} = Xe^{i\theta}$.

$$[\Phi]^T [M] [\Phi] = [I] \quad (3.36)$$

$$[\Phi]^T [[K] + i[D]] [\Phi] = \begin{bmatrix} \lambda_r^2 \end{bmatrix} \quad (3.37)$$

where $[I]$ is the identity matrix. Another important conclusion is that this also means the modal matrix is a non-singular invertible matrix. So, it is possible, in principle, to obtain a spatial description of the model from the knowledge of the modal model and *vice versa*.

Nevertheless, experimentally and generally speaking, a response model described by FRF data is obtained instead. When in steady-state and considering the frequency domain, the FRF $H(\omega)$ can simply be computed for each frequency ω :

$$H(\omega) = \frac{X(\omega)}{F(\omega)} \quad (3.38)$$

where $X(\omega)$ is the complex response and $F(\omega)$ the complex force. The FRF is also known as *receptance*, *mobility* or *accelerance*, depending on the response $X(\omega)$ being defined, respectively, as displacement, velocity or acceleration. These kinematic quantities can obviously be easily related between each other by simple mathematical operations of differentiation and integration. Therefore, the knowledge of the FRF in terms of a receptance, a mobility or an accelerance is irrelevant. So, if receptance is picked, it is possible to prove that the response model can be related to the modal model by (Maia and Silva (1997)):

$$[\alpha(\omega)] = [\Phi] \begin{bmatrix} \lambda_r^2 - \omega^2 \end{bmatrix}^{-1} [\Phi]^T \quad (3.39)$$

Starting with a spatial model it is possible to end up with a response model after going through an intermediate modal model. This sequence is commonly performed when the starting point is a theoretical analysis and is inside the line of thought of the forward approach. On the other hand, because systems are usually too complex and it is not feasible to model them analytically, the inverse approach is followed when the starting point is the response model with the measurement of the system's FRFs. There are many techniques that allow derivation of the modal characteristics of a given system from the experimentally obtained response model. The procedure is called Modal Identification.

In figure 3.5 a scheme of the whole discussion above is presented showing the existing relationships between the three covered models: spatial, modal and response.

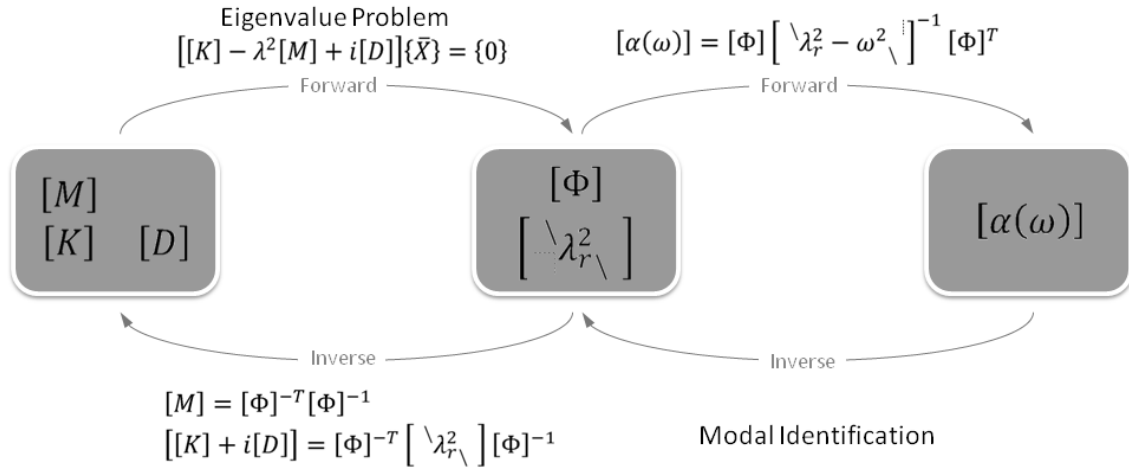


Figure 3.5: Dynamic models interrelation (hysteretic damping case).

Each term of the receptance matrix shown in equation (3.39) can be written as:

$$\alpha_{jk}(\omega) = \frac{\bar{X}_j}{F_k} = \sum_{r=1}^N \frac{{}_r\bar{A}_{jk}}{\omega_r^2 - \omega^2 + i\eta_r\omega_r^2} \quad (3.40)$$

where \bar{X}_j is the complex response amplitude in coordinate j , F_k is the amplitude of the force in coordinate k and ${}_r\bar{A}_{jk}$ is a complex quantity known as *modal constant* that can be written as:

$${}_r\bar{A}_{jk} = {}_r\bar{A}_{jk} e^{i {}_r\varphi_{jk}} = \phi_{jr} \phi_{kr} \quad (3.41)$$

in which ϕ_{jr} and ϕ_{kr} are, respectively, elements j and k of the mass normalized modal vector $\{\phi_r\}$ and ${}_r\bar{A}_{jk}$ and ${}_r\varphi_{jk}$ are, respectively, the modal constant amplitude and phase.

In practical terms, it is impossible to acquire every terms of the receptance matrix shown in equation (3.40) for continuous systems since they have infinite DOFs. Out-of-range modes will always exist as a consequence of the limitations of the measurement equipment in terms of frequency range.

When a FRF is regenerated starting from the modal parameters obtained after a process of modal identification, the receptance given by equation (3.40) shall be re-written as:

$$\alpha_{jk}(\omega) = \sum_{r=m_1}^{m_2} \frac{r\bar{A}_{jk}}{\omega_r^2 - \omega^2 + i\eta_r\omega_r^2} \quad (3.42)$$

where the number of modes was limited between m_1 and m_2 to illustrate that, in general, the EMA procedure does not always start below the first mode ($r = 1$) and it seldom continue to the highest mode ($r = N$). However, the fact that the frequency range is limited does not mean that the measured FRF data is unaffected by out-of-range modes which lie in the vicinity of the analysis. In fact, if the measured FRF data are compared with the corresponding identified FRFs if represented only by (3.42) differences will rise especially away from resonances and a total mismatch between anti-resonant frequencies is most likely to happen. One way of minimizing the consequences of using such a model is to introduce corrections on the identified FRFs, so that they approximate the measured data in the frequency range of interest by including extra terms in the response equation:

$$\begin{aligned} \alpha_{jk}(\omega) = & \sum_{r=1}^{m_1-1} \frac{r\bar{A}_{jk}}{\omega_r^2 - \omega^2 + i\eta_r\omega_r^2} + \sum_{r=m_1}^{m_2} \frac{r\bar{A}_{jk}}{\omega_r^2 - \omega^2 + i\eta_r\omega_r^2} + \\ & + \sum_{r=m_2+1}^N \frac{r\bar{A}_{jk}}{\omega_r^2 - \omega^2 + i\eta_r\omega_r^2} \end{aligned} \quad (3.43)$$

In this equation, the first term represents the low-frequency unmeasured modes, the second term represents the measured frequency range modes and the third term represents the high-frequency unmeasured modes. This is illustrated with the help of figure 3.6, where it can be observed that within the frequency range of interest the contribution of the low-frequency modes tends to approximate to a mass-like behaviour, while the contribution of the high-frequency modes tends to approximate to a stiffness effect (already shown before, for instance, by Ewins (1984)). Thus, the rather long expression (3.43) can be re-written in a more convenient (yet approximated) form as:

$$\alpha_{jk}(\omega) = \bar{R}_{jk}(\omega) + \sum_{r=m_1}^{m_2} \frac{r\bar{A}_{jk}}{\omega_r^2 - \omega^2 + i\eta_r\omega_r^2} \quad (3.44)$$

where the quantity $\bar{R}_{jk}(\omega)$ is a frequency dependent complex residual accounting for the effects of the out-of-range modes. It must be noted that the residual is only valid for that FRF in particular and for that specific frequency range. In such a case, the complex residual $\bar{R}_{jk}(\omega)$ can assume the approximate form of:

$$\bar{R}_{jk}(\omega) \cong -\frac{1}{\omega^2 \bar{M}_{jk}^R} + \frac{1}{\bar{K}_{jk}^R} \quad (3.45)$$

where the complex quantities \bar{M}_{jk}^R and \bar{K}_{jk}^R are, respectively, the mass and stiffness residuals.

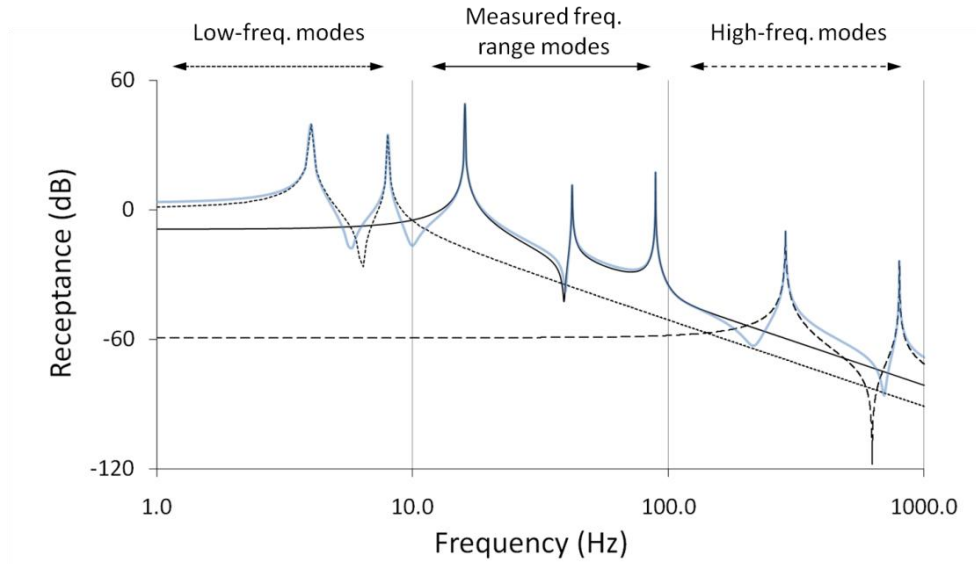


Figure 3.6: Numerical simulation to show how low-frequency and high-frequency modes affect the receptance in the measured frequency range.

3.4.2 The Characteristic Response Function (CRF)

The receptance as earlier described by equation (3.44) shows that every mode is dominant in the vicinity of its own natural frequency⁹. A mode is said dominant in a certain frequency range when the summed up contribution of all the other modes is small and its variation is negligible for the FRF at that range. Thus, it is reasonable to assume that the summed up contribution of all the other modes in the vicinity of mode r can be approximated by a constant. Therefore, and if the indexes are dropped for a matter of simplicity, the receptance as given by equation (3.44) can be written in the vicinity of mode r as:

⁹ This is often true for well isolated modes and considering that the modal constants are within the same order of magnitude.

$$\alpha(\omega) \cong \frac{\bar{A}}{\omega_r^2 - \omega^2 + i\eta_r \omega_r^2} + constant \quad (3.46)$$

This is the starting point for Maia *et al.* (1994) and Ribeiro (1999) to present the Characteristic Response Function (CRF). First, three short distanced frequencies ω_1 , ω_2 and ω_3 are picked showing that the quotient $\frac{\alpha_2 - \alpha_1}{\alpha_3 - \alpha_2}$ is independent of the local properties (residual terms contributions and modal constants) in the vicinity of mode r . From this point forward and after some mathematical manipulation in which an intermediate function γ_1 is defined based on the previous result, he presents what he calls the Characteristic Response Function (CRF):

$$\beta(\omega) = \frac{1}{\omega_r^2 - \omega^2 + i\eta_r \omega_r^2} \quad (3.47)$$

which is observed to be similar to a modal term of the receptance, but with unit modal constant, or, in other words, the CRF presents the form of the receptance for a Single DOF (SDOF) system. It is worth to mention that this means the CRF only accounts for the global properties of the system (characteristics of the structure) and is independent of its local properties (measurement coordinates). Therefore, because the numerator is unitary, it is easy to apply the inverse method:

$$\frac{1}{\beta(\omega)} = \omega_r^2 - \omega^2 + i\eta_r \omega_r^2 \quad (3.48)$$

It is easy to observe that the real part is a straight line with respect to ω^2 with negative unitary slope and that the imaginary part is a constant:

$$\begin{cases} \text{real}\left(\frac{1}{\beta(\omega)}\right) = \omega_r^2 - \omega^2 \\ \text{imag}\left(\frac{1}{\beta(\omega)}\right) = \eta_r \omega_r^2 \end{cases} \quad (3.49)$$

then, in the vicinity of each mode, this graphical representation must allow determining the resonant frequency and the hysteretic damping for that particular mode. Another advantage of this method is that both this straight lines highlights the existence of modes, since, far from the vicinity of the resonant frequencies, the CRF is meaningless (the initial assumptions do not apply anymore) and therefore these straight lines will not exist.

It is possible to obtain the CRF from experimental results by taking groups of three succeeding points from the receptance curves, using the following expression:

$$\beta(\omega_1) = \frac{1 - \frac{\alpha_2 - \alpha_1}{\alpha_3 - \alpha_2} \cdot \frac{\omega_3^2 - \omega_2^2}{\omega_2^2 - \omega_1^2}}{\omega_3^2 - \omega_1^2} \quad (3.50)$$

The determination of the modal constants requires a more complex mathematical approach, but it also uses equation (3.46) as a starting point:

$$\bar{A} = \frac{[\alpha_1 - \alpha_2](\omega_r^2 - \omega_1^2 + i\eta_r\omega_r^2)(\omega_r^2 - \omega_1^2 + i\eta_r\omega_r^2)}{\omega_1^2 - \omega_2^2} \quad (3.51)$$

As the global properties are already determined, for each pair of points (ω_1, α_1) and (ω_2, α_2) , a complex value for the modal constant of mode r is determined. In the vicinity of the mode all the pairs of points should give the same value, so averaging is performed.

Equation (3.51) does not guarantee the modal consistency is respected. Being aware of that fact, Silva, J. M. M. *et al.* (1996) and Ribeiro (1999) also provide an algorithm to correct this issue. However, this is only an issue if the modal identification is performed over results which make use of different excitation coordinate points. In the presented case this is not a problem, as the mass of the force transducer is quite reasonable when compared to the mass of the whole structure. This way, the force transducer is considered as part of the system and no coupling techniques (for mass cancelation) have to be followed, avoiding any chance of relating results obtained for different excitation points.

Finally, to determine the residuals, two points from the receptance curve must be chosen. It is suggested that these points are situated near anti-resonant frequencies and close to the frequency range limits, since these are locations that are less likely to be dominated by short distanced modes. Then, the following system of equations is solved, where the complex quantities \bar{M}_{jk}^R and \bar{K}_{jk}^R , the mass and stiffness residuals respectively, are determined:

$$\begin{cases} \alpha_{jk}(\omega_1) = -\frac{1}{\omega_1^2 \bar{M}_{jk}^R} + \sum_{r=m_1}^{m_2} \frac{r \bar{A}_{jk}}{\omega_r^2 - \omega_1^2 + i\eta_r\omega_r^2} + \frac{1}{\bar{K}_{jk}^R} \\ \alpha_{jk}(\omega_2) = -\frac{1}{\omega_2^2 \bar{M}_{jk}^R} + \sum_{r=m_1}^{m_2} \frac{r \bar{A}_{jk}}{\omega_r^2 - \omega_2^2 + i\eta_r\omega_r^2} + \frac{1}{\bar{K}_{jk}^R} \end{cases} \quad (3.52)$$

3.5 Damage in composite materials

3.5.1 Impact effects on composite materials

According to Cox and Flanagan (1997) the great weakness of laminates is their vulnerability to delamination. They have poor impact damage resistance and low post-impact mechanical properties (Tong *et al.* (2002)). Delamination, that is, the debonding between adjacent laminae, is of great concern since they significantly reduce the strength of the laminate. Delamination failure can be caused in undamaged laminates by excessive through-thickness loads. Once a laminate is damaged by impact and contains a small delamination crack, the critical through-thickness stress for failure drops dramatically, since the composite relies on the matrix toughness alone to resist delamination crack growth¹⁰.

For impacts that do not result in complete penetration of the target, experiments indicate that damage consists of delaminations, matrix cracking, and fibre failures. These impacts are often referred in the literature as *low-velocity impacts*. According to Abrate (1998), it has been consistently shown with experimental testing that delaminations occur only at interfaces between plies with different fibre orientations. If two adjacent plies have the same fibre orientation, no delamination will be introduced at the interface between them. For a laminate impacted on its top surface, at interfaces between plies with different fibre orientation, the delaminated area has an oblong or *peanut shape* (often quite irregular) with its major axis oriented in the direction of the fibres in the lower ply at that interface (figure 3.7).

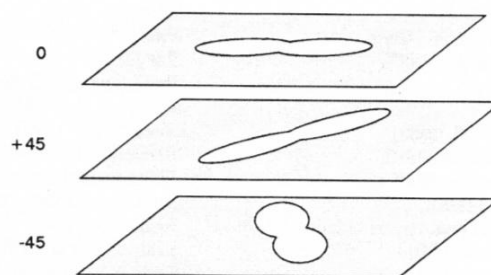


Figure 3.7: Orientation of delaminations (Abbate (1998)).

¹⁰ Through-thickness reinforcement in a quasi-laminar textile composite changes the picture entirely. Even if delamination flaws exist in advance, through-thickness reinforcement will arrest their growth as long as the critical stress for failure remains above some critical value. These structures are often called *3D woven textile composites* and are considered the second generation of composite materials (Miravete (1999)), the laminates being the first. They will not receive further treatment inside this work, as they are still not as common as tape laminates. Interested readers on this subject might want to read, for instance, Miravete (1999) or Tong *et al.* (2002).

After impact, there are many matrix cracks arranged in a complicated pattern that would be very difficult to predict, but it is not necessary to do so since matrix cracks do not significantly contribute to the reduction of the residual properties of the laminate. However, the damage process is initiated by matrix cracks which then induce delaminations at ply interfaces (figure 3.8).

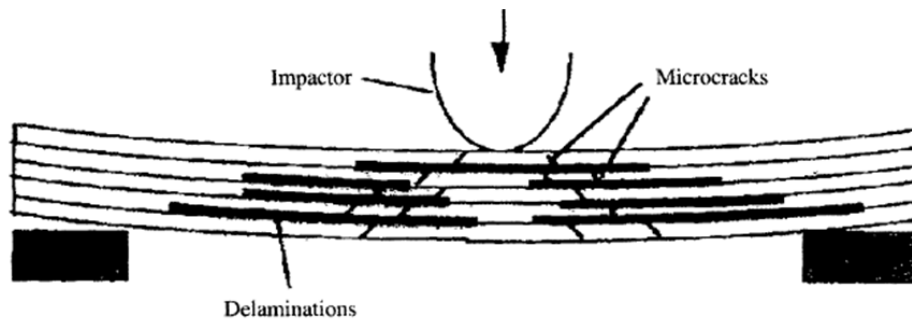


Figure 3.8: Delamination process in composite materials (Cantwell (2008)).

With thick laminates, matrix cracks are first induced in the first layer impacted by the projectile because of the high, localized contact stresses. Damage progresses from top to bottom, resulting in a pine tree pattern. For thin laminates, bending stresses in the back side of the laminate introduce matrix cracks in the lowest layer, which again starts a pattern of matrix cracks and delaminations but leads to a reversed pine tree pattern starting from bottom to top (figure 3.9).

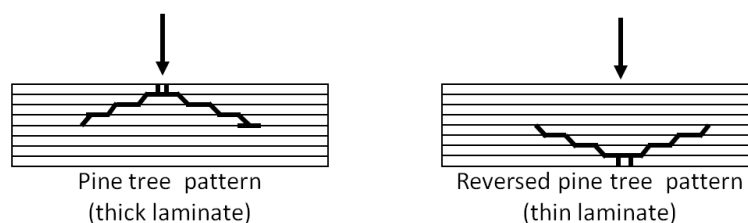


Figure 3.9: Pine tree and reverse pine tree damage patterns (Abrate (1998)).

The creation of matrix cracks does not require significant energy or cause a noticeable drop in stiffness. Also, according to several authors, delaminations generally do not affect much the natural frequencies, unless they are very large.

In general, delaminations are introduced at several interfaces and their size increase linearly with the kinetic energy of the impactor, but only after a certain threshold level is reached for its appearance. This threshold value is hard to determine experimentally because of experimental scatter from one specimen to another, and several tests are needed in order to determine the threshold level of the initial kinetic energy required to initiate delamination.

Abrate (1998) mentions several studies that indicate that damage is introduced when the contact force reaches a critical value which is the same for static tests and low-velocity impact tests. The force threshold value usually corresponds to the first discontinuity in the contact force history. The force threshold is very consistent from sample to sample and can be determined from a single test. This also suggests that similarities may be found between damage induced by impact loading and that produced by static loading. For example, Rilo *et al.* (2006) compare the damage obtained by low-velocity impacts in glass/epoxy and carbon/epoxy laminated plates with those obtained through quasi-static tests, in order to verify if low-velocity impacts can be modelled in laminated composite with quasi-static tests. The impact tests and the quasi-static tests used the same impactor and the same boundary conditions for fixing the specimens. The term of comparison between both tests was a plot of the force vs. displacement (figure 3.10). Both tests were setup so that they would produce the same maximum load (and not necessarily the same energy).

It was observed that the damage is more important in the opposite face to the force application, as the plate thickness rises. This happens in bending due to the longer distance from the specimen's face to the neutral fibre, leading to an increase of the traction stresses on this face. On the other hand, the maximum load did not always produce an identical deflection in the quasi-static test and in the one corresponding to impact, as can be seen in figure 3.11 (the most flexible the specimen, the most similar the deflection).

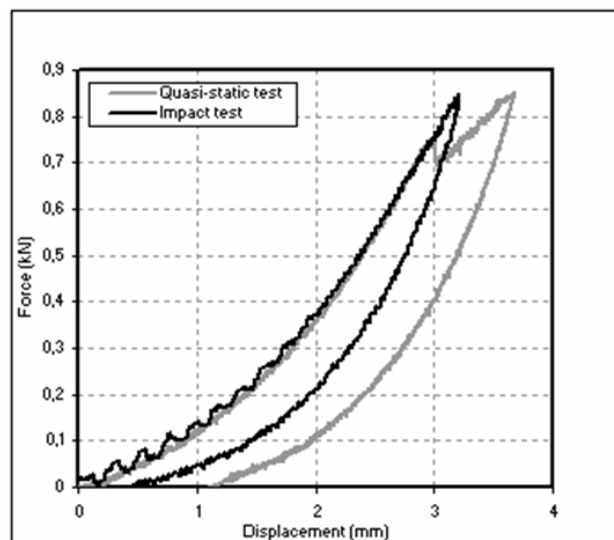


Figure 3.10: Force vs. displacement curves for comparing an impact test with a quasi-static test during damage introduction in a composite material (Rilo *et al.* (2006)).



Figure 3.11: Damage extension seen in the direction of the fibres oriented to 0° at the centre plate cross section (Rilo et al. (2006)).

Carvalho (2003) argues that for low to medium energy impacts the damage morphology might also include fibre breakage in the opposite side of the impact (which is subjected to traction loads). Figure 3.12 illustrates this situation, suggesting that the fibre breakage will most probably be invisible (as it is in the opposite side to the impact, generally hidden) and that a localized indentation will be, most likely, imperceptible.

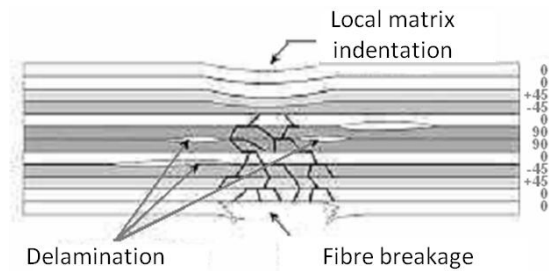


Figure 3.12: Failure modes of a laminate for a medium energy impact (Carvalho (2003)).

3.5.2 Damage effects on the response behaviour of composite materials

Impact damage is introduced only after the impact force reaches a certain threshold level. After the appearance of the first matrix crack, the crack will propagate and reach the interfaces between the current ply and adjacent plies. High transverse shear stresses will grow and delaminations appear. On the opposite side of the impact, due to the development of high tensile forces, fibre breakage may also occur (Abrate (1998), Carvalho (2003)).

When a delamination or debonding failure mode is concerned, friction between the interacting surfaces may occur, even for small bending deformations. Thus, since friction is an energy dissipation mechanism, it is reasonable to assume that damping may be used as a parameter for SHM, when this type of damage is concerned. In such a case, the material is locally heterogeneous and damping may be expected to increase (Zou et al. (2000)), dependent on

the deformation shape. The method presented herein is based on the assumption that different mode shapes have different sensitivities at the locations where delamination damage is present. This principle is somehow similar to the one used in many other methods such as the MSC or the MSS (Salawu and Williams (1994), Ho and Ewins (2000)).

Until now, it has been considered that a delamination type of damage would lead to an increase in the damping as a consequence of the energy loss due to friction. Nevertheless, if fibre breakage is introduced in the opposite face of the impact and if no significant delamination occurred, is it possible that the damping will decrease instead? A hint may come from Hadi and Ashton (1996) who experimentally determined the material damping of several GFRP specimens showing that the damping factor is larger at low fibre volume fractions and that it increases with increasing fibre orientation up to 30° . The damping factor decreases as the fibre orientation increases above 30° . According to these authors, this happens because the total strain energy is dominated by the in-plane shear strain energy, and this has its maximum value at this fibre orientation. Berthelot *et al.* (2008) argue that damping in FRPs depends on the constitution of the materials. At the constituent level, the energy dissipation in FRPs is induced by different processes such as the viscoelastic behaviour of matrix, the damping at the fibre-matrix interface or the damping due to damage. At the laminate level, damping is depending on the constituent layer properties as well as layer orientations and stacking sequence. Thus, altogether, if a fibre breakage occurs in a specimen with no delamination, than it is reasonable to assume that, for some mode shapes, damping could in fact decrease.

In fact, for thin laminates and in real situations, fibre breakage is likely to occur because of the bending stresses in the back side of the laminate. If one imagines that each fibre acts as a spring-damper and that the breakage corresponds to the interruption of the spring-damper connection, it is reasonable to assume that a local decrease in both stiffness and damping may happen. Furthermore, the debonding between two adjacent laminae will reduce the bending stiffness.

3.6 Proposal of a new damage index

3.6.1 Formulation of modal-based damage Indexes

All real structures dissipate energy when they vibrate. Energy is dissipated by frictional effects, for example that occurring at the connection between elements, internal friction in deformed members, and windage. The term damping is broadly used to denote the dissipation of energy

in (and the consequent decay of) oscillations of all types. The most common types of damping models are viscous, dry friction and hysteretic.

A delamination is a type of failure in composite laminates characterized by a debonding between one or more layers. Thus, it is reasonable to assume frictional forces will develop between these layers when bending motion is imposed as a consequence of shear stresses.

Consider that a delamination leads to increased values in the modal damping factors, η_r . The relative difference between the undamaged and damaged states of the modal damping values for mode r may be expressed by:

$$\Delta\eta_r^D = \frac{|\eta_r^D - \eta_r|}{\eta_r} \times 100\% \quad (3.53)$$

where the superscript D stands for damage. The damping factors can be obtained by using, for example, EMA techniques, which fundamentals were exposed in section 3.4 and that will be covered later.

The relative difference of the hysteretic damping factor when comparing the healthy and the damaged states is obtained independently of the coordinates under consideration, as it is based on global properties of the structure. However, in the case that a discrepancy exists due to localized damage, this means that some kind of function must be used to relate this global variation to the local coordinates of the structure.

By resorting to FE analysis, it is possible to obtain, with a reasonable degree of accuracy, a spatial description of the mode shapes and other physical quantities along the structure (such as strains, stresses, etc.). A generalized Plane Shape Function (PSF) is defined for mode r at a discretization node with coordinates (i, j) as any function of the mode shape:

$${}_rPSF_{ij} = {}_rPSF_{ij}(\psi_r(i, j)) \quad (3.54)$$

where $\psi_r(i, j)$ is the mode shape for the element with geometrical coordinates (i, j) , which may or may not be mass normalized. A proposal for a particular case of the PSF is done on the following sections.

Finally, it is assumed that the mode shapes and the natural frequencies will not suffer a considerable change when comparing the undamaged and damaged states of the structure¹¹.

¹¹ It is shown in section 5.3.2.1 that the damage only introduces slight variations in the mode shapes.

Consequently, the PSF will also remain essentially unchanged. Then, an index, called Damping Damage Indicator (DaDI), is proposed as:

$$DaDI_{ij} = \frac{\sum_{r=1}^N (\eta_r PSF_{ij} \cdot \Delta\eta_r^D)}{\sum_{r=1}^N \eta_r PSF_{ij}} \quad (3.55)$$

It can be seen that applying equation (3.55) requires only the damping factor values for both the damaged and undamaged structure in addition to the PSF that can be obtained at any stage with a FE model alone. As the modal damping factors are global properties of the structure, only one measurement coordinate is strictly required (i.e., response transducer), independently of the structure dimension and geometry.

It must not be forgotten that, when conceiving the DaDI, it was assumed no appreciable changes in frequency would be observed. However, especially if fibre breakage occurs, frequency is expected to be, as well as damping, possible complementary modal features to assess damage location. In such cases the DaDI alone may perform as a poor indicator and something else must be introduced. So, consider that a fibre breakage leads to decreases in the natural frequencies ω_r . The relative difference between the undamaged and damaged state of the natural frequency of mode r is expressed by:

$$\Delta\omega_r^D = \frac{|\omega_r^D - \omega_r|}{\omega_r} \times 100\% \quad (3.56)$$

As for the hysteretic damping, the relative difference of the natural frequencies between the healthy and damaged states is obtained independently of the coordinates, since it is based on a global property of the structure. Thus, some sort of function with arbitrary mode dependent physical quantities may also be used. Then, an index, called Frequency Damage Indicator (FreDI), is proposed as:

$$FreDI_{ij} = \frac{\sum_{r=1}^N (\omega_r PSF_{ij} \cdot \Delta\omega_r^D)}{\sum_{r=1}^N \omega_r PSF_{ij}} \quad (3.57)$$

Now it is time to combine the predictions from both the indexes DaDI and FreDI for the damage location. However, a question arises: which one is prominent over the other? The inclusion of weighting functions affecting both the indexes seems inevitable, leading to the final form of the index:

$$MuDI_{ij} = W_f \cdot \frac{FreDI_{ij}}{\max[|FreDI_{ij}|]} + W_d \cdot \frac{DaDI_{ij}}{\max[|DaDI_{ij}|]} \quad (3.58)$$

in which W_f is a weighting function affecting the frequency term and W_d is a weighting function affecting the damping term that will be treated next. This form of the index accounts for both the frequency and damping variations, as well as for the PSF mode shape based functions. Therefore, the index given by (3.58) will be hereafter called Multi-parameter Damage Indicator (MuDI).

The weighting functions' values are based on the dispersion of the variation of the modal frequencies and modal damping factors. The standard deviations $\sigma_{\Delta\eta}$ and $\sigma_{\Delta\omega}$ for the set of values $\Delta\eta_r^D$ and $\Delta\omega_r^D$ respectively are determined. Then, the frequency weighting function is defined as:

$$W_f = \frac{\sigma_{\Delta\omega}}{\sigma_{\Delta\eta} + \sigma_{\Delta\omega}} \quad (3.59)$$

It is easier to treat the weighting functions as if they are on the opposite sides of a scale. So, by imposing the following relationship to be respected:

$$W_f + W_d = 1 \quad (3.60)$$

the damping weighting function W_d can also be calculated.

In practice it is observed that $\sigma_{\Delta\eta} \gg \sigma_{\Delta\omega}$ for most situations, because $\Delta\eta_r^D \gg \Delta\omega_r^D$ and also possibly due to the magnitude of the uncertainties involved during the modal identification process¹². Consequently, the direct application of equation (3.59) is useless because it would lead to $W_f \cong 0$ and $W_d \cong 1$, or $MuDI_{ij} \cong DaDI_{ij}$. Equation (3.59) is therefore proposed to be re-written as:

¹² This can be observed, for instance, in figure E.9 (Annex E), while explaining the functioning of BETAlab. In the example shown, the relative standard deviation for the set of values used to determine the natural frequency is 0.060%, whereas it is 43.7% (700x greater!) when modal damping is at stake for the same mode.

$$W_f = \frac{\kappa \cdot \sigma_{\Delta\omega}}{\sigma_{\Delta\eta} + \kappa \cdot \sigma_{\Delta\omega}} \quad (3.61)$$

in which κ is a scale factor. While the identification of the natural frequencies is quite accurate, the same cannot be said for the damping factors. Both are determined by some sort of averaging over sets of data obtained during experimental testing. So, after the modal identification process is over, the obtained values for each of the natural frequencies ω_r and modal damping factors η_r are in fact averaged values with correspondent relative standard deviations $\% \sigma_{\omega_r}$ and $\% \sigma_{\eta_r}$ for each mode. The damping factor is, in most of the structural applications in engineering, very small and hard to determine. When in the presence of a set of data, its value float around an intermediate value, in view of which averaging is an easy tool available to estimate an approximate value of the damping factor. However, the fluctuations are still much more evident than those found when estimating the natural frequencies. As a consequence, it is observed that $\% \sigma_{\eta_r} \gg \% \sigma_{\omega_r}$ for any mode r . The relation between the standard deviations of the numerator of expressions (3.53) and (3.56) was used as a metric for the scale factor κ :

$$\kappa = \frac{\sum_{r=1}^N \sqrt{\% \sigma_{\eta_r}^2 + \% \sigma_{\eta_r}^D{}^2}}{\sum_{r=1}^N \sqrt{\% \sigma_{\omega_r}^2 + \% \sigma_{\omega_r}^D{}^2}} \quad (3.62)$$

Despite the fact that the way this scale factor is determined has no mathematical or physical support, until another one is proposed, one shall rely upon this as it will prove reasonably effective.

3.6.2 On choosing the plane shape functions

It is often difficult to model damping exactly because many mechanisms may be operating in a structure. However, for the internal dissipation mechanism, there is general agreement that the so-called *hysteretic model* is quite suitable. The mathematical model used to describe such hysteretic damping includes the loss factor in the stiffness as an imaginary component. So, the elastic deformation will include the effect of the damping and its changes, and so will do the strain energy.

In section 3.3.1 it was said that elastic materials, for which an elastic potential or strain energy density function exists, have an incremental work per unit volume given by:

$$\delta W = \sigma_i \delta \varepsilon_i \quad (3.63)$$

Boresi *et al.* (1992) say that “for adiabatic conditions and static equilibrium, the first law of thermodynamics states that during the displacement variations (...), the variation in work of the external forces δW is equal to the variation of internal energy δU for each volume element”. Thus, in volume V one has:

$$\delta W = \delta U \quad (3.64)$$

The internal energy U in a solid of volume V can be expressed in terms of the internal energy per unit volume, i.e., in terms of the strain energy density U_0 (Boresi *et al.* (1992):

$$U = \int_V U_0 dV \quad (3.65)$$

Using a slightly different notation than the one used previously and considering:

$$U_0 = \frac{1}{2} (\sigma_{xx} \varepsilon_{xx} + \sigma_{yy} \varepsilon_{yy} + \sigma_{zz} \varepsilon_{zz} + \sigma_{xy} \varepsilon_{xy} + \sigma_{xz} \varepsilon_{xz} + \sigma_{yz} \varepsilon_{yz}) \quad (3.66)$$

the strain energy in a solid can be defined as (Abrate (1998), Jones, R. M. (1999)):

$$U = \frac{1}{2} \int_V (\sigma_{xx} \varepsilon_{xx} + \sigma_{yy} \varepsilon_{yy} + \sigma_{zz} \varepsilon_{zz} + \sigma_{xy} \varepsilon_{xy} + \sigma_{xz} \varepsilon_{xz} + \sigma_{yz} \varepsilon_{yz}) dV \quad (3.67)$$

Now consider a thin plate, for which the assumption of a state of plane stress is valid, i.e., where the stresses are negligible with respect to the smaller dimension as they are not able to develop within the material and are small compared to the in-plane stresses. Therefore, the structural element can be analyzed as two-dimensional and the stress and strain tensors can be approximated by:

$$\sigma_{ij} = \begin{bmatrix} \sigma_{xx} & \sigma_{xy} & 0 \\ \sigma_{yx} & \sigma_{yy} & 0 \\ 0 & 0 & 0 \end{bmatrix} \quad \varepsilon_{ij} = \begin{bmatrix} \varepsilon_{xx} & \varepsilon_{xy} & 0 \\ \varepsilon_{yx} & \varepsilon_{yy} & 0 \\ 0 & 0 & \varepsilon_{zz} \end{bmatrix} \quad (3.68)$$

where the non-zero ε_{zz} term arises from the Poisson's effect, as will be shown later. In this case, equation (3.66) reduces to:

$$U_0 = \frac{1}{2} (\sigma_{xx} \varepsilon_{xx} + \sigma_{yy} \varepsilon_{yy} + \sigma_{xy} \varepsilon_{xy}) \quad (3.69)$$

Since the hysteretic damping assumes the loss by friction of a fraction of the strain energy, this might be a promising candidate for building a PSF to be used in the DaDI. However, before presenting the PSF, two simplifications are done:

- The distortion in the xy plane influence on the damping factor variation due to delamination damage was considered of no relevance. In fact, it tended to diminish the accuracy of the method. Therefore, only the part respecting extensional stresses and strains is considered;
- MuDI, as presented in equation (3.58), normalizes the DaDI index (and the FreDI as well) before weighing it. So, the constant coefficient in equations (3.66) and (3.69) can be dropped.

Definition of a PSF when damping changes are concerned in plane-like structures is proposed as:

$$\eta_r PSF_{ij} = r\sigma_{xxij} \cdot r\varepsilon_{xxij} + r\sigma_{yyij} \cdot r\varepsilon_{yyij} \quad (3.70)$$

where the subscript r stands for the mode number. This way, the DaDI presented earlier in equation (3.55) will be a function of both the extensional modal stress and strain shapes and modal damping factors variation. It must be clear that there are other possible combinations to be included in the PSF, but that kind of analysis is intentionally left outside this text.

With respect to the FreDI, it is worth remembering that the resonant frequencies are mainly considered as stiffness dependent. For a given load the strain is a measure of the flexibility of the structure, so it can be used as a PSF for the FreDI. Hence, when computing the FreDI the following form of the PSF is proposed:

$$\omega_r PSF_{ij} = \left| r\varepsilon_{xxij} + r\varepsilon_{yyij} \right| \quad (3.71)$$

where the modulus is used to guarantee that each mode's contribution is in the same direction, i.e., that the modal sensitiveness to damage is not cancelled by summing up a positive value of the PSF with a negative one when computing the FreDI. A simplified form of equation (3.71) for isotropic materials can be presented. For a state of plane stress and

considering the compliance matrix given earlier by (3.8), it can be shown that the strains-stress relationships for ε_{xx} , ε_{yy} and ε_{zz} are given by:

$$\begin{cases} \varepsilon_{xx} = \frac{\sigma_{xx}}{E} - \frac{\nu}{E} \sigma_{yy} \\ \varepsilon_{yy} = \frac{\sigma_{yy}}{E} - \frac{\nu}{E} \sigma_{xx} \\ \varepsilon_{zz} = -\frac{\nu}{E} (\sigma_{xx} + \sigma_{yy}) \end{cases} \quad (3.72)$$

Adding the two first equations, it is possible to obtain a relationship among the strains, such as:

$$\begin{aligned} \varepsilon_{xx} + \varepsilon_{yy} &= \frac{\sigma_{xx}}{E} - \frac{\nu}{E} \sigma_{yy} + \frac{\sigma_{yy}}{E} - \frac{\nu}{E} \sigma_{xx} = \\ &= \frac{1}{E} (\sigma_{xx} + \sigma_{yy}) - \frac{\nu}{E} (\sigma_{xx} + \sigma_{yy}) = -\frac{\varepsilon_{zz}}{\nu} + \varepsilon_{zz} \Leftrightarrow \\ &\Leftrightarrow \varepsilon_{xx} + \varepsilon_{yy} = \varepsilon_{zz} \left(1 - \frac{1}{\nu} \right) \end{aligned} \quad (3.73)$$

Thus, apart from a constant coefficient, the form of the PSF to be used in the FreDI and previously given by (3.71), can be re-written in a simplified equivalent form, dropping again the constant, as:

$$\omega_r PSF_{ij} = \left| r \varepsilon_{zz ij} \right| \quad (3.74)$$

Chapter 4

Modelling and testing

4.1 Specimens' build-up and material description

4.1.1 Material and layups

For the numerical and experimental validation of the proposed index, three types of CFRP specimens were tested: quasi-isotropic beam, quasi-isotropic plate and orthotropic plate. All the specimens were cut from rectangular plates obtained from the layup of prepreg layers which were cured in autoclaves.

The quasi-isotropic specimens are made from a $[0/45/135/90]_s$ layup. The designation *quasi-isotropic* is in accordance to ASN A 4135:1997 standard and to Reis (1996). Each layer is a woven prepreg constituted by Hexcel® G803 3K 5H satin carbon fibre impregnated in HexPly® 200 phenolique matrix (200/40%/G803). Both beam and plate specimens were made by the author as described in section 4.1.2 below. The prepreg was already available in the Escola

Superior de Tecnologia de Setúbal (ESTS) laboratorial facilities and originally belonged to the Portuguese Aeronautic Industry (OGMA).

The orthotropic specimens are made from either $[0/90]_{25}$ or $[90/0]_{25}$ layups. Each layer is an epoxy resin impregnated carbon fibre satin weave Cytec® Cycom® 934-37-3KT300 8H (such as that used in some parts of the Lockheed Martin C-130 airplane shown in figure 4.1). These specimens were produced at OGMA.

Table 4.1 presents a summary of all the specimens considered in this study, as well as their nomenclature within the text. Among other reasons, the dimensions of specimens A1 to A6 and B1 to B4 are chosen so that a rectangle whose side lengths ratio is not an integer is formed. This way, there are less chances for the occurrence of double-modes in vibration testing that could bring up some difficulties during the modal identification.



Figure 4.1: Lockheed Martin C-130 airplane.

Table 4.1: Specimens' types and designations adopted throughout the dissertation.

Qty.	Designation	Material	Layup	Behaviour	Dimensions	Side ratio
3	Beam ¹³ L1-L3	G803/200	$[0/45/135/90]_5$	Quasi-Isotropic	392x25x2mm	15.68
6	Plate A1 - A6	G803/200	$[0/45/135/90]_5$	Quasi-Isotropic	392x242x2mm	1.620
2	Plate B1 - B2	T300/934	$[90/0]_{25}$	Orthotropic	360x262x3mm	1.374
2	Plate B3 - B4	T300/934	$[0/90]_{25}$	Orthotropic	360x262x3mm	1.374

¹³ Contrary to the plates, which are all singular individual items, beams L1-L3 are in fact one unique cantilever beam of varying length.

4.1.2 Manufacturing

Plates A1 to A6 and the beam (table 4.1) were manufactured by the author in an autoclave at Instituto Superior de Engenharia de Lisboa (ISEL) with Hexply® G803/200 prepreg (figure 4.2). These specimens were cut from raw plates with overall dimensions 450x300mm. Several reasons, as illustrated in figures 4.4 and 4.3, were taken into account to reach these dimensions: the autoclave's measured usable area; the width of the prepreg roll and its optimal usability; the intended dimensions of the specimens A1 to A6 (as big as possible in order to obtain low frequency modes) and the aim of also obtaining tensile test specimens in both the plate's longitudinal and transverse directions.



Figure 4.2: ISEL's autoclave with the bagging schedule inside (left) and raw plates obtained after the polymerization process (right).

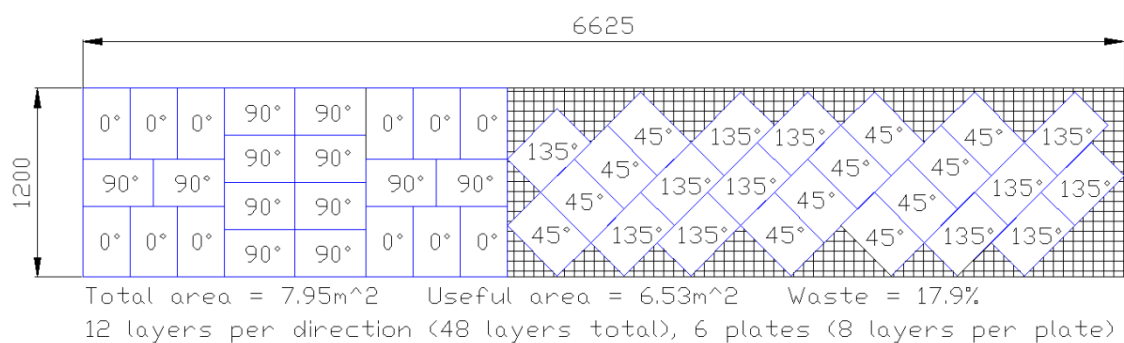


Figure 4.3: 1.2m width prepreg roll utilization for the production of 6 plates with 8 layers each.

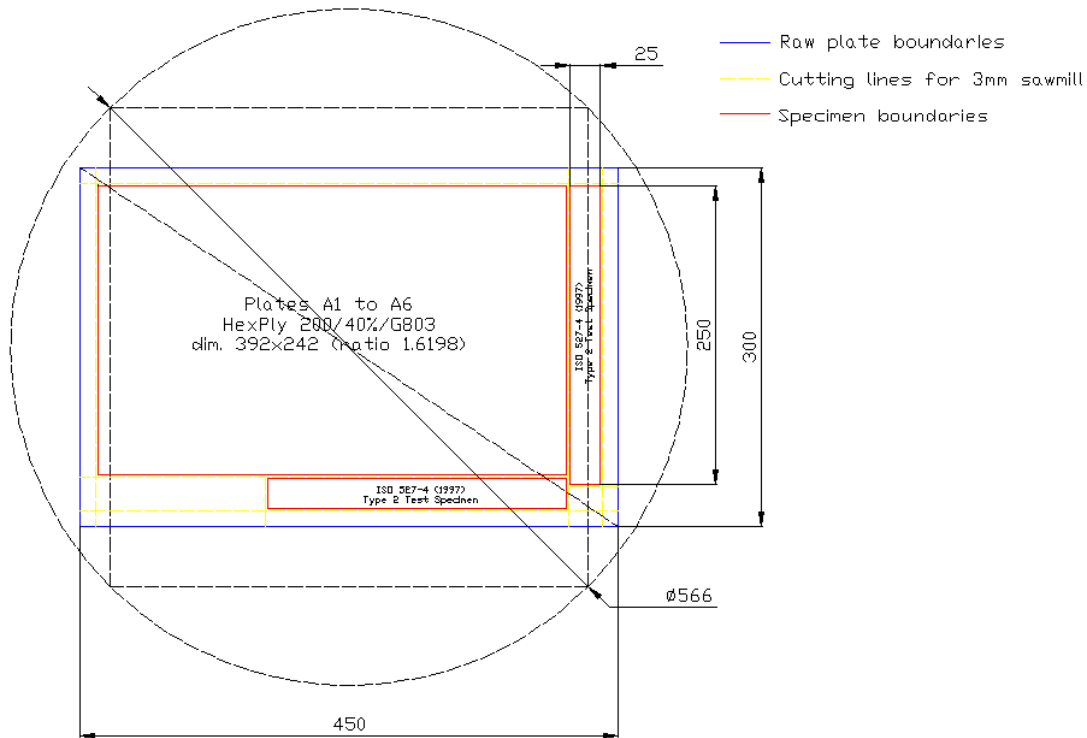


Figure 4.4: Implantation of the raw plate into the autoclave and specimens' cutting scheme.

The polymerization cycle was carried out according to a job plan from OGMA. The pressure and temperature charts are shown in figure 4.5. According to this chart, it can be seen that the whole curing process takes around 4 hours inside the autoclave in normal conditions.

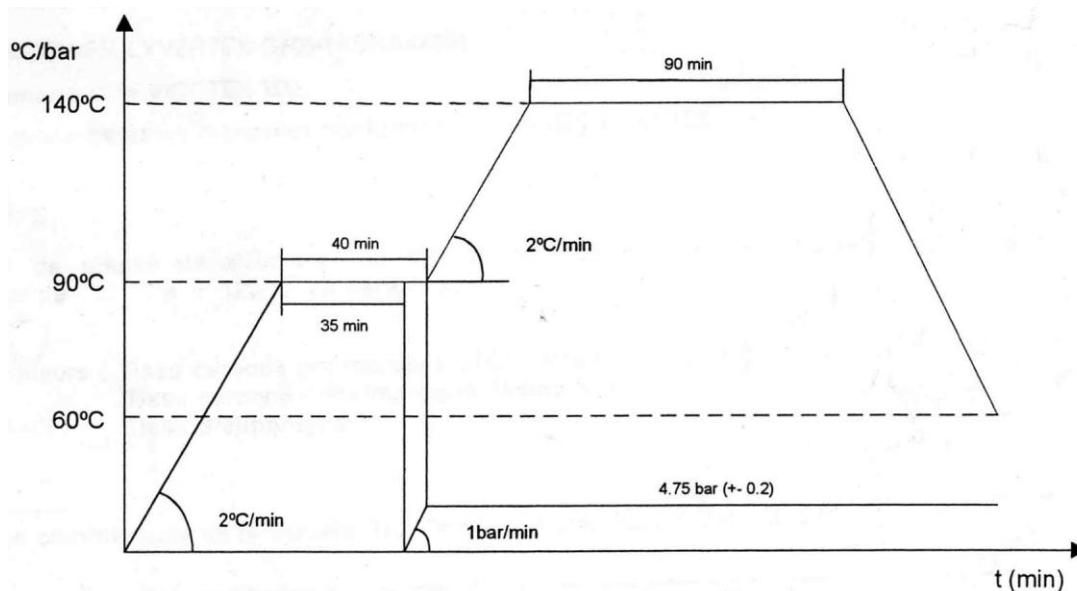


Figure 4.5: Polymerization cycle for production of specimens A1 to A6 and L1 to L3 (from OGMA's job plan no. 03/LAT/PRENSA - assembly no. F925.10902.200.00 A).

Before entering the prepreg into the autoclave, it is first necessary to prepare the layup over a rectangular mould with at least the same surface dimensions of the laminate (450x300x10mm)

(figure 4.6). To help during the layup process, a ruler was used to stretch one layer over the other by pushing it transversely to the fibre's direction, but one must be careful not to distort the layer being set up. Glass tempered moulds are used to keep flatness during the polymerization process because glass has a small thermal expansion coefficient when compared to common metallic alloys.

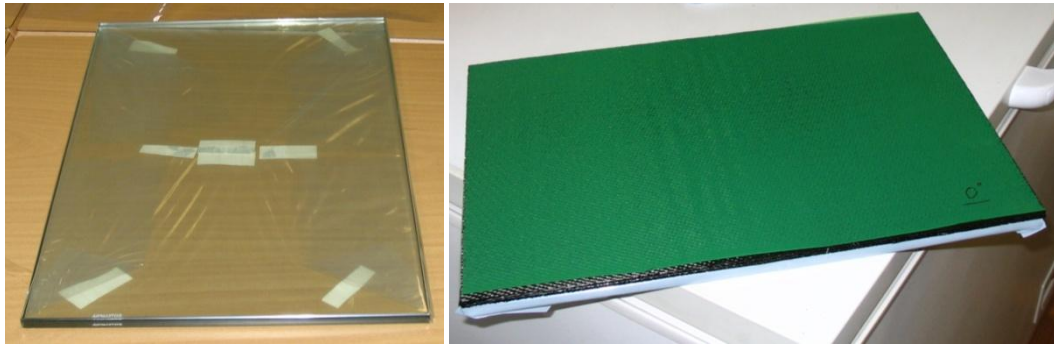


Figure 4.6: Glass tempered mould (left) and composite laminate mounted on the mould (right).

After this operation is concluded, it is necessary to proceed to vacuum bagging. There are three main purposes for vacuum bagging: application of compaction pressure to consolidate plies; extraction of moisture, solvents, and volatiles from curing composite; and to allow resin to flow and be absorbed without hydraulic lock. The sequence of materials used in the so called *bagging schedule* is shown in figure 4.7 and is mostly based in Travassos (1994). It can be seen that 2 laminates were produced simultaneously in each curing cycle. The glass moulding tool is wrapped up in a protective plastic film (the same material as the seal bag) and release film.



Figure 4.7: Bagging schedule for production of laminates A1 to A6 and L1-L3.

There are a lot of issues concerning the whole manufacturing process which lie outside the scope of this work. In the present study, most of the problems encountered were related to air leakage due to very small faults in the vacuum seal bag or poor tape sealing close to the vacuum pump hose. In fact, a total of 11 plates were produced by the mentioned process, 5 of which had well visible faults. Nevertheless, these 5 plates were later useful for tipping tensile test specimens and for the production of beams L1-L3 from a plate with only a localized defective region.

4.1.3 Overall dimensions and density

Table 4.2: Summary of the specimens' averaged values for the overall dimensions and density.

Designation	Length (mm)	Width (mm)	Thickness (mm)	Density (kg/m ³)
Beam ¹⁴ L1 - L3	-	25.19	2.13	1508
Plate A1 – A6	391.0	241.3	2.019	1508
Plate B1 – B2	359.4	261.7	2.875	1506
Plate B3 – B4	359.6	261.9	2.911	1491

4.2 Determination of mechanical properties

4.2.1 Young's modulus, shear modulus and Poisson's ratio

A *tensile test*, also known as *tension test* or *force-displacement test*, is a fundamental type of mechanical test that can be performed on a material. Tensile tests are simple, relatively inexpensive, and fully standardized, and allow for the determination of the Young's modulus, Poisson's ratio and, for isotropic materials, the shear modulus.

250x50mm specimens are used in accordance to ISO 527-4:1997 standard. They have two 50mm long grips attached to each of their tips (increasing the thickness in 3x). Two specimens

¹⁴ Specimens L1, L2 and L3 are cantilevered beams with 342, 292 and 242 mm lengths respectively. The density was determined from plates A1 to A6 since the material is the same.

(figure 4.8), perpendicular to each other, are cut from the raw plates in order to measure properties in both in-plane directions (the cutting scheme was previously shown in figure 4.4).

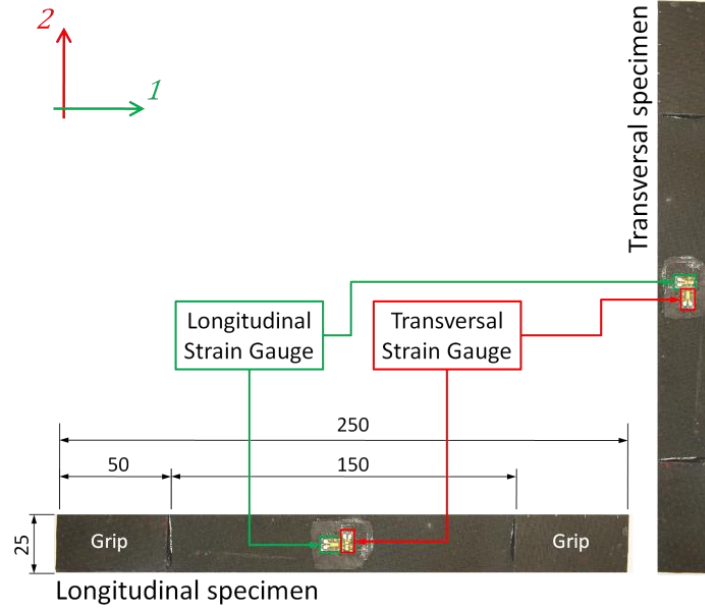


Figure 4.8: Example of the specimens used for the mechanical properties assessment in tensile testing.

These specimens are equipped with two strain gauges in both the longitudinal and transversal directions, which measure the respective strains, ε_1 and ε_2 . Experimental force-displacement tests were performed in a universal servo-hydraulic testing machine, INSTRON® 1342 under load control. The force was measured with a 250kN load cell. Keeping in mind Hooke's law, the Young's modulus E_1 of the material may be determined in the longitudinal direction of the specimen:

$$E_1 = \frac{\sigma_1}{\varepsilon_1} \quad (4.1)$$

where σ_1 and ε_1 are the stress and strain¹⁵, respectively, in the longitudinal direction. The Poisson's ratio is then determined by:

¹⁵ In fact, these values are approximated values (called *engineering* or *nominal* values of stress and strain).

$$\nu_{12} = -\frac{\varepsilon_2}{\varepsilon_1}; \quad \sigma_1 \neq 0; \quad \sigma_i = 0; \quad i = 2, \dots, 6 \quad (4.2)$$

For determining E_2 and ν_{21} it is necessary to perform another test, this time with the transversal specimen (the one in the vertical direction in figure 4.8)

Finally, from the symmetry of the compliance matrix (shown in section 3.3.1), one may try to assess the quality of the results using the relationship:

$$\frac{\nu_{12}}{E_1} = \frac{\nu_{21}}{E_2} \quad (4.3)$$

If the material has a quasi-isotropic behaviour, the transverse specimen is likely to provide similar results so that $E_1 = E_2 = E$ and $\nu_{12} = \nu_{21} = \nu$. In this case, it is also possible to determine the shear modulus from the tensile test:

$$G = \frac{E}{2(1 + \nu)} \quad (4.4)$$

As an example, figure 4.9 contains the plot of stress vs. strain for both specimens A2L and A2T in the elastic behaviour zone.

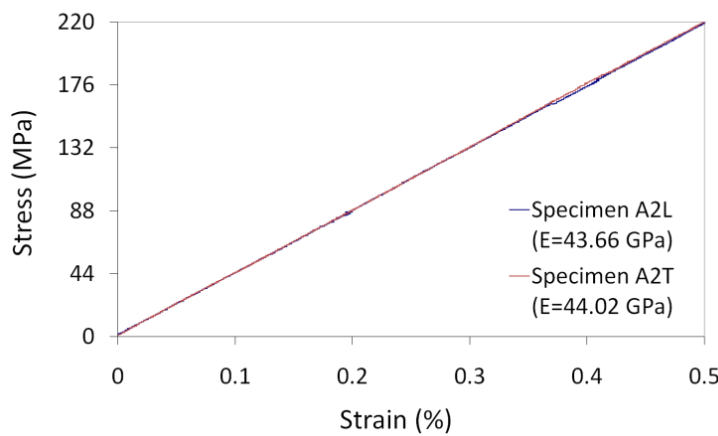


Figure 4.9: Stress-strain charts in the elastic behaviour zone for specimens A2L and A2T in both the longitudinal and transversal directions.

From all the structures built, only a few specimens were instrumented for the measurement of the Young's moduli and Poisson's ratios. The (averaged) results are shown on table 4.3.

Table 4.3: Summary of the specimens' measured mechanical properties.

Specimens	Behaviour	E_x (GPa)	E_y (GPa)	ν_{xy}	ν_{yx}
A2, A3	Quasi-Isotropic	44.64	44.64	not measured ¹⁶	not measured
B1, B2	Orthotropic	71.6	66.1	0.066	0.039

First, it is easy to observe that equation (4.3) is far from being satisfied with these Young's moduli and Poisson's ratios. Thus, during modelling, it was decided to use the average value of $\nu_{12} = 0.052$ instead, which is in agreement with Tan *et al.* (1999) and is close to the theoretical value presented later in table 4.6.

There is a difference between the Young's moduli in the x and y directions for the type 'B' specimens, even though it is not much ($\approx 8\%$). By the time these tests were executed, it was not known that plates B1 and B2 were slightly different from B3 and B4 with respect to their layups (see table 4.1 for further details). The differences are probably noticeable because the layers are textile satin-weaves: one side of the fabric is predominantly warp yarns; the other fill. It was only when the mode shapes were measured with a Scanning LDV (see section 4.4.3) that important differences were noticed in some of the mode shapes when comparing the experimental results and the FE model. By switching E_x with E_y in the material properties, the solution became much closer to the true behaviour of plates B3 and B4. This made it clear that the material used for specimen plates type 'B' would have to be treated as orthotropic instead of quasi-isotropic. In this case the use of equation (4.4) would be a gross approximation to determine the shear modulus, even though E_x is not much different from E_y .

For the experimental determination of the shear modulus, other type of test methods would have to be used, such as a torsion test or a three point bending test, but they were not performed. Thus, it became necessary to predict the shear modulus using theoretical approaches.

If the access to the impregnated laminae's properties is possible, then the laminate's properties, like the Young's moduli, Poisson's ratios and shear moduli, may be estimated, by using the procedure described earlier in section 3.3.3, from the CLT using equations (3.24), (3.26), (3.28), (3.29) and (3.30). This was the followed procedure for determining specimen

¹⁶ The Poisson's ratio was not measured with specimens A2 and A3, as only strain gauges in the longitudinal directions were used.

plates type 'B' theoretical properties, since the material properties of a single unidirectional tape layer of material T300/934 graphite/epoxy were available. The source was Zheng, D. (2007), whose values are very close to those presented for the same material by Morais *et al.* (2005) (table 4.5).

However, if there is no information concerning the impregnated yarn, the laminate's properties have to be predicted from the properties of the fibres and the matrix alone, as long as the volume fractions of either the fibres or the matrix are known. In this case and before using the CLT to determine the laminate's properties, it is necessary to determine the laminae's properties following the procedural steps in section 0 by using equations (3.16), (3.17), (3.18) and (3.19). Since no reliable source was found containing information about the Hexcel® G803/200 mechanical properties, the estimation was based in generic values presented by Silva, A. J. P. F. (2001), keeping in mind any result would be an approximated value (table 4.4).

Table 4.4: Mechanical properties for generic carbon HR fibres and phenolique resin (Silva, A. J. P. F. (2001).

Medium	Material	E (GPa)	G (GPa)	ν	V^{17}
Fibre	Carbon HR	230	50	0.3	57%
Resin	Phenolique	3	1.1	0.4	43%

Table 4.5: Specimens' type 'A' and 'B' material properties for a single (unidirectional-like) layer.

Specimens	Material	E_1 (GPa)	E_2 (GPa)	ν_{12}	G_{12} (GPa)	G_{23} (GPa)
Type 'A'	G803/200	132.4	6.858	0.343	2.486	-
Type 'B'	T300/934	137	10.6	0.4	5.4	3.5

¹⁷ The 57% fibres' volume fraction was obtained from HexPly® 200 135°C curing phenolique matrix product data sheet.

Table 4.6: Specimens' types 'A' and 'B' theoretical mechanical properties for the whole laminate.

Specimens	Material	E_x (GPa)	E_y (GPa)	ν_{xy}	ν_{yx}	G_{xy} (GPa)
Type 'A'	G803/200	48.38	48.38	0.33	0.33	18.16
Type 'B'	T300/934	74.48	74.48	0.057	0.057	5.4

Analysing the results presented in table 4.6, it should not be a surprise that both Young's moduli E_x and E_y are equal for the same laminate, once it is understood that the layups are symmetric with the same theoretical amount of fibres in any of the considered directions. Secondly, in agreement with the considerations presented in section 3.2 for textiles, the Young's moduli in table 4.6 are a bit larger than the experimental values presented in table 4.3. It is important to refer that, since only the properties of a unidirectional layer was available, the approximation that each satin weave layer is composed by two layers of orthogonal unidirectional layers with half the thickness each was thereby made. This means that instead of considering a stacking of 8 plies, 16 were considered instead, or $[0/90/45/135_2/45/90/0]_5$ for the quasi-isotropic specimens type 'A' and $[90/0/0/90]_{25}$ for the orthotropic specimens type 'B'. This approach is equivalent to the one followed by other authors, for instance Akkerman (2006) when evaluating the bending stiffness of woven fabric laminates or Thollon and Hochard (2009) when modelling damage in woven composites.

One important thing to be observed is that Poisson's ratio for specimens type 'B' is one order of magnitude smaller than for specimens type 'A'. While this is not a surprising result, it is useful to reinforce the idea that the Poisson's ratio depends greatly on the layup directions combinations, as has already been observed by many authors, such as Carvalho (2003). It is also interesting to observe that the quasi-isotropic layup presents a Poisson's ratio similar to the one that is observed in many metallic alloys (≈ 0.3).

Finally, when modelling, priority will be given to the results obtained experimentally, when available, over the theoretical ones.

4.2.2 Hysteretic damping

The constant hysteretic damping model is often used to describe the dynamic behaviour of structures undergoing various loading conditions. In order to introduce this model, textbooks usually start with the more conventional viscous damping model. When excited by a harmonic force at frequency ω , it can be easily proven (and all fundament texts on vibration theory show

it) that for each vibration cycle the system dissipates – through its viscous damper – a quantity of energy directly proportional to the excitation frequency. However, experimental evidence from tests performed on a large variety of materials show that damping due to internal friction (material hysteresis) is nearly independent of the forcing frequency (Lazan (1968)).

The specimen used for the hysteretic damping assessment was obtained from raw plate A4 (refer to table 4.1 for more details). This specimen has a rectangular cross section of 25x2mm and a length of 50mm between grips (figure 4.10). The length of the specimen is as short as possible, limited by the minimum space needed for the strain gauge and the testing machine clamps' geometry, to avoid buckling when compressive forces are applied during the force-displacement tests.

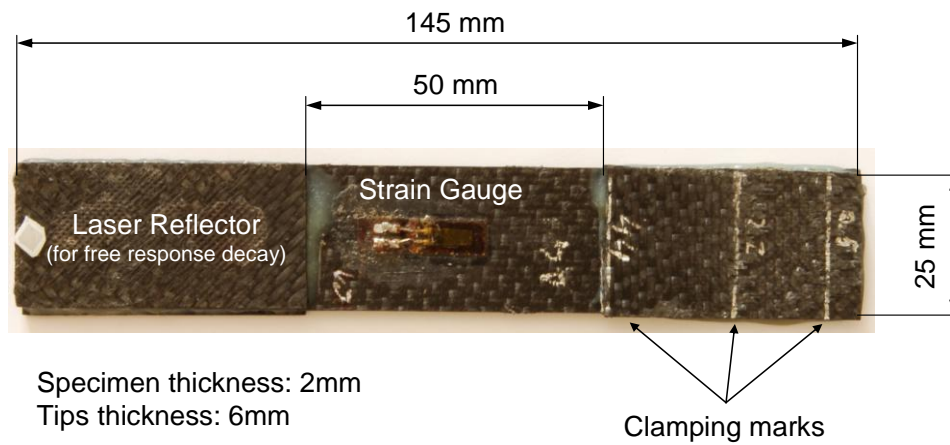


Figure 4.10: Carbon fibre laminate specimen for the hysteretic damping assessment (obtained from specimen plate type 'A').

4.2.2.1 Force-displacement testing

The experimental measurement of the hysteretic damping factor can be carried out by means of cyclic force-displacement tests in the elastic domain, for instance as presented by Ribeiro *et al.* (2005). It is easy to show that the energy dissipated per cycle of oscillation is given by the ellipse area of the force-displacement plot during a complete cycle:

$$W_{diss} = \pi k \eta X^2 \quad (4.5)$$

where k is the stiffness of the sample, η is the hysteretic damping factor and X is the amplitude of the response. This area, the integral of the force along the displacement, corresponds to the non-conservative work done per cycle. In other words, in a plot with force vs. displacement

signals at a given frequency, damping can be seen as a mechanism that introduces a lag between the signals and shows up as an elongated ellipsis. In fact, from Meirovitch (1986) it can easily be shown that the dissipated energy can also be written as:

$$W_{diss} = \pi F X \sin \theta \quad (4.6)$$

where F is the amplitude of the force and θ is the phase angle between the force and displacement response. Thus, from equations (4.5) and (4.6) it can be seen that the hysteretic damping factor can be evaluated from a force-displacement test by using one of the following relationships:

$$\eta = \frac{\text{ellipse area}}{\pi k X^2} \quad (4.7)$$

$$\eta = \frac{\sin \theta}{k \alpha} \quad (4.8)$$

where, as already presented by Jones, D. I. G. (2001), α is the ratio between X and F . Now, using the linear relationship between force and displacement:

$$F = kX \quad (4.9)$$

equations (4.7) and (4.8) can either be rewritten as:

$$\eta = \frac{\text{ellipse area} \cdot k}{\pi F^2} \quad (4.10)$$

or

$$\eta = \sin \theta \cong \theta \quad (4.11)$$

Equation (4.10) is a more than reasonable approximation for the most common materials used in engineering applications in which the damping factor is usually small ($\eta < 0.1$).

Furthermore, formulation of both equations (4.10) and (4.11) consider a sharp ellipse on its tip-ends, which is not true. In fact, the point of maximum/minimum displacement X does not correspond to the point of maximum/minimum force F in the hysteresis cycle, as shown in

figure 4.11. Since in most applications the damping ratio is very small, for practical purposes these approximations can generally be used without loss of accuracy.

For a matter of simplicity during this text, equation (4.10) will be referred to as the *areas method* and equation (4.11) as the *phase method*.

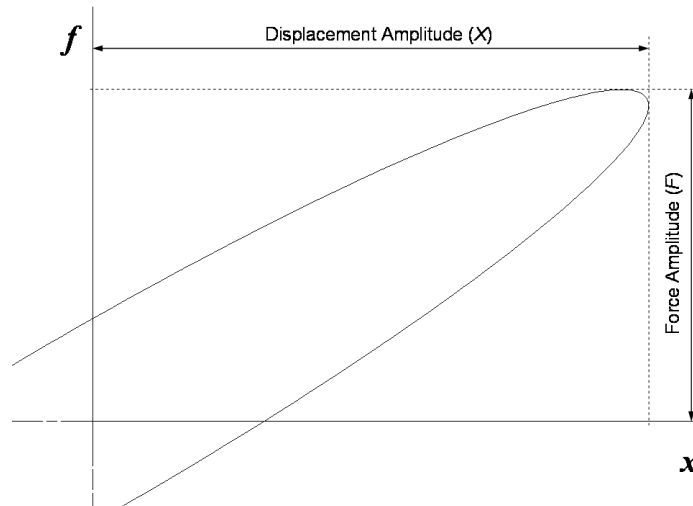


Figure 4.11: Hysteresis cycle (partial view).

Experimental force-displacement tests were performed in a universal servo-hydraulic testing machine, INSTRON® 1342 under load control. Figure 4.12 schematically represents the measurement chains of force and strain. In order to ensure that the load was properly applied to the specimen, the Proportional-Integral-Derivative (PID) values for feedback control of the testing machine were adjusted for each loading frequency. To measure the strain accurately, two strain-gages (HBM® LY11-350Ω) were bonded on both faces of the specimen, figure 4.10. The value of strain¹⁸ was the average of both signals to eliminate any effects due to possible bending.

Different force amplitudes and frequencies were used for the determination of the damping factor, 30 sinusoidal cycles being performed and recorded for each condition. The acquired data were force and strain at a sampling rate of 1000 points per cycle. The signals were not filtered, in order to avoid any phase disturbance between them (the time domain filters available would introduce phase shifts, which is not desirable when the phase between two

¹⁸ Because the hysteretic damping factor η is dimensionless and recalling that the *ellipse area* and stiffness k depend on the displacement X , the longitudinal strain can be used instead in the force-displacement tests when one wants to obtain the damping factor only. This can be shown by resorting to dimensional analysis over equations (4.7) or (4.10).

signals is wanted to be accurately assessed). For the experimental data so obtained, a force-strain plot was used to compute numerically the area of the ellipse for each cycle (figure 4.13, for a test performed at 0.1Hz, though the ellipse is too narrow to be visible) and the phase angle between the two signals was determined from a force and strain vs. time plot. Although the data naturally exhibited some level of noise, the integration process averaged it out and similar results were obtained for each cycle.

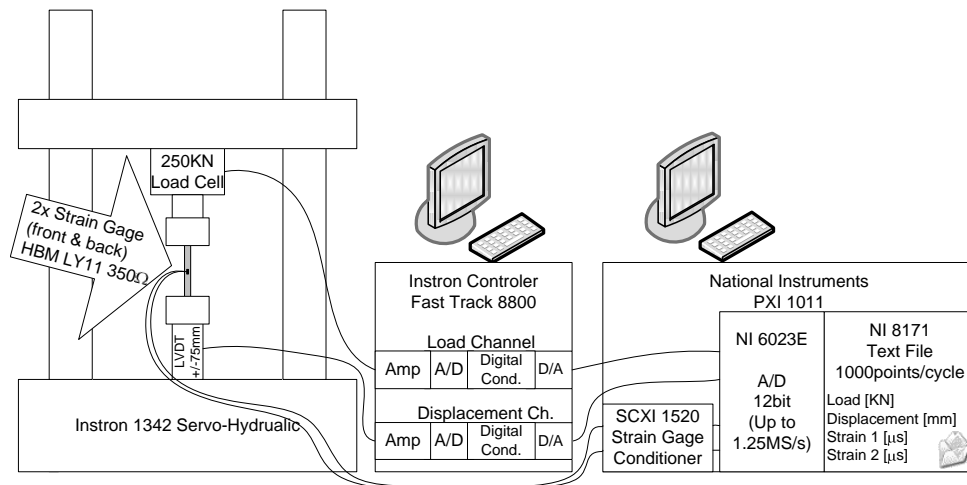


Figure 4.12: Force-displacement quasi-static test: testing hardware.

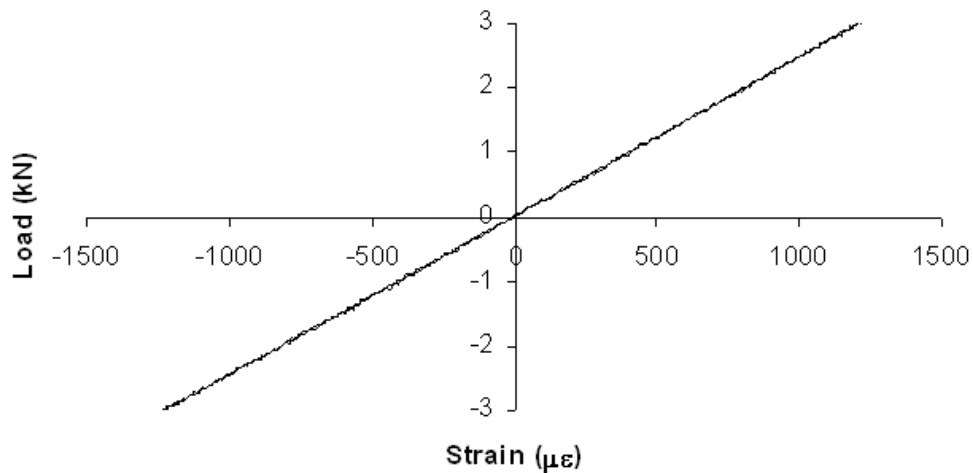


Figure 4.13: Force-strain plot for a load magnitude of $\pm 3\text{kN}$ and a frequency of 0.1Hz.

Tests were performed at different frequencies; however, for a 10Hz testing frequency the ellipse shown in figure 4.13 turned out to be much wider, as can be seen in the left side of figure 4.14. Although the immediate conclusion is that damping is having a considerable variation with frequency (contrary to the constant hysteretic model assumption), it was

observed that the damping had a negative value, meaning that the force was suffering from a delay relatively to the displacement. That can be seen on the right side of the same figure where both functions, force and strain, are plotted in the time domain. Since that would violate the causality principle, a deeper analysis was required. Measurement chain bias was considered a possible cause for this abnormality. By making some simple calculations, a force delay of approximately 0.1ms due to hardware constraints not possible to control was estimated.

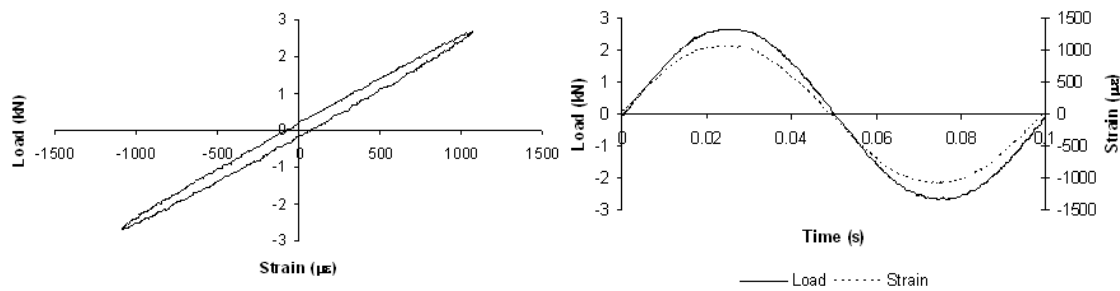


Figure 4.14: Force and strain for a load magnitude of $\pm 3\text{kN}$ and a frequency of 10 Hz. Left: force-strain plot; Right: superimposed force-time and strain-time plots.

In fact, different electronic equipments, with different processing times, are used to process the force and strain signals, introducing a phase shift; although small, it may be significant enough to pollute the results when it is added to the one (also small) originated by the damping in the cyclic force-displacement process. As the electronic induced phase shift is independent of the frequency load, it was decided to perform tests at 0.1, 1 and 10 Hz and to extrapolate (using a least-squares fit) the damping factor obtained to 0 Hz, eliminating the influence of the electronic equipment.

Tests were also carried out with different loading cases: traction-compression ($\pm 2\text{kN}$, $\pm 3\text{kN}$ and $\pm 4\text{kN}$), compression (-0.5kN to -3.5kN) and traction ($+0.5\text{kN}$ to $+6.5\text{kN}$).

Some extrapolations, for the estimation of the hysteretic damping by means of both the areas and phase methods (equations (4.10) and (4.11)) are shown in figure 4.15, where the intersection of the linear fit to the vertical axis corresponds to the hysteretic damping factor (represented by the independent term in the linear-fit equation). A summary of the results produced with both methods is shown in table 4.7.

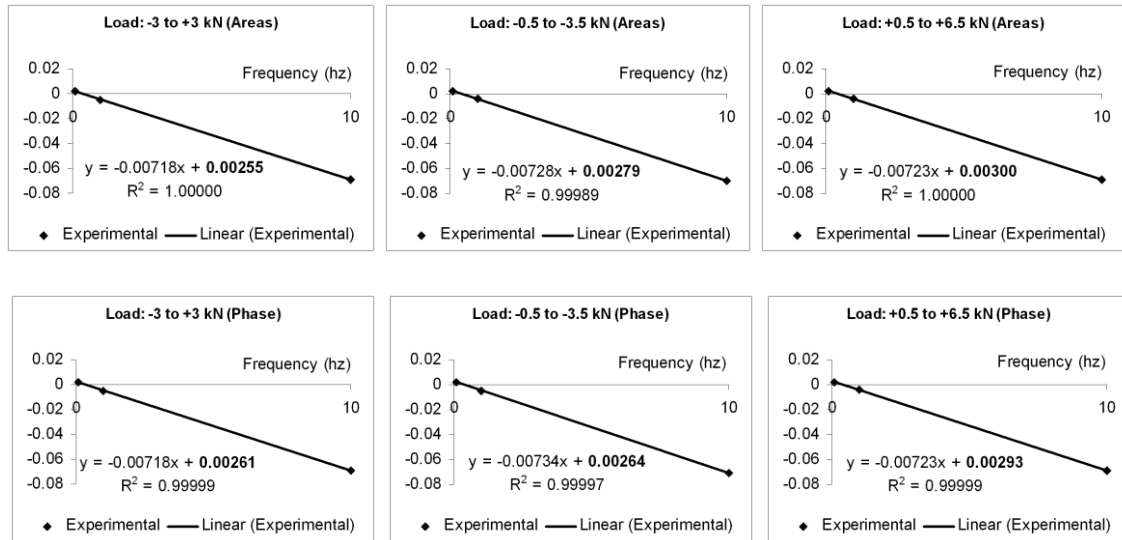


Figure 4.15: Numerical extrapolations for the estimation of the hysteretic damping factor: Upper row: areas method; Lower row: phase method.

Table 4.7: Hysteretic damping factor values obtained in the force-displacement tests.

Cycles type	Load (kN)	Areas method	Phase method
Traction-Compression (1)	-2 to +2	0.00300	0.00266
Traction-Compression (2)	-3 to +3	0.00255	0.00261
Traction-Compression (3)	-4 to +4	0.00267	0.00249
Compression-Compression	-0.5 to -3.5	0.00279	0.00264
Traction-Traction	+0.5 to +6.5	0.00300	0.00293
Average Damping		0.00280	0.00267
Max error (to avg)		9%	10%

Observation of figure 4.15 and table 4.7 leads to the following comments:

- Despite the fact that a sample of only 3 measurements at different frequencies was used to evaluate the linear fit, the correlation coefficients were very close to 1 in all cases;
- The angular coefficients of the linear fits are similar (close to -0.007), which means that the lag introduced by the electronics is constant and independent of the measurement setup;

- The results showed a maximum error of 9% (relatively to the mean value) for the areas method, which means a reasonable agreement for this kind of identification. When the phase method was used (equation (4.11), using the FFT), an error of 10% was obtained;
- The phase method seems to have a tendency to produce smaller values for the hysteretic damping factor than the areas method. However, the discrepancy of the hysteretic damping factor between the one obtained with the phase method (0.00267) and the one obtained with the areas method (0.00280) is smaller than 5%, which is believed to be an acceptable result, considering the magnitudes of the values.

These results sustain the assumption that the measurement chain could be the source for the inconsistency of the raw results. So, the values for the damping factor can and will be used from here on.

4.2.2.2 Free decay testing

The viscous damping factor can be evaluated from a free vibration test. By definition, the logarithmic decrement is the natural logarithm of the decay rate (ratio between two amplitudes spaced by n cycles):

$$\delta = \frac{1}{n} \ln \frac{x_i}{x_{i+n}} \quad (4.12)$$

In most applications the damping ratio is very small and the logarithmic decrement can be approximately given by:

$$\delta = 2\pi\xi \quad (4.13)$$

Since the model considered so far has been the hysteretic model, it may be interesting to explore the hypothesis from Ribeiro *et al.* (2005) that suggests the possibility of using the hysteretic model for the free vibration. If such suggestion is considered, the logarithmic decrement would be approximately given by:

$$\delta = \pi\eta \quad (4.14)$$

Within this hypothesis, free-vibration tests were performed to obtain the experimental free decay behaviour of a cantilevered beam. A reflective tape was attached on the free tip of the cantilevered beam (as previously shown in figure 4.10) and the time response obtained in terms of the velocity (a LDV was used - Polytec® Controller OFV-2802i and Polytec® Interferometer OFV-508). In order to avoid as much as possible any changes introduced by the data processing, the velocity itself was used. The initial conditions were introduced so that a displacement on the free tip of the specimen was high enough to produce a measured signal of good quality (high signal-to-noise ratio) but still within the linear behaviour range. The beam was clamped to a much stiffer and heavier structure, using 45mm of its length. The logarithmic decrement was measured using 2 amplitudes spaced by 49 cycles, and repeated, for each block of 50 amplitudes, thus providing a total of 350 values for the hysteretic damping factor (amplitude 1 with amplitude 50, amplitude 2 with amplitude 51, amplitude 3 with amplitude 52, and so on). The first 250ms of the time-signal used to compute the hysteretic damping factor for the free vibration decay is plotted in figure 4.16, showing that the influence of higher frequency modes already vanished. The results for the hysteretic damping factor obtained by the free-decay testing are shown in figure 4.17.

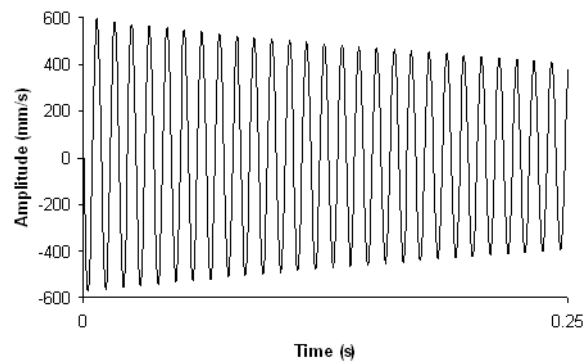


Figure 4.16: Experimental free decay velocity (cantilevered CFRP laminate).

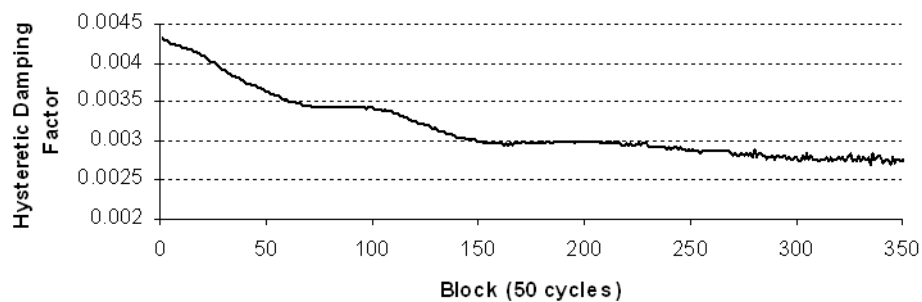


Figure 4.17: Hysteretic damping along superimposed time blocks of 50 cycles.

It is clear that the damping factor is not constant with time, starting with a value of 0.0043 and having an asymptotic tendency to a value of 0.0027, very close to the one obtained with the force-displacement test.

The same test was conducted, but this time the clamping force was increased (though it was not possible to quantify its value), leading to the results shown in figure 4.18.

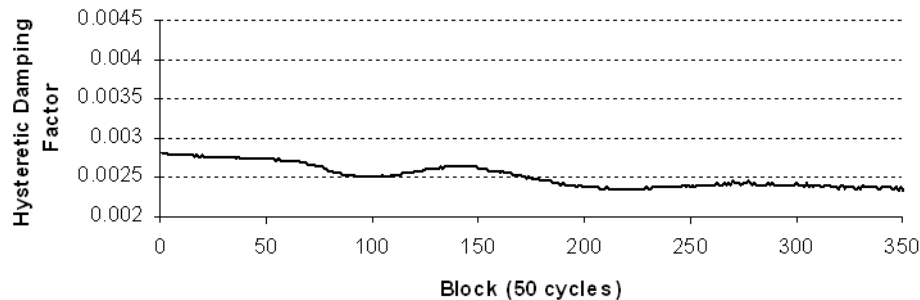


Figure 4.18: Hysteretic damping along superimposed time blocks of 50 cycles (larger clamping force).

As expected, the clamping mechanism is performing an important role on the process of the free vibration of the cantilevered specimen (note that the specimen was not moved from its original position and only the clamping force was increased). This time, the changes on the hysteretic damping factor are not as large (0.0028 in the beginning to 0.0024 at the end of the time signal), but it still represents a considerable variation (of 17%). The damping factor seems once more to converge when it achieves smaller amplitude levels of vibration.

In both cases, the hysteretic damping factor seems to oscillate, which may be a consequence of the influence of the clamping structure itself.

4.2.2.3 Validation of the test methods for damping assessment

To gain better insight about the method, it was decided to repeat the process, this time using an 800mm length steel beam with a $25 \times 6 \text{ mm}^2$ rectangular cross section. The purpose was to confirm if the boundary conditions on the free-vibration tests were, in fact, responsible for the variation of the damping factor, or if it was the composite material itself the reason for such a behaviour. First, a force-displacement test, ranging from +1 to +10kN was performed (to avoid buckling, compressive loading was not used), at three different frequencies of 0.1Hz, 1Hz and 10Hz, producing an estimation of the hysteretic damping factor of 0.00243 with the areas

method and 0.00218 with the phase method. After that, a free-vibration test was conducted, following the same procedure. A variable hysteretic damping, ranging from 0.0036 to 0.0023 was obtained, with a slight convergence in the end of the time signal, thus leading to conclude that the clamping mechanism has a strong nonlinear influence on the results for any cantilevered beam. Since the non-linearity is with the amplitude of the vibration, the value to be considered is that obtained for the smaller amplitudes; this value (0.0023) is within the range obtained for the force-displacement tests, thus supporting the assumed hypothesis.

To further increase the confidence in the results, it was decided to perform similar tests on a material with larger damping: a high density poly-urethane beam with a 25x15mm² rectangular cross section. Final results for the composite specimen, steel beam and poly-urethane beam are presented in table 4.8.

Table 4.8: Hysteretic damping results summary.

	Areas method	Phase method	Free-vibration
CFRP	0.00280	0.00267	0.0024
Steel	0.00243	0.00218	0.0023
High density poly-urethane	0.0167	0.0180	0.0186

These final results show that all the methods provide coherent results, given some of the previous considerations, for all the materials put under test. As a result, a confident value for the CFRP damping factor was obtained to be used later in this work.

4.3 Test setups for damage assessment

This section is intended to provide some guidelines and other information about the setups in the dynamic experimental testing for damage assessment (i.e., for obtaining FRFs to be subsequently parameterised by modal identification). For a detailed list of the equipment used, a table is presented in annex B¹⁹.

¹⁹ There are many reasons behind the use of different equipments and setups, in many cases practical reasons that the author was not able to control. The important thing to keep in mind for improving the

4.3.1.1 Specimen type 'L'

Specimen beam type 'L' was tested in a cantilevered configuration, as shown in figure 4.19. Three lengths for clamping the 437mm long specimen were considered: 50mm (case L3), 100mm (case L2) and 150mm (case L1).

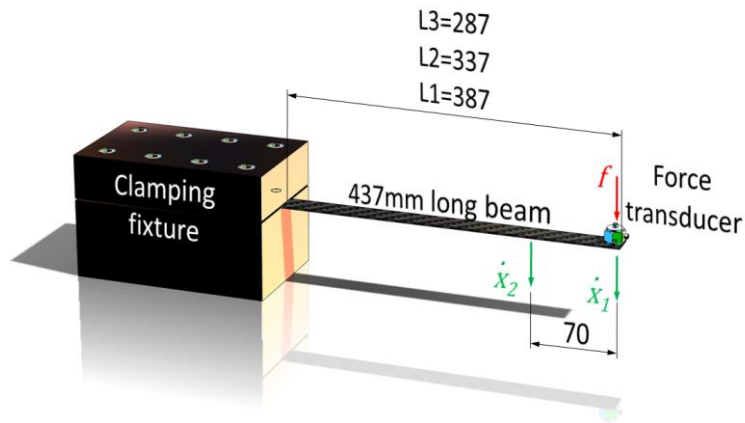


Figure 4.19: Specimen beams type 'L' experimental setup.

Experimental testing was carried out in the 40 to 1600 Hz frequency range with a stepped-sine excitation force applied by a stinger attached to an electromagnetic shaker (Brüel & Kjær® type 4809). Two response points, set 70 mm away from each other, were measured using a Dual-channel LDV from Polytec® (interferometer OFV-508 and controller OFV-2802i) and target reflective tape 3M Scotchlite™. The force was measured with a force transducer (Brüel & Kjær® type 8200) fastened to the free-end tip of the beam and connected to a charge amplifier (Brüel & Kjær® type 2706).

Stepped-sine excitation was used in order to evaluate nonlinearities due to damage. Tests were made using beam L1. The input force was controlled using the HARMONICA® software²⁰, which is the software that allows the use of a stepped-sine excitation. Three tests for different input forces were run: at 0.25N, at 0.5N and at 1.0N.

reliability on the results is that when comparing two states of a structure (e.g., healthy to damaged state), testing should be done under the same conditions, as much as possible.

²⁰ The HARMONICA® software is a custom made spectrum analyser. It was fully developed by the author in LabVIEW™ 7.1 from National Instruments™. It is able to measure transfer functions using an excitation force of the stepped-sine type, making it possible to experimentally assess dynamic systems' nonlinearities. The author felt the need to develop this software to accomplish the task of evaluating non-linearities in the presence of damage, as the commonly available tools do not allow for this kind of very specific testing. The program is freeware and available in the Internet for download at <http://ltodi.est.ips.pt/dmontalvao/downloads.htm>. Its manual and further information are available in the end of this thesis, in annex D.

4.3.1.2 Specimen type 'A'

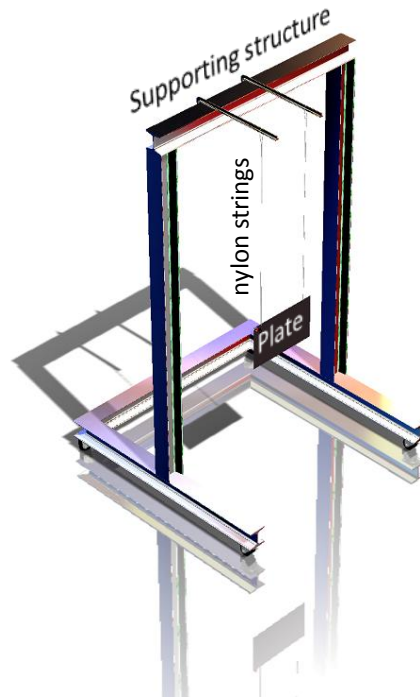


Figure 4.20: Specimen plates' types 'A' and 'B' experimental setup.

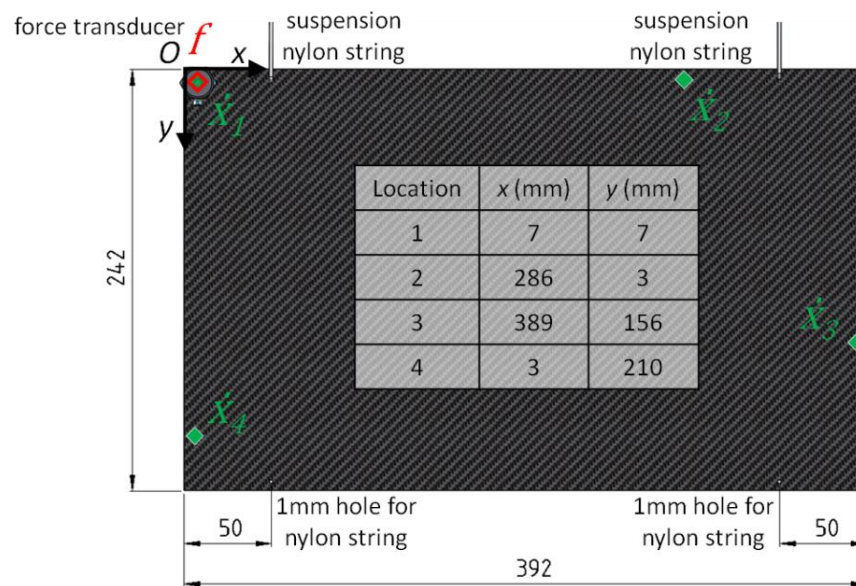


Figure 4.21: Specimen plate type 'A', with force excitation point and response measurement locations.

Specimen plate type 'A' was tested in a free-free configuration, suspended by two nylon strings set 50 mm away from the top corners, as shown in figure 4.20.

A PULSE™ system from Brüel & Kjær®, including a signal acquisition module (Brüel & Kjær® type 3109) and LAN interface module (Brüel & Kjær® type 7533), was used for both the signal generation and acquisition.

Experimental testing was carried out in the 0 to 800 Hz frequency range²¹ with multi-sine²² excitation signals introduced by means of a stinger attached to an electromagnetic shaker (Brüel & Kjær® type 4809). Four points, with coordinates²³ shown in figure 4.21, were used to measure the velocity response using a Dual-channel LDV from Polytec® (interferometer OFV-508 and controller OFV-2802i) and target reflective tape 3M Scotchlite™. The force was measured with a force transducer (Brüel & Kjær® type 8200) connected to a charge amplifier (Brüel & Kjær® type 2706) and fastened to the top left corner of the plate.

4.3.1.3 Specimen type 'B'

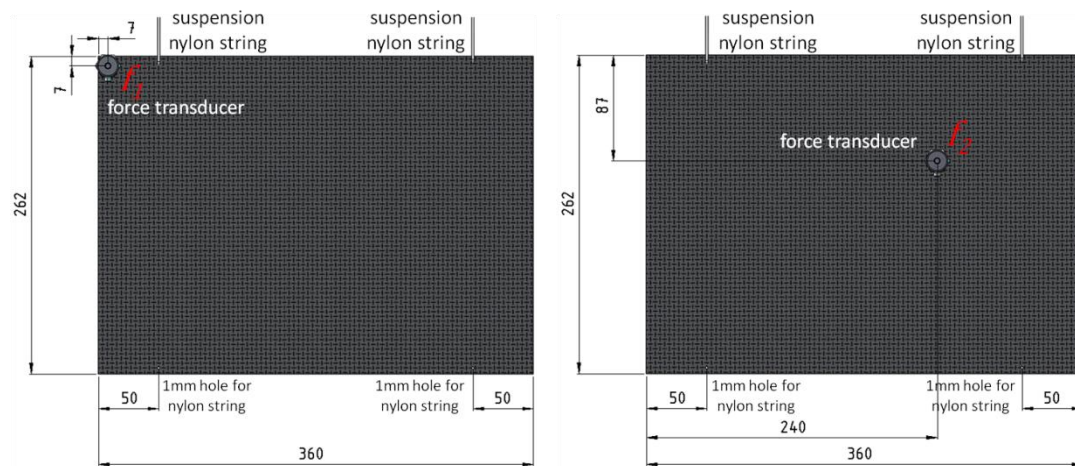


Figure 4.22: Specimen plate type 'B' force excitation points.

Specimen plate type 'B' was tested in a free-free configuration, suspended by two nylon strings positioned 50 mm away from the top corners, as shown in figure 4.20 above.

²¹ Except for the healthy state of plate A1, later on referred to as A1H, where testing was carried out in the 0 to 400 Hz frequency range. Soon after, the frequency range was increased in order to get more modes.

²² Multi-sine signals result from the superimposition of several sinusoidal signals, one for each frequency line of the spectrum, with the same amplitude. The resulting data can be transformed to the frequency domain using the FFT and then used to estimate the FRF of the system under test.

²³ Except for the direct FRF, all the other response measurement locations were chosen so that they would not be over a nodal line of the plate up to 400 Hz, as shown later in figure 5.12 of section 5.3.1.

A Polytec® Scanning LDV composed of a combination of head PSV-400, controller OFV-5000 and junction Box PSV-400, was used for both the signal generation and data acquisition.

Experimental testing was carried out in the 0 to 1600 Hz frequency range with sweep-sine²⁴ excitation signals introduced by means of a stinger attached to an electromagnetic shaker (Brüel & Kjær® type 4809). The force was applied at two positions: (i) at the top left corner, with coordinates (7, 7) mm; and at an inner point, with coordinates (240, 87) mm from the top left corner (figure 4.22). Force was measured using a force transducer (Brüel & Kjær® type 8200) with charge amplifier (Brüel & Kjær® type 2706). Response was measured on a 13x11 (143) nodes of a square-like element mesh with the Scanning LDV as better explained in section 4.4.3 below.

4.4 Finite element modelling

4.4.1 Relevance

Since damage corresponds to a degrading change with respect to a healthy state, it is necessary to have knowledge about such a condition. That is why this method, as many others, requires a description of that situation. This reference state can be obtained either experimentally, analytically or numerically. Also, being an objective of this work to study the location of the damage in a given specimen, a geometric description of the specimen is needed. These considerations suggest the use of FE models for the description of the healthy state of the structure. Nevertheless, experimental verification of such models is performed, as recommended by other authors, for instance Maia and Silva (1997) and Sohn *et al.* (2003).

In the present case-study, a force is measured by means of a force transducer that is treated as a structural element. In the event that a structural modification is included, such as the displacement of the force transducer, new well adjusted models are required, since this added mass has a significant value that cannot be neglected (the available force transducer has over 5% of the overall weight of the structure in all of the studied cases).

Numerical or FE models must be reliable and robust, and hence, experimental testing is anyway recommended for subsequent validation and/or updating.

²⁴ The sweep-sine (or swept-sine) method uses excitation signal of a sinusoidal shape whose frequency continuously varies (in the current case, increases) with the time. The resulting data can be transformed to the frequency domain using the FFT and then used to estimate FRF of the system under test.

The model can also be obtained experimentally, but expensive equipment, for instance a Scanning LDV, and somewhat time consuming testing, are required when such a model is sought to be obtained. Furthermore, to obtain an accurate experimental modal model of the structure, a lot of measurement points are needed, meaning that computational storage and performance are also a must. Numerical post-processing of the data with interpolation techniques is inevitable later on so that the modal displacement is converted into another physical quantity, for instance a strain. All summed up, it is much more time consuming to get a mesh description with the same refinement as when using FE modelling, which is a drawback when looking after localized damage. On the other hand, as with FE modelling, also here the properties of the material must be previously accurately known (such as the Young's modulus and Poisson's ratio).

These reasons bring back to the choice of using a validated FE model instead; moreover there are also uncertainties associated to any model even if it is mostly based on experimental data.

The method presented herein relies on such model to build the so called PSF defined earlier in section 3.6.1, a function of mode dependent physical quantities.

4.4.2 Applying FE modelling to composite materials

4.4.2.1 Introduction

One of the concerns when building the FE model of a composite material is whether it should be made using layered elements or not.

In section 3.3 it was shown that the behaviour of a laminate, from the macromechanical point of view and at least as long as it is orthotropic, can be described with the engineering constants of the laminate instead of those of the laminae.

One of the advantages of modelling a composite material as a homogeneous non-layered material is that it is possible to determine the engineering constants through of simple tests such as uniaxial tension tests. Furthermore, it is much simpler to define the material properties and real constants²⁵ in the FE modelling software for homogeneous rather than for layered materials, especially when woven preregs are used.

²⁵ In the sense used by ANSYS®.

Nevertheless, in the event suitable equipment for experimental determination of the engineering constants of the laminate is not available, these can be determined from the laminae's theoretical properties by using the method described in section 3.3.3. The engineering constants of the laminae can be obtained from manufacturer data sheets. To build the FE model with layered elements, the properties of a single ply can be determined first and the plate properties then built up using laminate theory.

Unless the study is meant to have a broader (e.g., failure criteria calculation), the first approach seems to be reliable enough for the assessment of the mode shapes in a rectangular plate: and this is really what is needed for the present study. A comparison between two models is made later on (section 4.4.5.3) in order to evaluate which is the best approach for the case-studies presented here.

4.4.2.2 Element types for modelling thin plates

According to Matthews, F. L. *et al.* (2000), the layered nature of composite materials means that only certain element types can be used efficiently within the FE analysis of composites. In theory, it would be possible to stack three-dimensional brick elements with one layer of bricks representing one ply of composite material, but such approach can be computationally expensive and, for thin laminates, it leads to ill-conditioned sets of equations.

In practice, it is much more usual to employ some type of shell element for thin components. Typically, the shell element is quadrilateral or triangular with nodes at the corners and some also have mid-side nodes. The shell is modelled in terms of its mid-surface plane rather than the complete volume. The standard bending theory is then used. This means that the deformation of the shell can then be defined by stretching (for the constant strain components) and rotation (for the linear strain components) of the shell's mid-thickness surface. There are several theories to be used, such as the Kirchhoff-Love, Reissner-Mindlin and "solid".

According to Nelson and Wang (2004) the most important difference between a typical Kirchhoff-Love shell element, like SHELL63 in ANSYS®, and a typical Reissner-Mindlin shell element, like SHELL181, is that any shell element based on the first theory does not allow for the computing of the transverse shear stresses. Hence, the resulting deformations may be underestimated, especially in thick shell structures. "ANSYS® 11 Elements Reference Manual" (2007) recommends SHELL181 if convergence difficulties are encountered, large strain capability is needed and for nonlinear structures; for a thin shell capability and if plasticity or creep is not needed, SHELL63 may be used instead.

If the model of a thin layered material is needed, ANSYS® offers, for instance, SHELL99 element for linear analysis, although element SHELL181 also is suitable for modelling thin layered materials. Other possibilities are the SHELL93 and SHELL281, as they have mid-side nodes capability, meaning they are particularly well-suited to model curved shells as they have 8 nodes (instead of 4 nodes) for quadrilateral elements.

For layered thick shells, a more suitable element is the “solid” shell, like SOLID46 in ANSYS®, which, according to Matthews, F. L. *et al.* (2000), has the geometrical definition of a solid element but the behaviour of a shell²⁶.

In Annex A, some of the most important characteristics of the elements chosen in the final FE models built (also see section 4.4.3) are presented, including the elements used to model a point mass and a spring, using ANSYS®, for the work presented in this thesis.

4.4.2.3 Modelling elastic constants of textile composites

The great challenge in modelling the elastic properties of textile composites is dealing sufficiently well with the very large variations in stress and strain that can occur within a textile even under uniform applied loads. A textile composite is a highly heterogeneous structure. It may be viewed (and is often modelled) as a three-dimensional tessellation of fibres, each of which is an approximately unidirectional composite and therefore transversely isotropic, with the plane of isotropy lying normal to the local fibre direction.

The macroscopic elastic constants of any continuous fibre polymer composite can be loosely divided into those that are fibre dominated and those that are matrix dominated (the division is clearest if most fibres are straight or almost straight.). The fibre dominated constants are those for which the associated material deformation involves axial straining, either in tension or compression, of some group of fibres. The matrix dominated constants are the rest. In a composite designed for any application requiring high stiffness, the critical elastic constants should all be fibre dominated.

The most important geometrical consideration in predicting fibre dominated elastic constants is simply the number of fibres per unit volume that point in any given direction. Out-of-plane components of the fibre orientations, whether they are a necessary consequence of the

²⁶ The element has any number of nodes, depending upon the actual formulation, but only two nodes through its thickness. Each node has only translational DOFs so that no rotational freedoms are explicitly defined.

architecture or arise as accidental waviness, are secondary. They introduce relatively small modifications to predicted in-plane elastic constants. Unless fibre waviness is excessive, it leads to knockdowns in composite stiffness that are too modest to be clearly distinguished from other sources of variance.

There are only a few elastic constants in most textile composites that could be regarded as matrix dominated. They include the through-thickness modulus in 2D and quasi-laminar textiles; and the in-plane shear modulus in a weave consisting of orthogonal fibres. Accurate prescription of fibre orientations and tow irregularities are not especially important in predicting the matrix dominated constants, as the stiffness of a unidirectional composite is very insensitive to the orientation of the load when the load is nearly transverse.

Many of the methods for analyzing stiffness recognize that the textile composites they deal with are quasi-laminar, because the fibre architecture is either a 2D structure or a 3D structure dominated by in-plane fibres arranged in layers. The geometry will then be described in a way that bears out its quasi-laminar character; and the analysis of stresses and strains will usually include steps based on standard laminate theory.

An approach to modelling the geometry of quasi-laminar textiles is to represent them just like conventional tape laminates. The geometry of the laminate is then completely described by the thicknesses, orientations, and stacking sequences of the layers (Cox and Flanagan (1997)).

4.4.3 Tests for FE model validation

FE model validation (for computing the PSF function correctly) was carried out with data obtained in the Vrije Universiteit Brussel (VUB) in Brussels using a Scanning LDV. A total of three missions were held to fulfil this task.

Specimen plates A1H to A4H (mission 1), A1D, A2D and A5H (mission 2) and B1H, B1D, B4H, B4D, B4'H and B4'D (mission 3) were tested. For the signal generation and data acquisition, two Scanning LDVs were used. The plates were suspended in a free-free configuration using two nylon strings positioned at a distance of 50mm from each of the two top corners.

In missions 1 and 2 the force was introduced at the top left corner of the plates, whereas in mission 3 the force was applied at two positions: the same as in figure 4.22 (section 4.3.1.3 above). The excitation force was of the sweep-sine type and it was introduced using an electromagnetic shaker (Brüel & Kjær® type 4809) and a threaded Teflon stinger. The force was measured with a force transducer (Brüel & Kjær® type 8200) and charge amplifier (Brüel & Kjær® type 2706).

The frequency range was from 0 up to 400 Hz (mission 1), from 0 to 800 Hz (mission 2) and from 0 to 1600 Hz (mission 3).

The responses were measured by the direct reflection of the LASER beam from the dark rough surface of the specimen (without using any kind of reflective tape), showing evidence of some noise in certain nodes. During missions 1 and 2, 13x9 (117) nodes of a square-like element mesh were used for the measurement of the velocity responses in specimen plates type 'A', whereas during mission 3 a total of 13x11 (143) nodes was used in specimen plates type 'B'. Since the plates had different dimensions, a different amount of measurement nodes was used (to preserve each square mesh approximate dimensions). These meshes covered the whole plate's surface as shown in the example figure 4.23 (for specimen plate type 'B').

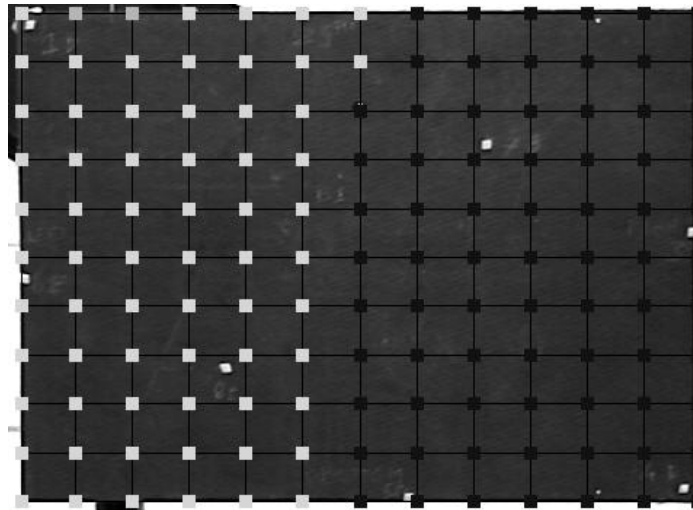


Figure 4.23: 13x11 Scanning LDV mesh of measurement responses over specimen plate type 'B'.

Mission 1 used a different Scanning LDV than missions 2 and 3. Some pictures from mission 1 are presented in figure 4.24: the Polytec® controller OFV-3001 and junction box PSV-Z-040M (left); the LASER head OFC-056 (centre); and a screenshot of the software during a measurement where the square-like mesh can be seen.

During missions 2 and 3 a Polytec® Scanning LDV, composed of a combination of head PSV-400, controller OFV-5000 and junction Box PSV-400, was used for both the signal generation and data acquisition, as shown in figure 4.25.



Figure 4.24: Illustrating pictures of the experimental apparatus during missions 1 and 2.



Figure 4.25: Mission 3 experimental apparatus.

4.4.4 Some considerations on FE modelling

Sohn *et al.* (2003) In a first stage, two programs were used for FE modelling: ABAQUS® 6.5.1 and ANSYS® 11. In order to evaluate which simulation would better fit the experimental results, several models were developed in both of these Computer Aided Engineering (CAE) applications. Specimen plate type 'A'²⁷ was used and its material was considered as being homogeneous and isotropic due to the quasi-isotropic layup and other reasons previously presented.

²⁷ Plate A1H was used as case-study for this assessment of the CAE packages.

Once the CAE application was chosen, the influence of the relevant parameters on the present study was assessed.

On the whole, a total of 48 simulations were run at this stage, during which the following parameters were changed:

- Mesh size, from coarse (40 elements) to fine (10400 elements), keeping always a quadrangular geometry;
- Element types inside the shell family:
 - ABAQUS®: S8R, S8R5, S4, S4R, S4R5, S3;
 - ANSYS®: SHELL63, SHELL93, SHELL181, SHELL281;
- Analysis type, namely Lanczos, Sub-space and QR Damped;
- Force transducer mass moments of inertia in the three directions, I_{xx} , I_{yy} and I_{zz} ;
- Active mass m_z and transverse masses m_x and m_y of the force transducer;
- Material's mass density;
- Material's Young's modulus;
- Material's Poisson's ratio;
- Plate thickness, length and width (within the measured values);
- Plate bi-dimensional geometry – “rectangularness”, or shape variation (within the measured values including some distortion);
- Push-rod stiffness.

It was taken into account the correspondence between the experimental and the numerical natural frequencies²⁸, but the main care was to guarantee that the numerical mode shapes would match the experimental results.

With respect to the type and number of elements it was concluded that an “intermediate” – or optimal - number of elements would lead to more accurate results rather than just over-refining the mesh. Also, shell elements with 4 nodes only and 6 DOFs per node proved to behave very satisfactorily. This conclusion stands even if "ABAQUS® 6.5 Theory Manual" (2007) states that element S8R5 (8 nodes, reduced integration) with 5 DOFs is adequate for thin plates while element S8R (8 nodes, reduced integration) with 6 DOFs per node is more adequate for thicker plates. This was not observed after both simulations were run. It must be mentioned, however, that the computational cost and memory usage was not a concern.

²⁸ From the 18 modes considered for validation, a maximum discrepancy of 5.7% and an average discrepancy of 2.7% were achieved with respect to the modal frequency values.

Another important conclusion that was obtained is that the mass moments of inertia I_{xx} and I_{yy} and active mass m_z of the force transducer have a strong influence on the results.

A change of the Young's modulus represents a constant relative change for all modes in the frequency range, which is not surprising as in this study the material is considered isotropic and homogeneous (for instance, by lowering the value of the Young's modulus 10% all the modes showed a 6% frequency decrease). On the other hand, a variation of the mass density of the plate did show up to have different effects for different modes, although those differences are not quite relevant (by lowering 10% the value of the mass density, the modal frequencies presented increase from 3% to 5%). A similar behaviour was observed when changing the plate's thickness.

Another property that showed up to have considerable influence on the FE model is the Poisson's ratio, especially on each mode shape.

With respect to the analysis type, no differences were found in any case when comparing Lanczos, Subspace and QR damped among each other. That should not be a surprise. First, the model is not complex, thus Block Lanczos and Subspace are expected to provide similar results. Secondly, QR damped makes use of the Block Lanczos itself. Considerations about the analysis type are made in annex A.

Finally, contrary to what is generally assumed, that only the active mass of the force transducer (part of the force transducer that is on the same side of the structure) has an influence on the results, the push-rod, which is attached to the other side of the force transducer, showed to play a strong influence on the results (as already shown by Montalvão (2003) and also in annex C of this work). The first measured mode shape for plate A1H is at around 15 Hz, but this mode did not show up in the first FE models. It was suggested that this could be a consequence of the push-rod stiffness, which was proved, when a spring with a stiffness of around 500 N/m was included in the FE model. It must be noticed that this value does not necessarily correspond to the push-rod's stiffness; it may rather represent the influence of the loading chain on the dynamic behaviour of the structure.

For validation (and choice) of the model and software to be used in the succeeding tasks, test data was obtained with a Scanning LDV from Polytec® in the VUB in Brussels (see section 4.4.3) and compared to the numerical (FE model) results. The data was first observed with the Polytec Scan Viewer 1.31 software and later processed with BETAlab® software²⁹ for

²⁹ BETAlab® is a custom made modal identification program. It was fully developed by the author in LabVIEW™ 7.1 from National Instruments™. It is used to find the modal parameters from experimental

improvement of the results³⁰. To illustrate the agreement between the FE and experimental models, part of the results are summarized in table 4.9. Only 5 from a total of 18 modes are shown (from the 11th till the 15th), but it must be stressed out that presentation of more modal shapes will not upraise further comments. From these results, it is possible to see that the model built with ANSYS® provides more consistent results for both frequency and mode shape than ABAQUS®, except for the 11th mode.

In summary, the following may be pointed out as the core parameters when trying to build a mode shape model of an isotropic plate like structure with an attached point added mass (of much lesser dimensions):

- Mesh size and FE element type;
- Added mass moments of inertia in the x and y directions (I_{xx} and I_{yy});
- Added mass in the z direction (m_z);
- Material Poisson's ratio.

Other properties, such as the plate's dimensions, mass density and Young's modulus are of course important, but since these are easy to measure with a reasonable degree of accuracy, they do not constitute a hindrance for obtaining an accurate modal model of the structure.

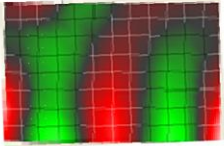
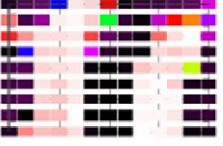
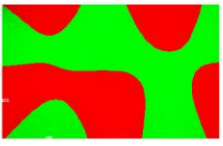
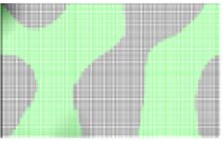
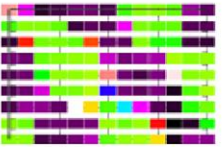
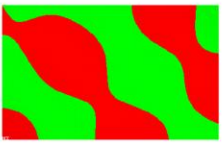
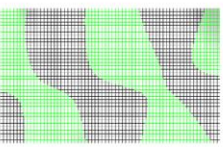
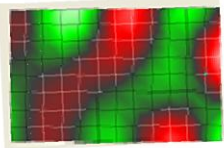
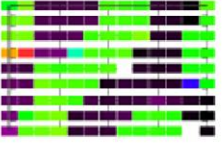

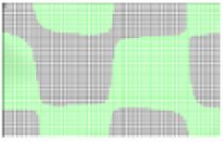
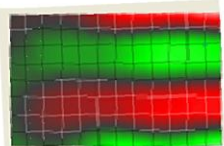
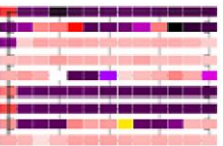
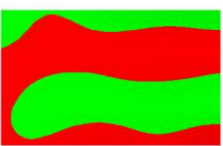
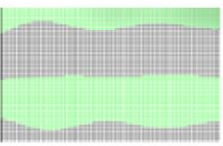
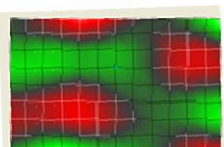
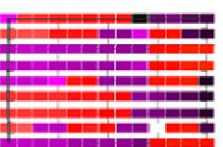
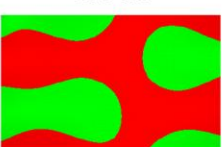

An adjusted model for the orthotropic cases (specimen plates type 'B') was also built. In fact, it is frequently recognized (Ibrahim and Seafan (1987), Friswell and Mottershead (1995)) that it is necessary to tune the FE models' parameters – either those that are valid for static (or quasi-static) situations or others difficult to accurately model, such as joints – in order to provide a reliable reproduction of the vibration test results. When performed systematically, this process is known as *Updating*. In the present case, the model parameters' adjustments were

FRFs. BETAlab® 7.05 is an up-to-date version of the now obsolete BETA® presented by Ribeiro (1999). This justified the need to develop an up-to-date programme, starting from scratch. BETAlab®'s manual and further information are available in the end of this book, in annex E.

³⁰ Because the post-processing accompanying software from Polytec® is not available in IST in Lisbon, freeware software Polytec Scan Viewer 1.31 was downloaded from the internet and used to take deeper look into the mode shape results. However, this later software only allows for on-screen visualization of the ODSs (either in the form of magnitude, phase, real or imaginary parts) that were identified by peak-picking in the prior software. This was done during one of the short-term periods (just a couple of working days) that the author stayed in the VUB, so there was no way to improve the available results afterwards: for instance, it was later observed that some modes were erroneously identified twice whereas others were not identified at all. Hence, the raw experimental data was post-processed once more, but this time using the modal identification software BETAlab® along with an auxiliary program especially developed to accomplish this task (annex E).

sufficiently small for obtaining the desired correspondence through a manual tuning of some of the material properties, namely the shear modulus.

Table 4.9: Comparison between experimental and numerical modes for specimen plate A1H (extract of the table comprising a total of 18 modes).

Mode no.	Experimental Results		Numerical (FE) Results	
	Polytec	BETAlab	Ansys S63 45x60	Abaqus S4 45x60
11	 469 Hz	 465 Hz	 486 Hz	 464 Hz
12	N/A	 554 Hz	 554 Hz	 535 Hz
13	 565 Hz	 567 Hz	 564 Hz	 555 Hz
14	 600 Hz	 600 Hz	 577 Hz	 573 Hz
15	 671 Hz	 672 Hz	 631 Hz	 615 Hz

4.4.5 Specimens' modelling

Bellow a description of the options taken when modelling the specimens in FE is presented. For further information about the elements chosen for each one of the specimens' models, see Annex A.

4.4.5.1 Beams type 'L'

Specimens type 'L' were modelled in ANSYS® 11 with SHELL63 elements (6 DOF per each of the 4 nodes) in a cantilever configuration, as shown in figure 4.26. The specimens, quasi-isotropic

CFRP G803/200 beams with rectangular cross sections, $[0/45/135/90]_s$ layups and approximate dimensions of 392x25x2mm, were modelled as isotropic homogeneous materials.

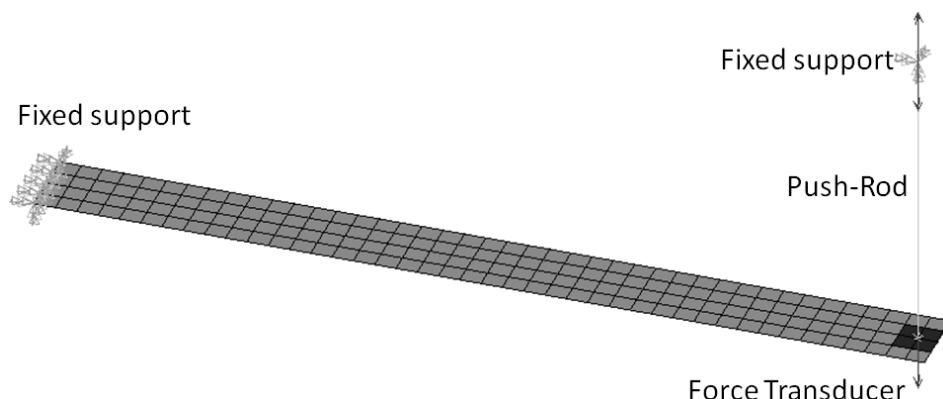


Figure 4.26: FE model of the specimen beam type 'L' with highlighted force transducer, push-rod and boundary conditions.

The length of the beam was changed with the help of the fixture in order to count on with three different sizes: beam L3 was modelled with a total of 42x4 (168) elements totalizing a length of 387 mm; beam L2 was modelled with a total of 36x4 (144) elements totalizing a length of 337 mm; and beam L1 was modelled with a total of 30x4 (120) elements totalizing a length of 287 mm.

4.4.5.2 Plates type 'A'

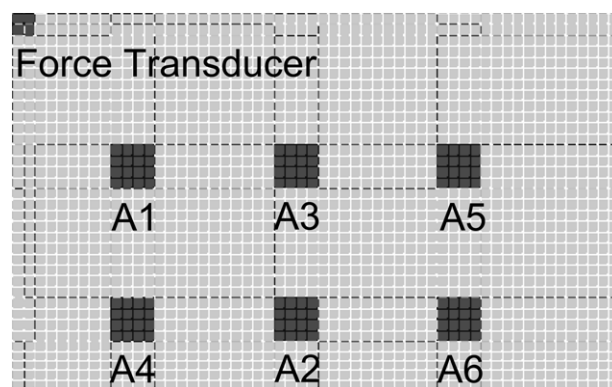


Figure 4.27: FE model of the specimen plate type 'A' with highlighted force transducer and damage locations.

Plates type 'A' were modelled in ANSYS® 11 with a total of 56x35 (1960) SHELL63 elements (6 DOF per each of the 4 nodes) in a free-free configuration, as shown in figure 4.27. The specimen, a quasi-isotropic CFRP G803/200 rectangular plate with a $[0/45/135/90]_s$ layup and

approximate dimensions of 392x242x2mm, was modelled as an isotropic homogeneous material.

This is also the model from which some of the obtained results are shown in table 4.9 of section 4.4.4 above, showing good agreement with the experimental modal results.

For the numerical simulations, damage was simulated at 6 different square regions. Further details about this subject can be found in section 5.2.1.

4.4.5.3 Plates type 'B'

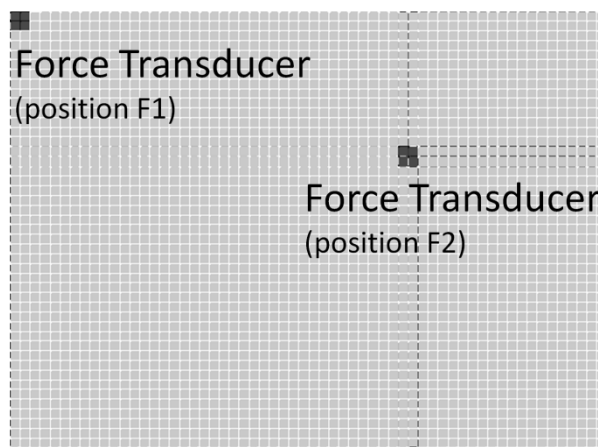


Figure 4.28: FE model of the specimen plate type 'B' with highlighted force transducer locations.

Plates type 'B' were modelled in ANSYS® 11 with a total of 60x44 (2640) SHELL63 elements (6 DOF per each of the 4 nodes) in a free-free configuration, as shown in figure 4.28.

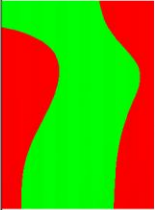
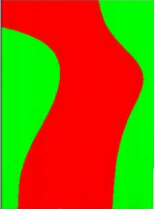
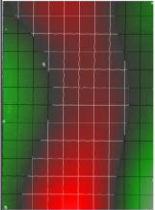
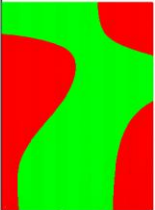
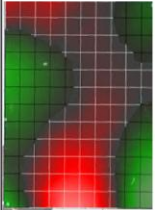
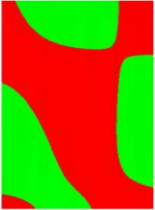
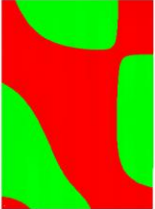
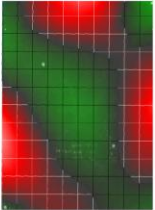
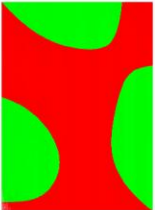
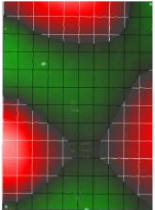
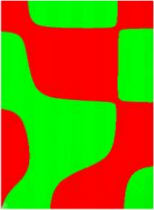
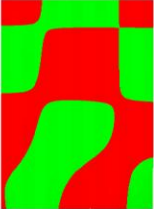
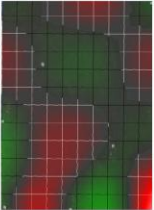
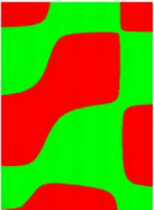
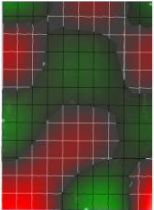
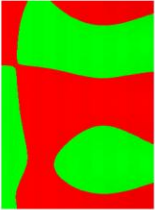
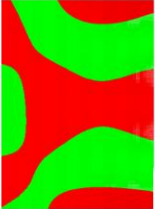
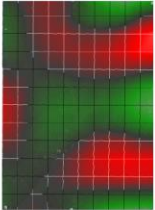
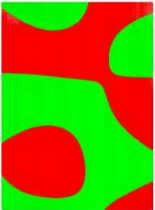
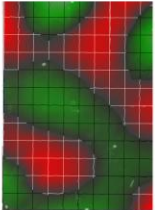
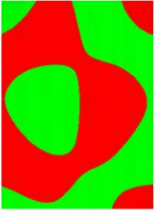
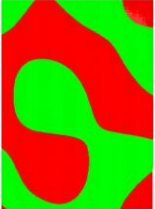
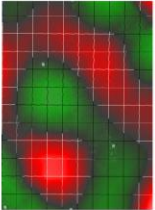
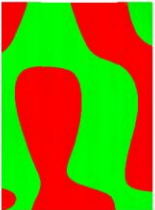
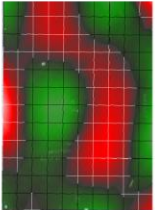
The specimens, orthotropic CFRP T300/934 rectangular plates with $[0/90]_{25}$ and $[90/0]_{25}$ layups and approximate dimensions of 360x262x2.875mm, were modelled as orthotropic homogeneous materials.

Two different possible locations for the force application were considered.

Modelling these plates as composite cross-ply laminates (introducing the local properties of the lamina instead of the global properties of the laminate and using SHELL99 elements instead) was also performed, but this approach was dropped because it did not improve the orthotropic homogeneous model and, at the same time, it showed up to be more complex for these specimens. Similarly, Hu and Wang (2009) concluded that the mechanical behaviour of a 10 ply plain weave carbon fabric laminate could be equivalently simulated by either a cross-ply model or an orthotropic homogeneous model. Some of the most illustrative results that helped to decide these choices are shown in table 4.10. Considering plate B2 (or B1, that is

similar) in which a lamina model was also used, the lamina model seems to be more suitable to describe mode no. 10 rather than the orthotropic homogeneous model. However, this does not seem to be the case for both modes no. 14 and 15, where the orthotropic homogeneous model is a better approach to the correspondent experimental mode shape. When comparing both layups (plate B2 vs. plate B4), some modes are similar (but not equal) to each other (in this case, modes no. 4 and mode no. 10).

Table 4.10: Comparison between experimental and numerical modes for specimen plates B2H and B4H (selection from the table comprising a total of 22 modes).

Mode no.	Specimen Plate B2 (and B1)			Specimen Plate B4 (and B3)		
	Lamina (FEM)	Orthotropic (FEM)	Experimental	Orthotropic (FEM)	Experimental	
4	 282 Hz	 263 Hz	 240 Hz	 270 Hz	 256 Hz	
6	 387 Hz	 370 Hz	 341 Hz	 361 Hz	 329 Hz	
10	 678 Hz	 700 Hz	 629 Hz	 675 Hz	 627 Hz	
14	 881 Hz	 865 Hz	 783 Hz	 856 Hz	 802 Hz	
15	 928 Hz	 952 Hz	 860 Hz	 910 Hz	 841 Hz	

4.4.5.4 Force transducer and push-rod modelling

It is considered that the force transducer, with a theoretical active mass of 18g (out-of plane direction), total mass of 21g and estimated mass moments of inertia $I_x=I_y=1.33 \times 10^{-6} \text{ kgm}^2$ and $I_z=8 \times 10^{-7} \text{ kgm}^2$, is part of the structure. The force transducer is modelled as a zero-thickness distributed mass with concentrated mass moments of inertia occupying a closely squared area of 2x2 elements. In spite of the fact that its real geometry is circular, the square area side is approximately of the same dimension of the diameter of the threaded mount pad.

The mass moments of inertia of the force transducer were modelled in a single node with a MASS21 element at the centroid of the 2x2 squared region. At this same point, a spring with 500N/m stiffness, modelled with a COMBIN14 line element, is attached in order to simulate some of the constraint effects introduced by the push-rod.

Chapter 5

Numerical and experimental validation of the proposed index

5.1 Some notes on the procedural guidelines

5.1.1 Structural components

Composite structures are usually low in weight when compared to equivalent structures of metallic alloys. In the proposed technique, one force transducer and a minimum of one response transducer are used so that at least one FRF may be extracted. Unless a hammer is used to introduce the input excitation force and non-contact transducers are used to measure the output response (such as a LDV), the mass per unit area of a transducer may be relatively large when compared to the mass per unit area of a composite panel. Also, for lightweight structures, the connecting wires and cables may have an influence on the results that is difficult to predict. Hence, it is recommended that attached transducers are treated as part of

the structure, thus avoiding the use of mass cancelling techniques which may increase the uncertainty of the results.

5.1.2 Extracting mode shapes and modal damping factors from the structure

In order to obtain a spatial description of the mode shapes of the structure, one of the following approaches can be used:

- A Scanning LDV, or similar device, is used to measure the responses in several nodes to a single-point excitation. Based on the out-of-plane displacements, the strains can be estimated using numerical methods;
- A FE model of the structure – that can be obtained with ANSYS® 11 or similar software, using an analysis of the type Modal (annex A) – can be used alternatively.

If a FE model is chosen, it is advisable to resort to experimental data, anyway, for validation, which means that both approaches can be used together. With the mode shapes, it is now possible to define the PSF in the forms presented earlier (or in any other way) since ${}_rPSF_{ij} = {}_rPSF_{ij}(\psi_r(i, j))$.

In order to identify the dynamic properties (modal damping factors and natural frequencies) of both the undamaged and damaged states of the structure, a modal identification technique is performed. In the present case, the modal damping factors are identified using BETAlab®, a custom made software (annex E), that makes use of the CRF (section 3.4.2), but any other suitable tools could be used instead.

5.1.3 Summary of the process

In the end, the damage indicator, as developed in chapter 3.6, is obtained from different types of input data. The output is a probability³¹ map for the location of damage over the full set of coordinates (x, y) that geometrically describe the model. Rather than just a formula, the way the proposed damage index is determined can be better understood as an algorithm, a finite

³¹ Sometimes the term “probability” will be used in the course of this text when referring to the damage location index. It would be more correct to use terms such as “likelihood” instead, as “probability” is not used in a strict mathematical sense. However, we thought the word “probability” would be quite suggestive.

sequence of instructions, an explicit step-by-step procedure for solving a problem. The whole sequential process is illustrated as a fluxogram-like scheme in figure 5.1, in which all the inputs for the damage index are represented.

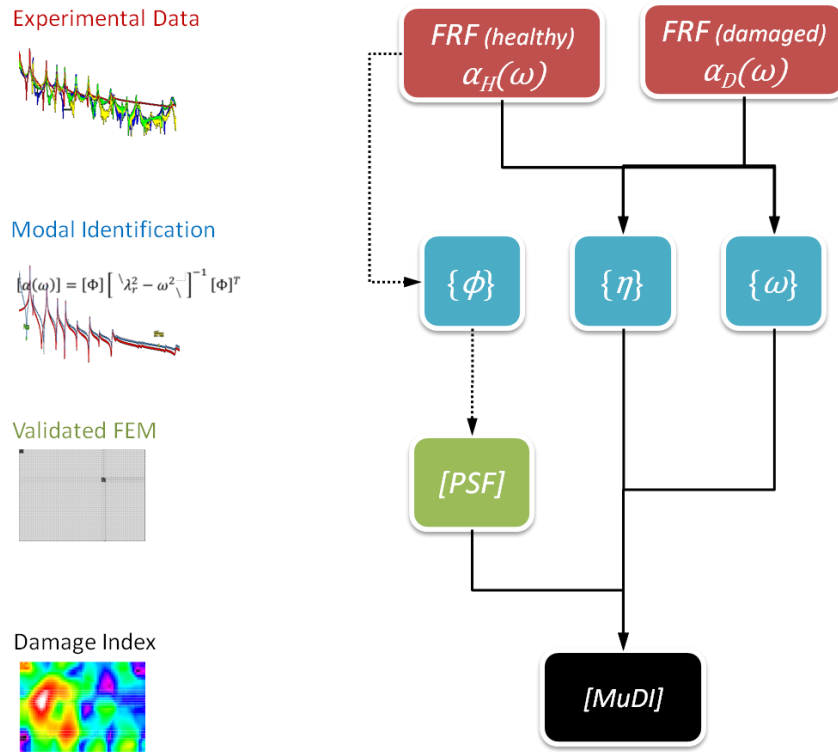


Figure 5.1: Schematic representation of the algorithm sequential stack (steps illustrated with broken lines are only required to validate the FE model).

The implementation of the whole procedure requires a lot of information to be processed; so, a program called MuDI³² (annex F) was developed with the aim of helping to perform the tasks shown in figure 5.1.

5.2 Numerical simulations

5.2.1 Damage characterization

In order to assess MuDI's performance, numerical examples were built for specimen type A (table 4.1): quasi-isotropic CFRP G803/200 rectangular plate with a $[0/45/135/90]_s$ layup and

³² MuDI[®] is a custom made program which allows implementing the damage location algorithm proposed in this work. It was fully developed by the author in LabVIEW[™] 7.1 from National Instruments[™]. Its manual and further information are available in the end of this thesis, in annex F.

approximate dimensions of 392x242x2mm. The specimen was modelled as an isotropic material according to section 4.4.5.2.

For the damage examples, 6 regions were considered, as already shown in figure 4.27 (section 4.4.5.2). Each of the 6 damaged locations is a square region modelled with 4x4 (16) elements, each region corresponding to an area of less than 1% of the total area of the plate.

Damage was characterized by a local variation of either the damping factor³³ or the Young's modulus by setting different values to each of the corresponding elements, providing a global variation in both the modal damping factors and natural frequencies. The following damage scenarios were considered:

- 100x damping factor increase³⁴ in each of regions A1 to A6;
- 10x damping factor increase in region A1 only;
- 10x Young's modulus reduction in region A1 only.

Also, multi-damage scenarios were considered by increasing the damping factor in 2 simultaneous regions by the same amount of 100x.

The simulations were all modelled in ANSYS® 11. FRFs were obtained by resorting to an analysis of the type Harmonic (annex A), which were afterwards subject to modal identification with BETAlab® (annex E).

5.2.2 Results³⁵

5.2.2.1 First results

A total of 18 mode shapes was used in this study, in the range of 0 to 800 Hz. The probability for the location of damage is shown by the index values along the plate. Areas with a larger index value are more likely to be damage locations. A summary of the results are presented in figure 5.2, for localized single 100x damping increase.

³³ The type of damping used is referred by ANSYS® as Frequency Independent (annex A).

³⁴ This increase was chosen in order to obtain modal damping factor variations of the same order of magnitude of the first experimental results (up to 200%).

³⁵ All the predictions for the damaged locations were computed following the method described in section 3.6.

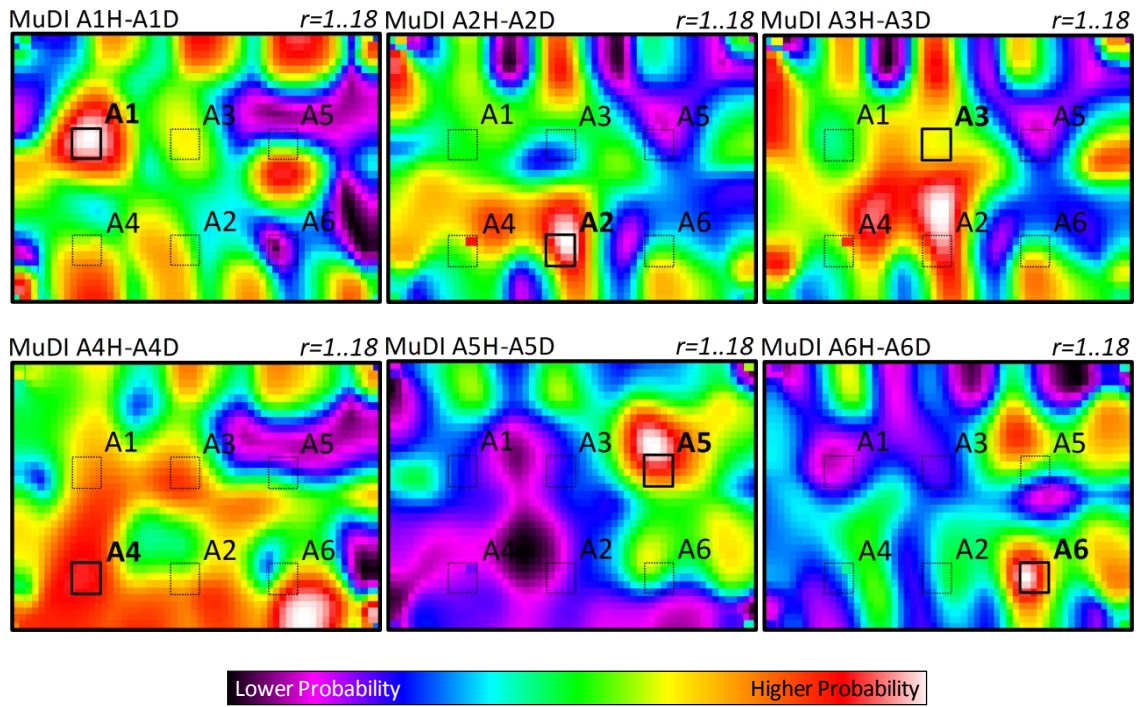


Figure 5.2: First numerical results – 100x localized damping increase.

Generally speaking, these results are encouraging, giving accurate locations for 4 out of 6 damage locations. Examples A3 and A4 seem to be the most problematic, as the index points to regions where its maximum values (whitish) are considerably farther away from the true damage region.

5.2.2.2 Influence of the number of modes and modal order

Although a thorough study was not carried out concerning the influence of the selected modes on the results, the index was tested using the first 8 modes (until 400Hz) and the last 10 modes (from 400Hz until 800Hz) separately. Evaluation of the damage location using the lower and higher order modes separately are presented in figures 5.3 and 5.4 respectively.

Observation of these pictures shows that not only the amount of available modes is important, but also that the lower order modes are more sensitive to localized damage and seemingly unavoidable. While lower order modes seem to indicate a sparser damage region when used separately, higher order modes tend to produce several false-positives. In summary, when compared to figure 5.2, it can be said that lower order modes provide a blurred distribution of the damage location whereas higher order modes sharpen the damage location prediction.

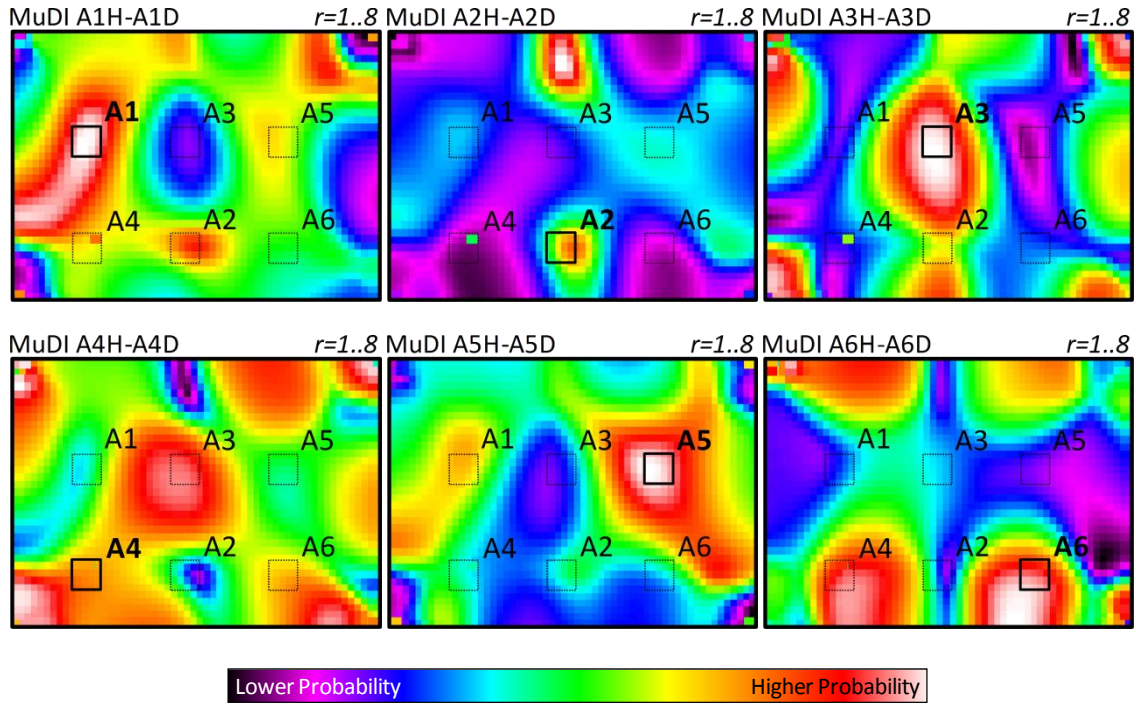


Figure 5.3: Influence of the number of modes and modal order: numerical results for the lower order modes 1 to 8 (up to 400Hz).

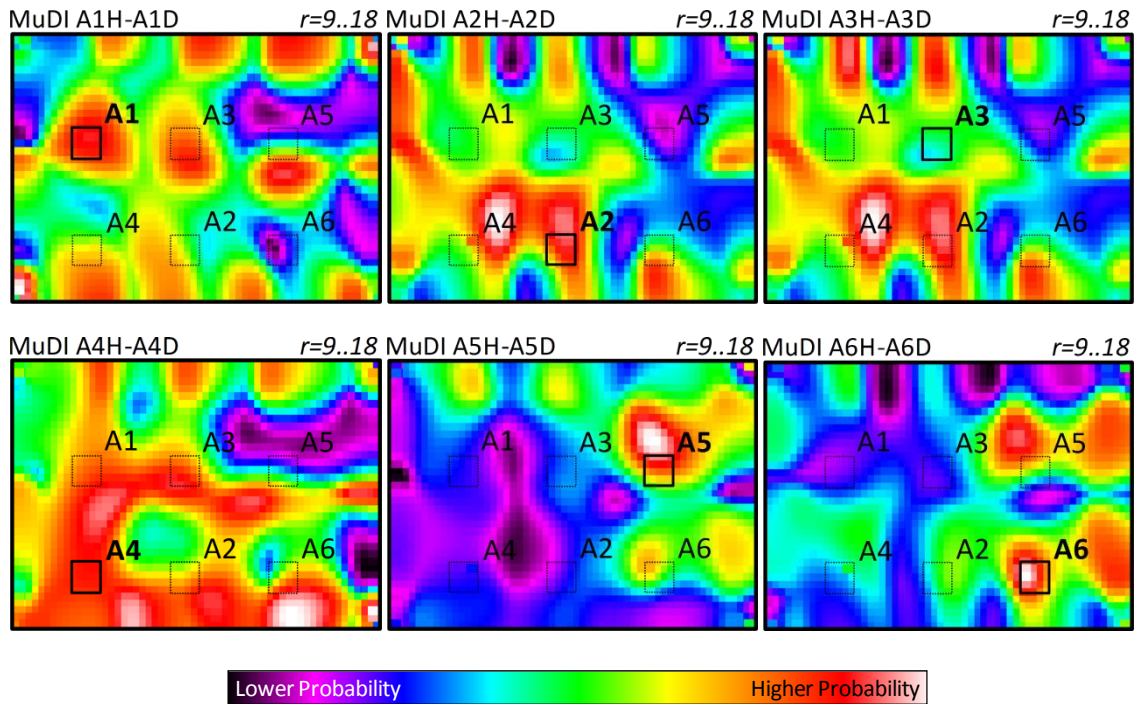


Figure 5.4: Influence of the number of modes and modal order: numerical results for the higher order modes 9 to 17 (from 400Hz up to 800Hz).

It is interesting to notice that some combinations of modes may be equally sensitive to different damage locations. For instance, it is impossible to distinguish case A2 from case A3 in the upper frequency range (figure 5.4), maybe as a consequence of modal symmetry. This idea

is reinforced by the results obtained for case A6 in the lower part of the frequency range (figure 5.3), where MuDI, having a symmetric aspect, points out a likelihood for the presence of damage in location A4.

Except for case A3 (A4 being a less clear case) in which the inclusion of higher order modes have worsen the results, the assertion that the use of as many modes as possible is desirable seems to be reasonable. This remark is suggested when figure 5.2 is compared to either one of figures 5.3 or 5.4.

5.2.2.3 The weighting functions and damage type

Equation (3.58) for computing the damage location is affected by weighting coefficients, W_f and W_d , which are metrics to quantify the contribution of both the frequency and damping variations when computing the index. These constants can be determined with equations (3.61) and (3.60) as explained in section 3.6.1 and can be seen as a first step to evaluate which type of damage prevails: whether it is mainly characterized by fibre breakage or delamination.

A total of 18 mode shapes was considered in this study, in the range of 0 to 800 Hz. Damage was introduced in region A1 in three different ways: 100x local damping increase; 10x local damping increase; and 10x local Young's modulus reduction. The results are shown in figures 5.5 to 5.7.

It can be seen that the weighting functions, which are based on the standard deviations of the frequency and damping variations, play an important role in the damage location procedure. In fact, they can provide hints on the type of damage more relevant for each case. In figure 5.6 the correct location of damage is achieved using the DaDI whereas in figure 5.7 it is exactly the opposite what is happening, i.e., it is the FreDI the responsible for the adequate location of damage. Despite the fact these weighting functions are only metrics and have, as far as now, neither a physical nor a mathematical meaning, they are proving effective in the damage location procedure.

The DaDI and the FreDI use, respectively, the relative differences of the damping factor and frequency between a system's reference and damaged states to search for the damage location. The relative differences are determined with equations (3.53) and (3.56), in which the numerator is the absolute value of a difference between two numbers. In fact, what is being calculated is the relative error (more specifically, the percent error). However, as useful as this can be, these expressions omit in which directions the modal parameters are evolving with damage.

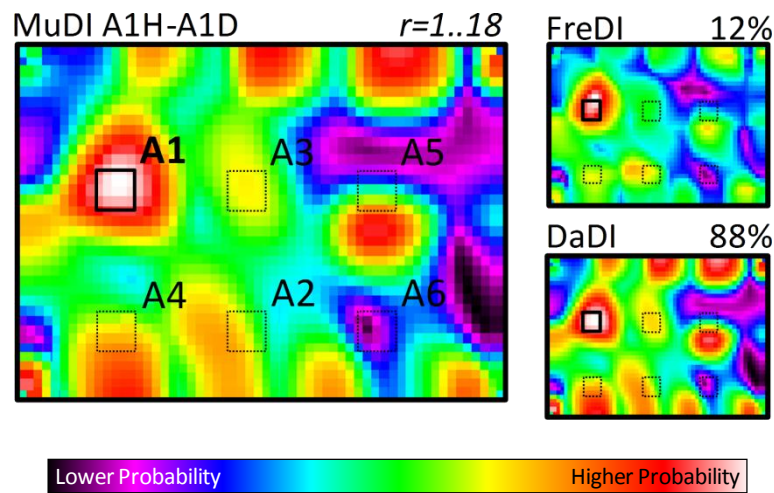


Figure 5.5: Numerical results and weighting coefficients for a damping increase of 100x in region A1. These weighting coefficients are those used in the first result illustrated in figure 5.2.

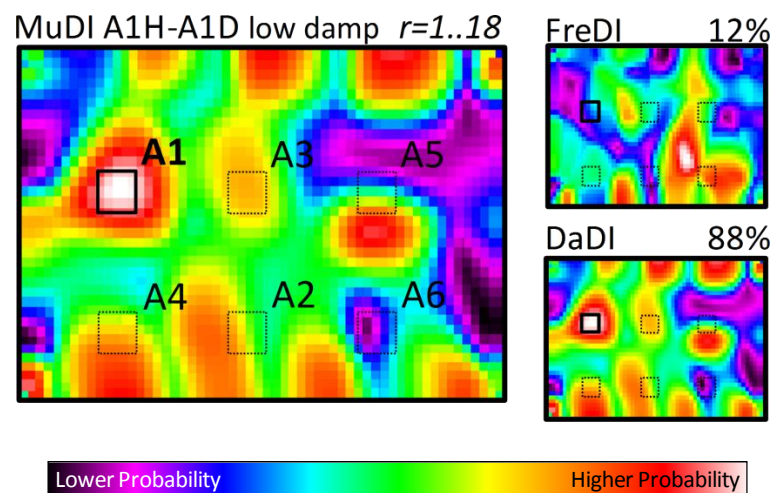


Figure 5.6: Numerical results and weighting coefficients for a damping increase of 10x in region A1.

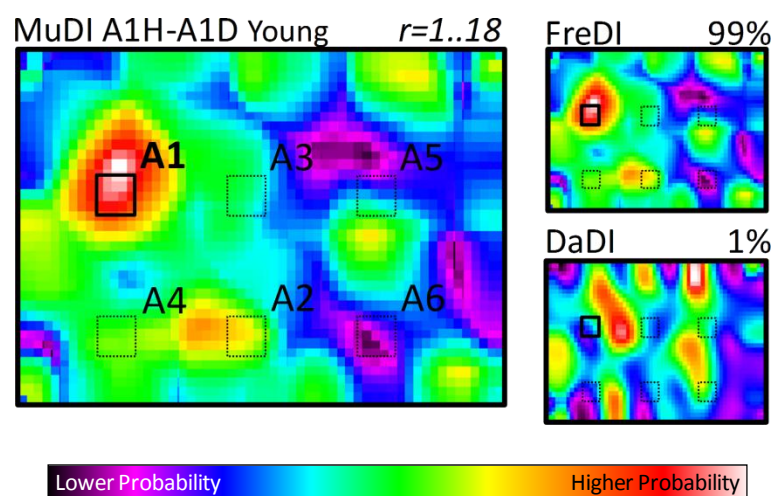


Figure 5.7: Numerical results and weighting coefficients for a reduction in the Young's modulus of 10x in region A1.

To have a perception about which is the direction the modal parameters are moving to, it is better to use the following expressions instead of (3.53) and (3.56):

$$\Delta\eta_r^D = \frac{\eta_r^D - \eta_r}{\eta_r} \times 100\%, \quad \Delta\omega_r^D = \frac{\omega_r^D - \omega_r}{\omega_r} \times 100\% \quad (5.1)$$

These equations are graphically represented in figure 5.8 for the three different damage scenarios under analysis.

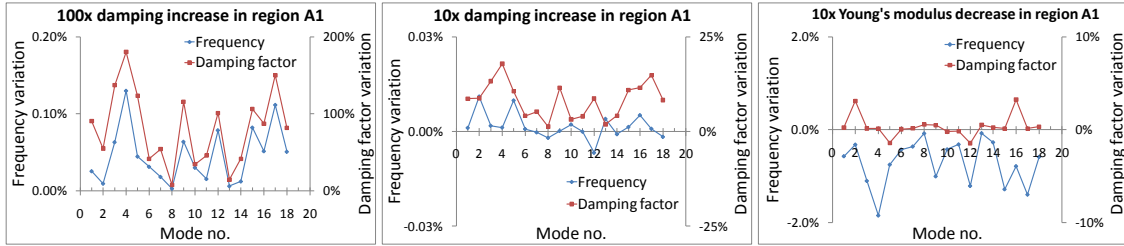


Figure 5.8: Relative differences of the damping factor and frequency for three different damage simulations in the same location.

From the above, there are some aspects that can be pointed out:

- The modal frequencies showed to be sensitive to any kind of damage, even when a local increase in the material's damping factor is imposed. Nevertheless, either for a large increase (100x) or a smaller increase (10x) in the local damping factor, these frequency shifts are still four orders of magnitude less than the modal damping factors' variations;
- For a large increase in the local damping factor (100x), the aspect of the modal frequencies' variations is very similar to the aspect of the modal damping factors' variations. A deeper analysis would be required to understand this result, especially when observing that the same similarity is not evident for a 10x increase. As a hypothesis, the way that ANSYS® deals with the structural damping may have some influence;
- For a 10x increase in the material's damping factor, the frequency presented shifts in both directions. Still, this is possibly mostly due to the order of magnitude of the involved values, which, being very low, might be the same order of magnitude of the uncertainties. The fact is FreDI, as shown in figure 5.6, is not able to correctly predict the damage location;
- Contrary to the previous point, for a 10x local reduction in the Young's modulus, the modal damping factors suffered variations that cannot be neglected. An interesting thing to notice is that these are much more significant than the modal frequency

changes for a 10x increase in the material's damping factor that suffered both from positive and negative fluctuations.

5.2.2.4 Multi-damage scenarios

The rationale behind this work was developed for scenarios with one damage location at each structural component. But, in order to understand if this could be something that could deserve further attention in the future, an attempt was made to apply the method to scenarios with two damaged areas. Three tests were conducted in which damping was increased 100x in two regions simultaneously: regions A1-A2, regions A1-A4 and regions A4-A5.

A total of 18 mode shapes was considered, in the range of 0 to 800 Hz. Results are presented in figure 5.9.

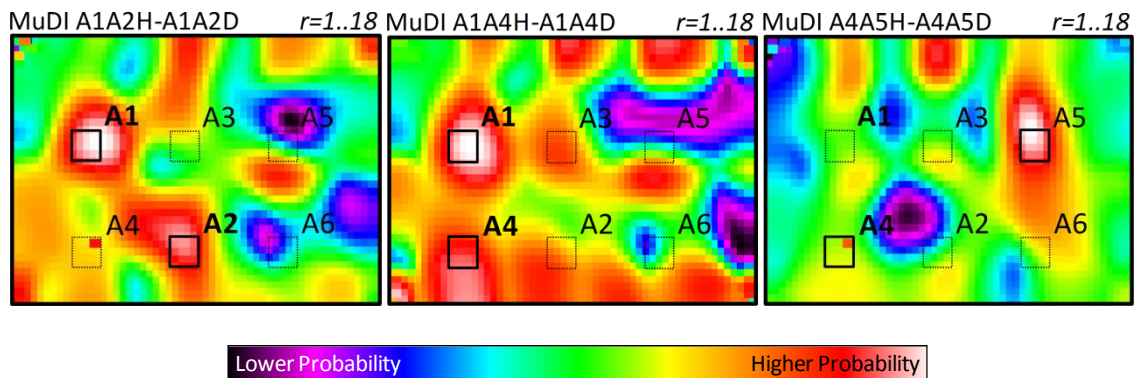


Figure 5.9: Numerical results for the multi-damage scenarios.

Except for case A4-A5 where a false-negative is unequivocal, the results suggest that, albeit further improvements are of course required, even for dual-damage scenario the proposed index might work for many cases as well.

The damage prediction in location A4 (being it present) does not stand out as it happens for other locations. This was expected to happen, since it was observed in examples with single damage as well. Again, this difference of sensitivity from one region to another is a possible consequence of the type and amount of modes available for computing the PSFs.

On the other hand, it is reasonable to assume that multi-damage scenarios, although probably giving some more false-positives, will have a tendency to increase more significantly the amount of false negatives, tending to highlight a location over another.

5.2.3 Final remarks

It may be observed that, in the studied examples, false-positives are more likely to occur rather than false-negatives, but in general the results are encouraging, since MuDI is a probability indicator (again, in the sense of likelihood) and generally shows a large value at the effective locations.

However, it must not be forgotten that these are numerical results only and that experimental evidence is still needed for settling more consistent conclusions.

5.3 Experimental examples

5.3.1 Damaging the specimens

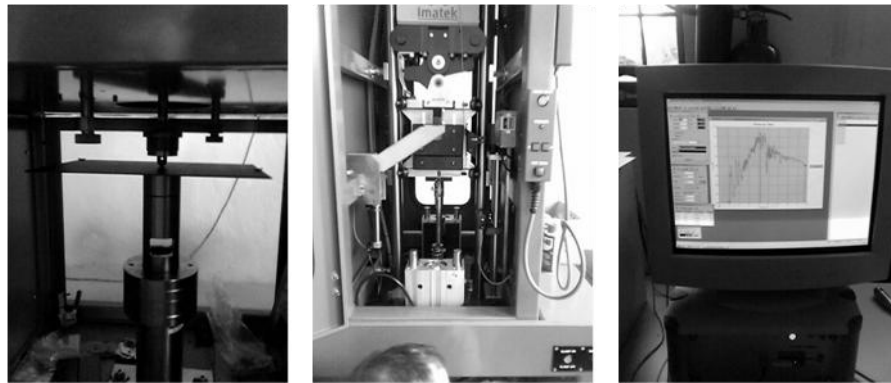


Figure 5.10: IMATEK® impact test machine photos.

Damage was introduced in several different ways, in order to reproduce real life unpredictable damage scenarios. Plates A1H and A2H were at first subjected to one impact in an IMATEK® impact testing machine from Escola Superior de Tecnologia de Abrantes (ESTA) (figure 5.10), turning the plates into damaged states A1D and A2D.

It was the purpose of this work to introduce BVID into the specimens; in other words, the impacts should be “low” to “medium” energy impacts. To qualify the impacts in such a way implies access to information that was not accessible at the time. A trial and error procedure was followed using defective plates that were manufactured using the same procedure and different indentator and drop heights. In the end, it was decided that a 15mm diameter hemispheric indentator with a total mass of 2.485kg dropped from a 275mm and a 225 mm height for, respectively, plates A1H and A2H, would produce the type of damage being looked

for. The plates were supported on a 50.8mm diameter aluminium cylinder with 12.1mm wall's thickness.

Considering that other authors (for instance, Abrate (1998) or Rilo *et al.* (2006)) assessed the similitude of impact results with those obtained from quasi-static loading, the damage was first introduced into plate A5H by quasi-static loading using a press machine, turning it into damaged state A5D. To obtain several degrees of damage for the same specimen, it was necessary to increase the severity of the damage already introduced for specimen plates type 'A' and this was done using the same press machine.

With respect to specimen plates' type B, plate B1H was subjected to quasi-static loading in a bench screw with an aluminium cylinder as indentator and sellotape roll (figure 5.11). Differently, plate B4H was subjected to impacts around the same spot.

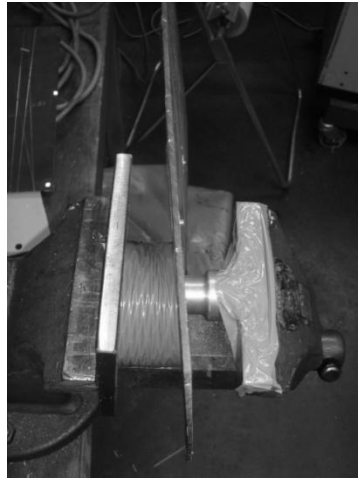


Figure 5.11: Damage introduction into specimen plate B1H.

To decide the locations for the damage that would provide good case studies, the mode shapes in the 0 to 400 Hz frequency range were superimposed and the coordinates for introduction of damage in plates A1H and A2H were chosen in such a way they would be close to the nodal lines of some modes and the anti-nodal lines of other modes. As a first approach, this seemed to be a reasonable choice for validation of the proposed technique since the algorithm is based on the premise that different modes have different sensitivities to damage. In all the other cases the introduction of damage did not have this in mind and can be seen as random choices.

Figures 5.12 and 5.13 show the overlap of the modal nodal lines (up to 400 Hz), the locations of the damage and of the measurement transducers. Damage locations identified with a mark (A2', A5' and B4') are obtained through a 180° rotation of the plate.

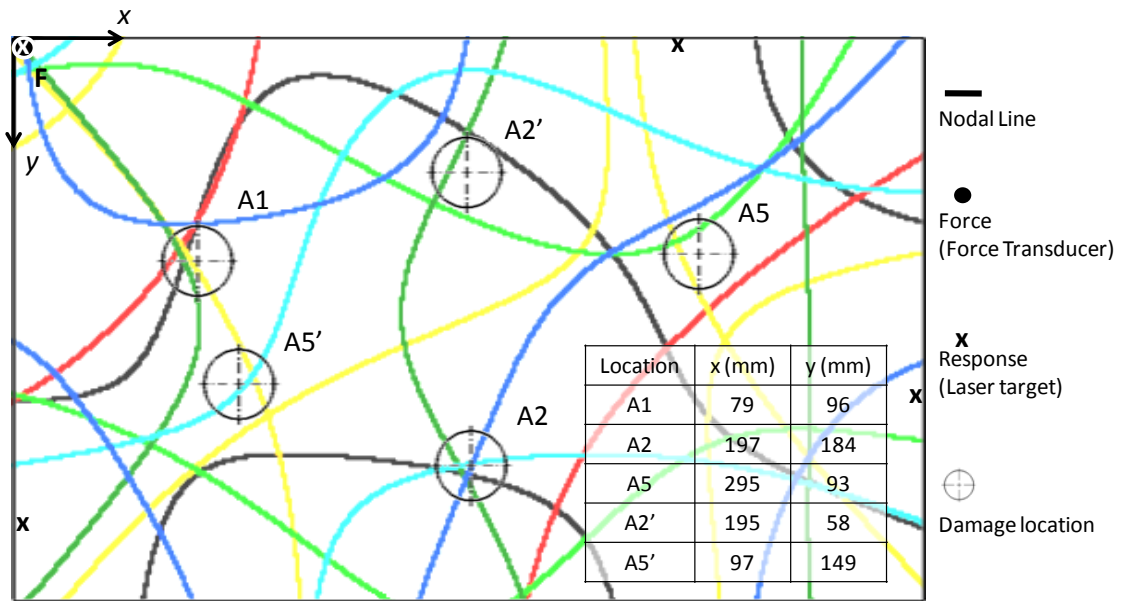


Figure 5.12: Experimental damage locations – specimen plates type 'A'.

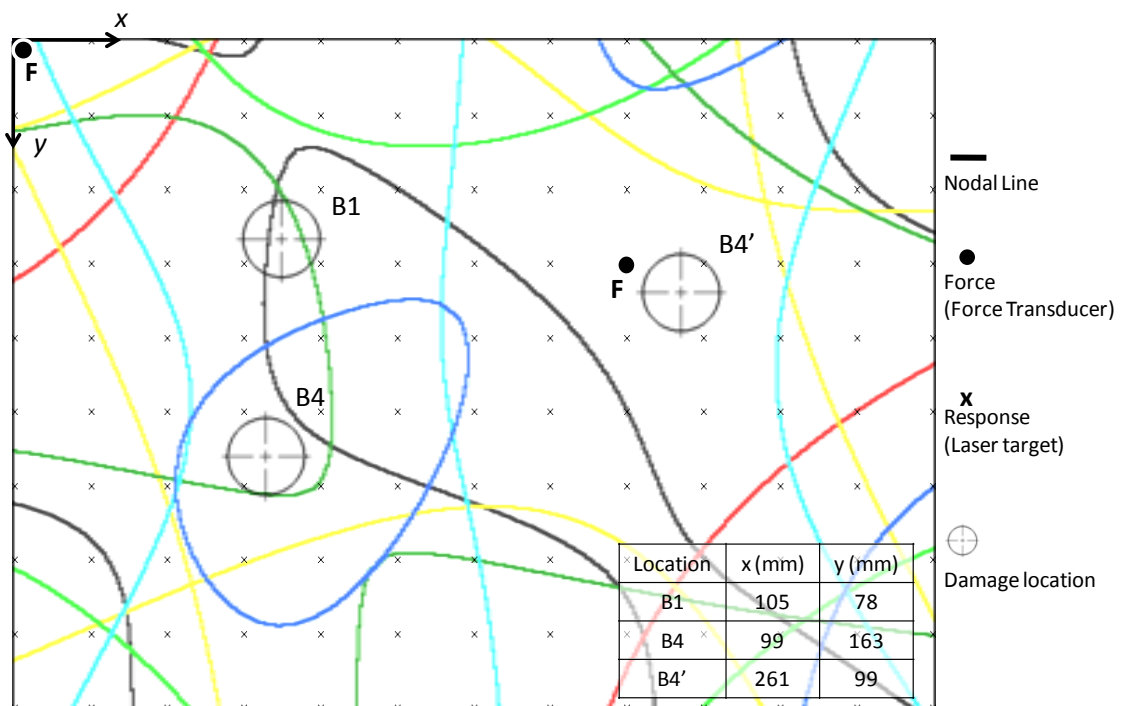
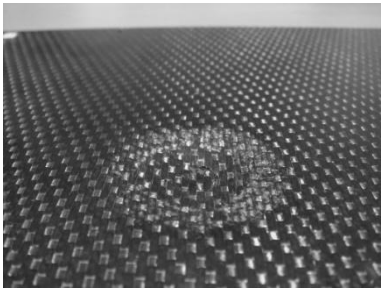
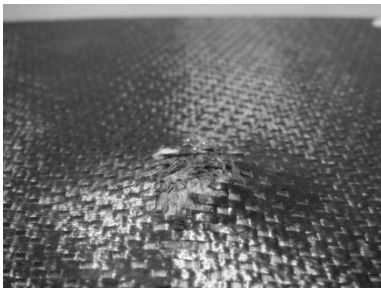
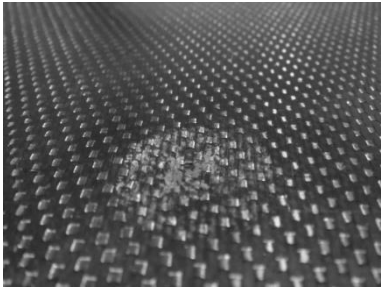
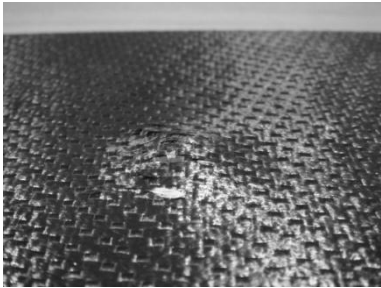
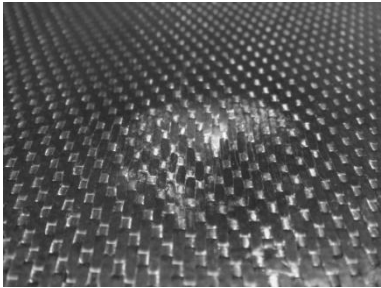
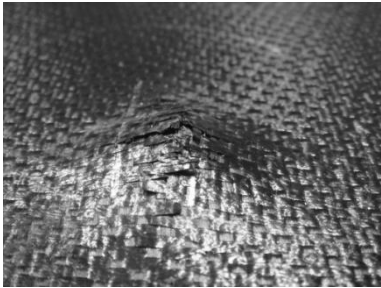
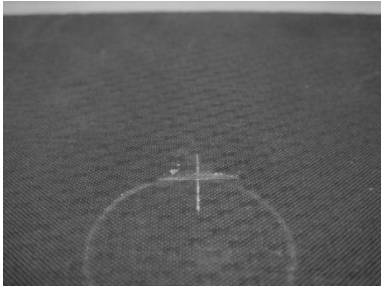
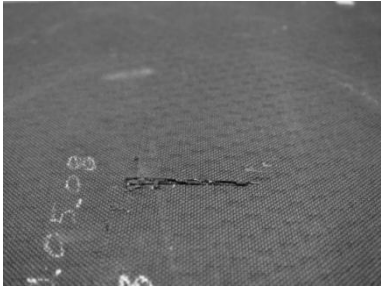

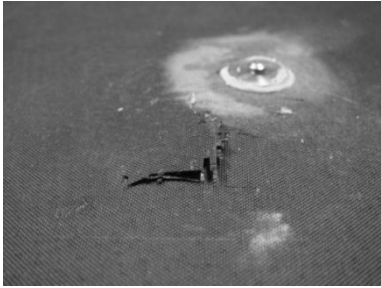


Figure 5.13: Experimental damage locations – specimen plates type 'B'.

In the case of specimen plates type 'A', only 4 responses were measured, using a Dual-channel LDV, as it is also represented in figure 5.12. The response locations are marked with crosses. Exception made to the direct FRF, all the other responses are measured away from nodal lines (in the 0 to 400 Hz frequency range) to avoid missing some modes. In the case of specimen plates type 'B' this did not represent a concern, since a Scanning LDV was used, covering a total of 143 response locations (figure 5.13).

Table 5.1: Snapshots of the final damage case in the loaded specimen plates (the images scales may not be exactly the same from case to case. All the photos were taken from around the same distance of 8 cm).

Case	Indentation side	Opposite side
A1DD		
A2DD		
A5DD		
B1D		
B4D		

Snapshots of the final damage in the involved specimens are shown in table 5.1. Specimen plates type 'A' are thinner ($\cong 2\text{mm}$) laminates. This is what is believed to be the main reason for damage not being the typical BVID as it seems to be for specimen plates type 'B', where damage is imperceptible on the indented side although it can be clearly seen on the opposite side.

In summary, it may be said that 2 experimental situations were studied:

- "Light" damage: cases A1D, A2D, A5D, B1D and B4D;
- "Heavy" damage: cases A1DD, A2DD and A5DD.

Attempts were made to characterise damage with other non-destructive non-vibration based techniques, with the aim of visualising the delaminated area and affected layers. A C-SCAN³⁶ was used, consisting on the immersion of the specimens into water and the scanning of the entire area with an ultrasonic probe. Yet, several problems were encountered. Specimen plates type 'A' are quite thin, needing higher frequency probes that were not available. The ultrasonic resulting images for specimen plates type 'A' are shown in figure 5.14. Although the used probe was not the most adequate (thus giving poor results), these images show similar features to pictures from Vaidya (2008).

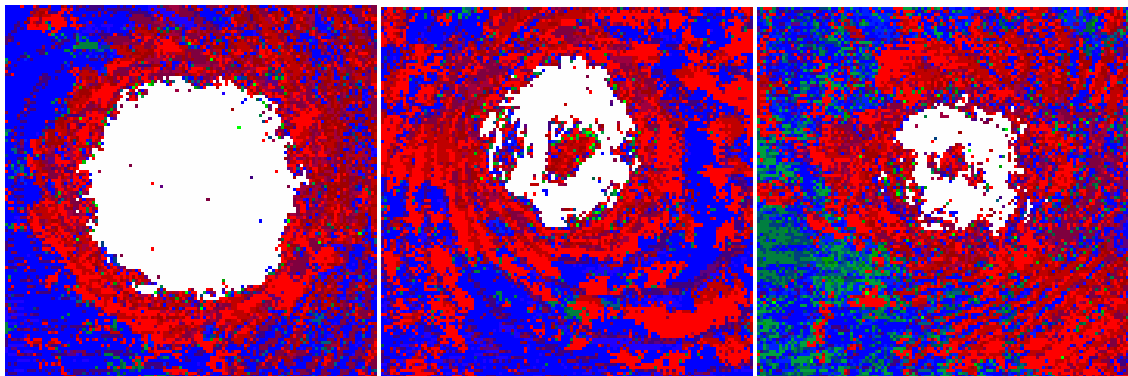


Figure 5.14: From left to right: ultrasonic imaging of specimen plates' cases A1DD, A2DD and A5DD.

³⁶ A C-SCAN is a through-thickness, ultrasonic, non-destructive inspection technique for composite materials. Among other faults, it is able to find voids, delaminations or the state of the resin cure.

5.3.2 Results³⁷

5.3.2.1 Modal parameters interpretation

The modal parameter interpretation, which will allow identifying if slight variations in the dynamic response are related or not to damage, is the core of this work.

The author's first approach was to compare results obtained for a "prototype" plate called A0 before and after introducing damage. This plate was the very first to be manufactured for this research work as a way for practicing and finding problems related to the manufacturing process of the specimens. Visible damage was afterwards introduced successively with quasi-static loading. The dynamic tests were done using 8 modes in the 0 to 400Hz frequency range. An earlier version of BETAlab[®] was used for the modal parameter identification. Results are shown in figure 5.15.

The major conclusions to be drawn from appreciation of these pictures are the following:

- The FRF functions for the same structure in different damage states are coherent;
- The damage introduces slight shifts in the modal frequencies, for which the largest variation observed was up to 2% only – this is in the same order of magnitude of the frequency shift observed for the numerical example in which the Young's modulus was locally decreased by 10 times (section 5.2.2.3, figure 5.8);
- The modal damping factors suffered important changes, showing variations over 30% for some modes (3rd, 4th and 8th).

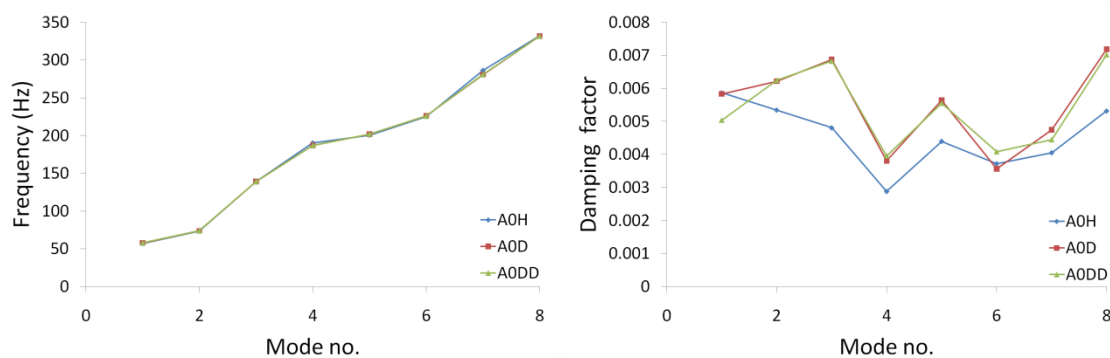
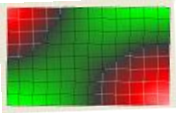
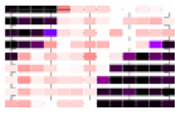
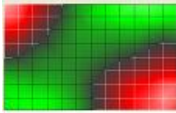
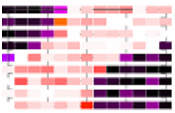
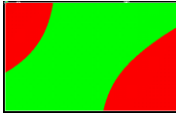
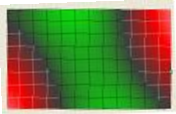

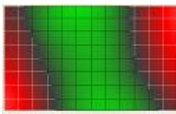

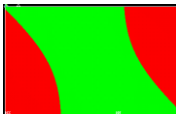
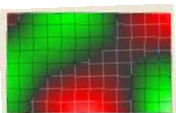
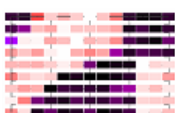

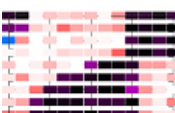




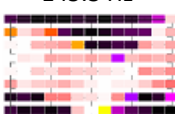
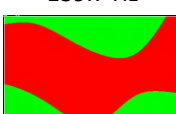

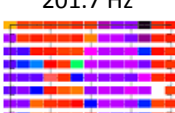

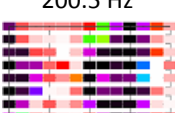





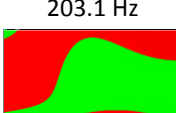

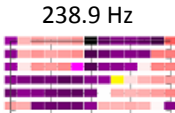


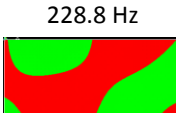

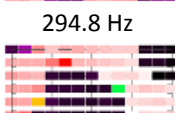
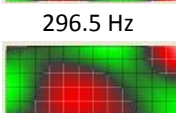
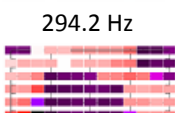



Figure 5.15: Frequency and damping between cases A0H, A0D and A0DD.

³⁷ All the predictions for the damage locations were computed following the method described in section 3.6.

For the other plates type 'A', a comparison was established between the undamaged and damaged states of specimen in order to understand if the mode shapes would present significant changes as a consequence of damage. It was observed that damage only introduces very slight variations that can hardly be noticed. Some illustrating results are shown in table 5.2, for the case A1H-A1D.

Table 5.2: Comparison between experimental and numerical modes for specimen plates A1H and A1D (first 8 modes in the 0 to 400Hz frequency range).

Mode no.	A1H		A1D		Numerical (FE)
	Polytec	BETAlab	Polytec	BETAlab	Ansys S63 45x60
1	 63.5 Hz	 61.8 Hz	 63.0 Hz	 61.6 Hz	 61.7 Hz
2	 78.5 Hz	 77.8 Hz	 78.5 Hz	 77.9 Hz	 74.7 Hz
3	 140.5 Hz	 145.7 Hz	 146.0 Hz	 145.3 Hz	 139.7 Hz
4	 199.0 Hz	 201.7 Hz	 199.5 Hz	 200.5 Hz	 190.6 Hz
5	 215.5 Hz	 215.3 Hz	 215.5 Hz	 214.6 Hz	 203.1 Hz
6	 236.5 Hz	 238.9 Hz	 238.0 Hz	 238.5 Hz	 228.8 Hz
7	 292.0 Hz	 294.8 Hz	 296.5 Hz	 294.2 Hz	 290.0 Hz
8	 355.2 Hz	 356.9 Hz	 354.5 Hz	 356.6 Hz	 350.5 Hz

All these first results showed the suitability of the previously stipulated lines. One of the postulates that was confirmed is that it is reasonable to assume that damage is likely to locally reduce the stiffness of the component (and thus a shift on the natural frequencies may happen). Furthermore, when a delamination is present, changes in damping caused by interlaminar friction are even more evident. Another assumption, that changes introduced by damage into the PSF may be considered negligible, was corroborated as well.

5.3.2.2 Specimen type 'L' (quasi-isotropic beam) damage location

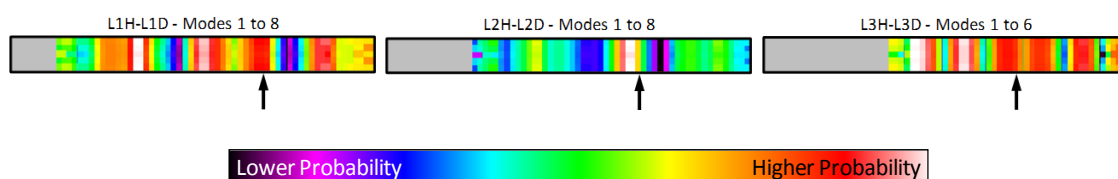


Figure 5.16: Experimental location results for specimen beam type 'L'.

Experimental testing was carried out in the 40 to 1600 Hz frequency range. Three lengths for clamping the 437mm long specimen were considered: 50mm (case L1), 100mm (case L2) and 150mm (case L3). Damage was introduced by quasi-static loading.

The probability for the location of damage is shown by the index values along the beam. Areas with a larger index value are more likely to be damage locations. A summary of the results are presented in figure 5.16 in which it can be seen that, in general, the index assumes large values close to the true damage region (pointed out with an arrow, about 123mm away from the right tip) and that false-positives are more likely to occur rather than false-negatives. However, these results cannot be considered acceptable, especially for cases L1 and L3. First, there was no information regarding a detailed experimental model with which the FE model could be validated, as it existed for the plate specimens. Despite the fact this is a very simple structure – a cantilever beam – it is not possible to guarantee that the clamp is efficiently constraining one of the beams' tips. This also means it is not possible to guarantee the adequate reproducibility of the experimental setup and thus the results may be largely influenced by external variables that are not possible to control. Furthermore, the small amount of available modes may be reducing the performance of the method.

However, the main reason behind the choice for using a beam at this stage is related to the suspicion that nonlinear effects may arise in the presence of damage. Tests were made using beams L1H and L1D. The input force was controlled using the HARMONICA[®] software, which makes use of a stepped-sine excitation. Three runs, in the 40-1600 Hz frequency range were

done: input force at 0.25N, 0.5N and 1.0N. To have a quick idea of the nonlinear behaviour between each run, the slope of the acceleration with respect to the value of the excitation force was determined. If a constant zero slope is found, this means the 3 FRF's are equal. The results are presented in figure 5.17.

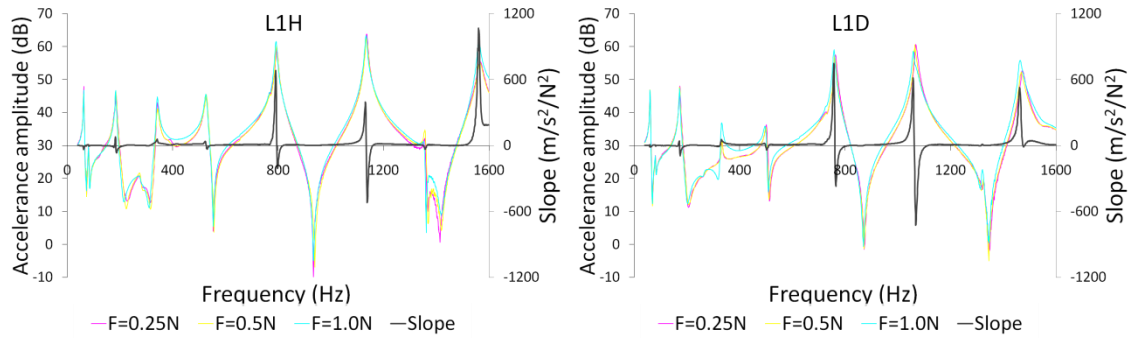


Figure 5.17: Attempt to evaluate nonlinear effects caused by damage.

The slope is represented by the grey curve. There are some modes that present large values for the slope, whereas others present small values. This could be an indicator that the experimental evaluation of non-linearities is a plausible candidate to be used as feature in the damage location procedure. Nevertheless, the large values for the non-linearities are very localized around the resonant frequencies, both for the healthy and damaged states, possibly due to experimental uncertainties that are common nearby these frequencies. Thus, in this particular case, this analysis is not reliable. A more systematic analysis on the use of experimental non-linearities could be useful for future works.

5.3.2.3 Specimen type 'A' (quasi-isotropic plate) damage location

A total of 18 mode shapes was used in this study, obtained during experimental testing in the 0 to 400 Hz and 0 to 800 Hz frequency ranges. Damage regions considered were A1, A2, A5 and their symmetric regions A2' and A5'. In some of the cases, damage suffered an increase by means of quasi-static loading. The damage locations were already shown in section 5.3.1 (figure 5.12).

The probability for the location of damage is shown by the index values along the plate. Areas with a larger index value are more likely to be damage locations. A summary of the results are presented in figure 5.18 in which it can be seen that, generally, the index assumes larger values close to the true damage region and that it seems that false-positives are more likely to occur rather than false-negatives.

However, figure 5.18 does not show results for the case in which A1H is involved. This is due to the fact that case A1H only was measured in the 0 to 400 Hz frequency range. Thus, the index was tested using what it shall be called as the *lower order modes*, corresponding to the 0 to 400 Hz frequency range with 8 modes only. Results for all cases are presented in figure 5.19.

Observation of figure 5.19 shows that not only the amount of available modes is important, but also the lower order modes are necessary in damage location techniques. In fact, while using the same amount of modes, most of the related cases are not very different from each other with respect to the damage location, and the probability area does not seem to be much sparser. This raises the question of what is the contribution of *higher order modes* in the results. To answer this question, the index was again plotted in figure 5.20, but this time in the 400 to 800 Hz frequency range.

It seems that, when used separately, higher order modes tend to provide several false-positives worsening the damage prediction than when lower order modes are used alone. This judgement is obviously dangerous and it should be stressed out that there is not enough data at this stage to formulate definitely such a conclusion, as no deeper analysis was made in order to understand how the choice of modes affect the results or to determine the optimal amount of modes to be used. As pointed out further ahead, another study would be required to assess the possibility of obtaining such a combination of modes (for a given specimen) that would allow for a uniform (or as close as possible to it) sensitivity across the entire specimen.

In the illustrated experimental examples, the remark that “*the use of as many modes as possible is desirable*” is not as evident as it was during the analysis of the numerical results.

However, as in the numeric simulations, the observation that some modes may be equally sensitive to different damage locations, possibly due to modal shape symmetry, is again pointed out. For instance, when considering the lower part of the frequency range (0 to 400Hz with modes 1 to 8 only), cases A2H-A2D, A2H-A2DD, A2’H-A2’D and A2’H-A2’DD are conducting to the prediction of the same damage location (A2), which is true for the first two cases but false for the other two.

Another observation that rises is how is the damage severity affecting the results: In spite of the fact that the damage was not quantified, it is clear that – as expected – the middle column on the previous figures is the one where best predictions were obtained as it corresponds to the most discrepant situation available between two states of the structure (AnH-AnDD).

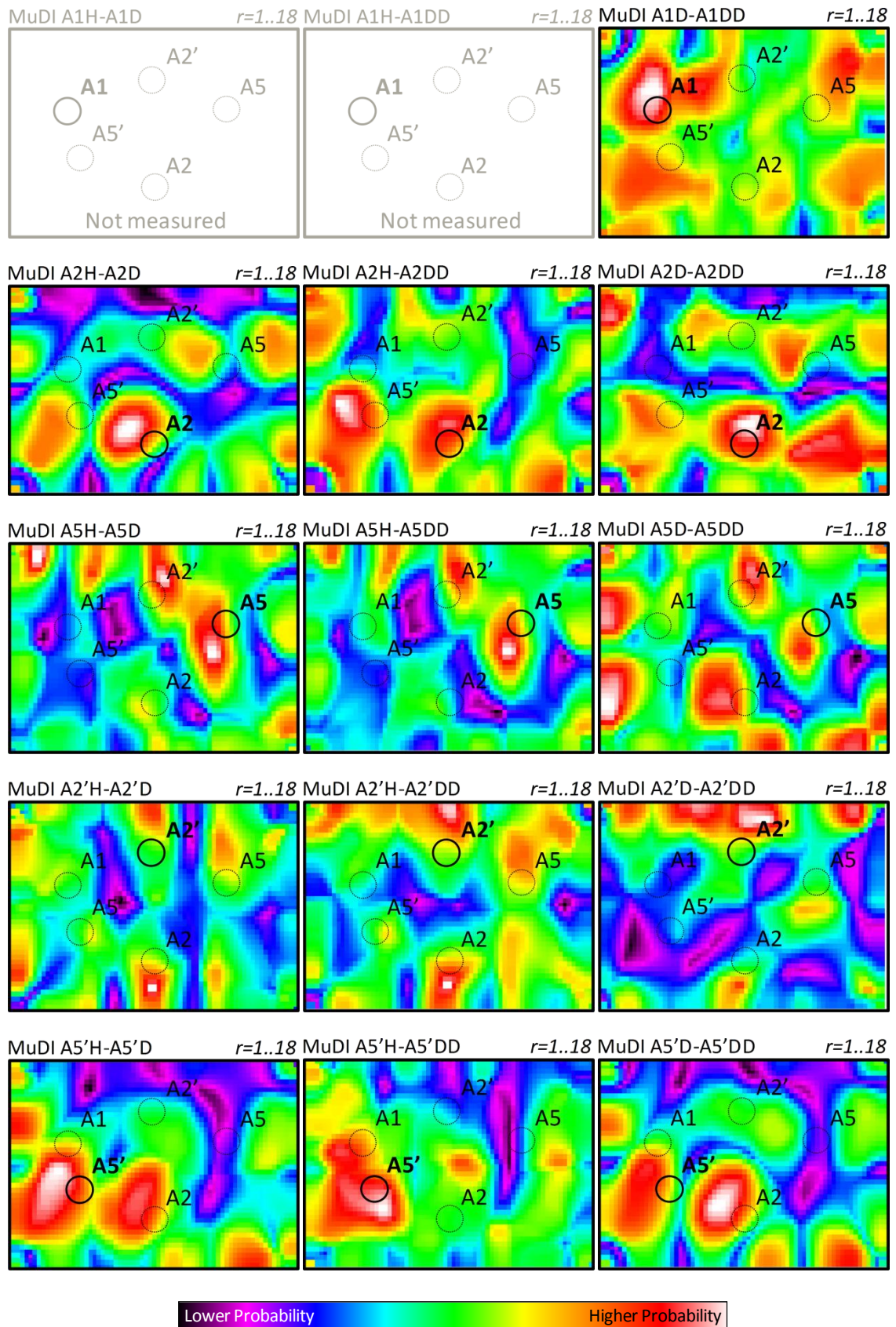


Figure 5.18: Experimental location results for specimen plate type 'A'.

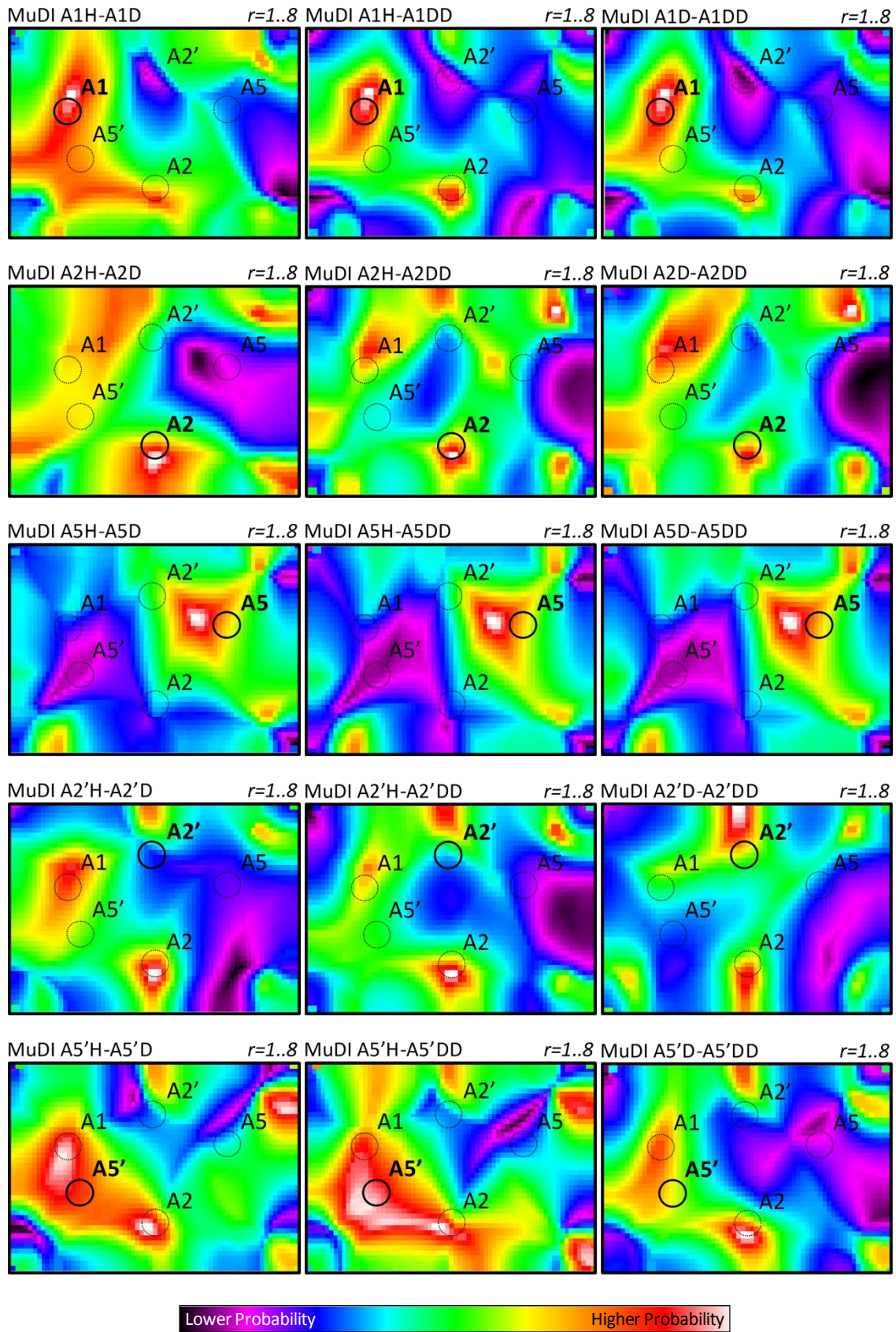


Figure 5.19: Experimental location results for specimen plate type 'A' – lower order modes.

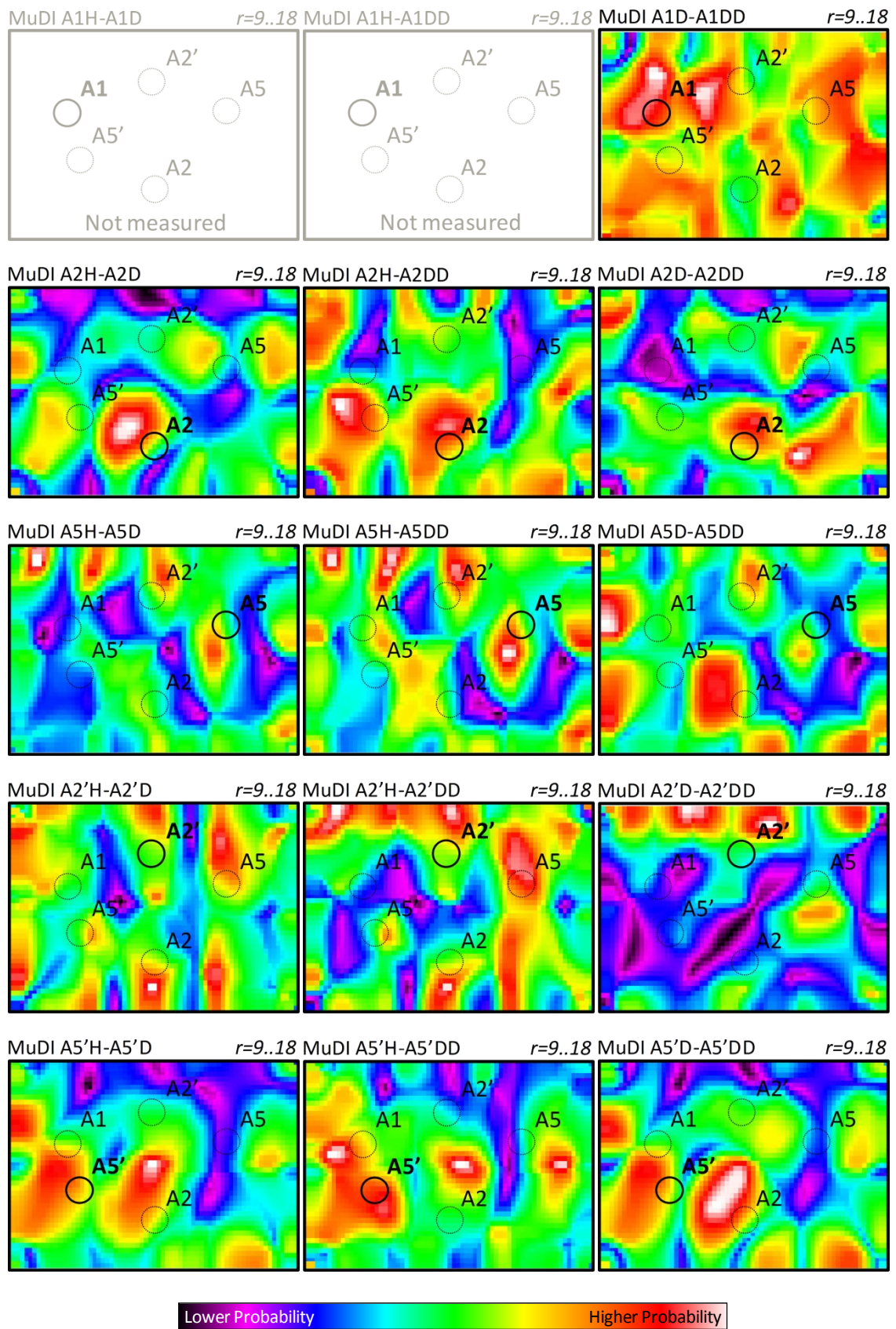


Figure 5.20: Experimental location results for specimen plate type 'A' – higher order modes.

A very simple exercise was performed, that will also help to gain deeper insight about the effects of the amount and combination of modes used in the damage location index. Every single element of figures 5.18 to 5.20 is going to be given a score (“Sc”) regarding the damage location is correctly identified or not. If the damage location is correctly identified (“OK”), it receives one point. However, it loses one point for each false-positive (“FP”) and for a false-negative (“FN”). If there is a false-negative, it is impossible to have a successful prediction (as only single damage is being considered in the studied examples), and so the final scoring for that case will always be negative (at least, -1). Nevertheless, false-positives may coexist with either false-negatives or correct predictions. The maximum scoring for a single case is +1, but there is no limit below. A score of +1 means the identification is *successful*. Scoring 0 (zero) means the correct location was identified, but there is at least another location that could be good as well; in such a case the location is said *doubtful*. Anything else (negative values) will be considered not satisfactory, and thus the prediction is called *unsuccessful* or considered a *failure*. When determining the percentage of success vs. the percentage of failure, doubtful locations will be distributed half and half between both. Despite the fact that subjectiveness was present when trying to follow this exercise rules, it could be a helpful indicator. The results are shown in table 5.3.

After analysing this table, in particular the highlighted fields, one may state the following (some remarks may have already been mentioned before):

- The most unsuccessful results were obtained when using the higher order modes (modes 9 to 18 in the 400 to 800Hz frequency range) with a percentage of success of 19% only, mainly due to the excessive amount of false-positives;
- The most successful results were obtained when using the lower order modes (modes 1 to 8 in the 0 to 400Hz frequency range) with a percentage of success of 63%. Using all the modes (modes 1 to 18 in the 0 to 800 frequency range) the percentage of success got slightly smaller, reaching 50%;
- Despite the fact the situation in which the lower order modes were used is the one that presented the most successful percentage (63%), for the particular case of damage H-DD (the most “aggressive”), that situation is no longer true if using all the 18 modes available. In fact, that is the only damage situation in which, overall, the scoring is positive (+1);
- The relative damage D-DD is the one producing the worst results, especially because it is the one presenting the least amount of successful predictions, with a total score of -9 against -6 for the two other relative damage scenarios.

Table 5.3: Scoring table of the experimental results with specimen plate type 'A'.

	H-D				H-DD				D-DD						
	OK	FP	FN	Sc	OK	FP	FN	Sc	OK	FP	FN	Sc			
	Modes 1 to 18												Sc		
A1	n.a.	n.a.	n.a.	n.a.	n.a.	n.a.	n.a.	n.a.	1	0	0	1	1	Successful	5
A2	1	0	0	1	0	-1	0	-1	1	0	0	1	1	Doubtful	3
A5	1	-2	0	-1	1	0	0	1	0	-2	-1	-3	-3	Unsuccessful	5
A2'	0	-1	-1	-2	1	-1	0	0	1	-1	0	0	-2	% Success	50%
A5'	1	-1	0	0	1	0	0	1	0	-1	0	-1	0	% Failure	50%
Sc	3	-4	-1	-2	3	-2	0	1	2	-4	-1	-3	-4		
	Modes 1 to 8												Sc		
A1	1	0	0	1	1	0	0	1	1	0	0	1	3	Successful	8
A2	1	0	0	1	1	-1	0	0	0	-1	0	-1	0	Doubtful	3
A5	1	0	0	1	1	0	0	1	1	0	0	1	3	Unsuccessful	4
A2'	0	-1	-1	-2	0	-1	-1	-2	1	0	0	1	-3	% Success	63%
A5'	1	-1	0	0	1	-1	0	0	0	-1	-1	-2	-2	% Failure	37%
Sc	4	-2	-1	0	4	-3	-1	-1	3	-2	-1	-1	-2		
	Modes 9 to 18												Sc		
A1	n.a.	n.a.	n.a.	n.a.	n.a.	n.a.	n.a.	n.a.	1	-1	0	0	0	Successful	1
A2	1	0	0	1	1	-1	0	0	0	-1	0	-1	0	Doubtful	3
A5	0	-1	-1	-2	1	-3	0	-2	0	-2	-1	-3	-7	Unsuccessful	9
A2'	0	-1	-1	-2	1	-2	0	-1	1	-1	0	0	-3	% Success	19%
A5'	0	-1	0	-1	0	-3	0	-3	0	-1	0	-1	-5	% Failure	81%
Sc	1	-3	-2	-4	3	-9	0	-6	1	-5	-1	-5	-15		
	8	-9	-4	-6	10	-14	-1	-6	6	-11	-3	-9			

The previous results do not show how the damping and frequency weighting coefficients, W_d and W_f respectively, are influencing (or being influenced by) the results. These coefficients translate the relative influence of the DaDI and FreDI on the MuDI as a measure of their relative relevance. Figures 5.21 to 5.25 exemplify how each of these indexes performs and how the FreDI and DaDI contribute to the damage location prediction from MuDI (these pictures are illustrative of any other observed cases).

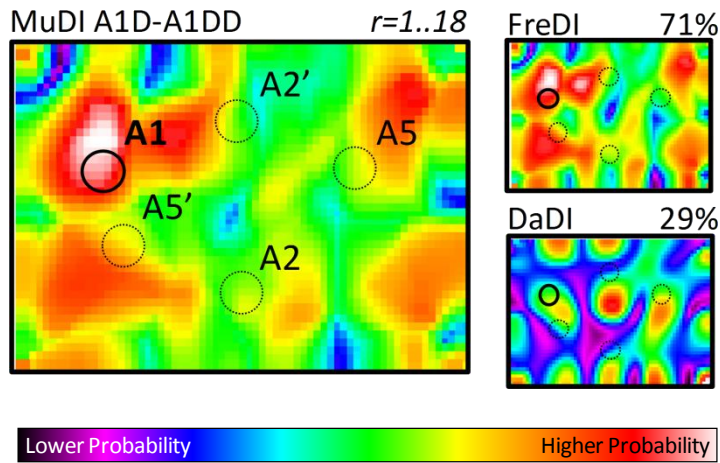


Figure 5.21: Experimental location results (MuDI, FreDI and DaDI) and weighting coefficients for damage case A1D-A1DD in the whole measured frequency range (0 to 800 Hz, modes 1 to 18).

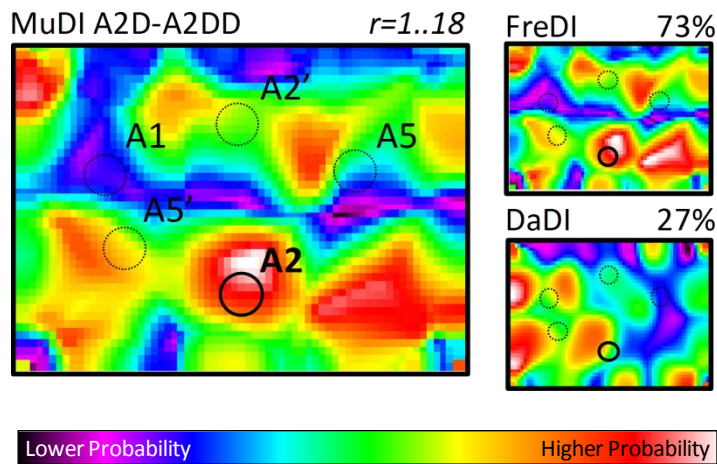


Figure 5.22: Experimental location results (MuDI, FreDI and DaDI) and weighting coefficients for damage case A2D-A2DD in the whole measured frequency range (0 to 800 Hz, modes 1 to 18).

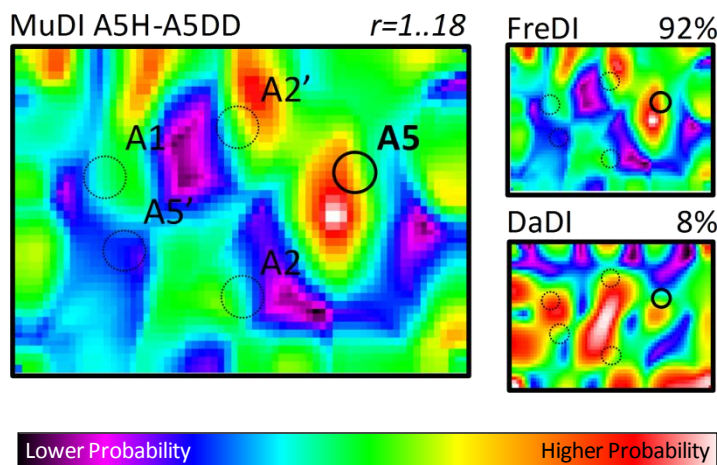


Figure 5.23: Experimental location results (MuDI, FreDI and DaDI) and weighting coefficients for damage case A5H-A5DD in the whole measured frequency range (0 to 800 Hz, modes 1 to 18).

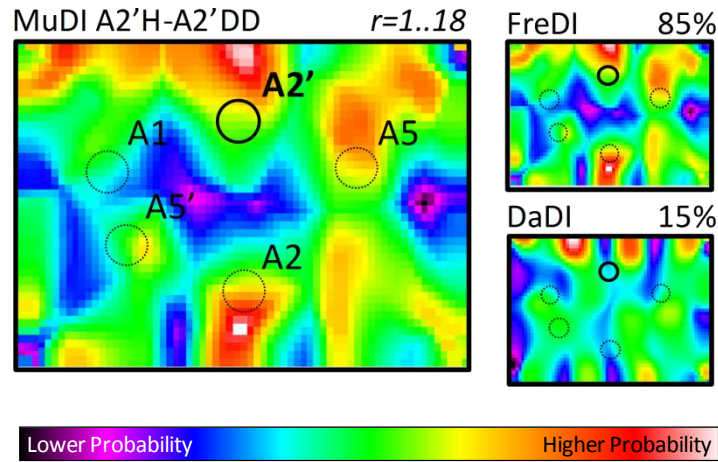


Figure 5.24: Experimental location results (MuDI, FreDI and DaDI) and weighting coefficients for damage case A2'H-A2'DD in the whole measured frequency range (0 to 800 Hz, modes 1 to 18).

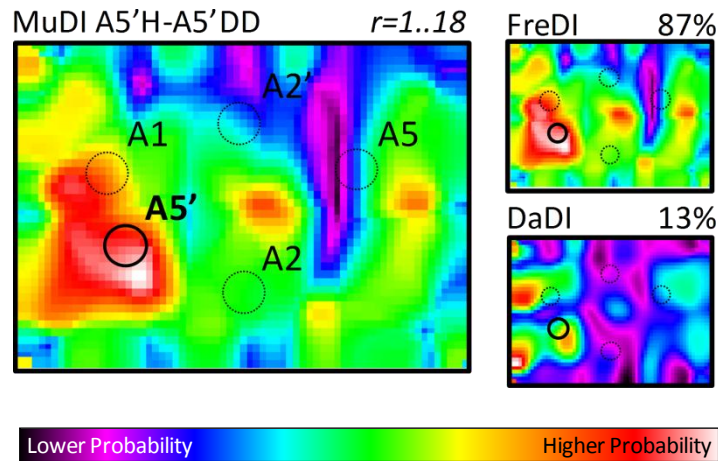


Figure 5.25: Experimental location results (MuDI, FreDI and DaDI) and weighting coefficients for damage case A5'H-A5'DD in the whole measured frequency range (0 to 800 Hz, modes 1 to 18).

As can be seen in these examples, the values of the weighting coefficients are a good measure of the relative quality of each index, as expected. Accordingly, a study about the performance of each index can be performed using the weighting coefficients.

The values of the weighting coefficients for all the results previously presented are shown in Table 5.4.

Table 5.4: Specimen plate type 'A' experimental weighting coefficients.

Damage Case	Modes 1 to 18		Modes 1 to 8		Modes 9 to 18	
	W_d	W_f	W_d	W_f	W_d	W_f
A1H-A1D			0.29	0.71		
A1H-A1DD			0.16	0.84		
A1D-A1DD	0.29	0.71	0.30	0.70	0.31	0.69
A2H-A2D	0.15	0.85	0.22	0.78	0.14	0.86
A2H-A2DD	0.14	0.86	0.19	0.81	0.09	0.91
A2D-A2DD	0.27	0.73	0.42	0.58	0.18	0.82
A5H-A5D	0.14	0.86	0.14	0.86	0.15	0.85
A5H-A5DD	0.08	0.92	0.05	0.95	0.10	0.90
A5D-A5DD	0.29	0.71	0.13	0.87	0.34	0.66
A2'H-A2'D	0.12	0.88	0.20	0.80	0.10	0.90
A2'H-A2'DD	0.15	0.85	0.12	0.88	0.16	0.84
A2'D-A2'DD	0.16	0.84	0.15	0.85	0.18	0.82
A5'H-A5'D	0.31	0.69	0.42	0.58	0.25	0.75
A5'H-A5'DD	0.13	0.87	0.12	0.88	0.13	0.87
A5'D-A5'DD	0.27	0.73	0.35	0.65	0.20	0.80

Table 5.4 by itself is difficult to analyse and interpret. Hence, to have a better insight, one column only, highlighted in grey, will be the object of the following analysis (in fact, to analyse either the damping weighting coefficient W_d or the frequency weighting coefficient W_f is irrelevant, since they are related to each other by the very simple relationship $W_f = 1 - W_d$; on the other hand, the evolution with increasing damage level is consistent whether all the modes or only some are used in the damage location). The highlighted grey column is plotted in figure 5.26 with respect to the damage case.

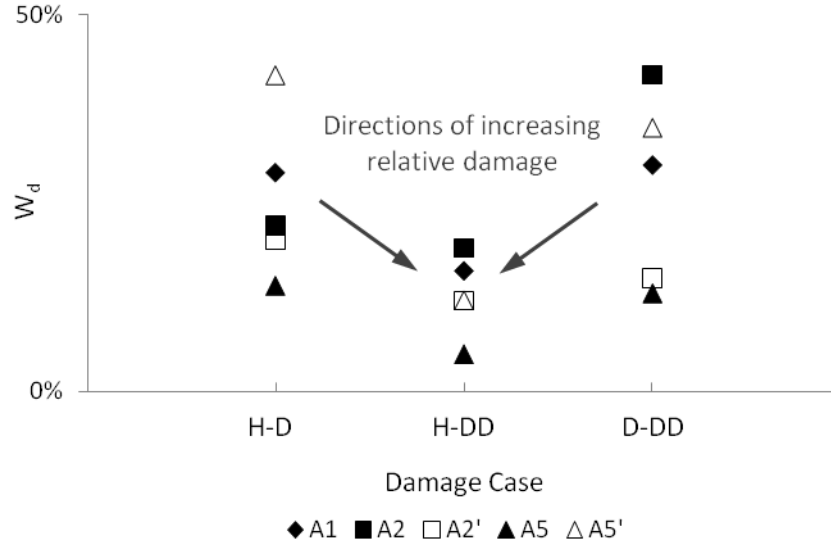


Figure 5.26: Specimen plate type 'A' experimental weighting coefficients – evolution with relative damage.

Figure 5.26 provides a hint on the usefulness of the weighting coefficients, not only in the damage location identification, but also on the quantification of damage and, possibly, even on the qualification of damage. The growth of damage noticeably leads to smaller values of the damping weighting coefficient or, in other words, to larger values of the frequency weighting coefficient.

15 damage scenarios allowed establishing 10 comparisons, and the previous observation is valid in all cases, showing coherence and consistency on the results. Damping has a more important influence on the index when the relative damage is smaller, which is to say that frequency has a more important influence on the index when the relative damage is larger. What might be happening is that by increasing damage fibres are breaking instead, having a more prominent effect rather than increasing the delamination region does. This, of course, needs further study and development in the sense that the micromechanics of the fracture should be detailed thoroughly to allow for further conclusions and eventual generalisation.

Nevertheless, from table 5.4 (or figure 5.26), it is notorious that the damping weighting coefficients W_d are much smaller than the frequency damping coefficients W_f . In fact, for the 15 damage scenarios W_d oscillated between 5% and 42%. As a consequence, MuDI is mostly governed by FreDI instead of DaDI, at least for the experimental cases studied and the way the weighing metrics were defined. In fact, observation of figures 5.21 to 5.25 show that, for the experimental studied examples, MuDI is not that different from FreDI. Still, it shows that DaDI, despite not providing good damage location predictions in any case, is giving a favourable

contribution by slightly fading eventual false-positives that would be very marked if FreDI was used alone.

Finally, it would be interesting to observe how the frequency and damping are changing with damage level. Plots of frequency and damping relative differences (equation 5.1) for specimen plates A1, A2 and A5 are presented in figure 5.27 to have a better insight about this subject.

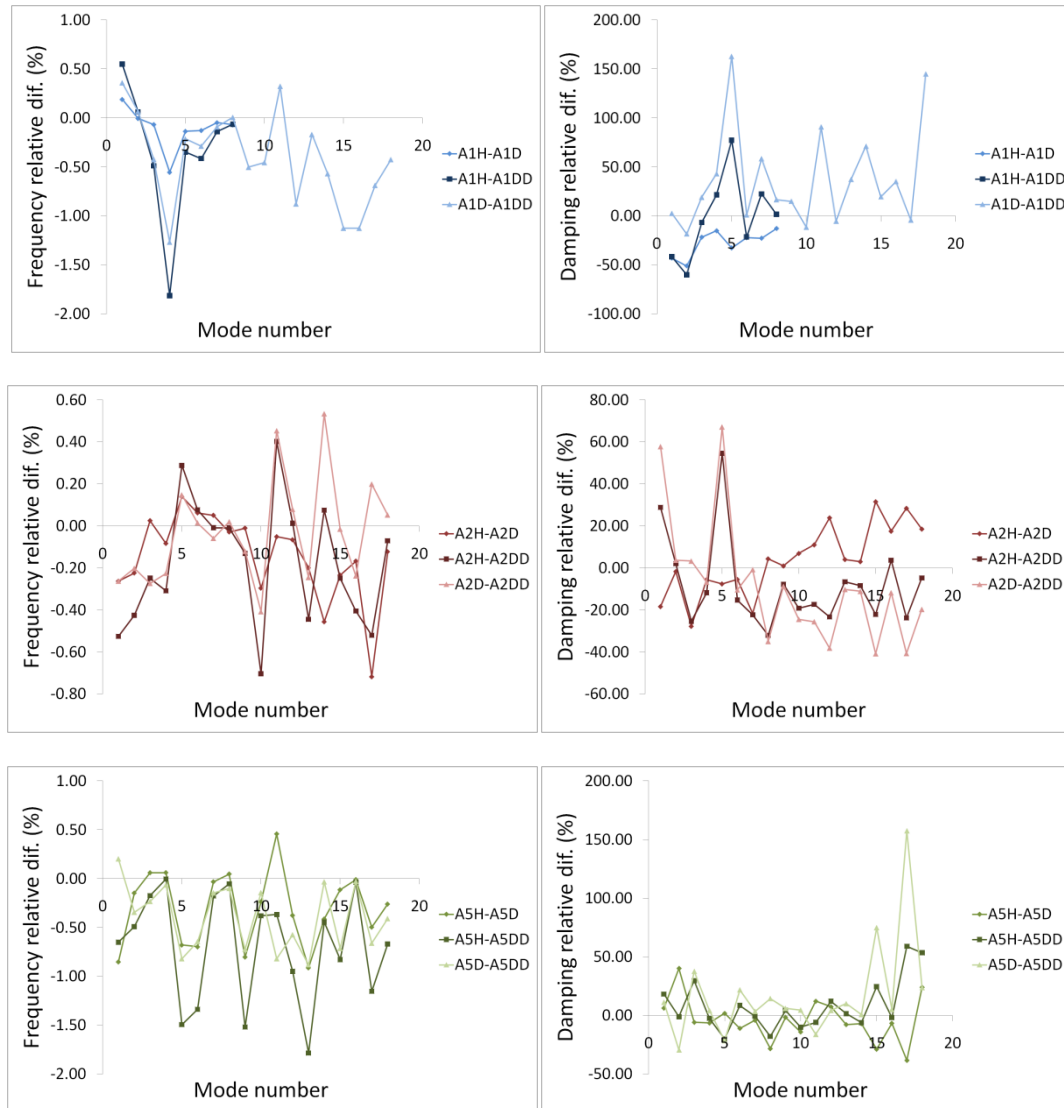


Figure 5.27: Frequency and damping relative differences for specimen plates A1, A2 and A5.

Overall, the first thing to be pointed out is that the frequency relative difference is roughly 50 times smaller than the damping relative difference (this is consistent for all the given

experimental examples)³⁸. When observing figure 5.27, the maximum (modulus) registered relative difference value for the frequency is 1.81% (case A1H-A1DD, 4th mode), approximately 100 times smaller than the maximum (modulus) registered value for the damping of 163% (case A1D-A1DD, 5th mode).

Table 5.4 and figure 5.26 show that, in general, $W_f > W_d$, which means FreDI is dominant over DaDI when computing the damage location index; in other words, the location of damage is mostly dominated by frequency, especially when the relative damage is larger. This is of course a consequence of the way the weighting coefficients are determined and adjustments could be made, as these are based on an empiric metric. The point is that the location of damage is, to a certain extent, accurately made with a strong contribution from the frequency shifts. This is, of course, consistent with the above remarks about the matter.

Another interesting thing to notice is that neither the frequency nor the damping relative differences are always moving in the same direction. Sometimes they are positive, while other times they are negative. This is of course contrary to the common assumptions that when damage occurs frequency will decrease as a consequence of the local stiffness reduction and that damping will increase as a consequence of the local friction increase. Although interesting, this matter is beyond the objectives of this work, and thus further study is needed to provide a straight explanation.

5.3.2.4 Specimen type 'B' (orthotropic plate) damage location

Experimental testing was carried out in the 0 to 1600 frequency range. Damage regions considered were B1 and B4 and the symmetric region B4'. Also, two different positions for application of the force were considered: (i) top left corner, with coordinates (7, 7) mm; and (ii) inner point, with coordinates (240, 87) mm. The force transducer has an overall mass of 21g: approximately 5% of the total mass of the structure. Thus, by changing the position of the force transducer, the modified structure will have a different dynamic behaviour, so it is reasonable to treat it as a new structure. As a consequence, 22 mode shapes were used for the case in which the force was applied at the corner, whereas only 20 modes were identified in the 0 to 1600 Hz frequency range for the case in which the force was applied at the inner point.

³⁸ The averaged value of the absolute discrepancies for the frequency was calculated in 0.374%, whereas the averaged value of the absolute discrepancies for the damping was calculated in 20.4%.

The probability for the location of damage is shown by the index values along the plate. Areas with a larger index value are more likely to be damage locations. A summary of the results are presented in figure 5.28 where, generally, the index assumes larger values close to the true damage region although a considerable amount of false-positives do appear.

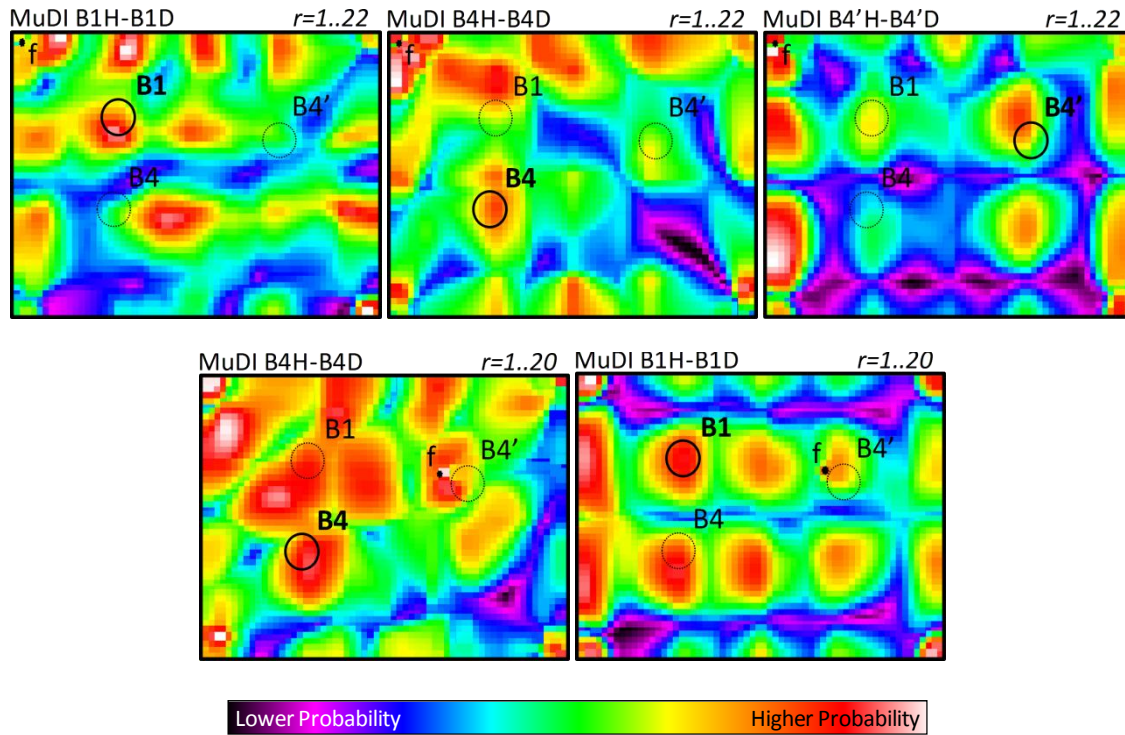


Figure 5.28: Experimental location results for specimen plate type 'B'.

It looks that the results are poorer for specimen plates type 'B' than for specimen plates type 'A'. One reason might be related to the severity of damage, which apparently is smaller for specimen plates type 'B' (table 5.1).

On the other hand, in these cases, the modal parameter identification procedure used receptance FRF's that were measured without target reflective tape. Consequently, the signal strength and the signal-to-noise ratio were lower than in the other cases, as illustrated by the sum of the 143 receptances from case B1H plotted in figure 5.29.

From the plot in figure 5.29 it is clear that the data are noisy, a tendency that increases with the frequency³⁹. This obviously did not happen for specimen plates type 'A' in which target

³⁹ It is noteworthy to remember that the CFRP plates are dark tarnished targets, not very suitable for the direct use of a LASER vibrometer in which reflectivity of the vibrating surface plays an important role in the quality of the results. Nevertheless, the results seem reliable enough to produce such estimations as those presented in figure 5.28.

reflective tape 3M Scotchlite™ was used in each of the four measurement points in order to increase the signal strength during testing.

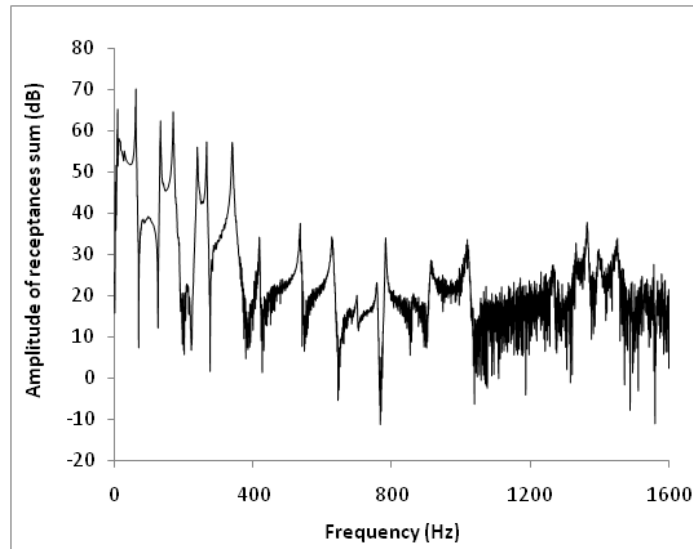


Figure 5.29: Plot of the amplitude in dB of the sum of the 143 receptance FRFs obtained with the Scanning LDV for case B1H.

Chapter 6

Conclusions and future work

6.1 Conclusions

A novel method for the location of delamination type damage in composite materials was proposed, using conventional, “low-cost” and generally easy to obtain equipment. This method is based on the modal damping factor and natural frequency variations from a reference state to a damaged state. It also makes use of the modal shapes, described by what is called a Plane Shape Function (PSF), as a tool that spatially describes the local sensitivity to damage. The damage location is assessed by an index that provides a measure of the probability (in the sense of likelihood) geometrical distribution.

It is possible to highlight the following advantages of this method:

- In theory, only one response transducer is needed (more may be required to avoid modal nodes and to reduce the uncertainty);

- It is applicable at low-cost to structures that have not been previously instrumented;
- So far, it was studied for rectangular plates and is expected to perform similarly for any bi-dimensional structure.

As disadvantages, the following can be pointed out:

- It either requires a reliable FE model or experimentally measured mode shapes;
- As other related methods, its success is strongly dependent on the combination of the mode shapes used;
- It is neither false-positive nor false-negative free, although false-positives seem more likely to occur.

Other comments to note are the following:

- It was confirmed that the frequency shifts are considerably small (less than $\approx 2\%$) and that the damping shifts can get considerably larger (up to $\approx 160\%$) when damage is present in CFRPs;
- The previous point does not invalidate that the frequency can be a good candidate to be used as feature for the damage location; it was experimentally shown that the uncertainty involved when measuring the modal frequency is small enough to allow it to be used as damage feature even for very slight variations⁴⁰;
- The uncertainty involved while measuring the modal damping factor may still be a hindrance for its use in damage location techniques;
- Both the previous points could be reasons behind the worse performance of DaDI when compared to FreDI;
- It is the belief of the author that, experimental uncertainties aside, the choice between damping and frequency as features for the damage location is mainly dependent upon the type of existing damage;
- Results show that the use of a greater amount of mode shapes to compute the damage index not always leads to better results;

⁴⁰ The environmental conditions were the same when measuring different damaged states, not introducing disturbing effects in the results.

- The modal sensitivity differences from a damage location to another are used in the method but also imply differences in its the performance for different damage locations.

Further research is still required, however, in order to improve the sensitivity of the method and avoid both false-positives and false-negatives. It is the belief of the author that further developments of this technique will allow both to provide a measure of the severity of damage and to distinguish between delamination and fibre breakage in CFRPs.

6.2 Future work

In order to improve the research developed in this work, some questions must be answered and some unfulfilled goals still deserve further developments. For example, the uncertainty in measuring the modal damping is still a drawback that is required to be overcome before damping can be more effectively used as feature in vibration-based damage detection.

From the questions that arose during this work, there are some suggestions for future work that could be stressed out:

- First, the optimal combination of modes to be used for computing the damage index is still a challenge worthy of attention. An optimization algorithm could be developed in order to automatize the choice of the best combination of modes so that the damage location prediction can be improved;
- A second objective is to make a methodical study in the pursuit of the PSF that better suit each of the location indexes (FreDI and DaDI) and how to customize it accordingly to particularities of each application, since many other PSF functions can be defined from the specimen's deformation;
- A third goal, related to the previous one, is to understand if the evolving direction of the modal parameters (damping factors and natural frequencies) can be treated the same way, i.e., if it is reasonable to consider the contribution of a damage increasing parameter the same way as a decreasing one;
- A fourth target is to quantify the severity of damage (or at least, to classify the type of damage) by improving the weighting metric.

To fulfil these major goals, there are of course experimental activities that must be performed over new test specimens, such as:

- To introduce damage in a more controlled way, i.e., using quasi-static force-displacement tests;
- To introduce a wider and quantified range of damage levels at the same location of similar specimens;
- To characterize delaminated damage through its thickness and area with a C-SCAN and relate it with the parameters involved;
- To test the method in-service in a real larger structure using Operational Modal Analysis (OMA) techniques.

References

- 1 "ABAQUS® 6.5 Theory Manual"(2007), *Version 6.5 Documentation for ABAQUS*, Dassault Systèmes Corp.
- 2 Abrate, S. (1998), "Impact on Composite Structures", Cambridge University Press.
- 3 Adams, R. D., Cawley, P., Pye, C. J. and Stone, B. J. (1978), "A Vibration Technique for Non-Destructively assessing the Integrity of Structures", *Journal of Mechanical Engineering Science*, Vol. 20, pp. 93-100.
- 4 Afolabi, D. (1987), "An Anti-Resonance Technique for Detecting Structural Damage", *Proceedings of the 5th International Modal Analysis Conference (IMAC V)*, London, England, UK, pp. 491-495.
- 5 Akkerman, R. (2006), "Laminate Mechanics for Balanced Woven Fabrics", *Compos B*, Vol. 37, pp. 108-116.
- 6 Aktan, A. E., Catbas, F. N., Grimmelsman, K. A. and Tsikos, C. J. (2000), "Issues in Infrastructure Health Monitoring for Management", *Journal of Engineering Mechanics*, Vol. 126(7), pp. 711-724.
- 7 Alampalli, S. (2000), "Effects of Testing, Analysis, Damage and Environment on Modal Parameters", *Mechanical Systems and Signal Processing*, Vol. 14(1), pp. 63-74.
- 8 Allemang, R. J. and Brown, D. L. (1982), "A Correlation Coefficient for Modal Vector Analysis", *Proceedings of the 1st International Modal Analysis Conference (IMAC I)*, Orlando, Florida, USA, pp. 110-116.
- 9 Alleyne, D. N. and Cawley, P. (1992), "The Interaction of Lamb Waves with Defects", *IEEE Transactions on Ultrasonics, Ferroelectrics and Frequency Control*, Vol. 39(3), pp. 381-397.
- 10 Ambu, R., Aymerich, F., Ginesu, F. and Priolo, P. (2006), "Assessment of NDT Interferometric Techniques for Impact Damage Detection in Composite Laminates", *Composites Science and Technology*, Vol. 66, pp. 199-205.
- 11 Andersen, P., Kirkegaard, P. H. and Brincker, R. (1997), "Filtering Out Environmental Effects in Damage Detection of Civil Engineering Structures", *Proceedings of the 15th International Modal Analysis Conference (IMAC XV)*, Orlando, Florida, USA, pp. 905-911.
- 12 Angelidis, N. and Irving, P. E. (2007), "Detection of Impact Damage in CFRP Laminates by means of Electrical Potential Techniques", *Composites Science and Technology*, Vol. 67, pp. 594-604.
- 13 "ANSYS® 11 Elements Reference Manual"(2007), *Release 11.0 Documentation for ANSYS*, Swanson Analysis Systems Inc.
- 14 "ANSYS® 11 Structural Guide"(2007), *Release 11.0 Documentation for ANSYS*, Swanson Analysis Systems Inc.
- 15 "ANSYS® 11 Theory Reference Manual"(2007), *Release 11.0 Documentation for ANSYS*, Swanson Analysis Systems Inc.
- 16 Asmussen, J. C., Brincker, R. and Ibrahim, S. R. (1999), "Statistical Theory of the Vector Random Decrement Technique", *Journal of Sound and Vibration*, Vol. 226(2), pp. 329-344.
- 17 Avitable, P. (2005), "I know that certain shaker excitations have different characteristics – but which is the best to use?" Society for Experimental Mechanics (SEM), Experimental Techniques.

- 18 Bamnios, Y., Douka, E. and Trochidis, A. (2002), "Crack Identification in Beam Structures using Mechanical Impedance", *Journal of Sound and Vibration*, Vol. 256(2), pp. 287-297.
- 19 Barnett, V. and Lewis, T. (1994), "Outliers in Statistical Data", John Wiley & Sons, Ltd.
- 20 Basseville, M., Abdelghani, M. and Benveniste, A. (2000), "Subspace-based Fault Detection Algorithms for Vibration Monitoring", *Automatica*, Vol. 36, pp. 101-109.
- 21 Battipede, M., Ruotolo, R. and Surace, C. (2001), "Damage Detection of Plate-like Structures", *Proceedings of the 4th International Conference on Damage Assessment of Structures (DAMAS 2001)*, Cardiff, Wales, UK, pp. 27-34.
- 22 Bernal, D. (2000), "Extracting Flexibility Matrices from State-Space Realizations", *Proceedings of the European COST F3 Conference on System Identification and Structural Health Monitoring*, Madrid, Spain, pp. 127-135.
- 23 Bernal, D. (2002a), "Load Vectors for Damage Localization", *Journal of Engineering Mechanics*, Vol. 128(1), pp. 7-14.
- 24 Bernal, D. (2002b), "Phase II of the ASCE Benchmark Study - Performance of the DLV Approach", *Proceedings of the 1st European Workshop on Structural Health Monitoring*, Ecole Noemale Supérieure, Cachan, Paris, France, pp. 161-168.
- 25 Bernal, D. and Gunes, B. (2002), "Damage Localization in Output-Only Systems: A Flexibility Based Approach", *Proceedings of the 20th International Modal Analysis Conference (IMAC XX)*, Los Angeles, California, USA, pp. 1185-1191.
- 26 Berthelot, J. M., Assarar, M., Sefrani, Y. and Mahi, A. E. (2008), "Damping Analysis of Composite Materials and Structures", *Composite Structures*, Vol. 85, pp. 189-204.
- 27 Berthelot, J. M. and Sefrani, Y. (2004), "Damping Analysis of Unidirectional Glass and Kevlar Fibre Composites", *Composites Science and Technology*, Vol. 64(9), pp. 1261-1278.
- 28 Betti, R. (2005), "Dynamic Methods for Damage Detection in Structures", *Advanced Course on Dynamic Methods for Damage Detection in Structures*, CISM (Centre International des Sciences Mécaniques), Udine, Italy.
- 29 Boltezar, M., Strancar, B. and Kuhelj, A. (1998), "Identification of Transverse Crack Location in Flexural Vibrations of Free-Free Beams", *Journal of Sound and Vibration*, Vol. 211(5), pp. 729-734.
- 30 Bonfiglioli, B., Strauss, A., Pascale, G. and Bergmeister, K. (2005), "Basic Study of Monitoring on Fibre Reinforced Polymers: Theoretical and Experimental Study", *Smart Materials and Structures*, Vol. 14, pp. 12-23.
- 31 Boresi, A. P., Schmidt, R. J. and Sidebottom, O. M. (1992), "Advanced Mechanics of Materials", John Wiley & Sons, Inc.
- 32 Brincker, R. and Andersen, P. (2003), "A Way of getting Scaled Mode Shapes in Output Only Modal Testing", *Proceedings of the 21st International Modal Analysis Conference (IMAC XXI)*, Kissimmee, Florida, USA, paper no. 141.
- 33 Brincker, R., Andersen, P., Kirkegaard, P. H. and Ulfkjaer, J. P. (1995a), "Damage Detection in Laboratory Concrete Beams", *Proceedings of the 13th International Modal Analysis Conference (IMAC XIII)*, Nashville, Tennessee, USA, pp. 668-674.
- 34 Brincker, R., Kirkegaard, P. H., Andersen, P. and Martínez, M. E. (1995b), "Damage Detection in an Offshore Structure", *Proceedings of the 13th International Modal Analysis Conference (IMAC XIII)*, Nashville, Tennessee, USA, pp. 661-667.

- 35 Cantwell, W. J. (2008), "Delamination Testing of Composites (Cantwell's 1st talk)", *International School on Impact Engineering of Composite Structures*, CISM (Centre International des Sciences Mécaniques), Udine, Italy.
- 36 Caponero, M. A., Pasqua, P., Paolozzi, A. and Peroni, I. (2000), "Use of Holographic Interferometry and Electronic Speckle Pattern Interferometry for Measurements of Dynamic Displacements", *Mechanical Systems and Signal Processing*, Vol. 14(1), pp. 49-62.
- 37 Carden, E. P. and Fanning, P. (2004), "Vibration Based Conditioning Monitoring: A Review", *Structural Health Monitoring*, Vol. 3(4), pp. 355-377.
- 38 Carvalho, R. J. S. (2003), "Resistência Residual de um Compósito de Matriz Epóxídica reforçado por Fibras de Carbono após Reparação", *PhD Thesis*, Instituto Superior Técnico, Technical University of Lisbon, Portugal (in Portuguese).
- 39 Castellini, P., Willemann, D. P. and Revel, G. M. (2005), "Application of a Laser Doppler Vibrometry for Structural Diagnostics on Composite Panels", *Proceedings of the 23rd International Modal Analysis Conference (IMAC XXIII)*, Orlando, Florida, USA, paper no. 371.
- 40 Cawley, P. (1997), "Long Range Inspection of Structures Using Low Frequency Ultrasound", *Proceedings of the 2nd International Conference on Structural Damage Assessment using Advanced Signal Processing Procedures (DAMAS 97)*, Sheffield, England, UK, pp. 1-17.
- 41 Cawley, P. and Adams, R. D. (1979), "The Location of Defects in Structures from Measurements of Natural Frequencies", *Journal of Strain Analysis for Engineering Design*, Vol. 14(2), pp. 49-57.
- 42 Chang, L. Y., Erickson, K. A., Lee, K. G. and Todd, M. D. (2004), "Structural Damage Detection using Chaotic Time Series Excitation", *Proceedings of the 22nd International Modal Analysis Conference (IMAC XXII)*, Dearborn, Michigan, USA, paper no. 221.
- 43 Choi, S. and Stubbs, N. (2004), "Damage Identification in Structures using the Time-Domain Response", *Journal of Sound and Vibration*, Vol. 275, pp. 577-590.
- 44 Cioara, T. G. and Alampalli, S. (2004), "Considerations on Damage Detection of a Structure using Vibration Test Data", *Proceedings of the 22nd International Modal Analysis Conference (IMAC XXII)*, Dearborn, Michigan, USA, paper no. 146.
- 45 Cole, H. A. (1968), "On-the-Line Analysis of Random Vibrations", AIAA Paper no. 68-288.
- 46 Cole, H. A. (1973), "On-line Failure Detection and Damping Measurement of Aerospace Structures by Random Decrement Signatures", NASA CR-2205.
- 47 Coppotelli, G., Di Conza, R., Mastroddi, F., Pascual, R. and Caponero, M. A. (2004), "Damage Identification in Composite Plates by Dynamic Displacement Measurements", *Proceedings of the International Conference on Noise and Vibration Engineering (ISMA 2004)*, Leuven, Belgium, pp. 417-432.
- 48 Cornwell, P. J., Doebling, S. W. and Farrar, C. R. (1997), "Application of the Strain Energy Damage Detection Method to Plate-Like Structures", *Proceedings of the 15th International Modal Analysis Conference (IMAC XV)*, Orlando, Florida, USA, pp. 1312-1318.
- 49 Cox, B. N. and Flanagan, G. (1997), "Handbook of Analytical Methods for Textile Composites", NASA CR-4750.
- 50 Curadelli, R. O., Riera, J. D., Ambrosini, D. and Amani, M. G. (2008), "Damage Detection by means of Structural Damping Identification", *Engineering Structures*, Vol. 30(12), pp. 3497-3504.

- 51 d'Ambrogio, W. and Fregolent, A. (2000), "The use of Antiresonances for Robust Model Updating", *Journal of Sound and Vibration*, Vol. 236(2), pp. 227-243.
- 52 Davies, P. and Hammond, J. K. (1984), "A Comparison of Fourier and Parametric Methods for Structural Systems Identification", *Journal of Vibration, Acoustics, Stress and Reliability in Design*, Vol. 106, pp. 40-48.
- 53 De Roeck, G. and Degrauwe, D. (2005), "Damage Identification of the Lanaye Cable-Stayed Bridge", *Proceedings of the 23rd International Modal Analysis Conference (IMAC XXIII)*, Orlando, Florida, USA, paper no. 264.
- 54 De Roeck, G., Teughels, A. and Reynders, E. (2005), "Damage Identification of Civil Engineering Structures Based on Operational Modal Data", *Proceedings of the 1st International Operational Conference on Modal Analysis (IOMAC 2005)*, Copenhagen, Denmark, pp. 115-126.
- 55 Deraemaeker, A. and Preumont, A. (2004a), "Modal Filters for Vibration Based Damage Detection", *Proceedings of the 2nd European Workshop on Structural Health Monitoring*, Forum am Deutschen Museum, Munich, Germany, pp. 844-851.
- 56 Deraemaeker, A. and Preumont, A. (2004b), "Modal Filters for Vibration Based Damage Detection", *Proceedings of the International Conference on Noise and Vibration Engineering (ISMA 2004)*, Leuven, Belgium, pp. 501-514.
- 57 Devriendt, C., De Sitter, G. and Guillaume, P. (2009), "An operational Modal Analysis Approach Based on Parametrically Identified Multivariable Transmissibilities", *Mechanical Systems and Signal Processing*, Vol. article in press(doi:10.1016/j.ymssp.2009.02.015).
- 58 Dilella, M. and Morassi, A. (2004), "The use of Anti-Resonances for Crack Detection in Beams", *Journal of Sound and Vibration*, Vol. 276, pp. 195-214.
- 59 Doebling, S. W., Farrar, C. F., Prime, M. B. and Shevits, D. W. (1996), "Damage Identification and Health Monitoring of Structural and Mechanical Systems from Changes in their Vibration Characteristics: A Literature Review", Los Alamos National Laboratory, USA.
- 60 Doebling, S. W., Farrar, C. R. and Prime, M. B. (1998), "A Summary Review of Vibration-Based Damage Identification Methods", *Shock and Vibration Digest*, Vol. 30(2), pp. 91-105.
- 61 Ewins, D. J. (1984), "Modal Testing: Theory and Practice", Research Studies Press, Ltd.
- 62 Farrar, C. R., Baker, W. E., Bell, T. M., Cone, K. M., Darling, T. W., Duffey, T. A., Eklund, A. and Migliori, A. (1994), "Dynamic Characterization and Damage Detection in the I-40 Bridge over the Rio Grande", Los Alamos National Laboratory, USA.
- 63 Farrar, C. R., Doebling, S. W. and Nix, D. A. (2001), "Vibration-based Structural Damage Identification", *Philosophical Transactions of the Royal Society of London Series A-Mathematical Physical and Engineering Sciences*, Vol. 359(1778), pp. 131-149.
- 64 Farrar, C. R., Sohn, H., Hemez, F. M., Anderson, M. C., Bement, M. T., Cornwell, P. J., Doebling, S. W., Lieven, N., Robertson, A. N. and Schultze, J. F. (2003), "Damage Prognosis: Current Status and Future Needs", Los Alamos National Laboratory, USA.
- 65 Farrar, C. R., Sohn, H. and Robertson, A. N. (2004), "Applications of Nonlinear System Identification to Structural Health Monitoring", *Proceedings of the 2nd European Workshop on Structural Health Monitoring*, Forum am Deutschen Museum, Munich, Germany, pp. 59-67.
- 66 Fasel, T. R. and Todd, M. D. (2005), "Effects of Data Acquisition and Generation on Using Upconverted Chaotic Waves for Active Structural Health Monitoring", *Proceedings of the 23rd International Modal Analysis Conference (IMAC XXIII)*, Orlando, Florida, USA, paper no. 210.
- 67 Feldman, M. (1997), "Non-Linear Free Vibration Identification via the Hilbert Transform", *Journal of Sound and Vibration*, Vol. 208(3-4), pp- 475-489.

- 68 Fox, C. H. J. (1992), "The Location of Defects in Structures: A Comparison on the use of Natural Frequency and Mode Shape Data", *Proceedings of the 10th International Modal Analysis Conference (IMAC X)*, San Diego, California, USA, pp. 522-528.
- 69 Friswell, M. I. and Mottershead, J. E. (1995), "Finite Element Updating in Structural Dynamics", Kluwer Academic Publishers.
- 70 Fritzen, C. P., Mengelkamp, G. and Guemes, A. (2002), "A CFRP Plate with Piezo-electric Actuators and Sensors as Self-Diagnosing Intelligent Structure", *Proceedings of the International Conference on Noise and Vibration Engineering (ISMA 2002)*, Leuven, Belgium, pp. 185-191.
- 71 Galvin, P. and Dominguez, J. (2005), "Modal Identification of a Pedestrian Bridge by Output-Only Analysis", *Proceedings of the 23rd International Modal Analysis Conference (IMAC XXIII)*, Orlando, Florida, USA, paper no. 63.
- 72 Golub, G. H. and Van Loan, C. F. (1983), "Matrix Computations", North Oxford Academic.
- 73 Gomes, A. J. M. A. and Silva, J. M. M. (1992), "CRACAR - A Computer Program for Detection of Cracks in Structural Elements through the Variation of their Natural Frequencies", *Internal Report*, Faculdade de Ciências e Tecnologia, New University of Lisbon, Portugal (in Portuguese).
- 74 Grisso, B. J., Martin, L. A. and Inman, D. J. (2005), "A Wireless Active Sensing System for Impedance-based Structural Health Monitoring", *Proceedings of the 23rd International Conference on Modal Analysis (IMAC XXIII)*, Orlando, Florida, USA, paper no. 236.
- 75 Grisso, B. J., Pears, D. M. and Inman, D. J. (2004), "Impedance-based Health Monitoring of Composites", *Proceedings of the 22nd International Modal Analysis Conference (IMAC XXII)*, Dearborn, Michigan, USA, paper no. 274.
- 76 Guan, H. and Karbhari, M. (2008), "Improved Damage Detection Method based on Element Modal Strain Damage Index using Sparse Measurement", *Journal of Sound and Vibration*, Vol. 309(3-5), pp. 465-494.
- 77 Guillaume, P., Hermans, L. and Van der Auweraer, H. (1999), "Maximum Likelihood Identification of Modal Parameters from Operational Data", *Proceedings of the 17th International Modal Analysis Conference (IMAC XVII)*, Kissimmee, Florida, USA, pp. 1887-1893.
- 78 Guillaume, P., Parloo, E., Verboven, P. and De Sitter, G. (2002), "An Inverse Method for the Identification of Localized Excitation Sources", *Proceedings of the 20th International Modal Analysis Conference (IMAC XX)*, Los Angeles, California, USA, pp. 1382-1388.
- 79 Guillaume, P., Verboven, P. and Vanlanduit, S. (1998), "Frequency-Domain Maximum Likelihood Estimation of Modal Parameters with Confidence Intervals", *Proceedings of the International Conference on Noise and Vibration Engineering (ISMA 23)*, Leuven, Belgium, pp. 359-366.
- 80 Gutschmidt, S. and Cornwell, P. J. (2001), "Statistical Confidence Bounds for Structural Health Monitoring", *Proceedings of the 19th International Modal Analysis Conference (IMAC XIX)*, Kissimmee, Florida, USA, pp. 193-198.
- 81 Hadi, A. S. and Ashton, J. S. (1996), "Measurement and Theoretical Modeling of the Damping Properties of a Uni-Directional Glass/Epoxy Composite", *Composite Structures*, Vol. 34, pp. 381-385.
- 82 Hamey, C. S., Lestari, W., Qiao, P. and Song, G. (2004), "Experimental Damage Identification of Carbon/Epoxy Composite Beams using Curvature Mode Shapes", *Structural Health Monitoring*, Vol. 3(4), pp. 333-353.

- 83 Hanagud, S. and Luo, H. (1997), "Damage Detection and Health Monitoring based on Structural Dynamics", *Structural Health Monitoring, Current Status and Perspectives*, Stanford University, Palo Alto, California, USA, pp. 715-726.
- 84 Harri, K., Guillaume, P. and Vanlanduit, S. (2008), "On-line Damage Detection on a Wing Panel using Transmission of Multisine Ultrasonic Waves", *NDT & E International*, Vol. 41(4), pp. 312-317.
- 85 Hatem, T. M., Foutouh, M. N. A. and Negm, H. M. (2004), "Application of Genetic Algorithms and Neural Networks to Health Monitoring of Composite Structures", *Proceedings of the 2nd European Workshop on Structural Health Monitoring*, Forum am Deutschen Museum, Munich, Germany, pp. 616-623.
- 86 He, J. and Ewins, D. J. (1985), "Analytical Stiffness Matrix Correlation using Measured Vibration Modes", *Modal Analysis: The International Journal of Analytical and Experimental Modal Analysis*, Vol. 1(3), pp. 9-14.
- 87 Hearn, G. and Testa, R. B. (1991), "Modal Analysis for Damage Detection in Structures", *Journal of Structural Engineering*, Vol. 117(10), pp. 3042-3062.
- 88 Heylen, W., Lammens, S. and Sas, P. (1998), "Modal Analysis Theory and Testing", K. U. Leuven - PMA, Belgium, Section A.6.
- 89 Hiroshi, H., Hassan, M. S. A., Hatsukade, Y., Wakayama, S., Suemasu, H. and Kasai, N. (2005), "Damage Detection of C/C Composites using ESPI and SQUID Techniques", *Composites Science and Technology*, Vol. 65, pp. 1098-1106.
- 90 Ho, Y. K. and Ewins, D. J. (2000), "On the Structural Damage Identification with Mode Shapes", *Proceedings of the European COST F3 Conference on System Identification and Structural Health Monitoring* Madrid, Spain, pp. 677-686.
- 91 Hochard, C., Aubourg, P. A. and Charles, J. O. (2001), "Modelling of the Mechanical Behaviour of Woven-fabric CFRP Laminates up to Failure", *Composites Science and Technology*, Vol. 61, pp. 221-230.
- 92 Hu, H. and Wang, J. (2009), "Damage Detection of a Woven Fabric Composite Laminate using a Modal Strain Energy Method", *Engineering Structures*, Vol. 31(5), pp. 1042-1055.
- 93 Hunt, D. L. (1992), "Application of an Enhanced Coordinate Modal Assurance Criterion", *Proceedings of the 10th International Modal Analysis Conference (IMAC X)*, San Diego, California, USA, pp. 66-71.
- 94 Ibrahim, S. R., Asmussen, J. C. and Brincker, R. (1997), "Vector Triggering Random Decrement Technique for Higher Identification Accuracy", *Proceedings of the 15th International Modal Analysis Conference (IMAC XV)*, Orlando, Florida, USA, pp. 502-509.
- 95 Ibrahim, S. R. and Seafan, A. A. (1987), "Correlation of Analysis and Test in Modelling of Structures and Review", *Proceedings of the 5th International Modal Analysis Conference (IMAC V)*, London, England, UK, pp. 1651-1660.
- 96 Inman, D. J., Farrar, C. R., Lopes Jr., V. and Steffen Jr., V. (2005), "Damage Prognosis for Aerospace, Civil and Mechanical Systems", John Wiley & Sons, Ltd.
- 97 Jacob, P. J., Desforges, M. J. and Ball, A. D. (1997), "Analysis of Suitable Wavelet Coefficients for Identification of the Simulated Failure of Composite Materials", *Proceedings of the 2nd International Conference on Structural Damage Assessment using Advanced Signal Processing Procedures (DAMAS 97)*, Sheffield, England, UK, pp. 31-40.
- 98 Jauregui, D. V. and Farrar, C. R. (1986a), "Damage Identification Algorithms Applied to Numerical Modal Data from a Bridge", *Proceedings of the 14th International Modal Analysis Conference (IMAC XIV)*, Dearborn, Michigan, USA, pp. 119-125.

- 99 Jauregui, D. V. and Farrar, C. R. (1986b), "Comparison of Damage Identification Algorithms on Experimental Modal Data from a Bridge", *Proceedings of the 14th International Modal Analysis Conference (IMAC XIV)*, Dearborn, Michigan, USA, pp. 1423-1429.
- 100 Johnson, E. A., Lam, H. F., Katafygiotis, L. S. and Beck, J. L. (2004), "The Phase I IASC-ASCE Structural Health Monitoring Benchmark Problem using Simulated Data", *ASCE Journal of Engineering Mechanics*, Vol. 130, pp. 3-15.
- 101 Johnson, T. J., Brown, R. L., Adams, D. E. and Schiefer, M. (2004), "Distributed Structural Health Monitoring with a Smart Sensor Array", *Mechanical Systems and Signal Processing*, Vol. 18, pp. 555-572.
- 102 Jones, D. I. G. (2001), "Handbook of Viscoelastic Vibration Damping", John Wiley & Sons, Ltd.
- 103 Jones, R. M. (1999), "Mechanics of Composite Materials", Taylor & Francis.
- 104 Kessler, S. S., Spearing, S. M. and Atalla, M. J. (2002), "In-Situ Damage Detection of Composites Structures using Lamb Waves Methods", *Proceedings of the 1st European Workshop on Structural Health Monitoring*, Ecole Noemale Supérieure, Cachan, Paris, France, pp. 374-381.
- 105 Keye, S., Rose, M. and Sachau, D. (2001), "Localizing Delamination Damages in Aircraft Panels from Modal Damping Parameters", *Proceedings of the 19th International Modal Analysis Conference (IMAC XIX)*, Kissimmee, Florida, USA, pp. 412-417.
- 106 Kim, B. H., Stubbs, N. and Park, T. (2005), "Flexural Damage Index Equations of a Plate", *Journal of Sound and Vibration*, Vol. 283, pp. 341-368.
- 107 Kim, B. S., Yoo, S. H. and Yeo, G. H. (2005), "Charaterization of Crack Detection on Gusset Plates using Strain Mode Shapes", *Proceedings of the 23rd International Modal Analysis Conference (IMAC XXIII)*, Orlando, Florida, USA, paper no. 150.
- 108 Kim, J. H., Jeon, H. S. and Lee, C. W. (1992), "Application of the Modal Assurance Criteria for Detecting and Locating Structural Faults", *Proceedings of the 10th International Modal Analysis Conference (IMAC X)*, San Diego, California, USA, pp. 536-540.
- 109 Kim, Y. H., Kim, D. H., Han, J. H. and Kim, C. G. (2007), "Damage Assessment in Layered Composites using Spectral Analysis and Lamb Wave", *Composites Part B: Engineering*, Vol. 38(7-8), pp. 800-809.
- 110 Kisa, M. (2004), "Free Vibration Analysis of a Cantilever Composite Beam with Multiple Cracks", *Composites Science and Technology*, Vol. 64, pp. 1391-1402.
- 111 Klein, L. A. (1999), "Sensor and Data Fusion: Concepts and Application", SPIE Press.
- 112 Kook, C. and Sohn, H. (2009), "Damage Diagnosis under Environmental and Operational Variations using Unsupervised Support Vector Machine", *Journal of Sound and Vibration*, Vol. 325(1-2), pp. 224-239.
- 113 Krawczuk, M., Ostachowicz, W. and Kawiecki, G. (2000), "Detection of Delaminations in Cantilevered Beams using Soft Computing Methods", *Proceedings of the European COST F3 Conference on System Identification and Structural Health Monitoring*, Madrid, Spain, pp. 243-252.
- 114 Kullaa (2002), "Elimination of Environmental Influences from Damage-Sensitive Features in a Structural Health Monitoring System", *Proceedings of the 1st European Workshop on Structural Health Monitoring*, Ecole Noemale Supérieure, Cachan, Paris, France, pp. 742-749.

- 115 Kyriazoglou, C., Le Page, B. H. and Guild, F. J. (2004), "Vibration Damping for Crack Detection in Composite Laminates", *Composites, Part A: Applied Sciences and Manufacturing*, Vol. 35, pp. 945-953.
- 116 Lamb, H. (1917), "On Waves in an Elastic Plate", *Proceedings of the Royal Society of London, Containing Papers of a Mathematical and Physical Character*, Vol. 93(651), pp. 293-312.
- 117 Law, S. S. and Lu, Z. R. (2005), "Crack Identification in Beam from Dynamic Responses", *Journal of Sound and Vibration*, Vol. 285, pp. 967-987.
- 118 Lazan, B. J. (1968), "Damping on Materials and Members in Structural Mechanics", Pergamon Press.
- 119 Lazarov, B. and Trendafilova, I. (2004), "An Investigation on Vibration-Based Damage Diagnosis in Thin Plates", *Proceedings of the 2nd European Workshop on Structural Health Monitoring*, Forum am Deutschen Museum, Munich, Germany, pp. 76-82.
- 120 Le Page, B. H., Guild, F. J., Ogin, S. L. and Smith, P. A. (2004), "Finite Element Simulation of Woven Fabric Composites", *Composites: Part A*, Vol. 35, pp. 861-872.
- 121 Lee, B. C. and Staszewski, W. J. (2002), "Modelling of Acousto-ultrasonic Wave Interaction with Defects in Metallic Structures", *Proceedings of the International Conference on Noise and Vibration Engineering (ISMA 2002)*, Leuven, Belgium, pp. 319-327.
- 122 Lekhnitskii, S. G. (1963), "Theory of Elasticity of an Anisotropic Elastic Body", San Francisco, Holden-Day.
- 123 Lenzen, A. (2005), "Identification of Mechanical Systems by Vibration Analysis for Health Monitoring and Damage Detection", *Proceedings of the 1st International Operational Modal Analysis Conference (IOMAC 2005)*, Copenhagen, Denmark, pp. 155-166.
- 124 Leontaritis, I. J. and Billings, S. A. (1985a), "Input Output Parametric Models for Non-Linear Systems .1. Deterministic Non-Linear Systems", *International Journal of Control*, Vol. 41(2), pp. 303-328.
- 125 Leontaritis, I. J. and Billings, S. A. (1985b), "Input Output Parametric Models for Non-Linear Systems .2. Stochastic Non-Linear Systems", *International Journal of Control*, Vol. 41(2), pp. 329-344.
- 126 Li, B., Chen, X. F., Ma, J. X. and He, Z. J. (2005), "Detection of Crack Location and Size in Structures using Wavelet Finite Element Methods", *Journal of Sound and Vibration*, Vol. 285, pp. 767-782.
- 127 Li, H. C. H., Weis, M., Herszberg, I. and Mouritz, A. P. (2004), "Damage Detection in a Fiber Reinforced Composite Beam using Random Decrement Signatures", *Proceedings of the 2nd European Workshop on Structural Health Monitoring*, Forum am Deutschen Museum, Munich, Germany, pp. 1091-1098.
- 128 Liang, C., Sun, F. P. and Rogers, C. A. (1994), "An Impedance Method for Dynamic Analysis of Active Material System", *Journal of Vibration and Acoustics*, Vol. 116, pp. 121-128.
- 129 Lieven, N. A. J. and Ewins, D. J. (1988), "Spatial Correlation of Mode Shapes: The Coordinate Modal Assurance Criterion (COMAC)", *Proceedings of the 6th International Modal Analysis Conference (IMAX VI)*, Kissimmee, Florida, USA, pp. 690-695.
- 130 Lifshitz, J. M. and Rotem, A. (1969), "Determination of Reinforcement Unbonding of Composites by a Vibration Technique", *Journal of Composite Materials*, Vol. 3, pp. 412-423.
- 131 Lin, M. (1999), "Development of SMART Layer for Built-In Structural Diagnostics", *Structural Health Monitoring 2000*, Stanford University, Palo Alto, California, USA, pp. 603-611.

- 132 Lin, S., Yang, J. N. and Zhou, L. (2005), "Damage Identification of a Benchmark Building for Structural Health Monitoring", *Smart Materials and Structures*, Vol. 14, pp. 162-169.
- 133 Liu, M. and Chelidze, D. (2005), "Flow Variance Method for Damage Identification", *Proceedings of the 23rd International Modal Analysis Conference (IMAC XXIII)*, Orlando, Florida, USA, paper no. 188.
- 134 Liu, X., Lieven, N. A. J. and Ambrosio, P. J. E. (2009), "Frequency response function shape-based methods for structural damage localisation", *Mechanical Systems and Signal Processing*, Vol. 23(4).
- 135 Lu, Y. and Gao, F. (2005), "A Novel Time-Domain Auto-Regressive Model for Structural Damage Diagnosis", *Journal of Sound and Vibration*, Vol. 283, pp. 1031-1049.
- 136 Luo, H. and Hanagud, S. (1997), "Dynamic Learning Rate Neural Network Training and Composite Structural Damage Detection", *AIAA Journal*, Vol. 35(9), pp. 1522-1527.
- 137 Lynch, J. P., Sundararajan, A., Law, K. H., Sohn, H. and Farrar, C. R. (2004), "Piezoelectric Structural Excitation using a Wireless Active Sensing Unit", *Proceedings of the 22nd International Modal Analysis Conference (IMAC XXII)*, Dearborn, Michigan, USA, paper no. 157.
- 138 Maheri, M. R. and Adams, R. D. (2003), "Modal Vibration Damping of Anisotropic FRP Laminates using the Rayleigh-Ritz Energy Minimization Scheme", *Journal of Sound and Vibration*, Vol. 259(1), pp. 17-29.
- 139 Maia, N. M. M. (2001), "Detecção de Dano Estrutural por Análise Dinâmica", *Habilitation Lecture*, Instituto Superior Técnico, Technical University of Lisbon, Portugal (in Portuguese).
- 140 Maia, N. M. M., Ribeiro, A. M. R., Fontul, M., Montalvão, D. and Sampaio, R. P. C. (2007), "Using the Detection and Relative Damage Quantification Indicator (DRQ) with Transmissibility", *Key Engineering Materials*, Vol. 347, pp. 455-460.
- 141 Maia, N. M. M. and Silva, J. M. M. (1997), "Theoretical and Experimental Modal Analysis", Research Studies Press, Ltd.
- 142 Maia, N. M. M., Silva, J. M. M., Almas, E. A. M. and Sampaio, R. P. C. (2003), "Damage Detection in Structures: from Mode Shape to Frequency Response Function Methods", *Mechanical Systems and Signal Processing*, Vol. 17(3), pp. 489-498.
- 143 Maia, N. M. M., Silva, J. M. M. and Ribeiro, A. M. R. (1994), "A New Concept in Modal Analysis: The Characteristic Response Function", *The International Journal of Analytical and Experimental Modal Analysis*, Vol. 9(3), pp. 191-202.
- 144 Maia, N. M. M., Silva, J. M. M. and Sampaio, R. P. C. (1997), "Localization of Damage using Curvature of the Frequency-Response-Functions", *Proceedings of the 15th International Modal Analysis Conference (IMAC XV)*, Orlando, Florida, USA, pp. 942-946.
- 145 Mares, C., Ruotolo, R. and Surace, C. (1999), "Using Transmissibility Data to Assess Structural Damage", *Proceedings of the 3rd International Conference on Damage Assessment of Structures (DAMAS 99)*, Dublin, Ireland, pp. 236-245.
- 146 Matthews, F. L. (1999), "Damage in Fibre Reinforced Plastics; Its Nature, Consequences and Detection", *Proceedings of the 3rd International Conference on Damage Assessment of Structures (DAMAS 99)*, Dublin, Ireland, pp. 1-16.
- 147 Matthews, F. L., Davies, G. A. O., Hitchings, D. and Soutis, C. (2000), "Finite Element Modelling of Composite Materials and Structures", Woodhead Publishing Ltd and CRC Press LLC.
- 148 Meirovitch, L. (1986), "Elements of Vibration Analysis", McGraw-Hill.

- 149 Messina, A., Jones, I. A. and Williams, E. J. (1992), "Damage Detection and Localization using Natural Frequency Changes", *Proceedings of the 1st Conference on Identification*, Cambridge, England, UK, pp. 67-76.
- 150 Messina, A., Jones, I. A. and Williams, E. J. (1996), "Damage Detection and Localization using Natural Frequency Changes", *Proceedings of the Conference on Identification in Engineering Systems*, Swansea, Wales, UK, pp. 67-76.
- 151 Messina, A., Williams, E. J. and Contursi, T. (1998), "Structural Damage Detection by a Sensitivity and Statistical-Based Method", *Journal of Sound and Vibration*, Vol. 216(5), pp. 791-808.
- 152 Miravete, A. (1999), "3-D Textile Reinforcements in Composite Materials", Woodhead Publishing Ltd and CRC Press LLC.
- 153 Mishnaevsky Jr., L. and Brøndsted, P. (2008), "Micromechanical Modelling of Damage and Fracture of Unidirectional Fibre Reinforced Composites: A Review", *Composite Materials Science*, Vol. 44(4), pp. 1351-1359.
- 154 Montalvão, D. (2003), "Determination of Rotational Terms of the Dynamic Response by means of Modal Analysis Techniques", *MSc Thesis*, Instituto Superior Técnico, Technical University of Lisbon, Portugal (in Portuguese).
- 155 Montalvão, D. and Fontul, M. (2006), "HARMONICA: Stepped-Sine Spectrum Analyzer for Transfer Function Measurement and Non-Linear Experimental Assessment", *Proceedings of the 5th International Conference on Mechanics and Materials in Design (M2D'2006)*, Porto, Portugal, ref. A0519.A0506.
- 156 Montalvão, D., Maia, N. M. M. and Ribeiro, A. M. R. (2006a), "A Review of Vibration-based Structural Health Monitoring with Special Emphasis on Composite Materials", *Shock and Vibration Digest*, Vol. 38(4), pp. 295-324.
- 157 Montalvão, D., Ribeiro, A. M. R. and Duarte-Silva, J. (2009), "A Method for the Localization of Damage in a CFRP Plate using Damping", *Special Issue on Inverse Problems in Mechanical Systems and Signal Processing*, Vol. 23, pp. 1846-1854.
- 158 Montalvão, D., Ribeiro, A. M. R., Maia, N. M. M., Duarte-Silva, J. and Cláudio, R. A. (2006b), "Damping Measurements on a Carbon Fibre Reinforced Laminate", *Proceedings of the International Conference on Noise and Vibration Engineering (ISMA 2006)*, Leuven, Belgium, pp. 447-459.
- 159 Montalvão, D., Ribeiro, A. M. R., Maia, N. M. M. and Silva, J. M. M. (2004a), "Estimation of the Rotational Terms of the Dynamic Response Matrix", *Shock and Vibration*, Vol. 11(3-4), pp. 333-350.
- 160 Montalvão, D., Ribeiro, A. M. R., Maia, N. M. M. and Silva, J. M. M. (2004b), "On the Estimation of Frequency Response Functions", *Proceedings of the International Conference on Noise and Vibration Engineering (ISMA 2004)*, Leuven, Belgium, pp. 2771-2785.
- 161 Morais, W. A., Monteiro, S. N. and d'Almeida, J. R. M. (2005), "Effect of the Laminate Thickness on the Composite Strength to Repeated Low Energy Impacts", *Composite Structures*, Vol. 70, pp. 223-228.
- 162 Moura Jr., J. R. V. (2005), "Damage Detection Techniques for Aeronautic Structures", *Proceedings of the 23rd International Modal Analysis Conference (IMAC XXIII)*, Orlando, Florida, USA, paper no. 101.
- 163 Moura Jr., J. R. V. and Steffen Jr., V. (2004), "Impedance-based Health Monitoring: Frequency Band Evaluation", *Proceedings of the 22nd International Modal Analysis Conference (IMAC XXII)*, Dearborn, Michigan, USA, paper no. 161.

- 164 Moura, M. F. S. F., Morais, A. B. and Magalhães, A. G. (2005), "Materiais Compósitos - Materiais, Fabrico e Comportamento Mecânico", Publindústria (in Portuguese).
- 165 Nayfeh, S. A. (2004), "Damping of Flexural Vibration in the Plane of Lamination of Elastic-viscoelastic Sandwich Beams", *Journal of Sound and Vibration*, Vol. 276(3-5), pp. 689-711.
- 166 Nejad, F. B., Rahai, A. and Esfandiari, A. (2005), "A Constrained Structural Damage Detection Method Using Static Noisy Data and Natural Frequencies", *Proceedings of the 23rd International Modal Analysis Conference (IMAC XXIII)*, Orlando, Florida, USA, paper no. 127.
- 167 Nelson, T. and Wang, E. (2004), "Reliable FE-Modelling with ANSYS®", *Proceedings of the 2002 International ANSYS® Conference*, <http://www.ansys.com/events/proceedings/2004/papers/24.pdf>.
- 168 Nichols, J. M., Moniz, L., Seaver, M. and Trickey, S. T. (2005), "Use of Holder Exponents and Fiber Optic Sensing for Detecting Damage in an Experimental Plate Structure", *Proceedings of the 23rd International Modal Analysis Conference (IMAC XXIII)*, Orlando, Florida, USA, paper no. 197.
- 169 Olson, C. C., Overbey, L. A. and Todd, M. D. (2005), "A Comparison of State-Space Attractor Features in Structural Health Monitoring", *Proceedings of the 23rd International Modal Analysis Conference (IMAC XXIII)*, Orlando, Florida, USA, paper no. 209.
- 170 Ostachowicz, W. and Zak, A. (2004), "Vibration of a Laminated Beam with Delamination including Contact Effects", *Shock and Vibration*, Vol. 11, pp. 157-171.
- 171 Pandey, A. K., Biswas, M. and Samman, M. M. (1991), "Damage Detection from Changes in Curvature Mode Shapes", *Journal of Sound and Vibration*, Vol. 145(2), pp. 321-332.
- 172 Pandit, S. W. and Metha, N. P. (1985), "Data Dependent System Approach to Modal Analysis Via State Space", ASME paper No. 85-WA/DSC-1.
- 173 Park, G., Cudney, H. and Inman, D. J. (1999), "Impedance-Based Health Monitoring Technique for Civil Structures", *Structural Health Monitoring 2000*, Stanford University, Palo Alto, California, USA, pp. 523-532.
- 174 Park, G., Rutherford, A. C., Sohn, H. and Farrar, C. R. (2005), "An Outlier Analysis Framework for Impedance-based Structural Health Monitoring", *Journal of Sound and Vibration*, Vol. 286, pp. 229-250.
- 175 Park, G., Sohn, H., Farrar, C. R. and Inman, D. J. (2003), "Overview of Piezoelectric Impedance-Based Health Monitoring and Path-Forward", *Shock and Vibration Digest*, Vol. 35(6), pp. 451-463.
- 176 Park, H. W., Kim, S. B. and Sohn, H. (2009), "Understanding a Time Reversal Process in Lamb Wave Propagation", *Wave Motion*, Vol. 46(7), pp. 451-467.
- 177 Park, J. M., Kong, J. W., Kim, D. S. and Yoon, D. J. (2005), "Nondestructive Damage Detection and Interfacial Evaluation of Single-Fibers/Epoxy Composites using PZT, PVDF and P(VDF-TrFE) Copolymer Sensors", *Composites Science and Technology*, Vol. 65, pp. 241-256.
- 178 Park, N. G. and Park, Y. S. (2003), "Damage Detection using Spatially Incomplete Frequency Response Functions", *Mechanical Systems and Signal Processing*, Vol. 17(3), pp. 519-532.
- 179 Park, Y. S., Park, H. S. and Lee, S. S. (1988), "Weighted-Error-Matrix Application to Detect Stiffness Damage by Dynamic-Characteristic Measurement", *Modal Analysis: The International Journal of Analytical and Experimental Modal Analysis*, Vol. 3(3), pp. 101-107.
- 180 Parloo, E., Guillaume, P. and Van Overmeire, M. (2003), "Damage Assessment Using Mode Shape Sensitivities", *Mechanical Systems and Signal Processing*, Vol. 17(3), pp. 499-518.

- 181 Parloo, E., Vanlanduit, S., Guillaume, P. and Verboven, P. (2002b), "Increased Reliability of Reference-based Damage Identification Techniques by using Output-only Data", *Proceedings of the International Conference on Structural Dynamics Modelling, Test, Analysis, Correlation and Validation*, Funchal, Madeira, Portugal, pp. 137-146.
- 182 Parloo, E., Vanlanduit, S., Guillaume, P. and Verboven, P. (2004), "Increased Reliability of Reference-based Damage Identification Techniques by using Output-only Data", *Journal of Sound and Vibration*, Vol. 270(4-5), pp. 813-832.
- 183 Parloo, E., Verboven, P., Guillaume, P. and Van Overmeire, M. (2002a), "Sensitivity-based Operational Mode Shape Normalization", *Mechanical Systems and Signal Processing*, Vol. 16(5), pp. 757-767.
- 184 Pascual, R., Golinval, J. C. and Razeto, M. (1997), "A Frequency Domain Correlation Technique for Model Correlation and Updating", *Proceedings of the 15th International Modal Analysis Conference (IMAC XV)*, Orlando, Florida, USA, pp. 587-592.
- 185 Patil, D. P. and Maiti, S. K. (2005), "Experimental Verification of a Method of Detection of Multiple Cracks in Beams based on Frequency Measurements", *Journal of Sound and Vibration*, Vol. 281, pp. 439-451.
- 186 Patterson, J. (2009), "New Large Aircraft Composite Firefighting", <http://www.airporttech.tc.faa.gov/safety/patterson2.asp>.
- 187 Peairs, D. M., Park, G. and Inman, D. J. (2005), "Impedance-based SHM Modeling using Spectral Elements and Circuit Analysis", *Proceedings of the 23rd International Modal Analysis Conference (IMAC XXIII)*, Orlando, Florida, USA, paper no. 232.
- 188 Peeters, B. and De Roeck, G. (1999), "Reference-based Stochastic Subspace Identification for Output-only Modal Analysis", *Mechanical Systems and Signal Processing*, Vol. 13(6), pp. 855-878.
- 189 Peeters, B. and De Roeck, G. (2000), "One Year Monitoring of the Z24-Bridge: Environmental Influences versus Damage Events", *Proceedings of the 18th International Modal Analysis Conference (IMAC XVIII)*, San Antonio, Texas, USA, pp. 1570-1576.
- 190 Peil, U., Mehdiannpour, M., Frenz, M. and Weilert, K. (2004), "Determination of the Inherent Damage of Older Structures", *Proceedings of the 2nd European Workshop on Structural Health Monitoring*, Forum am Deutschen Museum, Munich, Germany, pp. 243-250.
- 191 Penny, J. E. T., Wilson, D. A. L. and Friswell, M. I. (1993), "Damage Location in Structures using Vibration Data", *Proceedings of the 11th International Modal Analysis Conference (IMAC XI)*, Kissimmee, Florida, USA, pp. 861-867.
- 192 Pirner, M. and Urushadze, S. (2004), "Dynamic Response as a Tool for Damage Identification", *International Applied Mechanics*, Vol. 40(5), pp. 487-505.
- 193 Polimeno, U. and Meo, M. (2009), "Detecting Barely Visible Impact Damage Detection on Aircraft Composites Structures", *Composite Structures*, Vol. 91(4), pp. 398-402.
- 194 Qin, Q. and Zhang, W. (1998), "Damage Detection of Suspension Bridges", *Proceedings of the 16th International Modal Analysis Conference (IMAC XVI)*, Santa Barbara, California, USA, pp. 945-951.
- 195 Qing, X., Kumar, A., Zhang, C., Gonzalez, I. F., Guo, G. and Chang, F. K. (2005), "A Hybrid Piezoelectric/Fiber Optic Diagnostic System for Structural Health Monitoring", *Smart Materials and Structures*, Vol. 14, pp. 98-103.
- 196 Randall, R. B. (2002), "State of the Art in Monitoring Rotating Machinery", *Proceedings of the International Conference on Noise and Vibration Engineering (ISMA 2002)*, Leuven, Belgium, pp. 1457-1477.

- 197 Ratcliffe, C. P. (2000), "A Frequency and Curvature based Experimental Method for Locating Damage in Structures", *Journal of Vibration and Acoustics*, Vol. 122, pp. 324-329.
- 198 Ratcliffe, C. P. and Bagaria, W. J. (1998), "A Vibration Technique for Locating Delamination in a Composite Beam", *AIAA Journal*, Vol. 36(6), pp. 1074-1077.
- 199 Reis, L. F. G. (1996), "Análise do Dano Devido a Cargas de Impacto em Materiais Compósitos", *MSc Thesis*, Instituto Superior Técnico, Technical University of Lisbon, Portugal (in Portuguese).
- 200 Ren, Y. and Beards, C. F. (1995), "Identification of Joint Properties of a Structure using FRF Data", *Journal of Sound and Vibration*, Vol. 186(4), pp. 567-587.
- 201 Ribeiro, A. M. R. (1999), "Desenvolvimento de Técnicas de Análise Dinâmica Aplicáveis à Modificação Estrutural", *PhD Thesis*, Instituto Superior Técnico, Technical University of Lisbon, Portugal (in Portuguese).
- 202 Ribeiro, A. M. R., Silva, J. M. M., Maia, N. M. M., Reis, L. F. G. and Freitas, M. J. M. (2005), "Free Vibration Response using the Constant Hysteretic Damping Model", *Proceedings of the 11th International Conference on Vibration Engineering*, Timisoara, Romania, pp. 65-70.
- 203 Ricci, F., Banerjee, S. and Mal, A. K. (2004), "Health Monitoring of Composite Structures using Wave Propagation Data", *Proceedings of the 2nd European Workshop on Structural Health Monitoring*, Forum am Deutschen Museum, Munich, Germany, pp. 1035-1042.
- 204 Rilo, N. F., Ferreira, L. M. S. and Leal, R. A. C. P. (2006), "Low-Velocity Impact Analysis of Glass/Epoxy Plates", *Proceedings of the 5th International Conference on Mechanics and Materials in Design (M2D'2006)*, Porto, Portugal, ref. A0110.0092.
- 205 Rodrigues, J., Brincker, R. and Andersen, P. (2004), "Improvement of Frequency Domain Output-Only Modal Identification from the Application of the Random Decrement Technique", *Proceedings of the 22nd International Modal Analysis Conference (IMAC XXII)*, Dearborn, Michigan, USA, paper no. 92.
- 206 Ruotolo, R. and Surace, C. (1997), "Damage Detection Using Singular Value Decomposition", *Proceedings of the 2nd International Conference on Structural Damage Assessment using Advanced Signal Processing Procedures (DAMAS 97)*, Sheffield, England, UK, pp. 87-96.
- 207 Rytter, A. (1993), "Vibration Based Inspection of Civil Engineering Structures", *PhD Thesis*, Aalborg University, Denmark.
- 208 Safak, E. (1991), "Identification of Linear Structures using Discrete-Time Filters", *Journal of Structural Engineering*, Vol. 117(10), pp. 3064-3085.
- 209 Salawu, O. S. and Williams, C. (1994), "Damage Location using Vibration Mode Shapes", *Proceedings of the 12th International Modal Analysis Conference (IMAC XII)*, Honolulu, Hawaii, USA, pp. 933-939.
- 210 Sampaio, R. P. C. and Maia, N. M. M. (2004), "On the Detection and Relative Damage Quantification Indicator", *Proceedings of the 2nd European Workshop on Structural Health Monitoring*, Forum am Deutschen Museum, Munich, Germany, pp. 757-766.
- 211 Sampaio, R. P. C., Maia, N. M. M. and Silva, J. M. M. (1999), "Damage Detection using the Frequency-Response-Function Curvature Method", *Journal of Sound and Vibration*, Vol. 226(5), pp. 1029-1042.
- 212 Sampaio, R. P. C., Maia, N. M. M. and Silva, J. M. M. (2003), "The Frequency Domain Assurance Criterion as a Tool for Damage Identification", *Proceedings of the 5th International Conference on Damage Assessment of Structures (DAMAS 2003)*, Southampton, England, UK, pp. 69-76.

- 213 Sampaio, R. P. C., Maia, N. M. M., Silva, J. M. M. and Ribeiro, A. M. R. (2000), "On the use of Transmissibility for Damage Detection and Location", *Proceedings of the European COST F3 Conference on System Identification and Structural Health Monitoring*, Madrid, Spain, pp. 363-376.
- 214 Sanders, D. R., Kim, Y. I. and Stubbs, N. (1992), "Nondestructive Evaluation of Damage in Composite Structures Using Modal Parameters", *Experimental Mechanics*, Vol. 32(3), pp. 240-251.
- 215 Santos, J. V. A., Lopes, H. M. R., Vaz, M., Soares, C. M. M., Soares, C. A. M. and Freitas, M. J. M. (2006), "Damage Localization in Laminated Composite Plates using Mode Shapes Measured by Pulsed TV Holography", *Composite Structures*, Vol. 76(3), pp. 272-281.
- 216 Santos, J. V. A., Soares, C. M. M., Soares, C. A. M. and Maia, N. M. M. (2003a), "Análise de Erros na Identificação do Dano em Estruturas Laminadas", *VII Congresso de Mecânica Aplicada e Computacional*, Universidade de Évora, Portugal (in Portuguese), pp. 95-103.
- 217 Santos, J. V. A., Soares, C. M. M., Soares, C. A. M. and Maia, N. M. M. (2003b), "Structural Damage Identification: Influence of Model Incompleteness and Errors", *Composite Structures*, Vol. 62(3-4), pp. 303-313.
- 218 Santos, J. V. A., Soares, C. M. M., Soares, C. A. M. and Maia, N. M. M. (2004), "Modelos de Identificação do Dano com base nas Características Dinâmicas de Estruturas", *Métodos Computacionais em Engenharia (in Portuguese)*.
- 219 Santos, J. V. A., Soares, C. M. M., Soares, C. A. M. and Maia, N. M. M. (2005), "Structural Damage Identification in Laminated Structures using FRF Data", *Composite Structures*, Vol. 67, pp. 239-249.
- 220 Santos, J. V. A., Soares, C. M. M., Soares, C. A. M. and Pina, H. L. G. (1999), "Damage Identification of Composite Structures: a Numerical Model", *Mechanics of Composite Materials and Structures*, Vol. 6, pp. 363-379.
- 221 Santos, J. V. A., Soares, C. M. M., Soares, C. A. M. and Pina, H. L. G. (2000), "Development of a Numerical Model for the Damage Identification on Composite Plate Structures", *Composite Structures*, Vol. 48, pp. 59-65.
- 222 Saravanos, D. A., Birman, V. and Hopkins, D. A. (1994), "Detection of Delaminations in Composite Beams using Piezoelectric Sensors", *Proceedings of the 31st AIAA/ASME/ASCE/AHS/ASC Structures, Structural Dynamics and Materials Conference*, pp. 181-191.
- 223 Savov, K. and Wenzel, H. (2005), "System Identification and Damage Detection using Wavelet Analysis: Applications in Frame Structures", *Proceedings of the 1st International Operational Modal Analysis Conference (IOMAC 2005)*, Copenhagen, Denmark, pp. 511-518.
- 224 Shi, Z. Y. and Law, S. S. (2005a), "Parameter Identification-Based Damage Detection for Nonlinear Systems", *Proceedings of the 1st International Operational Modal Analysis Conference (IOMAC 2005)*, Copenhagen, Denmark, pp. 503-510.
- 225 Shi, Z. Y. and Law, S. S. (2005b), "Parameter Identification-Based Damage Detection for Linear Time-Varying Systems", *Proceedings of the 1st International Operational Modal Analysis Conference (IOMAC 2005)*, Copenhagen, Denmark, pp. 527-534.
- 226 Shu, D. and Della, C. N. (2004), "Vibrations of Multiple Delaminated Beams", *Composite Structures*, Vol. 64, pp. 467-477.
- 227 Sidhu, J. and Ewins, D. J. (1984), "Correlation of Finite Element and Modal Test Studies of a Practical Structure", *Proceedings of the 2nd International Modal Analysis Conference (IMAC II)*, Orlando, Florida, USA, pp. 185-192.

- 228 Silva, A. J. P. F. (2001), "Propagação de Delaminação em Compósitos de Matriz Polimérica", *PhD Thesis*, Instituto Superior Técnico, Technical University of Lisbon, Portugal (in Portuguese).
- 229 Silva, J. M. M. and Gomes, A. J. M. A. (1990), "Experimental Dynamic Analysis of Cracked Free-Free Beams", *Experimental Mechanics*, Vol. 30(1), pp. 20-25.
- 230 Silva, J. M. M. and Gomes, A. J. M. A. (1991), "Crack Modelling Using Torsional Springs", *Actas das Quartas Jornadas de Fractura, Sociedade Portuguesa de Materiais*, Instituto Superior Técnico, Technical University of Lisbon, Portugal (in Portuguese).
- 231 Silva, J. M. M. and Gomes, A. J. M. A. (1994), "Crack Identification of Simple Structural Elements through the use of Natural Frequency Variations: The Inverse Problem", *Proceedings of the 12th International Modal Analysis Conference (IMAC XII)*, Honolulu, Hawaii, USA, pp. 1728-1735.
- 232 Silva, J. M. M., Maia, N. M. M. and Ribeiro, A. M. R. (1996), "Structural Dynamic Identification with Modal Constant Consistency using the Characteristic Response Function (CRF)", *Machine Vibration*, Vol. 5(2), pp. 83-88.
- 233 Simmers Jr., G., Sodano, H., Park, G. and Inman, D. J. (2005), "Impedance-based Structural Health Monitoring to Detect Corrosion", *Proceedings of the 23rd International Modal Analysis Conference (IMAC XXIII)*, Orlando, Florida, USA, paper no. 56.
- 234 Sohn, H. and Farrar, C. R. (2001), "Damage Diagnosis using Time Series Analysis of Vibration Signals", *Smart Materials and Structures*, Vol. 10(3), pp. 446-451.
- 235 Sohn, H., Farrar, C. R., Hemez, F. M., Shunk, D. D., Stinemates, D. W. and Nadler, B. R. (2003), "A Review of Structural Health Monitoring Literature: 1996-2001", Los Alamos National Laboratory, USA.
- 236 Sohn, H., Farrar, C. R., Hunter, N. F. and Worden, K. (2001), "Structural Health Monitoring using Statistical Pattern Recognition Techniques", *Journal of Dynamic Systems Measurement and Control-Transactions of the ASME*, Vol. 123(4), pp. 706-711.
- 237 Sohn, H., Park, G., Wait, J. R., Limback, N. P. and Farrar, C. R. (2004b), "Wavelet-based Signal Processing for Detecting Delamination in Composite Plates", *Smart Materials and Structures*, Vol. 13(1), pp. 153-160.
- 238 Sohn, H., Park, H., Law, K. H. and Farrar, C. R. (2005), "Instantaneous Online Monitoring of Unmanned Aerial Vehicles without Baseline Signals", *Proceedings of the 23rd International Modal Analysis Conference (IMAC XXIII)*, Orlando, Florida, USA, paper no. 259.
- 239 Sohn, H., Wait, J. R., Park, G. and Farrar, C. R. (2004a), "Multi-Scale Structural Health Monitoring for Composite Structures", *Proceedings of the 2nd European Workshop on Structural Health Monitoring*, Forum am Deutschen Museum, Munich, Germany, pp. 721-729.
- 240 Spencer Jr., B. F., Sandoval, M. E. R. and Kurata, N. (2004), "Smart Sensing Technology: Opportunities and Challenges", *Journal of Structural Control and Health Monitoring*, Vol. 11(4), pp. 349-368.
- 241 Steenackers, G. and Guillaume, P. (2005), "Structural Health Monitoring of the Z-24 Bridge in Presence of Environmental Changes using Modal Analysis", *Proceedings of the 23rd International Modal Analysis Conference (IMAC XXIII)*, Orlando, Florida, USA, paper no. 297.
- 242 Stubbs, N., Kim, J. T. and Farrar, C. R. (1995), "Field Verification of a Nondestructive Damage Localization and Severity Estimation Algorithm", *Proceedings of the 13th International Modal Analysis Conference (IMAC XIII)*, Nashville, Tennessee, USA, pp. 210-218.
- 243 Stubbs, N. and Osegueda, R. (1990a), "Global Non-Destructive Damage Evaluation in Solids", *Modal Analysis: The International Journal of Analytical and Experimental Modal Analysis*, Vol. 5(2), pp. 67-79.

- 244 Stubbs, N. and Osegueda, R. (1990b), "Global Damage Detection in Solids—Experimental Verification", *Modal Analysis: The International Journal of Analytical and Experimental Modal Analysis*, Vol. 5(2), pp. 81-97.
- 245 Su, Z., Ye, L. and Bu, X. (2002), "Evaluation of Delamination in Laminated Composites based on Lamb Waves Methods: FEM Simulation and Experimental Verification", *Proceedings of the 1st European Workshop on Structural Health Monitoring*, Ecole Noemale Supérieure, Cachan, Paris, France, pp. 328-335.
- 246 Su, Z., Ye, L. and Lu, Y. (2006), "Guided Lamb Waves for Identification of Damage in Composite Structures: A review", *Journal of Sound and Vibration*, Vol. 295(3-5), pp. 753-780.
- 247 Sundararaman, S., Adams, D. E. and Rigas, E. J. (2005), "Characterizing Damage in Plates through Beamforming with Sensor Arrays", *Proceedings of the 23rd International Modal Analysis Conference (IMAC XXIII)*, Orlando, Florida, USA, paper no. 249.
- 248 Sundaresan, M. J., Ghoshal, A. and Schulz, M. J. (2001), "A Continuous Sensor to Measure Acoustic Waves in Plates", *Journal of Intelligent Material Systems and Structures*, Vol. 12(1), pp. 41-56.
- 249 Sundaresan, M. J., Grandhi, G., Schulz, M. J. and Kemerling, J. C. (2004), "Monitoring Damage Growth in a Composite Plate using a Continuous Sensor", *Proceedings of the 22nd International Modal Analysis Conference (IMAC XXII)*, Dearborn, Michigan, USA, paper no. 369.
- 250 Sundaresan, M. J., Pai, P. F., Ghoshal, A., Schulz, M. J., Ferguson, F. and Chung, J. H. (2001), "Methods of Distributed Sensing for Health Monitoring of Composite Material Structures", *Composites: Part A*, Vol. 32, pp. 1357-1374.
- 251 Tan, P., Liyong, T. and Steven, G. P. (1999), "Micromechanics Models for the Elastic Constants and Failure Strengths of Plain Composites", *Composite Structures*, Vol. 47, pp. 797-804.
- 252 Taylor, S. and Zimmerman, D. C. (2005), "Damage Detection in a Cargo Bay Frame using Ritz Vectors", *Proceedings of the 23rd International Modal Analysis Conference (IMAC XXIII)*, Orlando, Florida, USA, paper no. 355.
- 253 Testa, R. B. (2005), "Characteristics and Detection of Damage and Fatigue Cracks", *Advanced Course on Dynamic Methods for Damage Detection in Structures*, CISM (Centre International des Sciences Mécaniques), Udine, Italy.
- 254 Thien, A. B., Chiamori, H. C., Ching, J. T., Wait, J. R. and Park, G. (2005), "Piezoelectric Active Sensing for Damage Detection in Pipeline Structures", *Proceedings of the 23rd International Modal Analysis Conference (IMAC XXIII)*, Orlando, Florida, USA, paper no. 323.
- 255 Thollon, Y. and Hochard, C. (2009), "A General Damage Model for Woven Fabric Composite Laminates up to First Failure", *Mechanics of Materials*, Vol. 41(7), pp. 820-827.
- 256 Tippetts, T. and Hemez, F. M. (2005), "Non-Linear Models of Composite Laminates", *Proceedings of the 23rd International Modal Analysis Conference (IMAC XXIII)*, Orlando, Florida, USA, paper no. 10.
- 257 Tong, L., Mouritz, A. P. and Bannister, M. K. (2002), "3D Fibre Reinforced Polymer Composites", Elsevier Science Ltd.
- 258 Toyama, N. and Okabe, T. (2004), "Effects of Tensile Strain and Transverse Cracks on Lamb-Wave Velocity in Cross-Ply FRP Laminates", *Journal of Materials Science*, Vol. 39, pp. 7365-7367.
- 259 Tracy, J. J. and Pardo, G. C. (1989), "Effect of Delamination on the Natural Frequencies of Composite Laminates", *Journal of Composite Materials*, Vol. 23, pp. 1200-1215.

- 260 Travassos, J. M. C. (1994), "Produção de Materiais Compósitos de Elevado Desempenho Mecânico", *PhD Thesis*, Instituto Superior Técnico, Technical University of Lisbon, Portugal (in Portuguese).
- 261 Uhl, T. and Mendrok, K. (2004), "Overview of Modal Model based Damage Detection Methods", *Proceedings of the International Conference on Noise and Vibration Engineering (ISMA 2004)*, Leuven, Belgium, pp. 361-375.
- 262 Vaidya, U. K. (2008), "Characterization of Impact Damage", *International School on Impact Engineering of Composite Structures*, CISM (Centre International des Sciences Mécaniques), Udine, Italy.
- 263 Vanhonacker, P. (1980), "Differential and Difference Sensitivities of Natural Frequencies and Mode Shapes of Mechanical Structures", *AIAA Journal*, Vol. 18(12), pp. 1511-1514.
- 264 Vanlanduit, S., Parloo, E., Cauberghe, B., Guillaume, P. and Verboven, P. (2005), "A Robust Singular Value Decomposition for Damage Detection under Changing Operating Conditions and Structural Uncertainties", *Journal of Sound and Vibration*, Vol. 284, pp. 1033-1050.
- 265 Vecchio, A. and Van der Auweraer, H. (2001), "An Experimental Validation of a Model-Based Approach in Damage Detection and Validation", *Proceedings of the 3rd International Workshop on Structural Health Monitoring*, Stanford University, Palo Alto, California, USA, pp. 957-966.
- 266 Vecchio, A., Van der Auweraer, H., Ferraro, G., Garesci, F. and Petrone, F. (2002), "An Experimental Validation of a Model-Based Approach in Damage Detection and Localization", *Proceedings of the 1st European Workshop on Structural Health Monitoring*, Ecole Noemale Supérieure, Cachan, Paris, France, pp. 245-252.
- 267 Vescovo, D. D. and Fregolent, A. (2005), "Assessment of Fresco Detachments through a Non-Invasive Acoustic Method", *Journal of Sound and Vibration*, Vol. 285, pp. 1015-1031.
- 268 Wahab, M. M. and De Roeck, G. (1999), "Damage Detection in Bridges using Modal Curvatures: Application to a Real Damage Scenario", *Journal of Sound and Vibration*, Vol. 226(2), pp. 217-235.
- 269 Wahl, F., Schmidt, G. and Forrai, L. (1999), "On the Significance of Antiresonance Frequencies in Experimental Structural Analysis", *Journal of Sound and Vibration*, Vol. 219(3), pp. 379-394.
- 270 Wang, E. and Nelson, T. (2002), "Structural Dynamic Capabilities of ANSYS®", *Proceedings of the 2002 International ANSYS® Conference*, <http://www.ansys.com/events/proceedings/2002.asp>.
- 271 Wang, K., Inman, D. J. and Farrar, C. R. (2005), "Modelling and Analysis of a Cracked Composite Cantilever Beam Vibrating in Coupled Bending and Torsion", *Journal of Sound and Vibration*, Vol. 284, pp. 23-49.
- 272 Wei, Z., Yam, L. H. and Cheng, L. (2005), "NARMAX Model Representation and its Application to Damage Detection for Multi-layer Composites", *Composite Structures*, Vol. 68(1), pp. 109-117.
- 273 West, W. M. (1984), "Illustration of the Use of Modal Assurance Criterion to Detect Structural Changes in an Orbiter Test Specimen", *Proceedings of the Air Force Conference on Aircraft Structural Integrity*, pp. 1-6.
- 274 Wilson, E. L., Yuan, M. W. and Dicken, J. M. (1982), "Dynamic Analysis by Direct Superposition of Ritz Vectors", *Earthquake Engineering and Structural Dynamics*, Vol. 10, pp. 813-821.

- 275 Woon, C. E. and Mitchell, L. D. (1996a), "Variations in Structural Dynamics Characteristics caused by Changes in Ambient Temperature: I. Experimental", *Proceedings of the 14th International Modal Analysis Conference (IMAC XIV)*, Dearborn, Michigan, USA, pp. 963-971.
- 276 Woon, C. E. and Mitchell, L. D. (1996b), "Variations in Structural Dynamics Characteristics caused by Changes in Ambient Temperature: II. Analytical", *Proceedings of the 14th International Modal Analysis Conference (IMAC XIV)*, Dearborn, Michigan, USA, pp. 972-980.
- 277 Worden, K., Manson, G. and Fieller, N. R. J. (2000), "Damage Detection using Outlier Analysis", *Journal of Sound and Vibration*, Vol. 229(3), pp. 647-667.
- 278 Wowk, V. (1991), "Machinery Vibration: Measurement and Analysis", McGraw-Hill.
- 279 Wu, Z. S., Yang, C. Q., Harada, T. and Ye, L. P. (2005), "Self-Diagnosis of Structures Strengthened with Hybrid Carbon-Fiber Reinforced Polymer Sheets", *Smart Materials and Structures*, Vol. 14, pp. 39-51.
- 280 Yam, L. H., Wei, Z. and Cheng, L. (2004), "Nondestructive Detection of Internal Delamination by Vibration-based Method for Composite Plates", *Journal of Composite Materials*, Vol. 38(24), pp. 2183-2198.
- 281 Yan, A. M., Golinval, J. C., Peeters, B. and De Roeck, G. (2004), "A Comparative Study on Damage Detection of Z24-bridge: One-year Monitoring with Varying Environmental Conditions", *Proceedings of the 2nd European Workshop on Structural Health Monitoring Forum* am Deutschen Museum, Munich, Germany, pp. 791-799.
- 282 Yan, A. M., Kerschen, G., De Boe, P. and Golinval, J. C. (2005a), "Structural Damage Diagnosis under Varying Environmental Conditions - Part I: A Linear Analysis", *Mechanical Systems and Signal Processing*, Vol. 19, pp. 847-864.
- 283 Yan, A. M., Kerschen, G., De Boe, P. and Golinval, J. C. (2005b), "Structural Damage Diagnosis under Varying Environmental Conditions - Part II: Local PCA for Non-Linear Cases", *Mechanical Systems and Signal Processing*, Vol. 19, pp. 865-880.
- 284 Yang, J. N., Lei, Y., Pan, S. and Huang, N. (2003), "Identification of Linear Structures Based on Hilbert-Huang Transform Part II: Complex Modes", *Earthquake Engineering and Structural Dynamics*, Vol. 32, pp. 1443-1467.
- 285 Yoon, M. K., Heider, D., Gillespie, J. W., Ratcliffe, C. P. and Crane, R. M. (2005), "Local Damage Detection using the Two-dimensional Gapped Smoothing Method", *Journal of Sound and Vibration*, Vol. 279(1-2), pp. 119-139.
- 286 Yu, L., Yin, T., Zhu, H. P. and Xu, D. Y. (2005), "An Improved Genetic Algorithm for Structural Damage Detection", *Proceedings of the 1st International Operational Modal Analysis Conference (IOMAC 2005)*, Copenhagen, Denmark, pp. 361-368.
- 287 Zabel, V. (2004), "A Wavelet-Based Damage Detection Indicator for Reinforced Concrete Structures", *Proceedings of the 22nd International Modal Analysis Conference (IMAC XXII)*, Dearborn, Michigan, USA, paper no. 70.
- 288 Zabel, V. (2005a), "A Wavelet-based Approach for Damage Detection on Civil Engineering Structures", *Proceedings of the 23rd International Modal Analysis Conference (IMAC XXIII)*, Orlando, Florida, USA, paper no. 178.
- 289 Zabel, V. (2005b), "Application of Wavelet Decompositions' Energy Components to Damage Detection", *Proceedings of the 1st International Operational Modal Analysis Conference (IOMAC 2005)*, Copenhagen, Denmark, pp. 519-526.

- 290 Zak, A., Krawczuk, M. and Ostachowicz, W. (1999), "Vibration of a Laminated Composite Plate with Closing Delamination", *Proceedings of the 3rd International Conference on Damage Assessment of Structures (DAMAS 99)*, Dublin, Ireland, pp. 17–26.
- 291 Zang, C., Friswell, M. I. and Imregun, M. (2003a), "Structural Health Monitoring and Damage Assessment using Measured FRFs from Multiple Sensors, Part I: The Indicator of Correlation Criteria", *Proceedings of the 5th International Conference on Damage Assessment of Structures (DAMAS 2003)*, Southampton, England, UK, pp. 131-140.
- 292 Zang, C., Friswell, M. I. and Imregun, M. (2003b), "Structural Health Monitoring and Damage Assessment using Measured FRFs from Multiple Sensors, Part II: Decision Making with RBF Networks", *Proceedings of the 5th International Conference on Damage Assessment of Structures (DAMAS 2003)*, Southampton, England, UK, pp. 141-148.
- 293 Zhang, R., King, R., Olson, L. and Xu, Y. L. (2005), "Dynamic Response of the Trinity River Relief Bridge to Controlled Pile Damage: Modelling and Experimental Data Analysis Comparing Fourier and Hilbert-Huang Techniques." *Journal of Sound and Vibration*, Vol. 285, pp. 1049-1070.
- 294 Zheng, D. (2007), "Low Velocity Impact Analysis of Composite Laminated Plates", *PhD Thesis*, Graduate Faculty of the University of Akron, USA.
- 295 Zheng, S., Wang, X. and Liu, L. (2004), "Damage Detection in Composite Materials Based upon the Computational Mechanics and Neural Networks", *Proceedings of the 2nd European Workshop on Structural Health Monitoring*, Forum am Deutschen Museum, Munich, Germany, pp. 609-615.
- 296 Zhu, H. P. and Xu, Y. L. (2005), "Damage Detection of Mono-Coupled Periodic Structures based on Sensitivity Analysis of Modal Parameters", *Journal of Sound and Vibration*, Vol. 285, pp. 363-390.
- 297 Zimmerman, D. C. (2005), "Statistical Confidence using Minimum Rank Perturbation Theory", *Mechanical Systems and Signal Processing*, Vol. article in press (available online).
- 298 Zimmerman, D. C., Kaouk, M. and Simmermacher, T. (1995a), "On the Role of Engineering Insight and Judgement Structural Damage Detection", *Proceedings of the 13th International Modal Analysis Conference (IMAC XIII)*, Nashville, Tennessee, USA, pp. 414-420.
- 299 Zimmerman, D. C., Simmermacher, T. and Kaouk, M. (1995b), "Structural Damage Detection using Frequency Response Functions", *Proceedings of the 13th International Modal Analysis Conference (IMAC XIII)*, Nashville, Tennessee, USA, pp. 179-185.
- 300 Zou, Y., Tong, L. and Steven, G. P. (2000), "Vibration-Based Model-Dependent Damage (Delamination) Identification and Health Monitoring for Composite Structures - A Review", *Journal of Sound and Vibration*, Vol. 230(2), pp. 357-378.

Annex A - About ANSYS®

The information contained in this annex was mostly picked from "ANSYS® 11 Theory Reference Manual" (2007), "ANSYS® 11 Elements Reference Manual" (2007) and "ANSYS® 11 Structural Guide" (2007).

A.1 Elements used in ANSYS®

A.1.1 SHELL63 Elastic shell

The elastic shell element (SHELL63) has both bending and membrane capabilities. Both in-plane and normal loads are permitted. The element has 6 DOFs at each node: translations in the nodal x , y , and z directions and rotations about the nodal x , y , and z axes. Stress stiffening and large deflection capabilities are included.

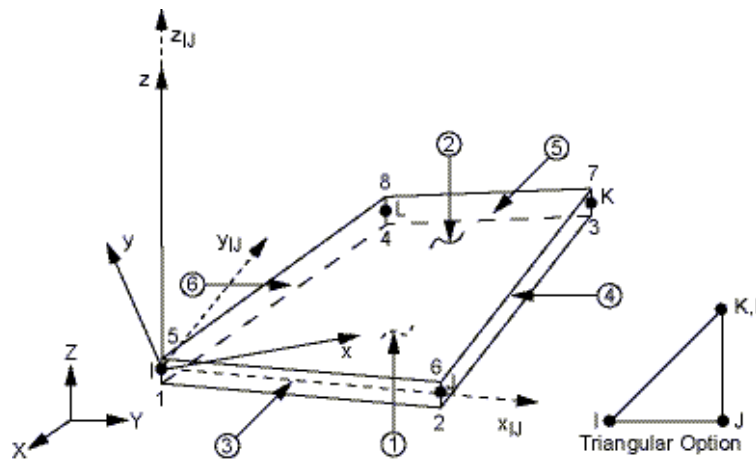


Figure A.1: SHELL63 geometry ("ANSYS® 11 Elements Reference Manual" (2007)).

The geometry, node locations, and the coordinate system for this element are shown in figure A.1. The element is defined by four nodes, four thicknesses, elastic foundation stiffness, and the orthotropic material properties. Orthotropic material directions correspond to the element coordinate directions.

The thickness is assumed to vary smoothly over the area of the element, with the thickness input at the four nodes. The element is, of course, allowed to have a constant thickness. Element loads are described in node and element Loads. Pressures may be input as surface loads (force per unit area) on the element faces as shown by the circled numbers on figure A.1.

The equivalent element load produces more accurate stress results with flat elements representing a curved surface or elements supported on an elastic foundation since certain fictitious bending stresses are eliminated.

For an isotropic material, important properties to be defined are: the Young's modulus E ; the Poisson's ratio ν ; material's density; and, when appropriate, the damping factor. For an orthotropic material, important properties to be defined are: the Young's moduli E_x , E_y and E_z ; the major Poisson's ratios ν_{xy} , ν_{yz} and ν_{xz} (or, alternatively, the minor Poisson's ratios); the shear moduli G_{xy} , G_{yz} and G_{xz} ; material's density; and, when appropriate, damping.

A.1.2 SHELL99 linear layered structural shell

The linear layered structural shell element (SHELL99) may be used for layered applications of a structural shell model. While SHELL99 does not have some of the nonlinear capabilities of SHELL91, it usually has a smaller element formulation time. SHELL99 allows up to 250 layers. The element has 6 DOFs at each node: translations in the nodal x , y , and z directions and rotations about the nodal x , y , and z axes. The geometry, node locations, and the coordinate system for this element are shown in figure A.2. The element is defined by eight nodes, average or corner layer thicknesses, layer material direction angles, and orthotropic material properties. Mid-side nodes may not be removed from this element.

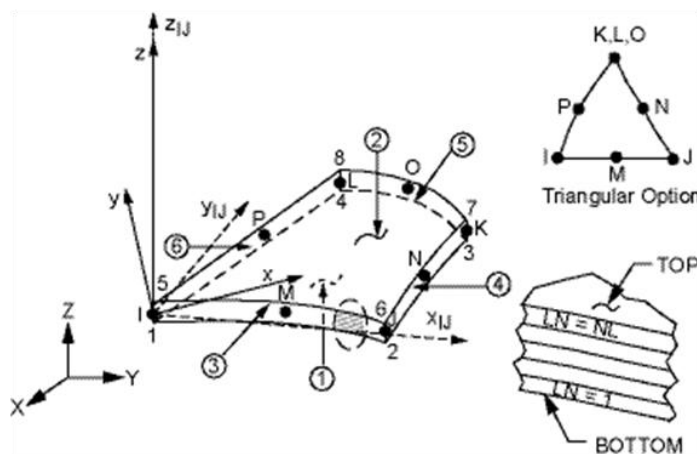


Figure A.2: SHELL99 geometry ("ANSYS® 11 Elements Reference Manual" (2007)).

The total number of layers must be specified. The properties of all layers should be entered, unless the properties of the layers are symmetrical about the mid-thickness of the element (in this case, only half of the properties of the layers, up to and including the middle layer - if any - need to be entered). The material properties of each layer may be orthotropic in the plane of

the element. Element loads are described in Node and Element Loads. Pressures may be input as surface loads on the element faces.

Important material properties to be defined are: the Young's moduli E_x , E_y and E_z ; the major Poisson's ratios ν_{xy} , ν_{yz} and ν_{xz} (or, alternatively, the minor Poisson's ratios); the shear moduli G_{xy} , G_{yz} and G_{xz} ; material's density; and, when appropriate, damping. In this case, the coordinate system is local instead of global (it is in layer coordinates), meaning that coordinate x is in the fibres longitudinal L direction and that coordinate y is in the transverse T direction.

Concerning some assumptions or restrictions, interlaminar transverse shear stresses are based on the assumption that no shear is carried at the top and bottom surfaces of an element. Further, these interlaminar shear stresses are only computed at the centroid and are not valid along the element boundaries. If accurate edge interlaminar shear stresses are required, shell-to-solid submodelling should be used.

A.1.3 MASS21 Structural mass

The structural mass element (MASS21) is a point element having up to 6 DOFs: translations in the nodal x , y , and z directions and rotations about the nodal x , y , and z axes. A different mass and rotary inertia may be assigned to each coordinate direction. The mass element is defined by a single node, concentrated mass components in the element coordinate directions (m_x , m_y and m_z), and rotary inertias (mass moment of inertias) about the element coordinate axes (I_x , I_y and I_z).

A.1.4 COMBIN14 Spring-Damper

The spring-damper element (COMBIN14) has longitudinal or torsion capability in 1D, 2D, or 3D applications. The longitudinal spring-damper option is a uniaxial tension-compression element with up to 3 DOFs at each node: translations in the nodal x , y , and z directions. No bending or torsion is considered. The torsion spring-damper option is a purely rotational element with 3 DOFs at each node: rotations about the nodal x , y , and z axes. No bending or axial loads are considered.

The spring-damper element has no mass. Masses can be added by using the appropriate mass element (such as the MASS21). The spring or the damping capability may be removed from the element.

The element is defined by two nodes, a spring constant k and damping coefficient c . The damping capability is not used for static or undamped modal analyses.

A.2 Eigenvalue and eigenvector extraction methods

Neglecting damping, the eigenvalue problem to be solved (previously given by (3.34)) reduces to:

$$[[K] - \omega_r^2[M]]\{\bar{X}\} = \{0\} \quad (\text{A.1})$$

Its extraction procedures include the Reduced, Subspace, Block Lanczos, Powerdynamics, Unsymmetric, Damped and QR Damped ("ANSYS® 11 Theory Reference Manual" (2007)).

According to Wang, E. and Nelson (2002), The Block Lanczos method is a very efficient algorithm to perform a modal analysis for large models. It is a fast and robust algorithm and used for most applications as the default solver. The Subspace method was popular in earlier years since very little computer resources were necessary to perform a modal analysis. However, compared with the Block Lanczos, the Subspace method is faster for small models but solution time increases as soon as larger models are considered. The Reduced method is an old eigensolver which works with reduced matrices in order to minimize the number of DOFs. Neither the Subspace nor the Reduced methods are popular today. The Powerdynamics method is a special algorithm based on the Subspace method, where the user is able to perform an undamped modal analysis of huge solid element models quite efficiently, especially when compared with the Block Lanczos method. The unsymmetric eigensolver is applicable whenever the system matrices are unsymmetric (e.g., an acoustic fluid-structure interaction problem results in unsymmetric matrices).

If damping is included, the QR Damped method can be used for symmetric matrices. This method consists of two parts: first, the Block Lanczos method is used to compute the solution of the undamped system (equation A.1). Hence, all natural frequencies and mode shapes will be calculated for zero damping. In a second step, the equation of motion now including the damping matrix is transformed with the matrices of undamped mode shapes into the modal subspace. After some mathematical manipulations, an extended eigenvalue problem can be formulated. The resulting eigenvalues of this problem are complex, but the effects of damping are not considered for the computation of the resulting mode shapes, which means that only undamped mode shapes are obtained.

The damped method, in contrast to the QR damped method, accounts for the damping matrix for the formulation of the considered eigenvalue problem. From a mathematical point of view this results in a so called *quadratic eigenvalue problem*. The obtained eigenvalues are again complex, but the effect of damping is also considered for the computation of mode shapes which has the consequence that all mode shapes are obtained in a complex form.

A.3 Modelling damping

ANSYS® allows using proportional or non-proportional damping. However, at a first glance, ANSYS® is not very clear in this aspect since the terminology used in "ANSYS® 11 Elements Reference Manual" (2007) turns out to be quite confusing. The confusion starts when the parameter DAMP is defined as *material dependent damping* and the parameter DMPR is defined as *constant material damping coefficient*. However, when introducing the damping in the preprocessor, DAMP is referred to only as *constant* and DMPR is referred to only as *frequency independent*.

Quoting Wang, E. and Nelson (2002), *"if the user wants to apply non-proportional damping but also likes to take advantage of working in the modal subspace ANSYS® provides a special method to do this. The modal analysis has to be done by using the QR Damped Method as an eigensolver. Every kind of non-proportional damping can be considered further in a transient, harmonic or in a spectrum analysis when performed in the modal subspace."* This is said to be a consequence of *"the modal superposition technique (used in the modal analysis) in its classical form cannot take into account the effects of non-proportional damping"*.

On the other hand, experimental evidence from tests performed on a large variety of materials show that damping due to internal friction (material hysteresis) is nearly independent of the forcing frequency (Lazan (1968)). Anyhow, the damping factor in most of the engineering materials is small to the point that both viscous and hysteretic damping models can be fair approximations for most of the real structures.

For these reasons, and also for a matter of simplicity, to choose the *constant* DAMP model instead of the *frequency independent* DMPR damping model does not seem to bring any noticeable benefit. It should be mentioned that the QR Damped method, which can only be run with DMPR, reduces the required solution time for a damped modal analysis significantly when compared to the Damped method.

A.4 Structural analysis types

According to "ANSYS® 11 Structural Guide" (2007), there are seven types of structural analyses available in the ANSYS® family of products. The primary unknowns (nodal DOFs) calculated in a structural analysis are displacements. Other quantities, such as strains, stresses, and reaction forces, are then derived from the nodal displacements.

The following types of structural analyses can be performed:

- Static analysis - used to determine displacements, stresses, etc. under static loading conditions;
- Modal analysis - used to calculate the natural frequencies and mode shapes of a structure;
- Harmonic analysis - used to determine the response of a structure undergoing harmonically time-varying loads, i.e., steady-state vibrations;
- Transient dynamic analysis - used to determine the time-history dynamic response of a structure to arbitrarily time-varying loads;
- Spectrum analysis - an extension of the modal analysis, used to calculate stresses and strains due to a response spectrum from the modal analysis. The spectrum analysis is often used instead of a transient dynamic analysis to determine the response of structures due to random or time-dependent (but ergodic) loading conditions such as earthquakes, wind loads, ocean wave loads, jet engine thrusts, rocket motor vibrations and so on (Wang, E. and Nelson (2002));
- Buckling analysis - used to calculate the buckling loads and determine the buckling mode shape. Both linear (eigenvalue) buckling and nonlinear buckling analyses are possible;
- Explicit dynamic analysis - Used to calculate fast solutions for large deformation dynamics and complex contact problems.

Thus, to compute the PSF a Modal analysis is run, whether it will be used in experimental or numerical examples. For the numerical examples, two Harmonic analysis have to be run with at least a change in one of the parameters (such as a set of elements' damping factors).

Annex B – Summary of the equipment used during the dynamic tests

Table B.1: Summary of the equipment used for the dynamic tests.

Equipment Type	Brand and Model	Dynamic Characterization of the Specimens			Systematic Errors Evaluation			Damage Assessment		
		Mission 1	Mission 2	Mission 3	Transducer Cable Effects	Push-rod Effects	Repeatability	Specimen Beam type 'L'	Specimen Plate type 'A'	Specimen Plate type 'B'
Computer	Various	X	X	X	X	X	X	X	X	X
Specialized Software	B&K ⁴¹ PULSE LabShop 6.1.5.65				X	X	X		X	X
	Harmonica 1.0							X		
	BETAlab 7.05.5b2							X	X	X
	MuDI 9.04.1b0							X	X	X
	Polytec Scanning Vibrometer	X	X	X						
	Mihail-Primoz Convert	X	X	X						X
Signal Acquisition Module	B&K 3109				X	X	X		X	
LAN Interface Module	B&K 7533				X	X	X		X	
Data Acquisition Module	NI DAQCard 6062-E							X		
Signal Conditioning Carrier	NI SC-2345							X		
Accelerometer Input Module	NI SCC-ACC01							X		
Analogue Output Module	NI SCC-AO10							X		
LASER Interferometer	Polytec OFV-508					X	X	X	X	
LASER Controller	Polytec OFV-2802i					X	X	X	X	
	Polytec OFV-3001	X								
	Polytec OFV-5000		X	X						X
LASER Junction Box	Polytec PSV-Z-040-M	X								
	Polytec PSV-400		X	X						X
LASER Head	Polytec OFC-056	X								
	Polytec PSV-400		X	X						X
Accelerometer	B&K Deltatron 4507				X					
	B&K Deltatron 4508				X					
Electromagnetic Shaker	B&K 4809			X	X	X	X	X	X	X
Power Amplifier	B&K 2706				X	X	X	X	X	X
Force Transducer	B&K 8200	X	X	X	X	X	X	X	X	X
Charge Amplifier	B&K 2635	X	X	X	X	X	X	X	X	X
Reflective Tape	3M Scotchlite Diamond Gr 983-10					X	X	X	X	
Glue	HBM Schnellklebstoff X60	X	X	X	X	X	X	X	X	X
Push-rod	Teflon	X	X	X	X	X	X	X	X	X
	Various					X				

Other generic equipment was used, such as: tripod for the LASER, glued mounting threads and glued clips for the transducers, 0.3~0.5mm nylon strings for the free-free simulated suspension, support structure (or ceiling), electrical coaxial connectors, etc.

⁴¹ B&K is an abbreviation for Brüel & Kjær®.

Annex C – On the improvement of experimental repeatability

C.1 Systematic and random errors

When dealing with experimental testing and signal processing, uncertainties will always be present and, up to a certain degree, it could be said they will increase with the amount of variables that interfere with the whole process. Such errors will have effects on the identification of the modal parameters and may lead to a faulty assessment of the damage location.

Errors can be categorized as systematic or random. Systematic errors can usually be avoided and are often due to a problem which persists throughout the entire experiment, for instance the incorrect calibration or inadequate utilization of the equipment. The structural material's susceptibility to the environment conditions, namely to temperature and moisture, is also a source for systematic errors. The systematic errors are reproducible inaccuracies that consistently divert all the measurements in the same direction, resulting in the deviation of the measured average value. Random errors, by contrast, will always be present even though the systematic errors were adequately removed. Random errors are statistical fluctuations (in either direction) in the measured data due to the precision limitations of the measurement chain. They usually result from the experimenter's inability to take the same measurement in exactly the same way to get exactly the same value. Examples of this kind of errors are the lack of sensitivity of the transducers, digital sampling or noise (as external disturbances that are not taken into account as such). The appearance of random errors is inevitable and leads to a random deviation of the results, with equal probability in both directions, in such a way that results float around an average value.

In summary, systematic errors are difficult to detect and cannot be analyzed statistically, because all of the data is off in the same direction (either too high or too low). Spotting and correcting for systematic error takes a lot of care. On the other hand, random errors can be evaluated through statistical analysis, but are something the experimentalist cannot eliminate completely and will always have to live with. The usual way for reducing them (providing he is doing the experiment under the same conditions) is by averaging the results over a large number of observations.

To avoid systematic errors and to ensure experimental repeatability, some testing was made. With these results, guidelines may be issued and a better understanding of the whole experimental process can be achieved.

First, it was assumed that the apparently equal specimens would behave exactly the same way, despite the fact that differences could be found in minor details. During manufacturing, it was not possible to guarantee that the fibres were along the supposed direction (within a reasonable tolerance). Also, during the polymerization process in the autoclave, it was not possible to take direct control over the way the resin flows to the bleeder, meaning that small changes in the specimen thickness could appear. During the cutting process, the slightest misalignment of the guiding rules will turn the specimens into trapeziums instead of rectangles and imperfections appear on the specimen's edges.

C.2 Accelerometers' cables effects

The effect of the transducers' cables on the results was appreciated by conducting tests on specimen plate A3H. Four Brüel & Kjær® miniature accelerometers were used for the responses measurement at the same time. Three different tests were done by changing the position of the accelerometers' connectors as illustrated in figure C.1. For the first two positions, type 4507 accelerometers were used, whereas type 4508 accelerometers were used for the last configuration. The results for the direct FRF are shown on figure C.2.

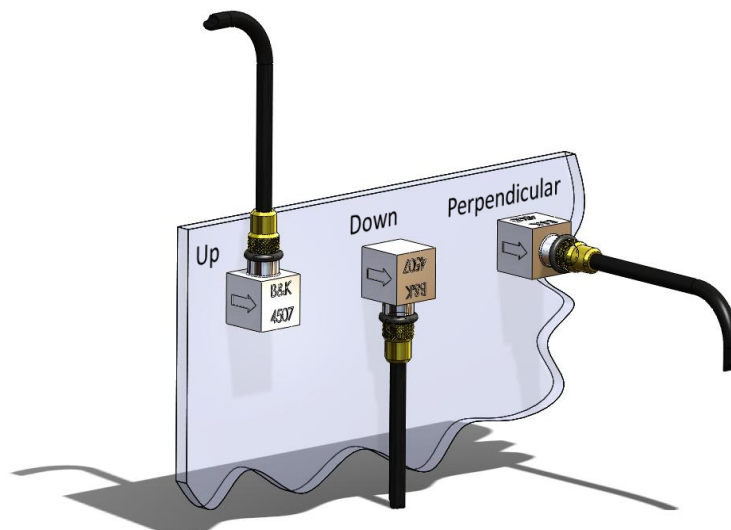


Figure C.1: Position of the accelerometers' connectors and cables.

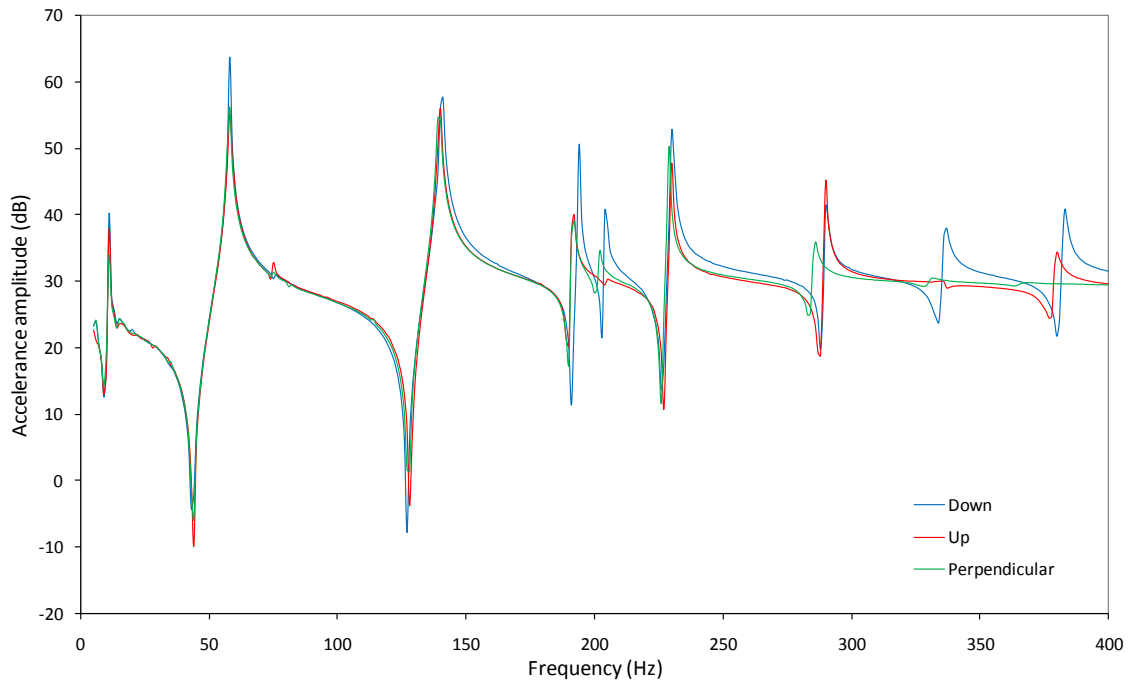


Figure C.2: Comparison between FRFs obtained using different configurations of the accelerometers' cables.

It can be observed that the cables have a noticeable influence on the experimental results that will most surely hide some of the smaller changes caused by damage. It is the belief of the author that this is mostly due to the lightness of the structure. The use of transducers attached to the structure results in undetermined added mass and stiffness effects. This was avoided by using a kind of non-contact equipment, a LDV, having the advantage of not physically interfering with the structure. As a disadvantage, for lightweight structures, it is not easy to perform the measurement if rigid modes with large displacements have not vanished (because the LASER lens is not isolated from the ground whereas the accelerometers are). Rigid modes appear because the specimen plate is suspended by long strings in two separate points simulating free-free boundary conditions, which can easily lead to pendulum motion.

C.3 Push-rod effects

Push-rods (often also referred in the literature as *stingers* or *drive rods*) are used to apply the excitation force from the shaker on the structure. The objective is to transmit controlled excitation to the structure in a given direction and, at the same time, to impose as little constraint on the structure as possible in all the other directions. Despite the connecting devices being designed to reduce the attachment influence between the shaker and the

structure, there will always be undetermined constraining effects and mass loading of the structure (Maia and Silva (1997)). Figure C.3 shows a typical drive-rod assembly.

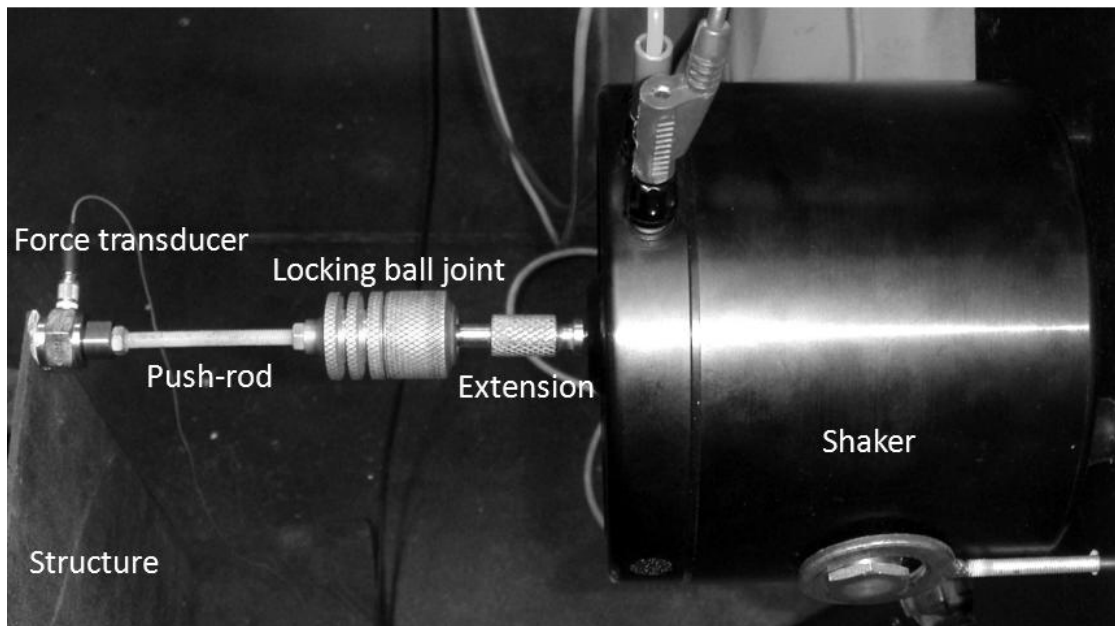


Figure C.3: Drive-rod connection between exciter and force transducer.

The locking ball joint fixture allows for simple alignment of the excitation direction, when the structure is not exactly perpendicular to the exciter's axial direction, also minimizing push-rod bending. In the present case, the extension is not adjustable and acts only as a connection between the shaker and the locking ball joint fixture. However, this push-rod is threaded over its whole length, allowing for simple adjustment of the positioning of the shaker along the excitation direction. Locking nuts on the tips of this push-rod will prevent it from twisting during vibration. The whole setup is completely removable and replaceable, thereby avoiding damage to the shaker, structure or transducers, while repositioning is done.

One consideration is that it is desirable that the push-rod is as stiff as possible in the longitudinal direction so that its first mode is above the frequency range of interest. However, in most cases, the structure responds to the excitation by both translating and rotating, and therefore, restraints are imposed and the force transducer will be affected by a reaction torque that will distort the force signal and introduce errors in the results. To avoid this, a flexible push-rod usually forms some part of the link between the shaker and the structure under test. The push-rod is designed so that it is relatively flexible to lateral and rotational motions between its ends, but very stiff axially. Polymers (such as in coating or Teflon® stingers) are used with the aim of increasing damping and attenuating the possible influence of push-rod modes.

Maia and Silva (1997) argue that, despite all the facts that are discussed about push-rods, “there is still no substitute for actually trying out several different push-rods during preliminary investigations to obtain one that is best suited.” Four different push-rods were tested, using the configuration shown in figure C.3, again using plate A3H: hardened steel wire, clothesline stranded steel cable, plastic coated clothesline stranded steel cable and threaded Teflon® stingers (figure C.4). The results for the direct FRF are shown in figure C.5.

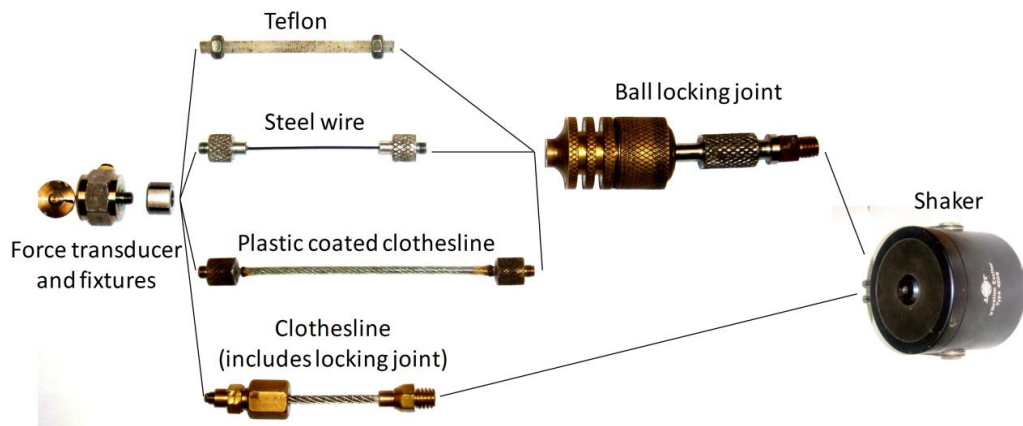


Figure C.4: Different types of push-rods and correspondent attachments to the shaker and to the structure (force transducer).

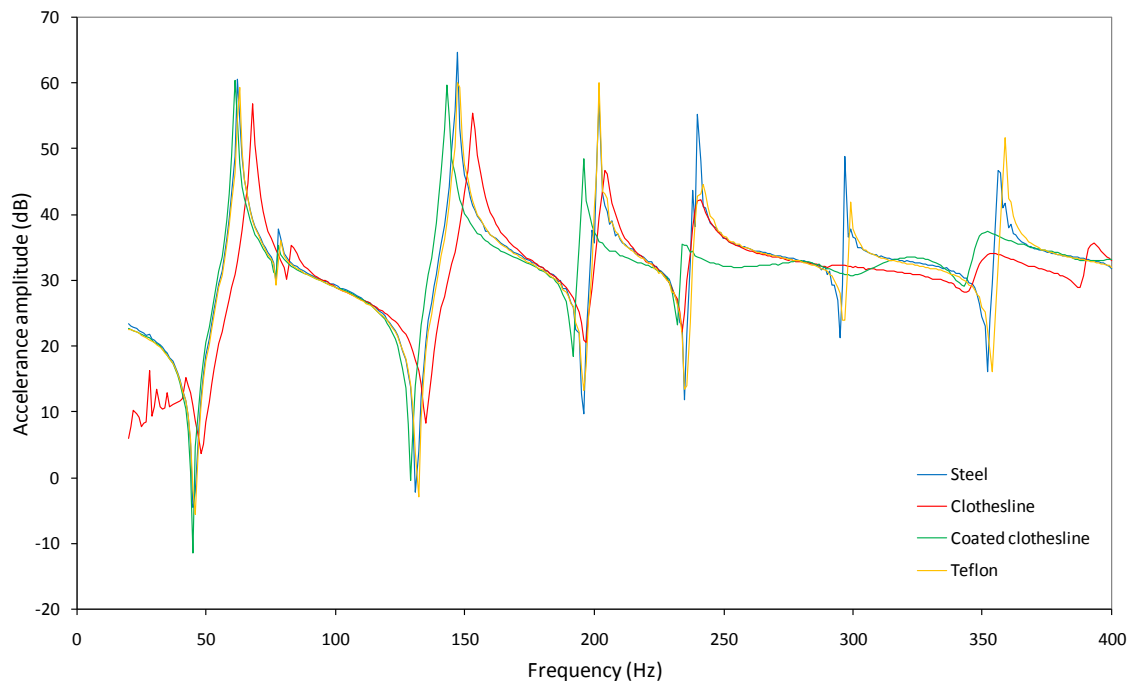


Figure C.5: Comparison between FRFs obtained using different push-rods.

Different push-rods largely affected the results, as already observed by Montalvão (2003) in another work. The best agreement was observed between the hardened steel wire and the threaded Teflon® stingers.

C.4 Repeatability

After the entire setup was chosen, repeatability tests were performed. Two types of repeatability tests were tried. The first one is concerned with differences between the specimen plates (which, in theory, should be equal). The second one is concerned with random errors, namely with those arising from the setting up of the experimental apparatus.

To evaluate possible differences in the dynamic behaviour of the specimens, the same test under the same conditions (as far as possible), was performed over specimen plates A1H, A2H, A3H and A4H. The results for the direct FRF are shown in figure C.6.

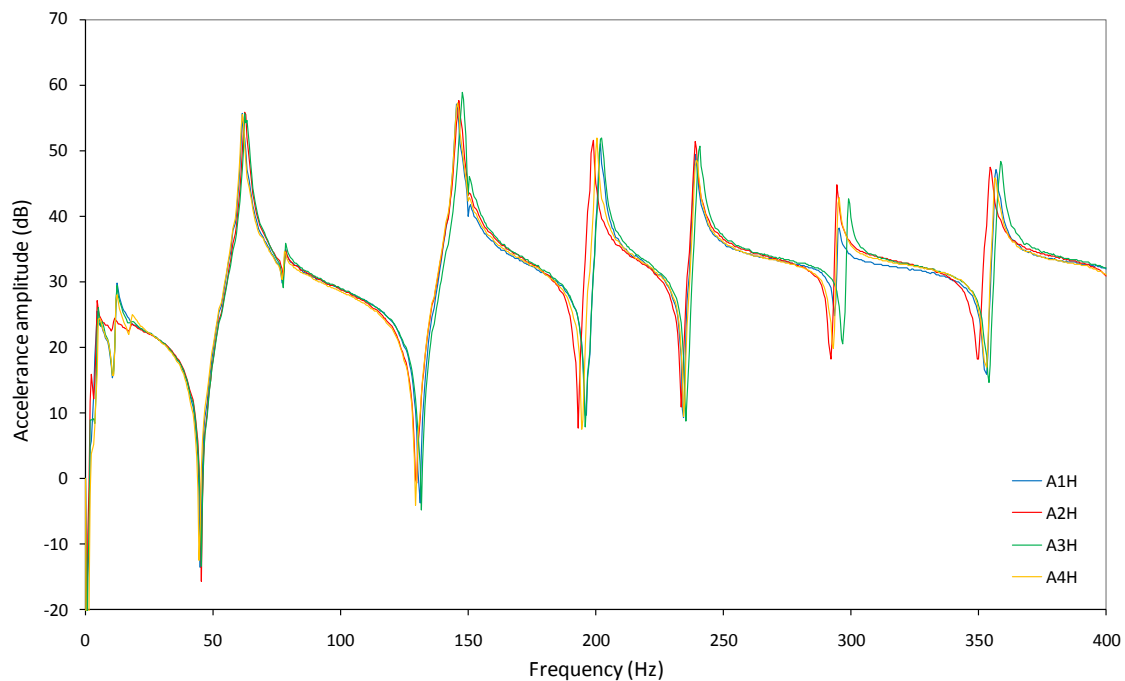


Figure C.6: Comparison between FRFs from different specimen plates.

Keeping in mind the whole manufacturing process, it was not hard to predict some variations might occur. As a consequence, although the same mode shapes were used, as discussed in the main body of this work, the slight differences in the natural frequencies were considered.

In order to assess random errors, tests were made using specimen plate A4H. A total of 20 tests including full assembly and disassembly of the experimental setup for each run was performed. The results for the direct FRF are shown in figure C.7.

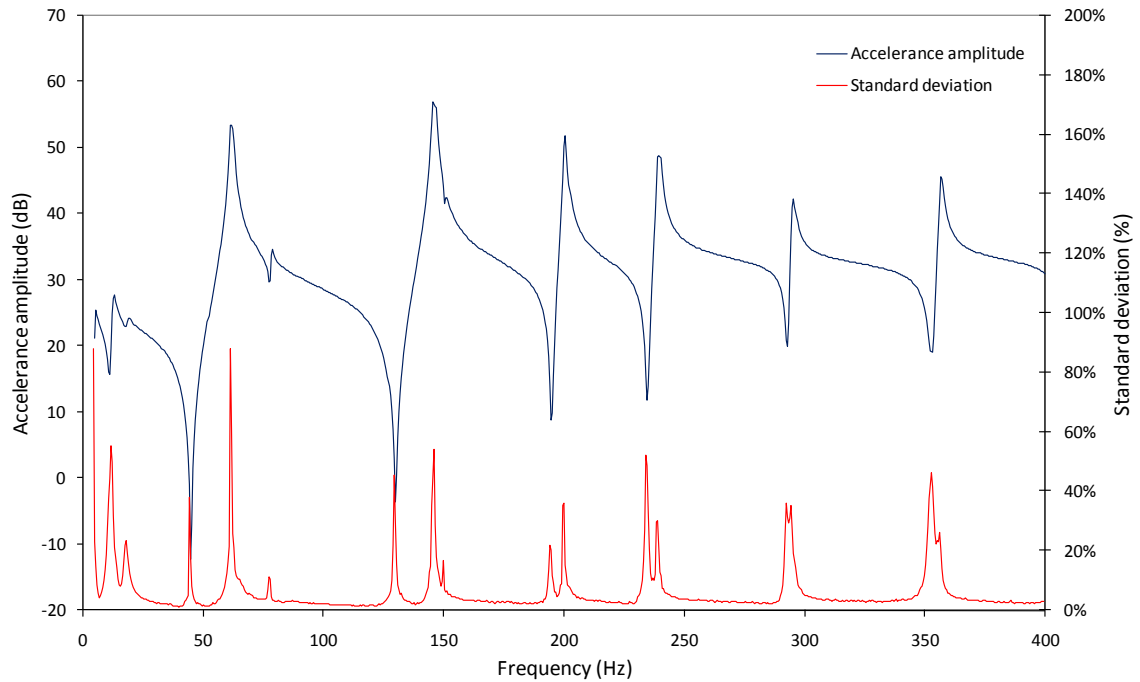


Figure C.7: Amplitude of the averaged accelerance and accelerance standard deviation after 20 measurements on plate A4H.

The major conclusion to draw is that the largest standard deviation values occur at the resonance and anti-resonance regions (what is perfectly normal), whereas away from these regions the standard deviation does not generally go beyond the 3%.

C.5 Final remarks

Two of the measurement chain components that had a strong influence on the experimental results were the accelerometers' cables and the push-rod. While the push-rod is inevitable⁴² unless one chooses to follow an OMA approach instead of EMA (thus bringing up several other issues), the influence of the accelerometers' cables can be minimized if non-contact devices are used, such as a LDV.

Finally, emphasis should be given to the idea that a powerful experimental method would be one that minimizes the amount of variables affecting the whole process. To achieve such an objective, a faithful reproduction of similar conditions must be assured when performing tests on different occasions, keeping in mind the environment external influence, such as the effect of the temperature.

⁴² Since hammer excitation would set up undesirable pendulum motion.

Annex D – HARMONICA[®] Software

D.1 Introduction

Many approaches are available to measure the dynamical behaviour of structures. According to Maia and Silva (1997), these approaches have been historically divided in Phase-Resonance methods (Normal Mode testing or Sine Dwell testing) and Phase-Separation Methods (Stepped-Sine and Broadband testing). The Phase-Separation Methods are the most generalized in the field of modal analysis, since they allow for the use of a single point force excitation, for example the one used with an impact hammer. Within these methods, one may find typical excitation techniques, like Random, Pseudo-Random, Sweep-Sine, Multi-Sine or Stepped-Sine.

For the techniques that use the Stepped-Sine approach, a shaker is used to excite the structure at a single, precisely controlled, frequency. After settling into the steady-state, it is possible to measure the amplitude and phase of the input and output signals at that given frequency, which means one can compute any transfer function (FRF or Transmissibility) without resorting to the Fourier Transform.

Since the signals are harmonic, the FRF $H(\omega)$ can simply be computed for each frequency ω as earlier mentioned in chapter 3.4.1:

$$H(\omega) = \frac{X(\omega)}{F(\omega)} \quad (\text{D.1})$$

where $X(\omega)$ is the complex response and $F(\omega)$ the complex force. The Transmissibility function can be computed in a similar way. The frequency is subsequently incremented, and the measurement process repeated.

From the above, it is easy to understand that it is possible, within the capabilities of the available equipment, to compute transfer functions for any frequency range with any spectral resolution. This is a versatility that commercial analyzers don't usually have, since most of them use the FFT, limiting the number of lines to powers of 2.

One of the major advantages of the Stepped-Sine technique is its large signal-to-noise ratio, since the energy is totally concentrated in a single spectral line of the frequency spectrum. The Broadband Testing techniques, require that an analogue-to-digital converter acquires the energy over the whole frequency spectrum. However, the energy distribution usually present

severe differences in amplitude along the frequency range. This is not an issue in the case of the Stepped-Sine, since all of the energy of the excitation/response is fully dedicated to a single spectral line and thus allowing for the proper settings for each frequency.

Another advantage of this technique is the possibility of experimentally assessing the nonlinear dynamic behaviour of a structure, since it is possible to precisely control one input/output as a reference channel. Near the resonant frequencies, the structure will respond with high amplitudes which strongly depend on the applied excitation. If the force is not controlled, the structural nonlinear behaviour (when it exists) can lead to inconsistent measurements representing difficulties to the analysis. Conversely, when using the Stepped-Sine technique, one can impose that the force has a constant value for each measurement frequency. Changing the value of the force for each measurement, allows for experimentally estimating the system nonlinearities. Nevertheless, because the force signal tends to have low values near the resonant frequencies, it may not be possible to maintain the same value for the force since the equipment (namely the signal generator) may become overloaded. One form of avoiding this situation consists on controlling a response instead of a force. However, in such case, a similar problem might occur near anti-resonant frequencies. These problems can be overcome if a lower limit level for the excitation/response to control is defined (whether it is the force or the response being controlled), although that might decrease the signal-to-noise ratio over the rest of the frequency spectrum. Hence, a compromise solution must be achieved in the beginning of each measurement, considering the purposes of the experimental test being carried out.

The most evident disadvantage of this method is the time consumed to perform each measurement. By its own nature, the Stepped-Sine technique is very time consuming, when compared to the other common techniques. However, some authors remarked that this is not a major objection when it takes a couple of days for setting up a large test (Aitavale (2005)).

D.2 Program overview

The HARMONICA[®] Stepped-Sine Spectrum Analyzer was fully developed by the author in LabVIEW[™] 7.1 from National Instruments[™]. It has the following main features:

- Single point Stepped-Sine excitation;
- Up to 8-channel simultaneous measurement of forces and responses;
- Optional constant control of a reference channel, which can be a force, acceleration, velocity or displacement, for nonlinear experimental assessment. The control is

independent of the type of transducer used (for instance, the control can be made in displacement using an accelerometer);

- Allows estimating transfer functions as FRFs or Transmissibility Functions.

This software is freeware and can be downloaded by any interested person at: <http://ltodi.est.ips.pt/dmontalvao/downloads.htm>.

D.3 Assessment of the software performance and tips

Testing the program was carried out using a NI-DAQCard™-6062E, a NI Signal Conditioning SC-2345 Carrier, NI SCC-ACC01 Accelerometer Input Modules and a NI SCC-AO10 Isolated Analogue Output Module. Several different tests were carried out to test the HARMONICA® program. To establish a reliable comparison, the same tests were also performed using a commercial program (PULSE™ from Brüel & Kjær®) and using Random and Multisine excitation signals. The results, further discussion and other details can be found in Montalvão and Fontul (2006), showing a good agreement between HARMONICA® and PULSE™.

In the remainder of this section, some tips are given on how to get the best results with HARMONICA®, based on the gained experience during the assessment of the software performance.

There are two very important parameters that should be carefully introduced on HARMONICA®'s setup before any measurement: transient delay and number of cycles after transient. The transient delay is the time the programme waits for vibration to settle for each generated sine frequency. The correct setting of this parameter strongly depends on the experience of the user and on the structure under test. At least one measurement, with a coarse spectral resolution (for the measurement not to take too long), should first be performed in order to perceive the adequate value to be set for the transient delay (0.1~1.0s should be enough). The number of cycles after transient defines the length of the recorded data from which the program will extract the amplitude and phase of the responses.

Before determining the Amplitude and Phase, the recorded data suffers some processing. First, eventual offsets of the signal are eliminated. Then, this same data suffers a narrow band filtering around the frequency of the signal, using a FFT based routine that returns the signals phase. Since the program will extract the RMS value of the sine to compute its amplitude at each frequency, the amplitude obtained can be seen as an average.

When using control of force, it is possible that the constant established value for the force cannot be hold near the resonant frequencies. As it is known, the resonant frequency occurs

for a minimum value of the force, and not for a maximum value of the response (the maximum value of the response occurs a little earlier). Since the force is achieving smaller values near the resonant frequencies, HARMONICA[®] will increase the amplifier gain in order for the force to hold constant around the specified value. It is clear that at a certain point it can happen that the maximum allowed amplifier gain is achieved, precluding the possibility of further increasing the value of the force.

When using control of response, a similar discussion can be formulated. Near the anti-resonant frequency it may not be possible to maintain the response specified level. Since the response is achieving smaller values near the anti-resonant frequencies, the HARMONICA[®] program will increase the amplifier gain in order to increase the exciting force and so to bring the response to the specified level. Again, this may not be possible if the amplifier gain achieves its maximum allowed value.

Better results were obtained by Montalvão and Fontul (2006) for control of response rather than for control of force. Near anti-resonant frequencies the response is locally very small. It should be clear that near the anti-resonant frequencies the force achieves large values and the local response small values at (exactly) the same time. This indeed happens simultaneously, since the mass of the system has locally negligible effects. Hence, when using control of force, the required amplifier gain near the anti-resonant frequencies is considerably smaller when compared to the rest of the frequency range. In such a case, the signal-to-noise ratio of the signal acquired from the response transducer is most probably very low, thus leading to greater dispersion on the results. For control of response this will be less evident near the resonant frequency, because the maximum response occurs earlier than the resonant frequency and not simultaneously.

In summary:

- the transient delay and the number of cycles after transient are core parameters for the correct signal acquisition;
- it seems that control in response is a promising way to obtain consistent results with HARMONICA[®] for the study of nonlinear effects.

D.4 System requirements

The HARMONICA was programmed in LabVIEW[™] 7.1 from National Instruments[™] for Microsoft[®] Windows[®]. Any requirements should be in accordance to those of this version from LabVIEW[™] 7.1. It is strictly necessary that NI-DAQ[™] Reference Drivers and Measurement &

Automation Explorer[®] are installed. These programs, which usually accompany any hardware from National Instruments[™], are used to configure the measurement hardware and also provide important libraries for HARMONICA[®] to work. NI-DAQ[™] is available for download at www.ni.com. HARMONICA[®] v1.0 was tested under NI-DAQ[™] 7.4 (Legacy).

The computer used was a Laptop with Intel[®] Pentium[™] M 1.4 GHz processor and 512Mb of RAM. The program was tested under Microsoft[®] Windows[®] XP environment.

This program is designed to be run with a resolution of (at least) 1024x768.

D.5 Channel definition on Measurement & Automation Explorer[®]

National Instruments[™] Measurement & Automation Explorer[®] is an application that usually accompanies the hardware and that allows to, amongst others:

- To configure National Instruments[™] hardware and software;
- To create and edit the channels' properties;
- To view devices and instruments connected to the system.

Before running HARMONICA[®], the hardware, software and channels should be properly configured. Refer to Measurement & Automation Explorer[®] manual for details on how to configure them.

However, some of the information, like the sensitivity of the transducers and their units are introduced in HARMONICA[®] itself, in such a way that the only information required on Measurement & Automation Explorer[®] (for each channel) is:

- Channel name;
- Range of the physical quantity to be measured (these values should be in Volts)⁴³;
- Sensor type (this should be a Voltage when using transducers such as accelerometers);
- Hardware device;

⁴³ Since the HARMONICA program is designed to be used with conventional transducers, such as accelerometers, vibrometers or force transducers, it is assumed that the range of the physical quantities to be measured is symmetrical, in such a way that the only relevant field to be accurately introduced on MAX is the upper value of the physical quantity's range (max value). The lower value (min) will be ignored by the program. If, for any reason, the range of the transducer is, for instance, between +5 and -3 Volts, the lower absolute value (3 Volts) should be chosen for both the max and min values of the physical quantity's range. Otherwise, if clipping occurs, the program may not be able to detect it.

- Hardware channel;
- Hardware input mode.

No other data, such as the physical quantity units or a sensor scaling formula need to be introduced. Figure D. shows an example of an input channel configuration on Measurement & Automation Explorer[®] for use with the HARMONICA[®] program.

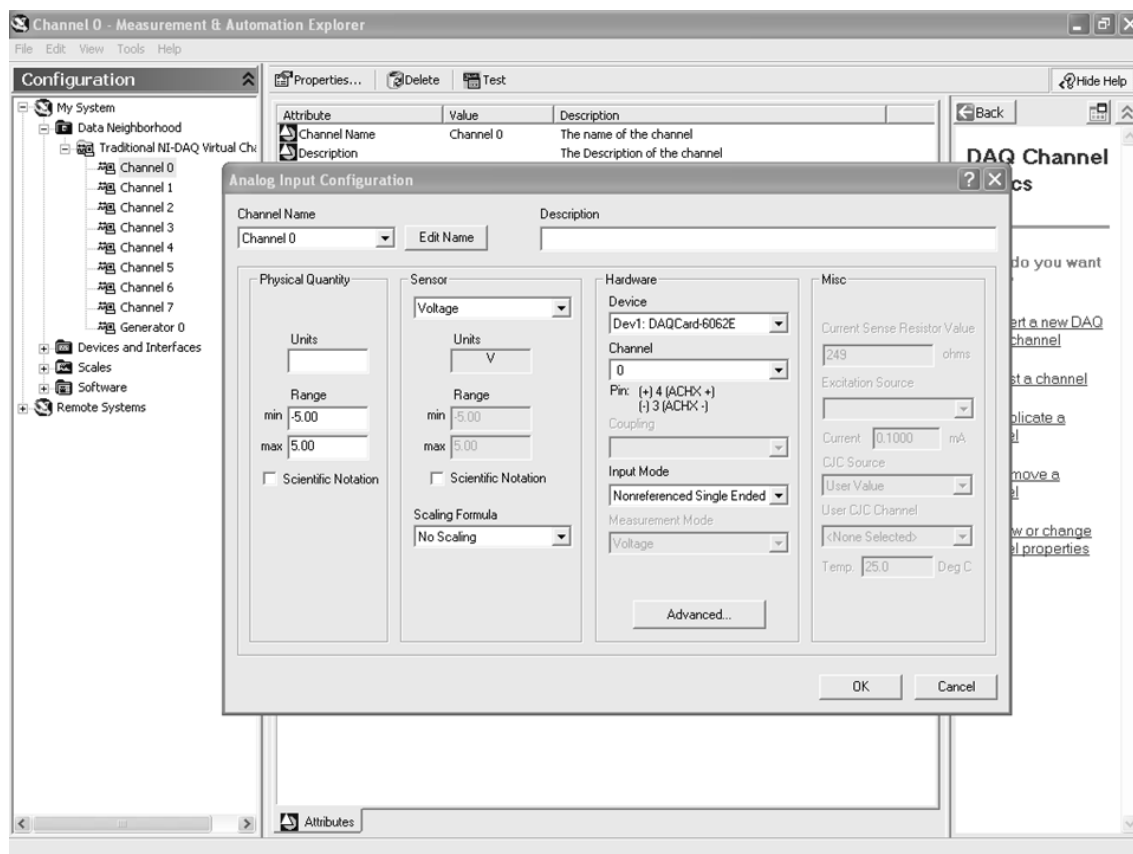


Figure D.1: Example of a channel configuration on Measurement & Automation Explorer[®].

D.6 Operation

D.6.1 Home Panel

The HARMONICA[®] is divided into 4 panels that should be played sequentially as follows:

- Home;
- Setup;
- Measurement;
- Results.

The Home panel is the panel that appears when the program is executed, and is solely used for presentation purposes.



Figure D.2: Home Panel.

Panels can be changed on the tabs on the upper left corner of the window. That should be done sequentially.

On the bottom, there are 4 buttons and one indicator. These are present in any of the 4 panels. From left to right, one has:

- EXIT – Exits HARMONICA[®] closing LabVIEW[™];
- About – Information regarding the author (name, contacts, etc.);
- Generator Status – Indicates if the program is generating a signal to the exciter;
- Stop Generator – Stops the generator, interrupting a measurement;
- Start Generator – Starts the generator, beginning a measurement.

D.6.2 Setup Panel

The Setup Panel is the most important one, since it is here that one fully defines the measurement setup.

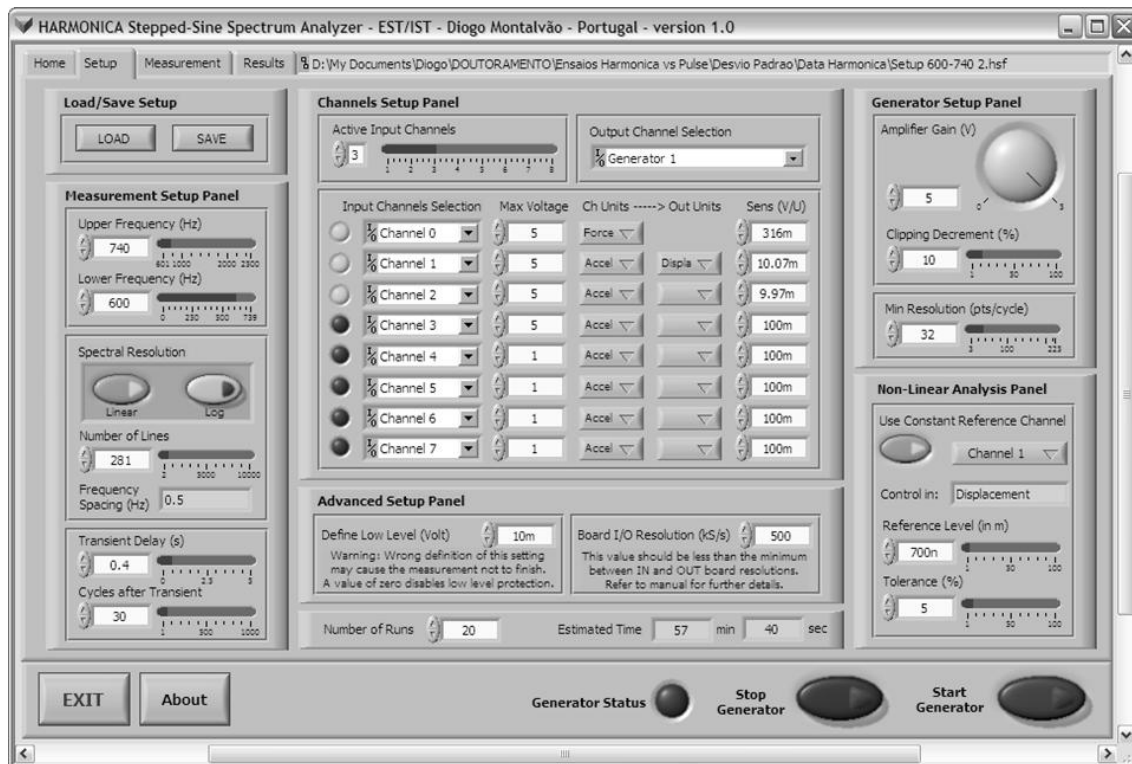


Figure D.3: Setup Panel.

The Setup Panel is divided into several smaller panels. Following this sequence, one has:

- Load/Save Setup:
 - Load – Loads a previously saved setup. The program will ask for files with the extension “.hsf”;
 - Save – Saves the current setup into a file with the extension “.hsf”.
- Measurement Setup Panel:
 - Upper Frequency (Hz) – Upper frequency of the frequency range;
 - Lower Frequency (Hz) – Lower frequency of the frequency range;
 - Spectral Resolution:
 - Linear⁴⁴ – The frequency spacing is constant, i.e., the absolute frequency spacing is the same for the entire frequency range;

⁴⁴ For example, if the measurement is made from the 200 to the 800 Hz, a Linear Spectral Resolution of 301 lines corresponds to a frequency spacing of 2 Hz (200Hz, 202Hz, 204Hz, 206Hz, ..., 796Hz, 798Hz, 800Hz).

- Log⁴⁵ – The frequency spacing is logarithmic, i.e., the relative (percentage) frequency spacing is the same for the entire frequency range. As a result, for lower frequencies the frequency spacing is smaller in absolute terms than for larger frequencies.
 - Number of Lines – Number of lines used to divide the frequency range. This also corresponds to the amount of sines generated during a run-up;
 - Frequency Spacing – Indicator of the frequency spacing. This is presented in Hz in case the Spectral Resolution is Linear, or in the form of a percentage in case the Spectral Resolution is Logarithmic;
 - Transient Delay⁴⁶ – Time waited for the system to settle for each generated sine. This parameter largely depends on the experience of the user and on the structure under test;
 - Cycles after Transient – Integer number of cycles used in the analysis after the system has settled. This can be seen as an average. The amplitude and phase of the signal will be extracted from this sine time wave.
- Channels Setup Panel⁴⁷:
 - Active Channels – Number of Input channels used in the experimental setup. The number of Input channels can vary from 1 to 8;
 - Output Channel Selection – Selection of the Output channel (generator);
 - Input Channels Selection – Selection of the Input channels to be used during measurement;
 - Max Voltage⁴⁸ – Maximum voltage allowed for the specified transducer, according to their technical specifications. It is necessary to have this

⁴⁵ For example, if the measurement is made from the 200 to the 800Hz, a Log Spectral Resolution of 301 lines corresponds to a frequency spacing of 0.46% (200Hz, 200.92Hz, 201.84Hz, 202.77Hz, ..., 792.68Hz, 796.33Hz, 800Hz).

⁴⁶ It is recommended that several run-ups are first executed with a rough Spectral Resolution in order for the user to understand how much the Transient Delay's adequate value is. In a free-free 800x25x6mm3 steel beam, with point excitation in one of its tips, it was found that a Transient Delay of 0.4s was the smallest adequate value.

⁴⁷ Only channels first defined in MAX can be selected (either Input or Output channels). If no channels were previously defined in MAX, execution of the program may cause errors, and the program can be aborted.

⁴⁸ When the program is executed, it will automatically retrieve the Max Voltage values from MAX for the first 8 Input channels defined. If a channel is changed in the Input Channels Selection, it is necessary to manually introduce a new value for the Max Voltage value relative to that channel.

parameter accurately defined, so that the clipping protection algorithm can be effective;

- Ch Units – Channel units of the specified transducer. For instance, if the transducer is an accelerometer, the units should be defined as “acceleration”;
 - Out Units – Output units of the transducer. The kinematic units can be converted by integration or differentiation. For example, the output units of an accelerometer can be converted to a displacement. This is particular useful when one wants to have control of the dynamic behaviour of the structure for nonlinear analysis;
 - Sens – Sensibility of the channel transducer in Volts per Channel Unit (Ch Unit) of the transducer.
- Generator Setup Panel:
 - Amplifier Gain⁴⁹ – The generator output signal expressed in Volts. The maximum value is retrieved from Measurement & Automation Explorer® for the Output Channel selected;
 - Clipping Decrement⁵⁰ – Clipping can be avoided based on the Max Voltage specified on Measurement & Automation Explorer® or in the Channels Setup Panel. If clipping occurs during a measurement, the program will decrease the Amplifier Gain by a percentage defined in this control;

⁴⁹ In the case the Use Constant Reference Channel of the Nonlinear Analysis is set to OFF, the gain output value will be constant for the whole frequency domain (unless clipping occurs). In the case the Use Constant Reference Channel of the Nonlinear Analysis is set to ON, the gain for the Output Channel value will vary between the value defined by the Amplifier Gain and zero. In this case, a large value for the Amplifier Gain should be defined, though caution should be made not to cause overload.

⁵⁰ Example of the Clipping Decrement function: If clipping occurs for a gain of 7V, and if the Clipping Decrement is defined to 10%, the Amplifier Gain will be temporarily reduced to 6.3 and the measurement repeated for that specific frequency. If clipping still occurs, the measurement will be repeated decreasing the Amplifier Gain by another 10% lowering it to 5.7V. When no clipping is detected, the program will carry on the measurement for higher frequencies, with the original Amplifier Gain of 7V.

- Min Sine Resolution⁵¹ – Minimum resolution (number of points per cycle) for each generated sine wave.
- Nonlinear Analysis Panel:
 - Use Constant Reference Channel – When this control is set to ON, the program will try to maintain a reference channel with a constant value (within a defined Tolerance value) for all the frequency range in the Output Units;
 - Reference Level⁵² – Value (in the Output Units) that should be measured by the reference channel in the whole frequency range;

⁵¹ Each sine is digitally generated with an integer number of points per cycle. The number of points per cycle is optimized between the Min Sine Resolution value and a Max Sine Resolution (which is based on the Board I/O Resolution, Upper Frequency, and number of Active Channels) so that the error between each generated frequency and the desired frequency is as small as possible. These errors occur due to the clock limitations of the board, and it is expectable to happen with any equipment. For better results, a low value should be defined for the Min Sine Resolution and a large value should be defined for the Board I/O Resolution. However, for very low Min Sine Resolution values, the generated sine wave can become excessively coarse. As an example, suppose the board has a clock frequency of 20MHz, the Min Sine Resolution is defined to 10 points/cycle, the Board I/O Resolution is 500kS/s, there are 4 Active Channels and the Upper Frequency is 1000Hz. For an asked frequency of, for instance, 798.00Hz, the optimized value for the number of points per cycle is 71, thus returning an output frequency of 797.99Hz. Conversely, if only a fixed sine resolution is defined, for instance 300 points/cycle for all the stepped-sines, the closest frequency to 798.00Hz the board can produce as an Output is 803.21Hz. The reason for the dependency of the output resolution (points/cycle) with the number of channels is related to the fact that better accuracy is achieved in the algorithms when both the input and output resolutions are synchronized. The closer the values of the Min Sine Resolution and Board I/O Resolution are, the greatest can be the difference between the asked frequency and the generated frequency, as a consequence of hardware constraints.

⁵² The program will automatically adjust the Amplifier Gain in order to maintain the Reference Level of the Reference Channel within a defined Tolerance value in the Output Units. The Amplifier Gain is iteratively adjusted in order for the measured signal of the transducer to fall between the Reference Level \pm Tolerance(%). It is recommended that several run-ups are first executed with a rough Spectral Resolution in order for the user to understand which are the adequate values for the Reference Level and Tolerance. After definition of the adequate Reference Level boundary, several measurements can now be carried out with the desired setup for different Reference Levels for nonlinear behaviour assessment. In the case one is using a Force as the Reference Channel, it may happens that it is not possible to hold the Reference Level constant around Resonance Frequencies, as a consequence of the Force achieving very low values. In the case one is using a Response as the Reference Channel, it may happens that it is not possible to hold the Reference Level constant around Anti-Resonance Frequencies, as a consequence of one or more Responses achieving very low values. In both situations the program will try to raise the output level of the Reference Channel by temporarily increasing the Amplifier Gain. This may lead to one of two situations: overload of one channel (detected by clipping) or the gain achieves its maximum value allowed (defined in the Amplifier Gain control). If any of these situations occur, the Reference Level control algorithm is interrupted for that specific frequency.

- Tolerance – Percentual tolerance accepted around the Reference Level. The lower this value is, the longer the measurement can take.
- Advanced Setup Panel:
 - Define Low Level⁵³ – This value, defined in Volts, is used as a protection for situations that occur during testing in which the board does not send the signal to the generator. Those situations can occur if other programs are running in background, such as an anti-virus. This is very effective if more than one channel is being measured simultaneously (especially if a force and at least a response are being measured), but can fail if only one channel is being measured. What the program does is to measure all the amplitudes of the time signals and verify if the amplitudes (in Volts) are below the defined level. In such a case, the measurement at that frequency will be repeated. To turn this protection off, a value of zero should be chosen;
 - Board I/O Resolution⁵⁴ – Smallest value in kS/s (kilosamples per second) between the Input and Output resolutions of the Hardware Board being used.
- Other controls and indicators:
 - Number of runs⁵⁵ – Number of times the whole measurement defined in the setup will be repeated;
 - Estimated Time⁵⁶ – Estimated time for the whole measurement to take. This value is a gross estimate.

⁵³ Inadequate definition of this setting may cause the measurement not to finish. A value of zero disables low level protection. It is recommended that one run-up is first executed with a rough Spectral Resolution in order for the user to understand which the adequate value is for the Low Level.

⁵⁴ The program will try to automatically retrieve this value. In case that value is not correct, the user should introduce it manually. Also, if the user does not intend to work near the limits of the board, it is possible to define a lower resolution. If this value is higher than the minimum value between the Input or Output resolutions of the Board, it is possible that the measurement is interrupted and that the program is abruptly terminated.

⁵⁵ Since the Stepped-Sine excitation technique is by nature a slow process, this can be a useful tool if one wants to, for instance, later estimate the standard deviation of the results or perform any kind of statistical processing.

⁵⁶ When using a Constant Reference Channel, it is possible that the measurement time is many times greater than the value presented herein.

D.6.3 Measurement panel

This is a merely indicative panel, which is active during the test run-ups. Once during a run-up it is not possible to change to other panel. This panel is constituted by the following:

- **Waveform Real-Time Non-Filtered Full Signal** - In this graph the full waveforms are plotted as acquired directly by the transducers without any filtering or signal processing. The purpose is to give the user a perception whether the system has settled into steady-state vibration or not. A green vertical line is plotted marking the end of the Transient Delay time and the beginning of the measurement record;

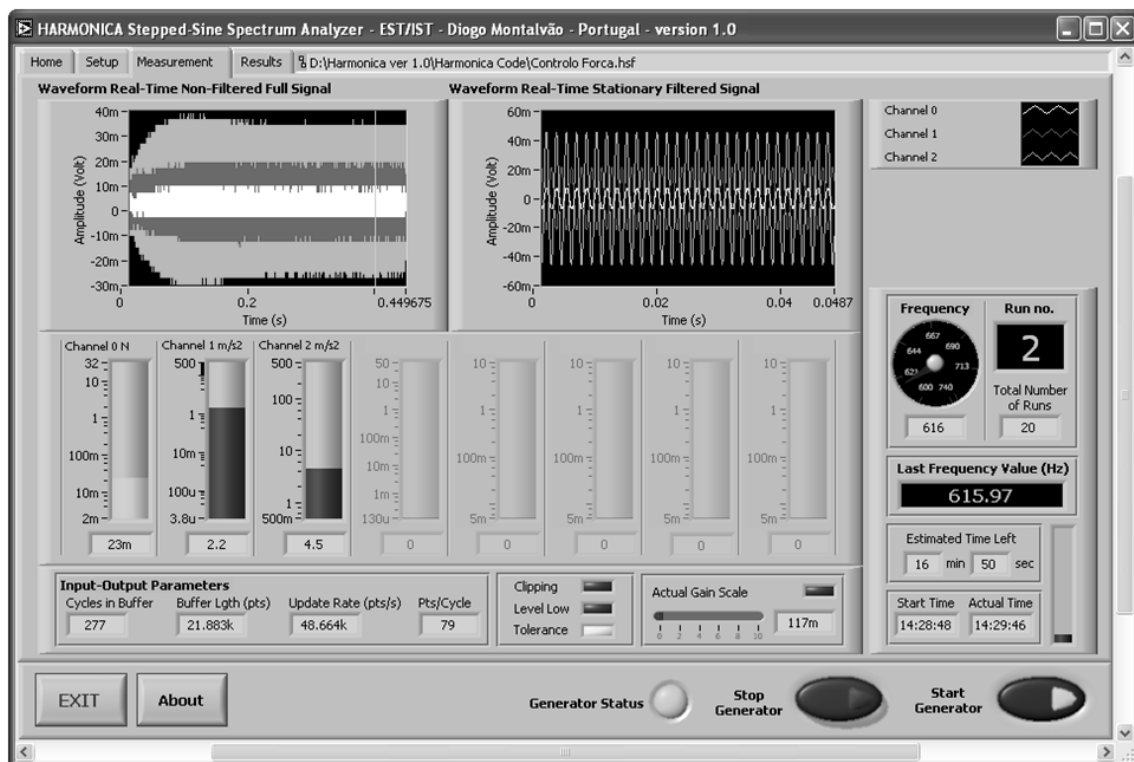


Figure D.4: Measurement Panel.

- **Waveform Real-Time Stationary Filtered Signal** - In this graph only the recorded signal is plotted, after being filtered and processed. For each frequency, the data corresponding to the number of Cycles after Transient is presented;
- **Tanks** - The dark green tanks are used to represent the level of the signals acquired by the transducers, represented in the Output Units, during each Stepped-Sine. These tanks use a logarithmic scale. If clipping occurs on any channel, the tank corresponding to that channel will turn to red temporarily. If using a Constant Reference Channel, the colour of the correspondent tank will be light green;
- **Input-Output Parameters** - Indicators of the data given to the Board for generating and measuring a Stepped-Sine at each frequency: Cycles in Buffer (number of cycles),

Buffer Length (number of points or samples) and Update rate (points or samples per second). These parameters are calculated based on the data introduced in the Setup Panel and on the optimization algorithm used to define the best number of points per cycle for each frequency;

- Clipping - Whenever a transducer reaches its Max Voltage level, this indicator turns red, and the measurement is repeated for that frequency with an Amplifier Gain lowered temporarily by a percentage defined in the Clipping Decrement control. Whenever this indicator is on, the measurement time will increase;
- Low Level - Whenever all the amplitudes of the time signals (in Volts) are below the Low Level defined on the Setup, this indicator turns cyan, and the measurement is repeated using exactly the same parameters. This is used as a protection for situations that occur during testing in which the board does not send the signal to the generator. Those situations can occur if other programs are running in background, such as an anti-virus. Whenever this indicator is on, the measurement time will increase;
- Tolerance⁵⁷ - When using a Constant Reference Channel, the Amplifier Gain has to be iteratively adjusted in order for the measured signal of the transducer to fall within the Reference Level \pm Tolerance (%). When the program is doing these iterations, this indicator turns yellow. Whenever this indicator is on, the measurement time will increase;
- Actual Gain Scale - Value of the Amplifier Gain. This value can change if clipping occurs and if a Constant Reference Channel was defined;
- Frequency - This indicator is used to indicate the desired Stepped-Sine frequency that the program is trying to generate;
- Run no. - Indicator of the measurement run number;
- Last Real Frequency Value - The frequency actually generated by the hardware equipment on the previous Stepped-Sine;
- Estimated Time Left - Indicator of the estimated time left for the whole measurement to finish. This value is always changing according to the history of the measurement. On the beginning of the first run, it will present the same value as presented on the Setup Panel. If the Clipping, Low Level or Tolerance indicators are activated, the Estimated Time Left will be corrected. After finishing one run, and if other runs are to be performed, the Estimated Time Left will now be based on the time taken to finish the previous measurement run;

⁵⁷ Whenever the Clipping, Low Level or Tolerance indicators are on, the measurement time will increase.

- Start Time and Actual Time - Clock-time when the measurement started and actual clock-time. These values are based on the desktop clock. It is not advised to change clock settings during a measurement, since the total time taken to perform the whole measurement is estimated based on these values.

D.6.4 Results panel

In this panel the final results are presented. It is also here that the user defines the format of the data to be saved.

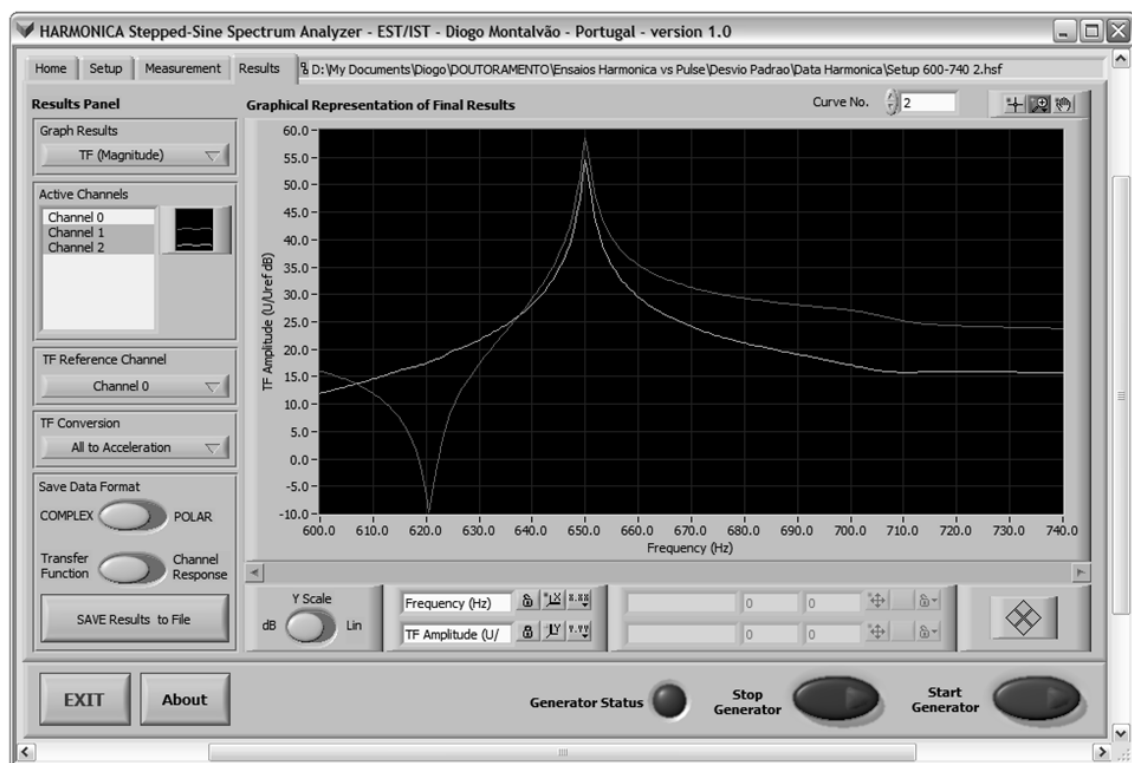


Figure D.5: Results Panel. Plot of two FRFs' amplitudes.

This panel is constituted by the following:

- Graph Results:
 - TF (Amplitude) – Plots the amplitude against frequency of a Transfer Function relating the Active Channels and the TF Reference Channel. The Transfer Function can either be in the form of a FRF or a Transmissibility Function. This control is used for graphical presentation purposes only;
 - TF (Phase) – Plots the phase (in degrees) against frequency of a Transfer Function relating the Active Channels and the TF Reference Channel. The

Transfer Function can either be in the form of a FRF or a Transmissibility Function. This control is used for graphical presentation purposes only;

- Ch Response – Plots the amplitude of the Channel responses against frequency. It can be seen as the Amplitude of the Fourier Spectrum of the Channel responses. This control is used for graphical presentation purposes only.
- Active Channels – Allows the user to decide which channels to be plotted. It is also here that the user defines which channel results will be saved;
- TF Reference Channel – Reference channel for the Transfer Function. The TF Reference Channel can either be a force (and thus one obtains an FRF – response over force) or a channel response (and thus one obtains the FRF inverse – force over response - or a Transmissibility Function – response over response);
- Ch Conversion – Conversion of the kinematic units of the measured responses (options include: no conversion, all to acceleration, all to velocity and all to displacement). This conversion does not affect channels defined as forces;
- Save Data Format – Definition of the data format and type to be saved. The results can be saved either in the Complex format (real and imaginary parts) or Polar format (amplitude and phase in radians). The data type to be saved can either be in the form of a Transfer Function (Active Channel over TF Reference Channel) or in the form of a Channel Response. Only the Active Channels will be saved;
- Save Results to File^{58, 59} – After setting the previous parameters, this button should be pressed in order to save the results. A Pop-Up Window will appear for each Active Channel. Each file will correspond to a single Active Channel having all the data concerning all run-ups (refer to chapter 5 for further information on the file formats);
- Y Scale – Defines whether the Y scale is linear or expressed in dB. This control is used for graphical presentation purposes only;

⁵⁸ If for any reason saving a specific channel is cancelled by the user, that channel will not be saved and the program will continue to open Pop-Up windows for the rest of the channels. Also, only the Active Channels will be saved.

⁵⁹ The results to be saved are independent from the Graph Results selection to be plotted - TF (Amplitude), TF (Phase) or Ch Response. For example, if the Graph Results is set to Ch Response but the Save Data Format is set to Transfer Function, the results to be saved are in the form of a transfer function and not in the form of a channel response spectrum. All the other settings previously explained, except for the Graph Results, will have effects on the saved data.

- Curve no. – Selection of the measurement curve corresponding to a run number. This control is used for graphical presentation purposes only;
- Other buttons and fields – Other buttons can be found under the Graphical Representation of Final Results. These are standard LabVIEW™ controls for XY Graphs.

D.7 File format

The results are saved in a Tab Separated Values file (text file), with the default extension *.txt*. The first row of this file identifies the data type in each column, by means of the use of a numerical code, as can be seen in figure D.6.

	A	B	C	D	E	F	G	H
1	0	1.1	2.1	3.1	1.2	2.2	3.2	
2	600.006	128.092	127.936	127.442	35.198	35.406	35.408	
3	602.011	135.023	135.403	134.999	36.614	36.682	36.516	
4	604.029	142.609	142.163	142.121	40.124	40.286	39.851	
5	606.006	150.615	150.507	150.256	40.014	39.779	39.871	
6	607.995	159.22	158.991	159.048	42.756	42.567	42.707	
7	610.016	169.527	169.386	169.229	45.089	45.045	44.886	
8	611.995	180.44	180.139	180.194	47.161	47.037	47.014	
9	613.987	191.56	191.62	191.167	50.318	50.348	49.986	
10	615.972	203.512	202.628	202.326	59.59	59.416	60.132	
11	618.028	218.778	219.004	218.696	57.291	57.387	57.228	

Figure D.6: Example of a results file generated by HARMONICA® (some cells were conveniently hidden for presentation purposes).

The first column corresponds to the generated frequency, and is identified in the first row with a “0”.

The other columns have a X.Y code in which X identifies the run number and Y the type of data. There are eight types of data:

1. Real Part of the Transfer Function;
2. Imaginary Part of the Transfer Function;
3. Real Part of the Channel Response;
4. Imaginary Part of the Channel Response;
5. Amplitude of the Transfer Function;
6. Phase of the Transfer Function (in radians);

7. Amplitude of the Channel Response;
8. Phase of the Channel Response (in radians).

According to this, it is possible to see that figure D.6 is presenting data concerning to the Complex Transfer Function (real and imaginary parts) of a measurement carried out in 3 successive runs.

D.8 Future versions

Like with any other software, there are of course some issues that were not taken into consideration when developing HARMONICA[®]. A future version of HARMONICA[®] could benefit from the following:

- Inclusion of an option to record the time-signals;
- An option to redo the measurement at single frequencies could exist (with different “transient delay” and “cycles after transient” settings, for instance);
- Inclusion of a real-time FRF display in the measurement panel;
- Inclusion of a well-suited filter, especially designed for this kind of signal. The author is already working out on this subject.

Annex E – BETAlab[®] Software

E.1 Introduction

The BETAlab[®] is a modal identification software application built under LabVIEW™ 7.1 environment from National Instruments™. It makes use of the CRF function (see section 3.4.2) developed by Maia *et al.* (1994), Silva, J. M. M. *et al.* (1996) and Ribeiro (1999). The algorithm identifies the modal parameters from experimental FRF data considering the receptance (presented in section 3.4.1) as:

$$\alpha_{jk}(\omega) = \bar{R}_{jk}(\omega) + \sum_{r=m_1}^{m_2} \frac{r\bar{A}_{jk}}{\omega_r^2 - \omega^2 + i\eta_r\omega_r^2} \quad (\text{E.1})$$

in which:

$$\bar{R}_{jk}(\omega) \cong -\frac{1}{\omega^2 \bar{M}_{jk}^R} + \frac{1}{\bar{K}_{jk}^R} \quad (\text{E.2})$$

Thus this application allows regenerating the FRF curve analytically. In the case a reasonable amount of FRFs is obtainable, corresponding to different measurement points, it also allows representing graphically the mode shapes for bi-dimensional systems (in other words, the modal vectors become available).

There are, of course, commercial applications available, such as Modent from ICATS or Test.Lab from LMS, which have a much wider range of engineering applications and are able to present as good results as BETAlab[®] when modal identification is concerned. However, the development of BETAlab[®] tool still presents several advantages, namely to the research groups, being the most obvious benefit the economical one.

E.2 Program overview

BETAlab[®] is a custom made modal identification program. It was fully developed by the author in LabVIEW™ 7.1 from National Instruments™. It is an up-to-date version of the now obsolete BETA[®] originally presented by Ribeiro (1999).

BETAlab[®] uses the CRF (see section 3.4.2) to determine the global and local modal properties (natural frequencies, modal damping factors and complex modal constants).

It has the following main features:

- Fully interactive platform;
- Identification of the modal properties of MIMO⁶⁰ systems;
- Processing of an indefinite number of experimental FRFs;
- Real-time presentation of the regenerated curve for quality judgement;
- Possibility of choice of interactive (slow) or automatic (fast) identification;
- Determination of residuals for regeneration of the experimental curve (interactive or automatic);
- SDOF analysis, meaning each mode is treated independently of the others and usually the order of identification is (almost) irrelevant;
- Semi-automatic improvement of the results (minimization of the influence of modes over each other);
- Allows manually editing the results (not recommended, only experienced users should do it);
- Allows saving the results in Tab Separated Values files (text files) for access with programs such as Sun® Microsystems OpenOffice.org Calc or Microsoft® Excel®;
- Allows saving the current identification and proceeding with it later;
- Accepts three different data files as inputs (designated as *Harmonica*, *Pulse Single* and *Mihail-Primož*).

E.3 System requirements

BETAlab[®] was programmed in LabVIEW™ 7.1 from National Instruments™ for Microsoft® Windows®. Any requirements should be in accordance to those of this version from LabVIEW™ 7.1. It was tested in a laptop computer with Intel® Pentium™ M 1.4 GHz processor and 512Mb of RAM. The program was tested under Microsoft® Windows® XP environment.

This program is designed to be run with a resolution of (at least) 1024x768.

It is strictly required that LabVIEW™ 7.1 runtime engine is installed on the computer, since it does not come with an install wizard.

⁶⁰ Version 7.05.5b2 does not include modal consistency, so in fact this version is more adequate to Single Input Multiple Output (SIMO) systems.

E.4 Operation (tutorial)

The operation of BETAlab[®] is better understood if explained as a tutorial. This is directed to users and not to developers. We shall explore an example, in this case the modal identification of the data for specimen plate A1D from this thesis.

After installing and running LabVIEW™, left-click once on “open” (figure E.1, left). A new window will appear where you have to search for the root directory called “BETAlab v7.05.5b2.vi” (figure E.1, right). Choose to open the file BETAlab.vi.

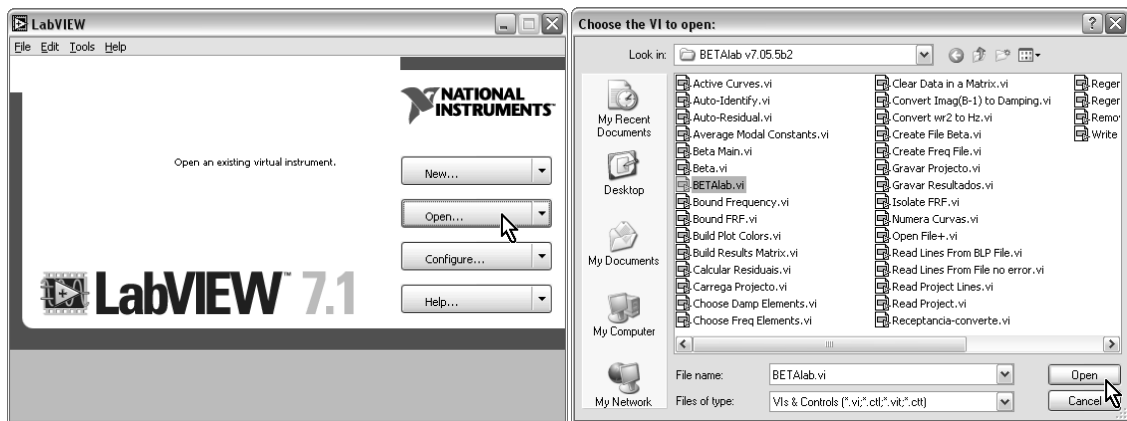


Figure E.1: Opening BETAlab[®] VI.

Another window will open. This new window is BETAlab[®]'s front panel. Before doing anything else, you have to push the button “Run” (near the upper left corner of the window, as shown in figure E.2).

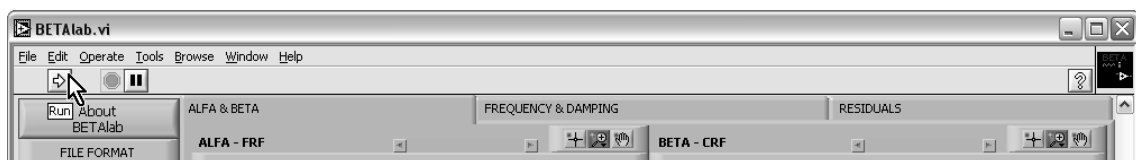


Figure E.2: Starting BETAlab[®] VI.

At this moment, BETAlab[®] is running. The first thing to do is to load the experimental FRFs⁶¹. In the present example, the experimental data was obtained with PULSE™ LabShop™ from Brüel

⁶¹ The file formats of the experimental FRFs is described in section E.5.

& Kjær®. So, move your cursor and left-click once on “Pulse (Single)” in “File Format”. Then, left-click on “ADD FRFs” and a popup window will appear. You must search and select one single file with the experimental data. After selecting the file, another popup will ask which kind of data is being added (figure E.3). In the present case, the experimental FRFs were measured with a Dual-channel LDV, and no data conversion was performed. So, the data is in the form of mobility⁶².

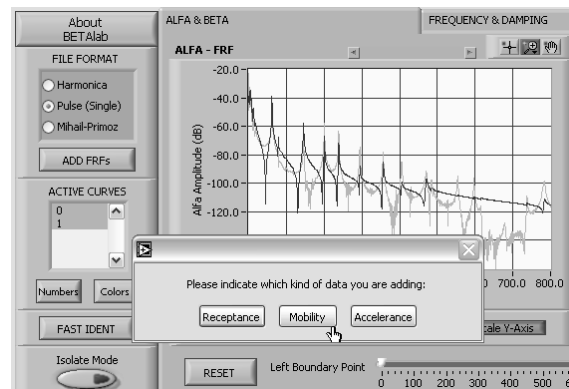


Figure E.3: Converting FRF data to receptance.

This operation must be repeated as many times as the number of files that are going to be processed at the same time. After adding all the FRFs (in our case, there are four), active curves will show as selected (grey background). These are also the curves that appear in the two graphics to the right. The first graphic (ALFA-FRF) represents the receptance FRFs, whereas the second graphic (BETA-CRF) represents the correspondent CRF's. Notice that, at this time, the CRF seems to be a noisy meaningless random function. It is also possible to change the numbering and the colours of the plots to the right. We shall leave the colours as they are by default, but will change the numbering, according to that adopted in figure 4.21 (section 4.3.1.2). The new numbering shall be 1, 2, 3 and 4. The program only allows sequential numbering. Thus, only the first number is defined. Left-click on “Numbers” and set the starting number as “1”. Left-click on “Ok” to close the popup window. The screen should now look as shown in figure E.4.

⁶² BETAlab is designed to work with receptances, so a conversion must be done before starting the modal identification.

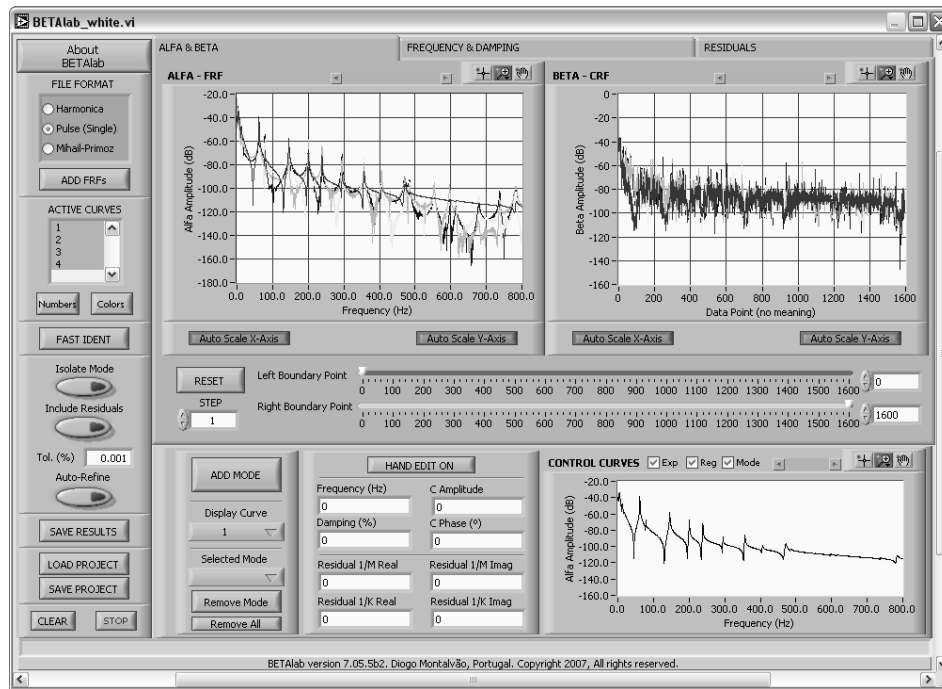


Figure E.4: BETAlab[®] screen after introducing the FRF input data.

It is now time to identify one single mode. First, we must zoom in closer to the region where we are going to make the modal identification, always looking into “ALFA-FRF” plot. The plot “BETA-CRF” will be used later. We shall start with the first mode (around the 60 Hz). To zoom, we must use the sliders “Left Boundary Point” and “Right Boundary Point”. These sliders are graduated in terms of data points. In the present case, there are 1600 points, which means there is a 0.5 Hz frequency resolution, since the frequency range is from the 0 to the 800 Hz. Left-click on the “Right Boundary Slider” and keep the mouse button pressed while moving the slider to the left. The plot will only refresh after you stop clicking. Do the equivalent with the “Left Boundary Slider” so that you are looking only towards the first mode around the 60 Hz. The sliders have some numbers inside a box to the right. In the end, you should be reading something like 96 in the “Left Boundary Slider” box and 145 in the “Right Boundary Slider” box. If you are having trouble doing so by dragging the sliders, you can use the keyboard to manually insert these values into the boxes. The “ALFA-FRF” and “BETA-CRF” plots should look similarly to Figure E.5.

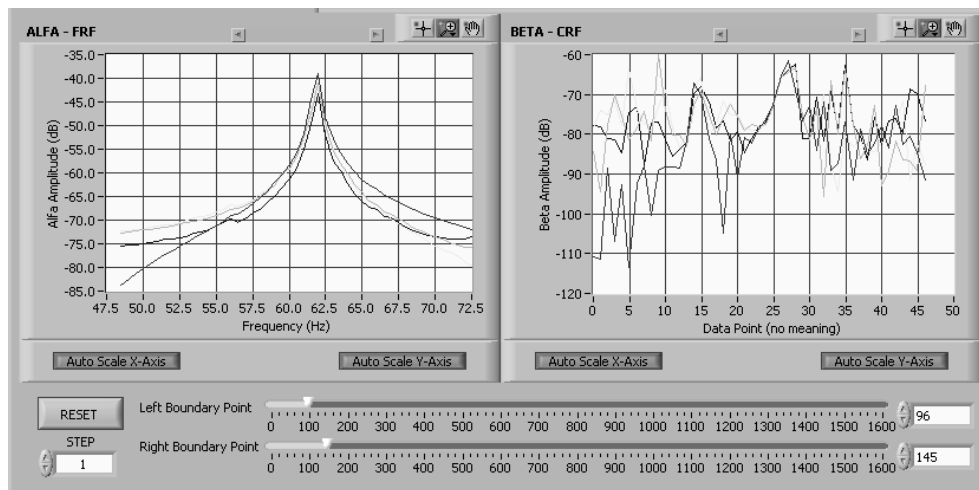


Figure E.5: Zooming towards one single mode.

If we look to the “BETA-CRF” plot to the right, it is still meaningless. However, according to equation (3.47) (section 3.4.2) the CRF should represent “the form of the receptance for a SDOF system.” An important concept that must now be introduced is the “STEP”, which is a natural number, positioned just below the “ALFA-FRF” plot. This number is the difference (or distance) between the points to be used while determining the CRF. For example, if we have the sequence of integer numbers from 1 to 10 and we say the step is 3, we are only looking into numbers 1, 4, 7 and 10 in our analysis. This was proven appropriate in order to reduce the effect of noise (Ribeiro (1999)). Also, values of the step up to 10 can be usually chosen without problems because the modes are generally well separated. Nevertheless, if there are, let’s say two nearby modes, the step may “blur” these modes into a single one. A rule could be that the step should be as small as possible, but enough for the CRF to look similar to a SDOF receptance. An example is shown in figure E.6 where the “BETA-CRF” graphic is represented for different values of the step.

Having defined the step (in our case, a value of 5 will be used), the modal identification procedure starts. Now we must left-click over “FREQUENCY & DAMPING” on the tab in the upper part of the window. Two plots, called “FREQUENCY” and “DAMPING”, will appear in the places where the plots “ALFA-FRF” and “BETA-CRF” previously were (figure E.7).

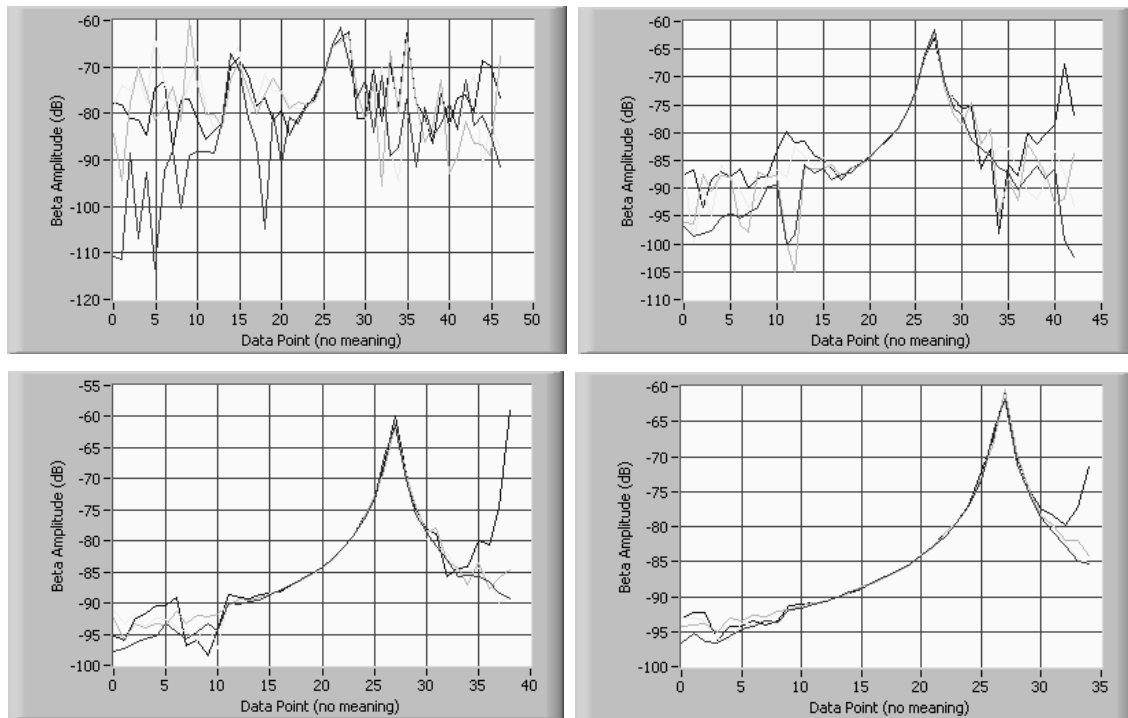


Figure E.6: Example of the influence of the “STEP” in the quality of the CRF. From top-left to right-bottom the value of the step is 1, 3, 5 and 7 respectively.

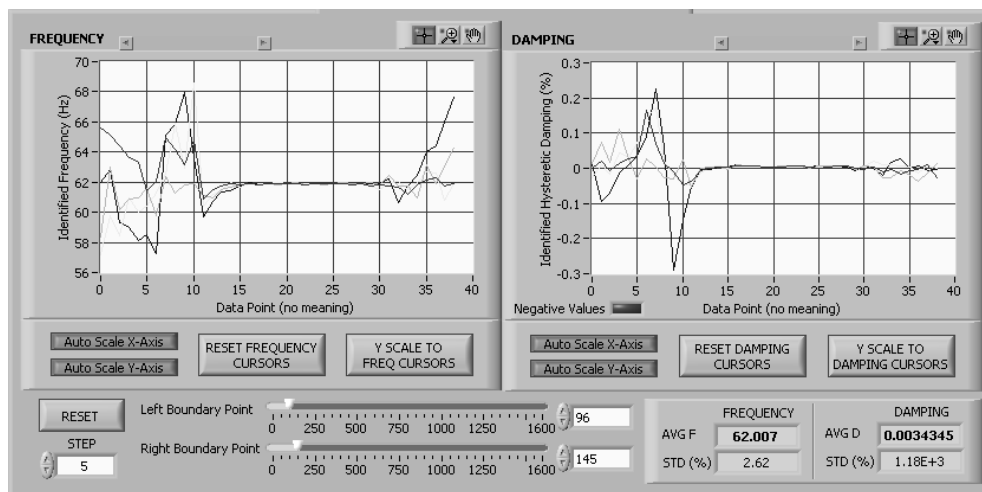


Figure E.7: Frequency and Damping screens for the modal identification.

These plots are “stable” (practically constant) in the regions near the resonant frequency and very noisy in the rest of the domain. This happens as a consequence of the CRF being only valid in the vicinity of modes. Now we must narrow our region of analysis in order to only include the “stable” region in our analysis. First, left-click on both buttons “RESET FREQUENCY CURSORS”. Two horizontal yellow lines will appear in each plot. All the data that are in between these lines will be used in the modal identification, whereas all the data outside these lines will not be included. By left-clicking over one of these lines and dragging it, we can fix narrower limits for our analysis. We should move the upper lines downwards, whereas the

lower lines should be moved upwards (figure E.8). This operation must be done for both frequency and damping in this order.

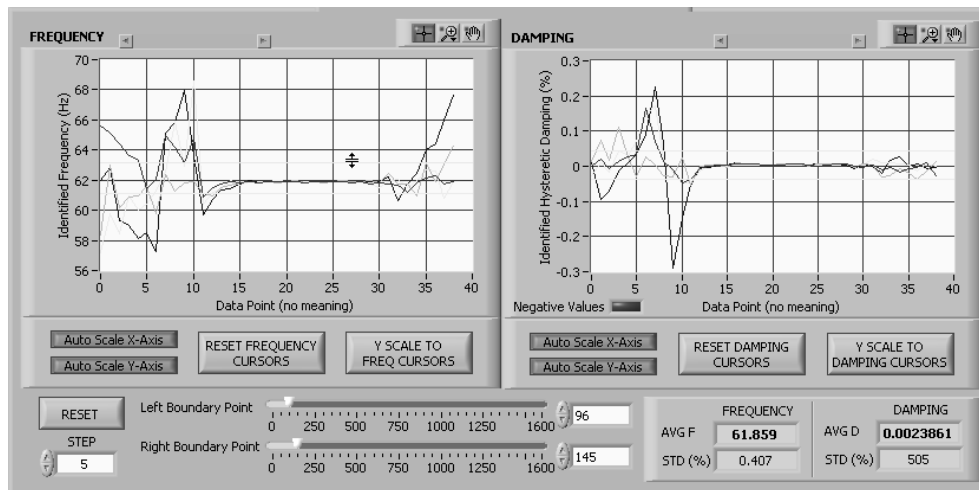


Figure E.8: Frequency and Damping screens for the modal identification: moving the band yellow horizontal lines.

After fixing these new limits, we can continue narrowing our analysis by pushing the buttons “Y SCALE TO FREQ CURSORS” and “Y SCALE TO DAMPING CURSORS”. This will make a zoom to the data contained in between the horizontal yellow lines.

The yellow lines can again be moved, and the buttons “Y SCALE TO FREQ CURSORS” and “Y SCALE TO DAMPING CURSORS” be pushed with the left mouse button as before. When to stop, is difficult to tell and depends on the user’s experience. A suggestion is to keep an eye on the red light “Negative values” in the lower corner of the damping graphic. Outside the natural frequencies, negative values for the damping are being determined, which obviously does not make sense. Thus, we will continue this process until the bright red light turns into dark green (figure E.9).

The next step is to drag the “Left Boundary Point” and “Right Boundary Point” sliders so that the region is narrowed only to the stabilized area (in our case, we are going to fix the left and right sliders values into 112 and 135 respectively). Finally, we push the button “ADD MODE”, and the first mode is identified. The frequency and damping values that are going to be saved are presented just under the “DAMPING” plot, as it can be seen in either of figures E.7, E.8 or E.9. Seeing that the “FREQUENCY” and “DAMPING” plots are quite irregular, the standard deviations (STD) are also determined.

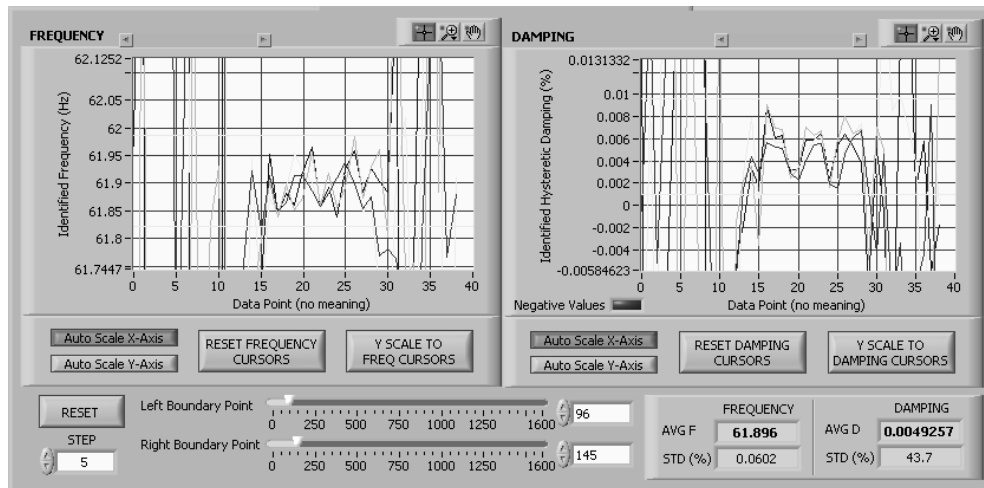


Figure E.9: Frequency and Damping screens for the modal identification: turning the “Negative values” red light off (into dark green).

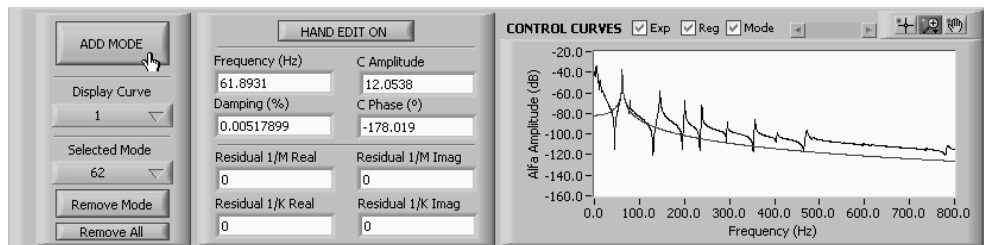


Figure E.10: Lower part of BETAlab® screen after identifying the first mode.

After left-clicking on the “ADD MODE” button, several things happened, which can be seen in the lower part of the screen (figure E.10). First, a blue plot appear in the graphic “CONTROL CURVES”, corresponding to the identified mode. Since only one mode is identified, equation (3.44) only contains one term, corresponding to a SDOF system. The identified modal parameters are just to the left. The frequency and damping are global properties of the system, but the modal constants are local properties. Thus, the former properties are singular for every receptance. We can switch between receptances shown in the graphic “CONTROL CURVES” in the “Display Curve” ring selector. This can be used to visually assess the quality of the identification.

To ensure we will not lose any data, we can save our work by pushing the button “SAVE PROJECT” in the lower left part of the window. From this time forward, the filename will appear on the lower bar from the left. If we want, we can recover from this point later by pushing the button “LOAD PROJECT.” Saving the project is also very important because the application MuDI® (annex F) for the implementation of the damage location algorithm requires .bl4 files (BETAlab® project files) as input data.

To start identifying the second mode, we go back to the first screen by left-clicking on “ALFA & BETA” on the tab in the upper part of the window. Again, we drag the sliders to the right towards the next mode (figure E.11).

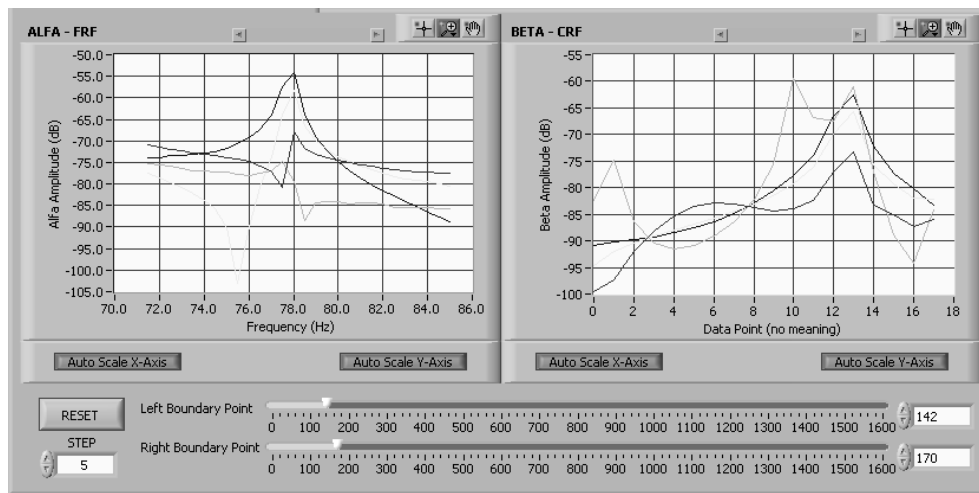


Figure E.11: Going towards the identification of the second mode.

It seems the CRF is quite irregular (specially the green one), even though a value of 5 is used for the step. This is possibly due to the first mode being dominant over this one, because they are not that far away from each other. It would be desirable to remove the influence of the identified modes from the experimental curve. BETAlab[®] offers that possibility with the button “Isolate Mode” on the left-middle part of the window (figure E.12).

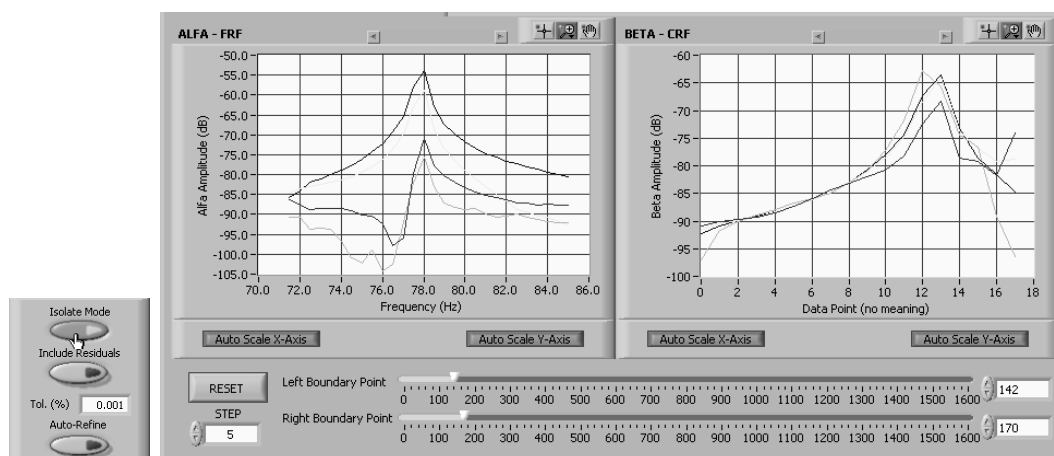


Figure E.12: Going towards the identification of the second mode, after isolating the first mode from the experimental results.

After isolating the first mode from the experimental results, both the FRF and the CRF corresponding to the second mode are much more evident. The button “Isolate Mode” can, in fact, be turned on from the beginning to the end of the analysis.

Now the process is fully repeated until the end of the frequency range: selecting an adequate value for the step (can be the same), moving to the “FREQUENCY & DAMPING” tab, narrowing the band of analysis in both “FREQUENCY” and “DAMPING” graphics, and adding the mode with “ADD MODE”. Let us take a look into the results at this stage (figure E.13), after pushing the button “RESET” (resets the sliders to the lower and upper boundary of the frequency range).

The “ALFA-FRF” plot looks very noisy. This is because “Isolate Mode” button is turned on, i.e., we are representing the difference between the experimental curve (black in the “CONTROL CURVES” graphic) and the regenerated one (red in the “CONTROL CURVES” graphic).

Now, if we move to the “RESIDUALS” tab (figure E.14), and considering the ring selector “Display Curve” is showing “1”, we can observe that the regenerated curve (red plot) is not a perfect match to the experimental curve (black slashed plot). This is because the influence of modes outside the frequency domain is not being taken into account. In fact, the red plot corresponds to equation (3.44) but without the residual terms given by (3.45).

To determine the residuals in BETAlab[®], two points from the experimental curve must be chosen. It is suggested that these points are situated near anti-resonant frequencies and close to the frequency range limits, since these are locations that are less likely to be dominated by nearby modes. Anyhow, several combinations must be tried sometimes and in some occasions it is not easy to find a satisfying solution in the whole frequency range under analysis.

To determine the residuals manually, we shall first ensure that the “Test” box is checked, showing a new curve in the graphics area that is the real-time regenerated FRF for the current position of the “Mass” and “Stiffness” cursors. The cursors are moved by drag-and-drop while clicking on the left mouse button and are (by default) over the experimental FRF. When the test curve matches the experimental curve, left-click on “UPDATE RESIDUAL”. An indicator named “Residual” will turn into bright red to indicate the regenerated curve is being affected by the mass and stiffness residuals (figure E.15). The residual may be deleted from the analysis by pushing the button “REMOVE RESIDUAL”.

Because the residuals are local properties, we must do the same for the other curves. The selection of the curve to be shown in the “REGENERATED ALFA (FRF) CURVES” graphic is done in the “Display Curve” ring selector below. When many curves are to be identified, it can be useful to use the tool “UPDATE ALL”, but the results might not be as accurate⁶³.

⁶³ Since a self-explanatory window will pop-up and because only expert users should resort to this feature, no further details will be given here.

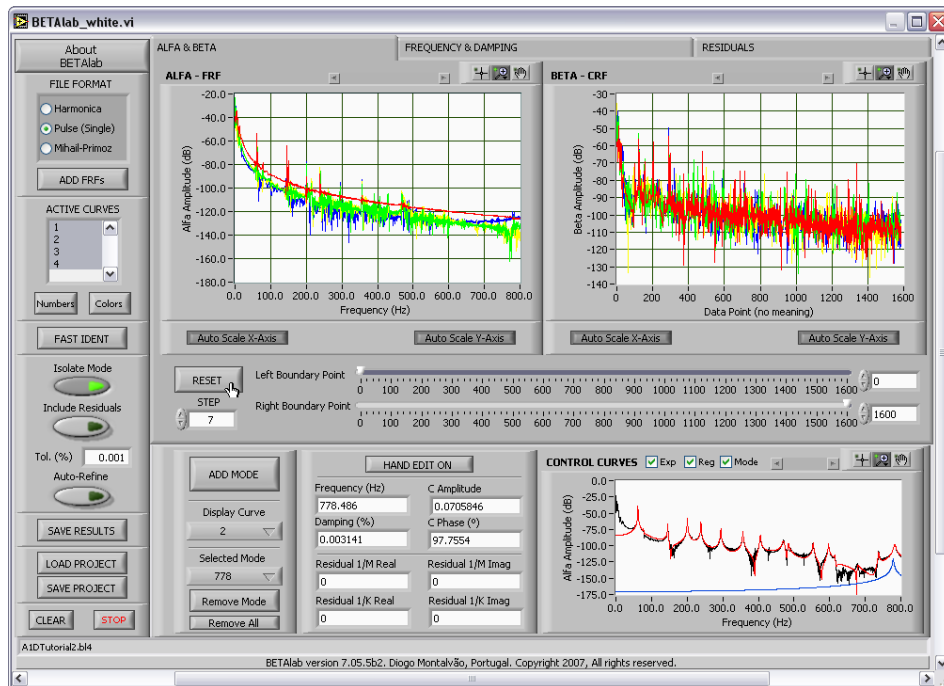


Figure E.13: BETAlab[®] screen after finishing one identification round.

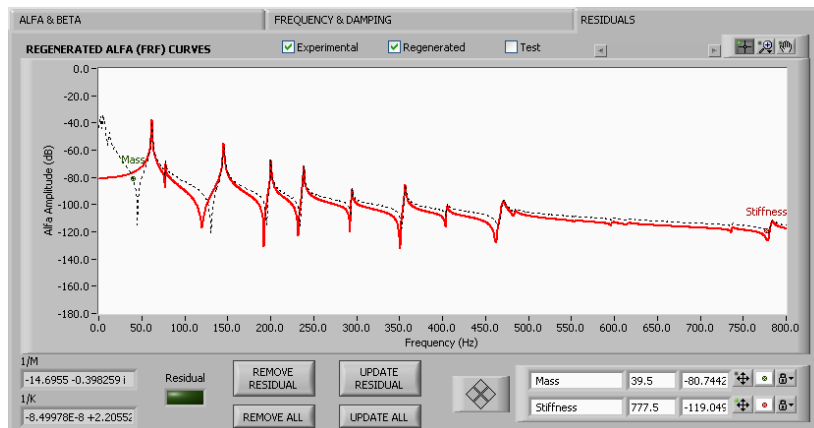


Figure E.14: Regenerated and experimental curve before determining the residuals.



Figure E.15: Regenerated and experimental curve after determining the residuals for curve number 1 (direct FRF).

Finally, to improve the quality of the results, the modal identification process should proceed from the beginning. “Isolate Mode” button should remain. It is also offered the possibility of treating the residuals as modes exactly the same way by pushing the button “Include Residuals”. In theory, after assuring these two buttons are on, one should go to the ring selector “Selected Mode”, choose a new mode (say the first mode at around 62 Hz), remove it by left-clicking on “Remove Mode”, and re-identify it. This way, the influence of outside modes is minimized. However, this would make the process even more time consuming, not to say impracticable. As an alternative to this task that could get very laborious, the user is suggested to use the feature “Auto-Refine”. This is a very simple and quite efficient iterative algorithm that will make the re-identification of all modes by using the same parameters previously defined by the user. A tolerance must first be defined by the user (the default value is 0.001%). If the discrepancy between all the i^{th} and i^{th-1} identified values is less than 0.001%, then the iterative algorithm stops and is said to be *convergent*. Otherwise, it will carry on making new calculations. In the event it is not converging, the user may interrupt the algorithm, albeit there is no undo option available and the results will be according to the last iteration.

The BETAlab[®] screen after finishing the whole described procedure should look similar to the one presented in figure E.16.

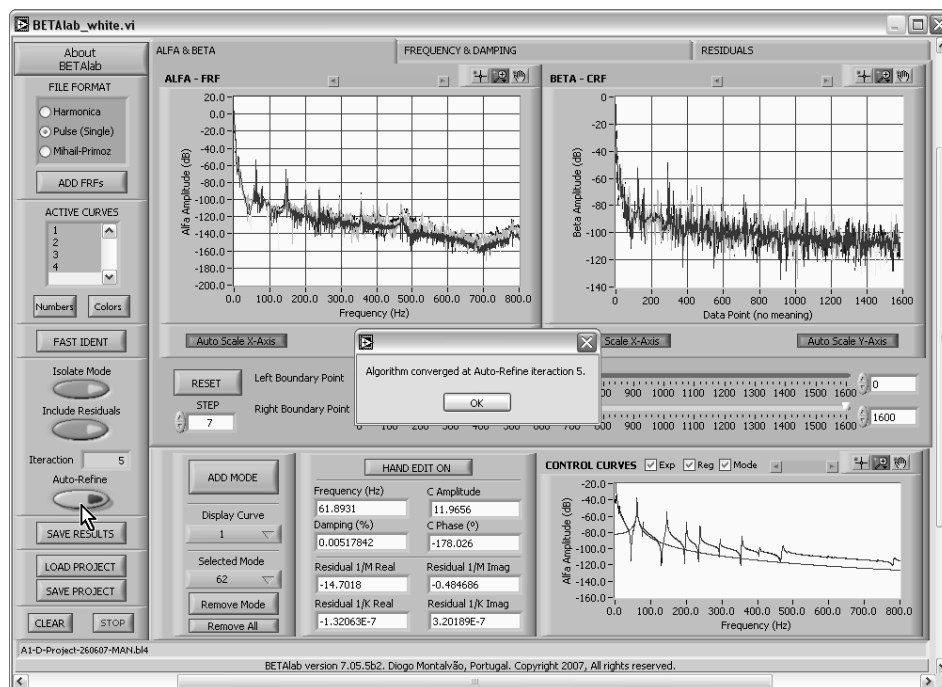


Figure E.16: BETAlab[®] screen after finishing the whole identification process.

Other several features that were not mentioned include LabVIEW™ internal commands (for instance, the way graphics are handled) and:

- **HAND EDIT ON** – By pushing this button, all the results (natural frequencies, modal damping factors, modal complex amplitudes, modal complex phases and real and imaginary parts of the inverse of the residuals) may be manually edited. It accepts any number and is only meant to be used by expert users. A popup warning window will be shown once;
- **FAST IDENT** – Performs an automatic full identification of the experimental FRFs. A popup window prompting the user for data input shows up. The way the program handles this information is explained. Poor results are always expected, especially for noisy data. This is meant to be used by expert users only and to give a quick overview on the dynamic properties of the structure;
- **CLEAR** – Clears all the data. To be used when starting a fresh modal identification of another system;
- **Remove All** – Clears all the data, except the input FRFs;
- **STOP** – Stops running BETAlab®.

E.5 File formats (input)

The experimental data may be in one of three available input formats: *Harmonica*, *Pulse (Single)* or *Mihail-Primoz*. The first format is the one obtained with the software HARMONICA®, developed by the author and presented in annex D. When saving the data with HARMONICA®, data must be saved as “complex” instead of “polar”. This file format allows multiple FRFs to be included in the same file. This file format is schematically explained in figure E.17.

	A	B	C	D	E	F	G
1	0	1.1	2.1	3.1	1.2	2.2	3.2
2	600.006	128.092	127.936	127.442	35.198	35.406	35.408
3	602.011	135.023	135.403	134.999	36.614	36.682	36.516
4	604.029	142.609	142.163	142.121	40.124	40.286	39.851
5	606.006	150.615	150.507	150.256	40.014	39.779	39.871
6	607.995	159.22	158.991	159.048	42.756	42.567	42.707
7	610.016	169.527	169.386	169.229	45.089	45.045	44.886
8	611.995	180.44	180.139	180.194	47.161	47.037	47.014
9	613.987	191.56	191.62	191.167	50.318	50.348	49.986
10	615.972	203.512	202.628	202.326	59.59	59.416	60.132
11	618.028	218.778	219.004	218.696	57.291	57.387	57.228

Figure E.17: HARMONICA®'s input file format example (some cells were conveniently hidden for presentation purposes).

The second format is obtained with PULSE™ LabShop™ from Brüel & Kjær®. Each FRF data must be saved separately from the others as “Pulse File Ascii”. This format has several headers that are not used and must be discarded. Only three columns are effectively needed, by this order: frequency, FRF real part and FRF imaginary part. If the file is built in Sun® Microsystems OpenOffice.org Calc or Microsoft® Excel®, the first cell must be positioned in the 2nd column and 84th row. This file format is schematically explained in figure E.18.

	A	B	C	D
78				
79	Z-index:		1	
80	Date:		24-01-2006	
81	Time:		20:26:37:995	
82	Relative time:		0.00E+00	
83	Z-axis:		0.00E+00	
84	1	0.00E+00	-5.09E+00	0.00E+00
85	2	1.00E+00	2.83E+01	-5.01E+00
86	3	2.00E+00	7.79E+00	-2.06E+01
87	4	3.00E+00	-6.56E+01	-2.47E+01
882	799	7.98E+02	-4.75E+02	-1.48E+02
883	800	7.99E+02	-4.75E+02	-1.48E+02
884	801	8.00E+02	-4.71E+02	-1.48E+02
885	TagsBegin:			
886	OverLoad:		FALSE	
887	OverLoadRatio: []		0.00E+00	

Figure E.18: PULSE™'s input file format example (some cells were conveniently hidden for presentation purposes).

The third format, Mihail-Primoz, is obtained with a separate software, programmed in MatLab®, which makes use of a third party software. This application receives as input an Universal File Format (UFF) file from the Polytec® Scanning LDV and extracts all the FRF data (or other custom fields) into an ASCII file that BETAlab® is able to read. Basically, there is a routine named “UFFASCII.m”, developed by Mihail Fontul from Instituto Superior Técnico (IST), that calls “readuff.m”, developed by Primoz Cermelj from the University of Ljubljana in Slovenia. The format is named *Mihail-Primoz* after their authors. This file format allows multiple FRFs to be included in the same file. This file format is schematically explained in figure E.19.

	Number of FRFs						Frequency					
	A	B	C	EK	EL	EM	DRW	DRX	DRY	DRZ	DSA	DSB
1	143											
2	0.5	1.0	1.5	70.5	71.0	71.5	1597.5	1598.0	1598.5	1599.0	1599.5	
3	-3.80E-01	1.05E-01	8.21E-02	-3.38E-02	-7.10E-02	3.30E-01						
4	-7.13E-01	-6.22E-03	-2.49E-01	4.45E-02	-8.78E-03	2.21E-01						
5	-3.42E-01	-4.03E-01	-3.35E-01	1.25E-01	2.28E-01	1.01E-01						
3200	-6.48E-01	2.15E-01	1.22E-01	-6.13E-01	-6.74E-01	-5.78E-01						
3201	-4.09E-02	-4.13E-02	1.89E-01	3.40E-01	-4.82E-01	-1.11E-01						
3202	-8.08E-02	1.36E-01	3.13E-01	3.84E-01	-9.75E-02	-7.12E-01						
3203	-6.88E-02	1.76E-01	-1.89E-01	-5.13E-02	-1.05E-01	-1.82E-01						
3204	2.99E-01	-4.35E-02	-3.44E-02	2.38E-02	-1.38E-01	-3.67E-01						
3205	3.25E-01	-1.44E-01	3.21E-02	-6.50E-01	8.43E-01	5.12E-02						
6400	1.23E+00	-5.81E-01	-6.15E-01	5.47E+00	1.88E+00	8.36E-01						
6401	7.04E-01	-4.03E-01	-4.15E-01	3.26E+00	2.18E+00	7.74E-01						
6402	1.21E+00	-4.19E-01	-5.57E-01	5.09E+00	1.98E+00	4.04E-01						
6403												

Each of these n columns belong to single FRFs
(in this example, $n=143$)

Figure E.19: Mihail-Primoz's input file format example (some cells were conveniently hidden for presentation purposes).

E.6 File formats (output)

After the modal identification is complete, the results may be saved in "Tab Separated Values" (.txt) format by using the button "SAVE RESULTS", which structure is explained in figure E.20. Data can be accessed using any regular text editor, Sun® Microsystems OpenOffice.org Calc or Microsoft® Excel®.

Nevertheless, this format is not suitable for being read by BETAlab® or other software, as it does not include all the information, such as the experimental FRFs. The results should also be saved using the "SAVE PROJECT" button. The format in which this file is saved is much more complex and has the extension ".bl4" (the number "4" is used to show its compatibility until BETAlab® version 7.04.x) and can be read by other softwares, such as MuDI®, as mentioned before.

E.7 Auxiliary programs

An auxiliary program was developed in order to represent the measured mode shapes, using a file with the geometrical Cartesian coordinates and a file with the corresponding modal properties obtained from BETAlab® (a file with extension .bl4). A screenshot is shown in figure E.21.

Horizontal zoom (input) → Step (input) → Vertical frequency and damping zooms (input)

	Left Boundary	Right Boundary	Step	Frequency	Damping	TD Freq %	STD Dmp %	High Freq Boundary	Low Freq Boundary	High Dmp Boundary	Low Dmp Boundary	C Real 0	C Imag 0	C Real
1	112	135	5	61.893051	0.005178	0.053405	32.732201	61.930836	61.831123	0.008382	0.00188	-1.358482	-0.412182	9.3
2	274	306	7	145.613571	0.004176	0.06306	27.198304	145.847361	145.422607	0.00627	0.00243	-6.801781	-0.001903	-1.4
3	143	166	5	77.831017	0.004336	0.115024	31.057877	78.078401	77.573036	0.008255	0.00047	-0.327034	-0.080541	-0.2
4	383	415	5	200.603165	0.00287	0.024622	16.247276	200.716053	200.484633	0.003671	0.00132	-2.174378	-0.148128	-5.1
5	453	484	5	238.641057	0.002641	0.01292	8.455731	238.70253	238.584473	0.003218	0.00211	-1.729578	-0.096608	-4.1
6	576	602	6	294.630735	0.003028	0.008385	5.237631	294.736786	294.628662	0.003357	0.00278	-0.406056	-0.051031	-2.2
7	636	726	6	356.642242	0.003077	0.013527	8.320243	356.744334	356.53653	0.003536	0.00260	-0.310632	-0.031656	1.6
8	792	827	8	405.373657	0.003606	0.014435	8.346071	405.507234	405.22641	0.004303	0.002338	-0.176743	-0.034576	1.4
9	954	980	5	483.324635	0.00583	0.052393	15.156538	484.887634	483.28653	0.008034	0.003542	-0.107275	-0.056374	-0.6
10	912	963	7	470.491791	0.00887	0.036703	12.846538	471.60675	469.471924	0.011011	0.00642	-0.357911	-0.155383	-1.8
11	1034	1115	5	553.357336	0.00301	0.027535	15.193294	554.510132	553.476379	0.004045	0.00093	-0.019546	-0.004351	0.6
12	1183	1204	4	597.131958	0.00254	0.014813	6.751151	597.422485	596.873161	0.002834	0.00205	-0.026232	-0.002668	0.5
13	1220	1233	4	615.346008	0.004422	0.009201	5.222826	615.452271	615.222229	0.004876	0.00376	-0.027721	-0.002223	-0.0
14	1335	1371	9	678.886414	0.005771	0.023261	3.580802	679.234373	678.283142	0.007607	0.004536	0	0	0
15	1452	1430	9	737.365601	0.002285	0.014737	11.351367	737.662303	737.005615	0.003185	0.00145	-0.025747	-0.003168	-0.1
16	1557	1587	9	782.977173	0.005632	0.015848	4.76722	783.173749	782.719666	0.006309	0.00505	-0.244353	-0.040071	1.6
17	1540	1566	7	778.486084	0.003141	0.035738	28.614136	779.426341	777.314636	0.006978	0.000232	0	0	-0.0
18	421	440	4	215.048431	0.003253	0.107115	55.144536	215.58393	214.14888	0.007665	0.000112	0	0	0.1
19														
20														
21	Curve	11M Real	11M Imag	11K Real	11K Imag									
22	0	-14.701784	-0.484686	-1.52E-07	3.20E-07									
23	2	6.822331	-0.200615	1.10E-07	-7.02E-03									
24	3	-4.831548	0.435333	3.53E-08	6.35E-06									
25	1	-6.762463	0.382764	-1.06E-07	-1.85E-06									
26														
27														
28	BETAlab v7.05.3a1													
29	26-06-2007													
30														
31														
32	Frequency Vector (Hz)													
33	0.5													
34														
35	793.5													
36	806													
37														
38	Regenerated Curves													
39	[0, 0, 0]													
40	1.489511													
41	0.372303													
42	1.77E-06													
43	1.76E-06													
44														
45	[1, 0, 0]													
46	0.685241													
47	0.171356													
48	-1.54E-06													
49	-1.50E-06													
50														
51	[2, 0, 0]													
52	-0.69131													
53	-0.172875													
54														

Complex modal constants (output)

Standard deviations of frequency and damping (output)

Complex residuals (output)

Frequency and Damping (output)

BETAlab version and date (output)

Frequency vector (input)

Complex regenerated FRFs (output)

Figure E.20: BETAlab[®] results file structure (some cells were conveniently hidden for presentation purposes).

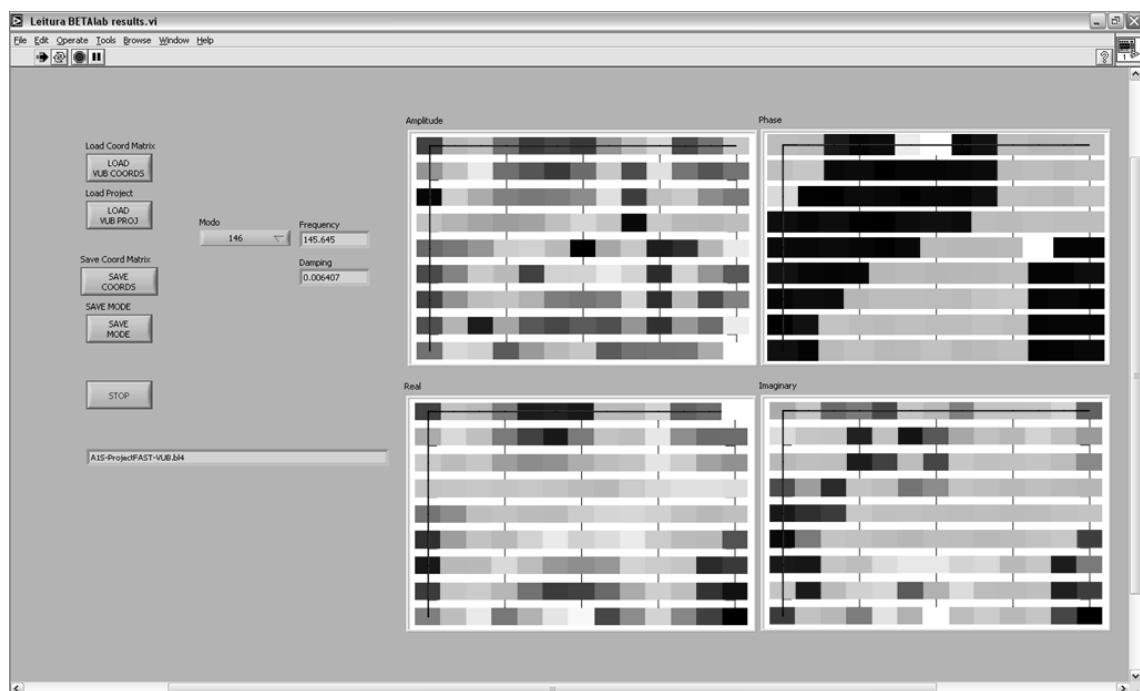


Figure E.21: BETAlab[®] auxiliary application screenshot for representing the mode shapes.

E.8 Future versions

BETAlab[®] is a software that the author foresees having commercial potential, due to its good performance and ease-of-use. However, version 7.05.5b2 still lacks offering the user some crucial features.

On the one hand, the identification process is fully manual, time consuming and requires the user to be focused and careful. On the other hand, it offers a fully automatic, quick, yet non controllable way of processing the data, with the inevitable increasing loss of accuracy and in many times an incorrect choice of modes, especially for noisy data. Somewhere in the middle could be a more balanced offer. An intermediate option, combining the best features of the existing ones, would be quite useful, increasing the speed of the identification process while retaining a good level of reliability.

Another interesting feature it could provide, that might boost the software to higher standards, would be to represent the mode shapes, based on the geometrical description of the response measurement points. There already exists an auxiliary application to do it, but it still constitutes a very crude version.

Those are only some of the improvements that might be made in the near future. Other obvious improvements might include modal consistency enforcing, more efficient code and self explanatory callouts when putting the mouse pointer over buttons and indicators. In summary, the following features are proposed for inclusion in future versions:

- Possibility of semi-automatic identification (the user tells the program the neighbourhoods around the modes and the program identifies the modes based on these “hints”);
- Representation of 3D mode shapes based on the Cartesian geometrical description of the response locations;
- Modal consistency, so that it can adequately process FRFs from MIMO measurements;
- More efficient and structured programming, so that it does not become slow while processing a lot of data (a problem it actually has);
- Self-explanatory help callouts when leaving the mouse pointer over buttons and indicators.

Annex F – MuDI[®] Software

F.1 Introduction

The MuDI[®] is a software built for plotting a geometrical probability map for the location of damage over bi-dimensional surfaces. It computes the probability for the damage location by following the procedure explained in section 3.6. The fundamental equation is:

$$MuDI_{ij} = W_f \cdot \frac{FreDI_{ij}}{\max[FreDI_{ij}]} + W_d \cdot \frac{DaDI_{ij}}{\max[DaDI_{ij}]} \quad (F.1)$$

where $FreDI_{ij}$ is the frequency damage index in coordinate (i, j) , $DaDI_{ij}$ is the damping damage index in coordinate (i, j) and W_f and W_d are weighting coefficients such that $W_f + W_d = 1$.

F.2 Program overview

MuDI[®] is a program that searches for the most likely to be damage locations in a composite laminate by following the whole procedure explained in section 3.6. The algorithm is based on the systems' mode shapes and the shifting of both the natural frequencies and the modal damping factors. The software was fully developed by the author in LabVIEW[™] 7.1 from National Instruments[™].

This software is still in a beta version and will probably be improved to be included, together with BETAlab[®], in a future complete software suite. The actual version is not meant to be the best for more industrial applications. Therefore, many of the features will not be explained here as a more straightforward and user friendly application is yet to be developed. This means some efforts should be made in the field of automatization, avoiding the risk of subjective judgements and the need of experienced users. As it is, it offers a range of possibilities for data treatment, most of all with the aim of evaluating the performance of the proposed index. One of the most important features to be pointed out is the possibility that the software offers for the user to manually pick a set of modes he considers most reliable for computing the damage index.

F.3 System requirements

The MuDI[®] version 9.04.1b0 was programmed in LabVIEW[™] 7.1 from National Instruments[™] for Microsoft[®] Windows[®]. Any requirements should be in accordance to those of this version from LabVIEW[™] 7.1. It was tested in a laptop computer with Intel[®] Core[™] Duo 2.4 GHz processor and 4Gb of RAM. The program was tested under Microsoft[®] Windows[®] XP environment.

This program is designed to be run with a resolution of (at least) 1024x768.

It is strictly required that LabVIEW[™] 7.1 runtime engine is installed on the computer, since it does not come with an install wizard.

F.4 Operation (tutorial)

The operation of MuDI[®] is better understood if explained as a tutorial. This is directed to users and not to developers. We shall explore an example, in this case the location of the data for specimen plate B1 (case B1H-B1D) from this thesis.

After installing and running LabVIEW[™], left-click once on “open” (figure F.1, left). A new window will appear where you have to search for the root directory called “MuDI v9.04.1b0” (figure figure F.1, right). Choose to open the file MuDI.vi.

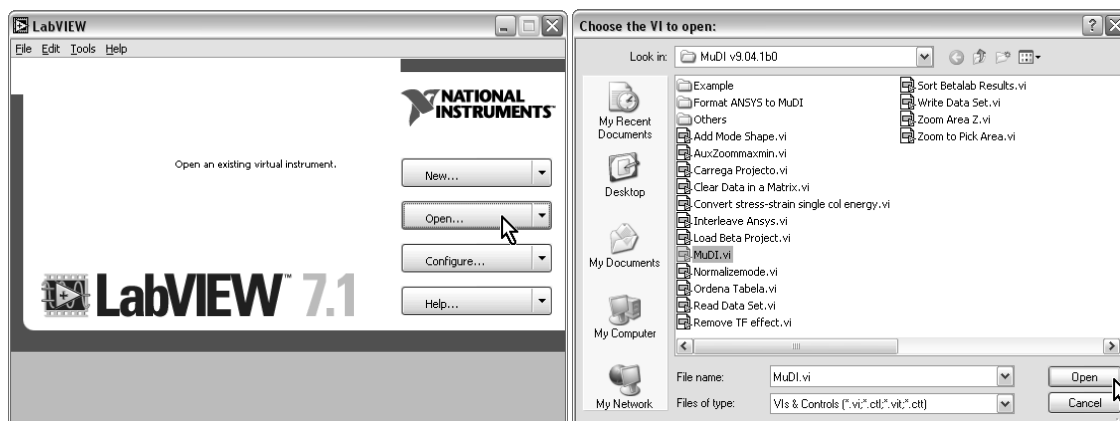


Figure F.1: Opening MuDI[®] VI.

Another window will open. This new window is MuDI[®]'s front panel. Before doing anything else, the button “Run” must be pushed (near the upper left corner of the window, as shown in figure F.2).

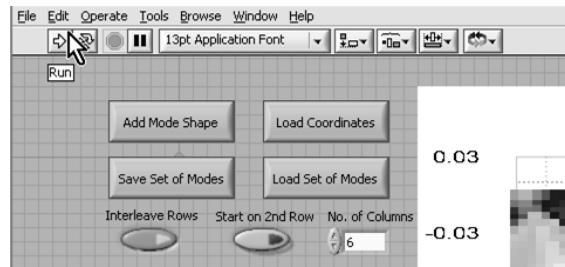


Figure F.2: Starting MuDI® VI.

At this moment, MuDI® is running. The first thing to do is to load the input files, as follows:

- One file containing the coordinate system of the bi-dimensional model. This is a text file with 3 tab delimited columns. The first column identifies the node number, the second column is the coordinate in the x direction and the third column is the coordinate in the y direction. To load the file containing the geometrical Cartesian coordinates, left-click on “Load Coordinates” (figure F.3);
- One file containing the set of modes, which in fact are the PSF functions (alternatively, a set of files containing individual modes can also be loaded, as we will see later). This is a text file with several tab delimited columns that can result in large file sizes. For each mode shape, there is an associated group of columns. For instance, when building the strain based PSF functions, the output files from ANSYS® have 6 columns: ε_x , ε_y , ε_z , γ_{xy} , γ_{xz} and γ_{yz} . Then, the set of modes is assembled as a file with sequential groups of tab separated columns containing the PSF functions’ elements for each mode shape. This can be done using, for instance, Microsoft® Excel® or MuDI® application itself. Consequently, for a system where 20 modes are considered, a total amount of $6 \times 20 = 120$ columns will be used. Each row corresponds to the mode number and must be sorted exactly the same way the coordinate file is in order to have a match. To load the file containing the FE model mode shapes (in this case, strains), left-click on “Load Set of Modes” (figure F.4);
- Two files containing the results from the modal identification for both the reference (healthy) and damaged structures. These files are in “bl4” format, which is the format BETAlab® uses when saving a project. To load the file containing the BETAlab®’s project for both the structural healthy and damaged states, left-click on “Load Beta Project H” and “Load Beta Project D” (figures F.5 and F.6 respectively).

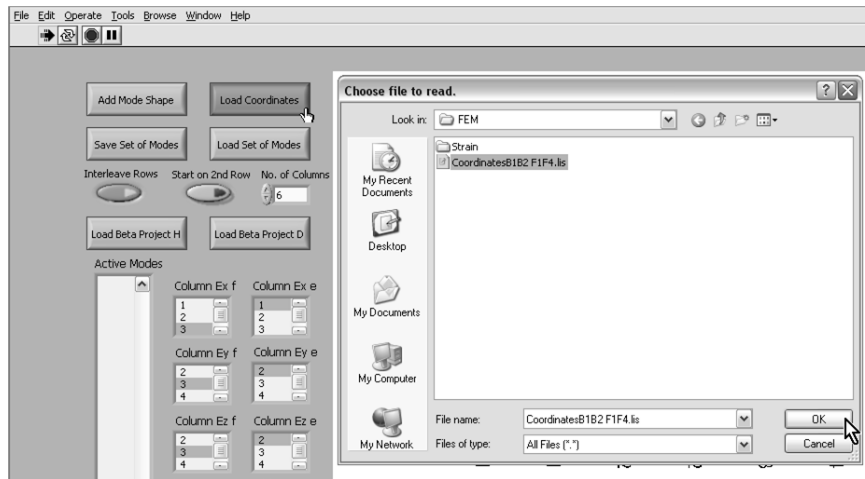


Figure F.3: Loading the file containing the geometrical Cartesian coordinates.

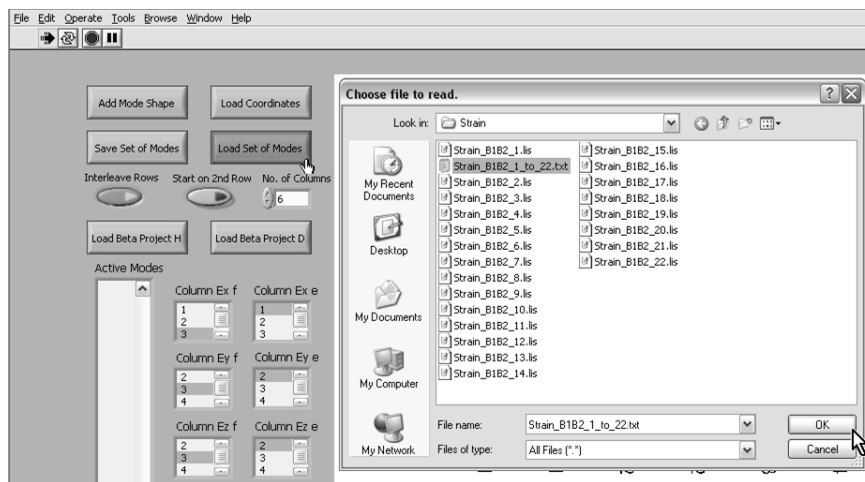


Figure F.4: Loading the file containing the FE model mode shapes (strains).

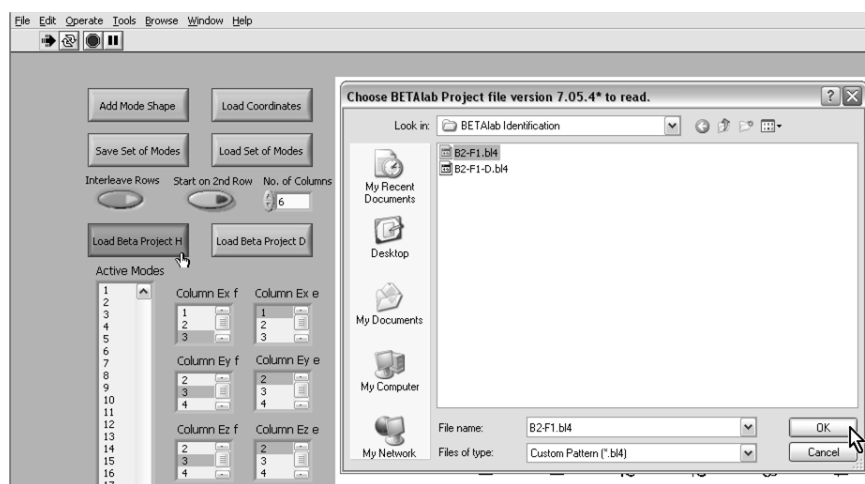


Figure F.5: Loading the file containing the BETALab[®]'s project for the structural healthy state.

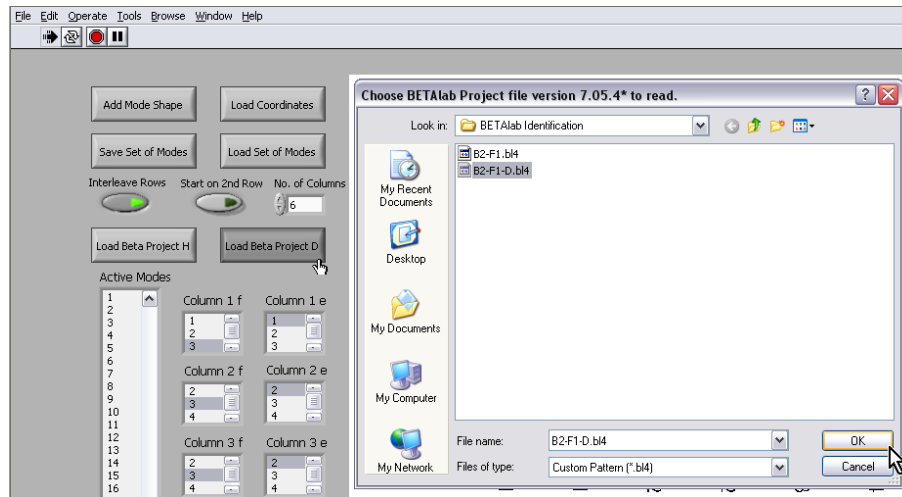


Figure F.6: Loading the file containing the BETAlab[®]'s project for the structural damaged state.

The next steps include several tasks, which are very easy to perform, since most only require buttons to be pushed. Before we explain the subsequent operations, a presentation of what the screen should look like in the end is shown in figure F.7.

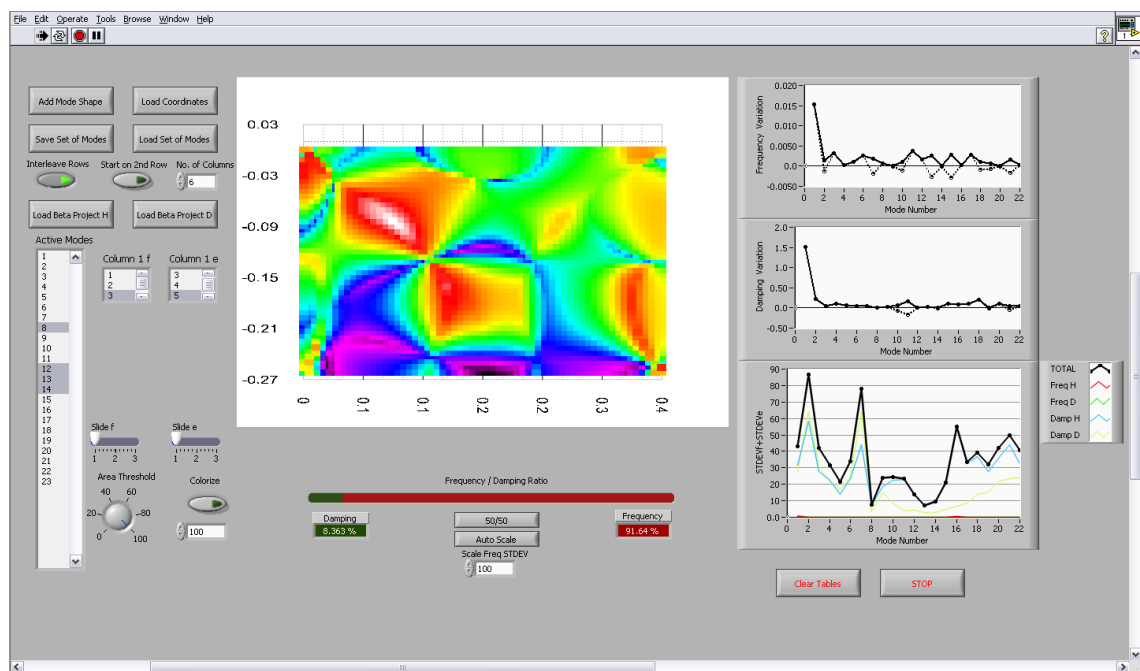


Figure F.7: MuDI[®]'s final screen for case B1H-B1D considering only modes 8 and 12 to 14.

In the above example, only modes 8 and 12 to 14 (the choice of the modes is taken for exemplification purposes only) are used for estimation of the damage location. To achieve this result, the following settings must be used:

- Interleave Rows – This is needed to be active when there are two results per node referring to either face of the surface. This happens, for instance, when we ask the FE

program to give the solution in terms of strains or stresses. If the material is symmetric around the neutral plane, the results will also be symmetric;

- Start on 2nd Row – This button selects in which of the first two lines of the file obtained from the FE software it starts reading the PSF. In other words, the face of the bi-dimensional model is selected. In many cases (mostly owe to the material properties), it is irrelevant whether this is turned on or off;
- No. of columns –It is the number of columns of the file containing the PSF's. For instance, when saving the strains in ANSYS®, 6 columns exist in the following order: ε_x , ε_y , ε_z , γ_{xy} , γ_{xz} and γ_{yz} . Since the last two columns are zero in the present example, column 5 can be used, for instance, to include the strain energy based PSF as given by equation (3.70);
- Active modes – The modes used for computing the damage location are selected here by left-clicking on them while maintaining the “Ctrl” keyboard button pressed. In the present example, only modes conducting to a cumulated error less than 20% are used. The cumulated error is shown in the bottom graphic to the right;
- Slide f – If the PSF given by (3.71) is used, this should be set to 1. It defines the amount of terms to be included in $PSF_{ij}^{\omega r}$;
- Slide e - If the PSF given by (3.70) is used, this should be set to 1. It defines the amount of terms to be included in $PSF_{ij}^{\eta r}$;
- Column 1 f – If the PSF given by (3.71) is used, this should be set to 3, defining the column ε_z of the PSF to be read as the first term of $PSF_{ij}^{\omega r}$;
- Column 1 e – If the PSF given by (3.70) is used, this should be set to 5 defining the column $\sigma_x \varepsilon_x + \sigma_y \varepsilon_y$ of the PSF to be read as the first term of $PSF_{ij}^{\eta r}$;
- Area Threshold and Colorize– Area of the plate shown in the probability map. If this value is set, for instance to 10%, only the 10% most probable areas for damage to be located are shown. This only affects the results when the button “Colorize” is active;
- 50/50 – Sets $W_f = W_d$;
- Auto Scale – Allows determining W_f (and W_d) based on equations (3.61) and (3.60). The determined values are shown in the “Frequency / Damping Ratio” red and green bar;
- Scale Freq STDEV – Custom value of κ (scale term given by equation (3.62)). Allows using a custom value for W_f . When the Auto Scale button is left-clicked this assumes a value determined with equation (3.61). It can manually be edited: if $\kappa = 0$ then $W_d = 100\%$ and if $\kappa \rightarrow +\infty$ then $W_f = 100\%$;

- Clear Tables – Clears all memory to start a new analysis;
- Stop – Stops running MuDI®.

Figure F.7 shows only the final probability description without distinguishing the contributions of DaDI and FreDI. These indexes can be shown individually by rotating the mouse wheel in the up direction (figure F.8).

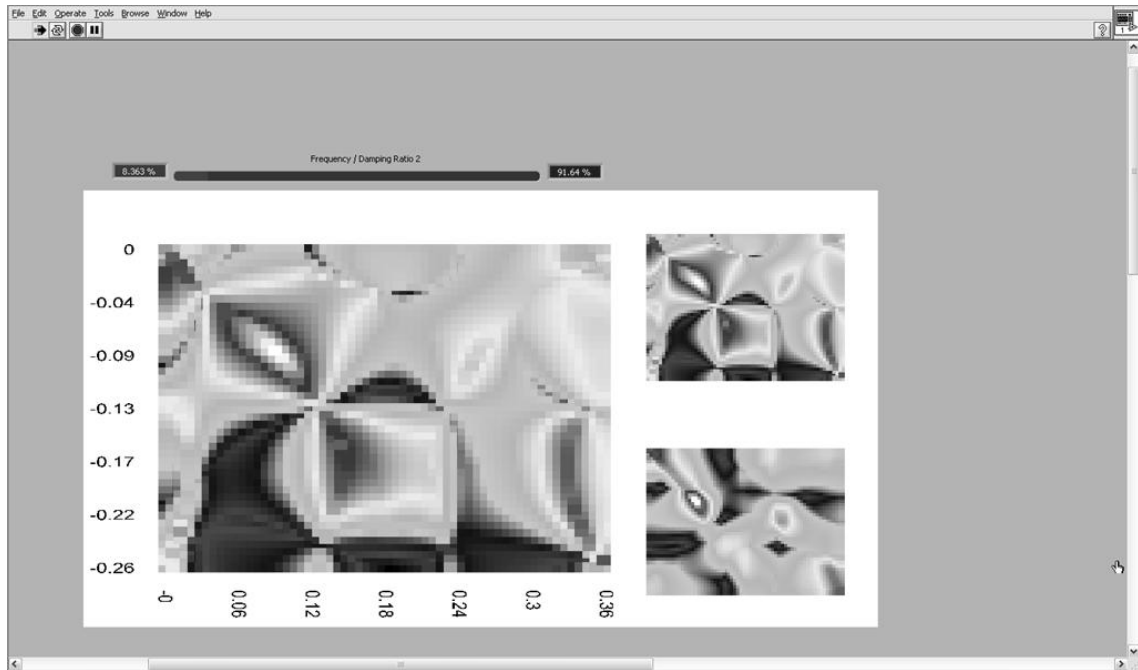
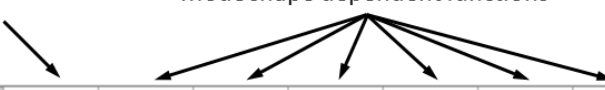


Figure F.8: MuDI®'s upper part of the final screen for case B1H-B1D considering only modes 8 and 12 to 14 in which the cumulated error is less than 20%. Top right plot is FreDI's probability map alone and bottom right plot is DaDI's probability map.

F.5 File formats (input)

An important thing that was not mentioned so far is how to build, using MuDI®, the file containing full sets of modes. When saving mode shapes with ANSYS®, these are saved as files with extension “.lis”. These files have headers that must be removed. The mode shape files for a single mode r should look somewhat like figure F.9. The first column is the node number, whereas the other columns are the PSF's – or the mode shape dependent functions – at the correspondent nodes.

Node number Mode shape dependent functions



	A	B	C	D	E	F	G
1	2	6.97E-05	0.000112	-8.61E-05	0.008565	1.28E+03	3.97E+05
2	2	-6.97E-05	-0.00011	8.61E-05	-0.00857	1.28E+03	3.97E+05
3	5491	0.000348	0.000292	-0.0003	0.011113	1.49E+04	6.82E+05
4	5491	-0.00035	-0.00029	0.000303	-0.01111	1.49E+04	6.82E+05
5	5493	0.000251	0.001523	-0.00084	0.009953	1.73E+05	7.08E+05
6	5493	-0.00025	-0.00152	0.000842	-0.00995	1.73E+05	7.08E+05
5485	8233	7.87E-05	0.001179	-0.0006	0.009048	9.32E+04	5.35E+05
5486	8233	-7.87E-05	-0.00118	0.000595	-0.00905	9.32E+04	5.35E+05
5487	8234	0.000151	0.000899	-0.0005	0.008205	5.61E+04	4.20E+05
5488	8234	-0.00015	-0.0009	0.000497	-0.00821	5.61E+04	4.20E+05
5489	8235	0.000375	0.000396	-0.00037	0.007282	2.15E+04	3.08E+05
5490	8235	-0.00038	-0.0004	0.000365	-0.00728	2.15E+04	3.08E+05

Figure F.9: Mode shape file format example (some cells were conveniently hidden for presentation purposes).

To build a file containing a full set of modes, one must first ensure no files were previously loaded. To do so, left-click on “Clear Tables” followed by “Add Mode Shape”. As many files as needed can be added, but care must be taken with the sequential order which is very important to be respected. An example of the process is shown in figure F.10, where it can be seen that files that are added appear on the “Active Modes” indicator.

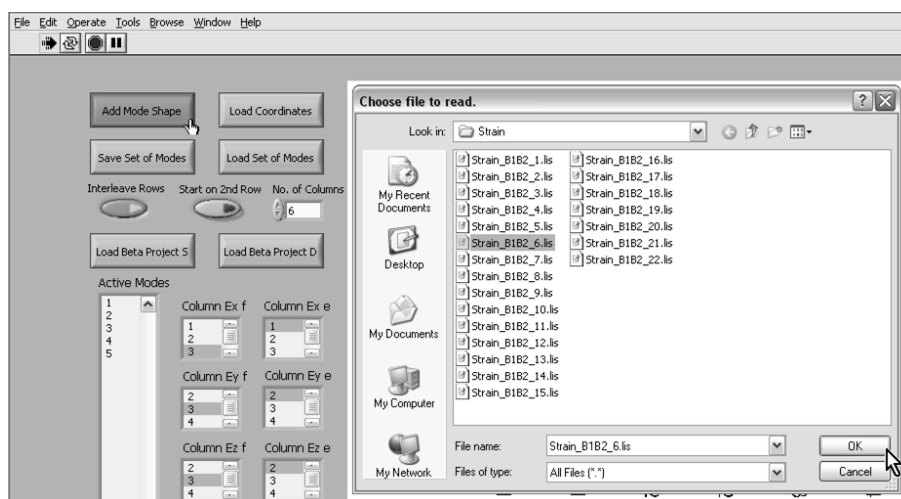


Figure F.10: Loading the files containing FE mode shapes individual modes (strains).

After adding all the modes, the file containing the full set of modes can be created, by pushing the button “Save Set of Modes”. Basically, what it does is to create a file which groups all these individual files by inserting the data in sequential columns. Thus, in the present example in which each file has 6 columns (except the first, that corresponds to the node numbers), the

first mode will occupy columns 2 to 7, the second mode will occupy columns 8 to 13, the third mode will occupy columns 14 to 19, and so on.

The file containing the nodes' coordinates is made of 4 columns only, as shown in figure F.11.

	Node number	Coordinates		
		x	y	z
	A	B	C	D
1	2	0	0	0
2	5491	0.006	-0.006	0
3	5493	0	-0.006	0
2743	8233	0.35351	-0.24395	0
2744	8234	0.35351	-0.2499	0
2745	8235	0.35351	-0.25584	0

Figure F.11: Coordinates file format example (some cells were conveniently hidden for presentation purposes).

Finally, the file formats used for computing the frequency and damping shifts is not editable in ASCII format. These files are BETAlab[®] projects, with extension “.bl4”, and should only be created with BETAlab[®].

F.6 Future versions

MuDI[®]'s version 9.04.1b0 is still an approximation of what a more user-friendly and easy-to-use version of this software should be. Thus, there are too many aspects that should be addressed. The most obvious are: it should be possible to save the results; the graphical display should be completely redesigned (as it is, it distorts the aspect ratio); it should have a more user-friendly interface. Other improvements might include automatization on the choice of the modes to be included in the analysis.